Control authority for active damping of combustion instabilities

ROEL A. J. MÜLLER

Preface

This dissertation was written in the context of my doctoral thesis at the Technische Universität München. The great majority of the work was done at IfTA Ingenieurbuero für Thermoakustik GmbH – IfTA for short – in Gröbenzell near München, in the context of the project LIMOUSINE.

I would like to thank my advisor, professor Wolfgang Polifke, and daily supervisor Jakob Hermann for their guidance and support during this research.

Furthermore I would like to thank my research partners (supervisors and fellows) from the LIMOUSINE project for the pleasant cooperation and stimulating project meetings.

I am grateful for the help I received from Robert Widhopf-Fenk and all the colleagues that were working at the software department of IfTA during my research. The developers who worked on the Argus software implemented lots of improvements without which the measurements presented in this thesis and their post-processing would have been much more cumbersome. Besides, their endless tips on better computer usage in the broadest sense helped this thesis and the underlying research in innumerable ways. The preliminary work by Constanze Temmler helped setting up the simulations in taX and CFX.

Finally I would like to thank my family and friends (many of whom were my colleagues at IfTA) who supported and motivated me throughout this project.

Summary

Modern gas turbines are required to follow increasingly stringent emission regulations. Since lean-premixed combustion causes lower NO_x emissions than traditional combustion (rich diffusion flames), it has become prevalent in modern combustion systems. Unfortunately, lean-premixed flames are also susceptible to combustion instabilities. These emerge when for a certain operating point there is a positive feedback loop between the acoustics of the system and fluctuations of the heat release. Unstable combustion can lead to an increase of pollutants or even structural damage. Avoiding unstable operating points restricts the operational envelope of a gas turbine.

The work described in this thesis is conducted at Ingenieurbüro für Thermoakustik GmbH – 'IfTA' for short – in Gröbenzell near München, Germany.

Active instability control (AIC) is a promising and flexible solution for undesired combustion oscillations. IfTA offers AIC as a commercial product. Widespread application is impeded by the unpredictability of control authority, and the lack of a framework for its assessment in practical situations. This thesis investigates control authority for active damping of combustion instabilities in experiment and simulation.

For the experimental part, two combustors are constructed and operated as thermoacoustic quarter-wave oscillators. Both combustors are run with thermal power P_{th} up to 50 kW and equivalence ratio Φ between a half and unity. The stability behaviour of the combustors is similar for these operating conditions, where greatest instability is found near stoichiometric operation. An AIC system developed at IfTA is applied to both combustors, by modulation of the fuel flow rate, while a pressure sensor is used for input.

This approach is effective on one combustor, dubbed the 'Hummer' test rig. In best cases, the amplitude of the oscillation is reduced by a factor 20. The same approach is tried, but shows ineffective on the other combustor, dubbed the 'Limousine' rig. The cause of this difference in control authority was not obvious from the constructional differences between the two combustors.

Summary

The one-dimensional acoustic network model 'taX', developed at the Technische Universität München (TUM), is extended to assess active control in a quantitative manner, focusing on the hardware implementation. In commercial AIC systems, actuation is commonly realised using *direct dive valves* (DDVs). Since the loudspeaker was the only actuator available in the original network model, a DDV is modelled to be used as an alternative active acoustic element.

The DDV element for taX is based on mass conservation and a time-varying hydraulic resistance. The resistance depends on the fluctuating valve opening. The results of the model, in terms of acoustic wave transfer functions, are compared to experimental data.

The influence of mixing and convection of the fuel between injector and flame is investigated in CFD (ANSYS CFX). AIC is implemented in simulation analogous to experiment. The distribution of the convective time between fuel injector and flame is evaluated and used to estimate the response of the heat release to modulation of the fuel mass flow. Based on these data, the damping effect of AIC on the Hummer test rig can be reproduced in simulation. As in experiment, AIC on the Limousine test rig has insufficient control authority. Comparison of the convective time distributions between fuel injector and flame suggests that the fuel–air mixing before the flame is the critical difference between the combustors, leading to the discrepancy in control authority.

Zusammenfassung

An moderne Gasturbinen werden immer strengere Emissionsvorschriften gestellt. Da eine magere, vorgemischte Verbrennung den NO_x-Ausstoß im Vergleich zur herkömmlichen Verbrennung (fette Diffusionsflamme) verringert, ist diese in modernen Verbrennungssystemen weit verbreitet. Leider sind diese mager vorgemischten Flammen auch anfällig für Verbrennungsinstabilitäten. Diese entstehen, wenn es für einen bestimmten Betriebspunkt eine positive Rückkopplung zwischen der Akustik des Systems und den Schwankungen der Wärmefreisetzung gibt. Instabile Verbrennung kann zu erhöhten Schadstoff-Emissionen oder strukturellen Schäden führen. Das Umgehen der instabilen Betriebspunkte führt zu eine Einschränkung des Betriebsbereiches der Gasturbine.

Die in dieser Dissertation beschriebenen Arbeiten sind bei dem Ingenieurbüro für Thermoakustik GmbH – kurz „IfTA" – in Gröbenzell bei München durchgeführt.

Active Instability Control (AIC) ist eine vielversprechende und flexible Lösung zur Vermeidung unerwünschter Verbrennungsschwingungen, die von IfTA vertrieben wird. Die Anwendung wird durch die Unvorhersehbarkeit der Kontroll-Autorität und dem Fehlen eines Ansatzes diese Autorität in praktischen Situationen modulieren zu können erschwert. In dieser Arbeit wird die Kontroll-Autorität bei der aktiven Dämpfung von Verbrennungsinstabilitäten im Experiment und anhand von Simulationen untersucht.

Für den experimentellen Teil sind zwei Brenner gebaut und als thermoakustische Viertel-Wellen-Oszillatoren betrieben. Beide Brenner werden mit thermischen Leistungen P_{th} bis zu $50\,kW$ und Luftzahlen zwischen eins und zwei ($1 < \Lambda < 2$) versorgt. Das Stabilitätsverhalten und dessen Abhängigkeit von den Betriebsbedingungen ist für beide Brenner ähnlich. Die stärksten Instabilitäten werden in der Nähe des stöchiometrischen Betriebes gefunden. IfTA's *active instability control* (AIC)-System ist an beiden Brennern angewendet, indem die Kraftstoffzufuhr moduliert wird, um den Verbrennungsprozess zu stabilisieren. Ein Drucksensor dient als Eingang für den Regler.

Zusammenfassung

Dieser Ansatz ist wirksam bei dem Brenner genannt „Hummer". Bei den erfolgreichsten Messungen wurde die Amplitude der Schwingung um ein Faktor 20 reduziert. Der gleiche Ansatz ist bei dem anderen Brenner (dem „Limousine") angewandt, doch kann hier keine Wirkung beobachtet werden. Die Ursache für diesen Unterschied in der Kontroll-Autorität war aus den baulichen Unterschieden zwischen den beiden Brennern nicht ersichtlich.

Das eindimensionale, akustische Netzwerk-Modell „taX", entwickelt an der Technische Universität München (TUM), ist erweitert um sowohl eine aktive Kontrolle, als auch besonders den Einfluss der Hardware-Implementierung quantitativ bewerten zu können. In kommerziellen AIC-Systemen wird die Betätigung häufig mit Servoventilen (*Direct Drive Valves* – DDVs) realisiert. Da der Lautsprecher das einzige aktive Stellglied in dem ursprünglichen Netzwerkmodell war, ist ein DDV als alternatives aktives Element modelliert.

Das DDV-Element für taX basiert auf Massenerhaltung und einem zeitvariablen hydraulischen Widerstand. Der Widerstand ist abhängig von der schwankenden Ventilöffnung. Die Ergebnisse, in Form von Schallwellenübertragungsfunktionen sind mit den experimentellen Daten verglichen.

Der Einfluss der Vermischung und Konvektion zwischen der Kraftstoffeinspritzvorrichtung und der Flamme ist in CFD (ANSYS CFX) untersucht. AIC ist in der Simulation analog zum Experiment implementiert. Die Verteilung der konvektiven Zeit zwischen der Kraftstoffeinspritzung und der Flamme ist ausgewertet und wird verwendet um die Reaktion der Wärmefreisetzung auf die Modulation des Kraftstoffmassenstromes zu schätzen. Basierend auf diesen Daten ist die dämpfende Wirkung der AIC an dem Hummer-Brenner in der Simulation reproduziert. Wie im Experiment, verfügt die AIC an dem Limousine-Brenner nicht über eine ausreichende Kontroll-Autorität. Der Vergleich zwischen den konvektiven Zeitverteilungen vom Brennstoffinjektor zur Flamme weist darauf hin, dass der Mischungsprozess von Kraftstoff und Luft stromaufwärts der Flamme gesehen, den entscheidenden Unterschied zwischen den Brennern darstellt, welcher zu der Differenz in der Kontroll-Autorität führt.

Samenvatting

Moderne gasturbines moeten aan steeds strenger wordende emissie-eisen voldoen. Arm voorgemengde verbranding (*Lean-premixed combustion*) is een techniek die de NO_x-uitstoot verminderd in vergelijking met traditionele verbranding (met rijke diffusievlammen) en wordt daarom tegenwoordig algemeen toegepast. Helaas zijn arm voorgemengde vlammen ook vatbaarder voor verbrandingsinstabiliteiten, die ontstaan wanneer er voor een bepaald bedrijfspunt een positieve terugkoppeling ontstaat tussen de akoestiek van het systeem en fluctuaties in de warmteafgifte. Onstabiele verbranding kan leiden tot een verhoogde uitstoot van schadelijke stoffen of zelfs materiële schade aan de installatie. Aangezien bedrijfspunten waarbij instabiliteit optreedt vermeden moeten worden, beperkt dit de flexibiliteit waarmee de turbine bedreven kan worden.

Het onderzoek beschreven in dit proefschrift is uitgevoerd bij Ingenieurbüro für Thermoakustik GmbH – afgekort als „IfTA" – in Gröbenzell bij München in Duitsland.

Actieve onderdrukking (*active instability control* – AIC) is een veelbelovende en flexibele maatregel tegen ongewenste verbrandingsinstabiliteiten, die door IfTA commercieel wordt aangeboden. Wijdverbreide toepassing wordt echter gehinderd door de onvoorspelbaarheid van de effectiviteit van de controle (*controle-autoriteit*), en het ontbreken van een systematisch methode waarmee deze controle-autoriteit voor praktische situaties voorspeld kan worden. Dit proefschrift onderzoekt de controle-autoriteit bij de actieve demping van instabiele verbranding in experiment en simulatie.

Voor het experimentele gedeelte zijn twee branders gebouwd die zich als thermoacoustische kwart-golf-resonatoren gedragen. Beide branders worden gevoed met een thermisch vermogen P_{th} tot 50 kW en een lambdawaarde tussen één en twee ($1 < \Lambda < 2$). Voor deze bedrijfsparameters hebben de beide branders vergelijkbare trends in stabiliteit, waarbij de sterkste instabiliteit wordt gevonden rond stoïchiometrische condities. IfTA's AIC-systeem is geïnstalleerd op beide branders, waarbij de brandstoftoevoer gemoduleerd word door een regelaar met een druksensor als input.

Deze aanpak is effectief op één van beide branders (de „Hummer"), waarbij de amplitude van de instabiliteit in de succesvolste experimenten met een factor 20 verminderd wordt. Dezelfde aanpak is geprobeerd op de andere brander (de „Limousine"), maar bleek daar niet effectief. Dit verschil in controle-authoriteit liet zich niet verklaren uit de verschillen in ontwerp tussen beide branders.

Het één-dimensionale akoestische netwerkmodel „taX", is ontwikkeld aan de Technische Universität München (TUM). Dit model is uitgebreid om het effect van actieve controle kwantitatief te kunnen beoordelen, met het zwaartepunt op de uitvoering van de hardware. In commerciële AIC systemen worden servoventielen (*direct dive valves* – DDVs) vaak als actuator ingezet. Aangezien luidsprekers de enige beschikbare actuatoren waren in het oorspronkelijke netwerkmodel, is een model van een DDV ontwikkeld, dat als actief akoestisch element in taX gebruikt kan worden.

Het DDV-element is geformuleerd op basis van massabehoud en een tijdsafhankelijke hydraulische weerstand, waarbij de weerstand afhankelijk is van de variabele ventielopening. De resultaten van het model, in de vorm van akoestische golfoverdrachtsfuncties, worden vergeleken met experimentele data.

De invloed van het mengproces en de convectie van de brandstof tussen injector en vlam is nader onderzocht met CFD (ANSYS CFX). AIC is, analoog aan de experimentele aanpak, in de simulatie geïmplementeerd. De verdeling van de convectieve tijd tussen injector en vlam is geëvalueerd en gebruikt om de respons van de warmteafgifte op modulatie van de brandstof-massastroom te schatten. Met behulp van deze gegevens kon de succesvolle toepassing van AIC op de Hummer worden gereproduceerd in de simulatie. Net als in het experiment heeft AIC onvoldoende autoriteit bij de brander Limousine. Een vergelijking van de verdelingen van de convectieve tijd tussen brandstofinjector en de vlam suggereert dat het mengproces van brandstof en lucht voor de vlam het kritieke verschil is tussen beide branders, waardoor het verschil in controle-authoriteit te verklaren is.

Contents

Contents

Contents

Appendices 224

List of figures

List of tables

Nomenclature

Upright X and Y are placeholders for context-dependent units.

Latin

Italics, upper case

A	m^2	Area
ASD_X	X^2	Auto-spectral density
B	T	Magnetic flux density
C_p	J/K	Heat capacity at constant (static) pressure
C_V	J/K	Heat capacity at constant volume
$Coh_{X,Y}$	–	Coherence
$CSD_{X,Y}$	XY	Cross-spectral density
D	m	Diameter
E	J	Energy
F	–	Form factor
F	N	Force
H	J	Enthalpy
$\overset{\star}{H}$	J	Formation enthalpy
He	–	Helmholtz number: $He \equiv \omega L_{\mathrm{max}}/c$
I	A	Electric current
$\bar{\bar{I}}$	–	Identity matrix: $I_{i,j} = \begin{cases} 1 & \text{if } i = j \\ 0 & \text{else} \end{cases}$
$\vec{J}_X$	X/(m^{2}s)	Flux of quantity X
LHV	J	Lower heating value
K	N/m	Stiffness
L	m	Length

M	–	Mach number: $M \equiv u/c$
N	–	Number
Nu	–	Nusselt number: $Nu = h_{\mathrm{cv}} L / k_{\mathrm{cd}}$
P	W	Power
Pr	–	Prandtl number: $Pr = C_p \mu / k_{\mathrm{cd}}$
Q	J	Heat
R	Ω	Electric resistance
$\tilde{R}$	J/(kg K)	Specific gas constant: $\tilde{R}_X = \underline{R} / \underline{m}_X$
$\underline{R}$	J/(kmol K)	Universal gas constant
Re	–	Reynolds number: $Re \equiv \rho\, u\, L / \mu$
RI	–	Rayleigh index
S	m/s	Speed
T	K	Temperature
U	V	Voltage
V	m³	Volume
W	J	Work
X	X	Various temporarily used quantities
Y	Y	Various temporarily used quantities
Z	Pa/(m/s)	Acoustic impedance

Italics, lower case

c	m/s	Speed of sound
f	Hz	Ordinary frequency: $f \equiv \omega/(2\pi)$
h	W/(m² K)	Heat transfer coefficient
i	–	(Row) index
j	–	(Column) index
k	–	Index
k	m⁻¹	Wave number
k_{cd}	W/(m K)	Heat conductivity
m	kg	Mass
n	kmol	Amount of substance
n	–	Amplification factor

$\vec{n}$	–	Unit normal vector
p	Pa	(Static) pressure
$\dot{q}$	W/m^3	Heat release rate per volume
s	rad/s	Laplace-domain coordinate: $s \equiv i\omega$
s	J/K	Entropy
t	s	Time
u	m/s	Velocity
$\vec{x}$	m	Position vector: $\vec{x} = (x, y, z)^{\mathrm{T}}$
x	m	Coordinate, usually stream-wise
y	m	Coordinate
z	m	Coordinate, usually span-wise, right handed

Calligraphic

$\mathcal{A}$	–	Absorption coefficient
$\mathcal{C}$	–	Coefficient
$\mathcal{D}$	–	Transfer function of a pure delay
$\mathcal{G}$	X/Y	Transfer function
$\mathcal{H}$	X/Y	Impulse response
$\mathcal{L}$	Ω s	Self-inductance
$\mathcal{O}$	X	Order of magnitude
$\mathcal{Q}$	–	Quality factor
$\mathcal{R}$	–	Reflection coefficient
$\mathcal{S}$	(m/s)/Y	Source coefficient
$\mathcal{T}$	–	Transmission coefficient
$\mathcal{X}$	kmol/kmol$_{\text{tot}}$	Mole fraction
$\mathcal{Y}$	kg/kg$_{\text{tot}}$	Mass fraction

Sans-serif

A	System matrix
B	Input matrix
C	Output matrix
D	Feedthrough matrix
S	Scattering matrix
T	Transfer matrix

Fraktur

$\mathfrak{F}$	Fourier transform
$\mathfrak{H}$	Hilbert transform
$\mathfrak{I}$	Imaginary part
$\mathfrak{L}$	Laplace transform
$\mathfrak{R}$	Real part

Double struck

$\mathbb{C}$		Complex plane
$\mathbb{N}$		Natural numbers: $\mathbb{N}_0 = 0, 1, 2, \ldots;\quad \mathbb{N}_1 = 1, 2, 3, \ldots$
$\mathbb{R}$		Real numbers
f	m/s	Downstream travelling characteristic wave amplitude: $f \equiv \frac{1}{2}\left(\frac{p'}{\rho c} + u'\right)$
g	m/s	Upstream travelling characteristic wave amplitude: $g \equiv \frac{1}{2}\left(\frac{p'}{\rho c} - u'\right)$

Greek

Upper case

Λ	–	Air excess ratio: $\Lambda = 1/\Phi$
Φ	–	Equivalence ratio

Lower case

γ	–	Heat capacity ratio : $\gamma \equiv \tilde{C}_p \big/ \tilde{C}_V$
ϵ	–	Emissivity
ζ	–	Hydraulic loss coefficient: $\zeta \equiv \Delta p_{\text{st}} \big/ \left(\frac{1}{2} \rho\, u^2 \right)_{\text{ref}}$
η	X/Y	Damping, units depend on definition
λ	m	Wave length: $\lambda \equiv c / f$
μ	Pa s	Dynamic viscosity
ρ	kg/m^3	Density
σ	s	Temporal dispersion / standard deviation
σ_{SB}	W/(m^2 K^4)	Stefan–Boltzmann constant: $\sigma_{\text{SB}} \approx 5.67 \cdot 10^{-8}\, \text{W}/(\text{m}^2\,\text{K}^4)$
φ	rad	Phase
τ	s	Delay
$\bar{\bar{\tau}}$	Pa	Viscous stress tensor
ω	rad/s	Angular frequency

Subscripts

abs	Absolute		d	Discharge
ac	Acoustic		dn	Downstream
act	Actuator		dom	Dominant
air	Air		ec	End correction
amp	Amplifier		env	Environment
an	Analytical		eq	Equivalent
C	Cycle or contour		fl	Flame
ca	Cavity		ft	Filter
cld	Cold flow		F	Fuel
cv	Convection		G	Gauge
cc	Combustion chamber		H	Hydraulic
cd	Conduction		hot	Hot flow
CL	Closed loop		in	Inlet
cn	Cone		kin	Kinetic

L	Laminar	rw	Raw
ls	Loudspeaker	S	Sensor
M	Motor	sm	Sample
max	Maximum	st	Stagnation
min	Minimum	sp	Spool
nk	Neck	sys	Systemscr
nom	Nominal	T	Turbulent
OL	Open loop	tot	Total
out	Outlet	th	Thermal
pl	Plenum	up	Upstream
rd	Radiation	vl	Valve
R	Resonance	vcl	Voice coil
ref	Reference	wl	Wall

Mathematical notation

Mathematical constants

e	Euler's number: $e \approx 2.7183$
i	Imaginary unit: $i^2 \equiv -1$
π	Archimedes' constant: $\pi \approx 3.1416$

Modifiers

$\vec{\circ}$	Vector
$\dot{\circ}$	Quantity per time
$\tilde{\circ}$	Quantity per mass
$\overset{\smile}{\circ}$	Quantity per mole
$\hat{\circ}$	Phasor
$\bar{\circ}$	Time-average
$\circ'$	Harmonic / small deviation from time-average
$\circ''$	Unstructured deviation from time-average (noise)

$\circ_{\text{II},3}$ (For example) 3rd harmonic of mode 'II'

$\circ^*$ Complex conjugate

$\circ^{\text{T}}$ Matrix transpose

Derivatives

Derivatives are written using Euler notation and the nabla symbol (∇).

$\text{d}_X\circ$	Derivative (with respect to X)
$\partial_X\circ$	Partial derivative (with respect to X)
$[\partial_X\circ]_Y$	Partial derivative (with respect to X, at constant Y)
$\vec{\nabla}\circ$	Gradient: $\vec{\nabla}\circ \equiv \left(\partial_x\circ, \partial_y\circ, \partial_z\circ\right)^{\text{T}}$
$\vec{\nabla}\cdot\circ$	Divergence
$\vec{\nabla}\times\circ$	Rotation
$\text{D}_t\circ$	Material derivative: $\text{D}_t\circ \equiv \partial_t\circ + \vec{u}\cdot\vec{\nabla}\circ$

Other acronyms

AD	Digital–analogue
AIC	Active instability control
ANSYS	<u>An</u>alysis <u>Sys</u>tem, a developer of engineering simulation software
BVM	Burning velocity model
CFD	Computational fluid dynamics
CFX	CFD software, developed by ANSYS
CLTF	Closed-loop transfer function
CTA	Constant temperature anemometry
DA	Digital–analogue
DDV	Direct dive valve
DFT	Discrete Fourier transform
DSP	Digital signal processor

Nomenclature

ECFM	Extended coherent flame model
EMA	Exponential moving average
FFT	Fast Fourier transform
ICP	Integrated-circuit piezoelectric
IEPE	Integrated electronics piezoelectric
IfTA	Ingenieurbüro für Thermoakustik GmbH
ITN	Initial training network
LC	Limit cycle
LES	Large eddy simulation
LIMOUSINE	Limit cycles of thermoacoustic oscillations in gas turbine combustors
LMS	Least mean squares
LVDT	Linear variable differential transformer
MEMS	Micro electro-mechanical system
MIMO	Multiple inputs, multiple outputs
NIST	National Institute of Standards and Technology
OLTF	Open-loop transfer function
OMDS	Oscillation Monitoring and Diagnostic System
PC	Personal computer
PDE	Partial differential equation
PMT	Photo multiplier tube
RANS	Reynolds-averaged Navier–Stokes
RMS	Root mean square, also known as quadratic mean
SAS	Scale-adaptive simulation
SISO	Single input, single output
SLPM	Standard litre per minute
SST	Shear stress transport
taX	1-D thermoacoustic network model, developed at the TUM
TUM	Technische Universität München

1 Introduction

The research described in this thesis investigates the question of control authority for active damping of combustion instabilities. The research was conducted at IfTA Ingenieurbüro für Thermoakustik GmbH – 'IfTA' for short – in Gröbenzell near München. IfTA offers *active instability control* (AIC) as a commercial solution to combustion instabilities. The scope and context of this thesis will be elaborated in this introduction.

Thermoacoustics – from Greek $\theta\epsilon\rho\mu\acute{o}\varsigma$ (hot) and $\alpha\kappa o\upsilon\sigma\tau\iota\kappa\acute{o}\varsigma$, which is the adjective form of the verb $\alpha\kappa o\acute{\upsilon}\omega$ (to hear) – is the science describing the interaction between heat transfer and sound. In the case of a mutual amplification of an acoustical field and fluctuation of the heat release by a flame, this phenomenon can lead to great amplitudes of pressure oscillation. The interest for this field of research was kindled by several observations in the late 18th century, as reviewed in sec. 1.1. In those days thermoacoustic phenomena were considered to be a fascinating, even delightful curiosity.

This attitude changed during the middle of the 20th century, when thermoacoustic oscillations started appearing in industrial installations. At higher amplitudes, combustion oscillations can cause severe material damage, for instance as shown in fig. 1.1.

These problems were first found in rockets and jet engine afterburners, described in sec. 1.2. Later combustion instabilities appeared in turbines engines. Power generating gas turbines are introduced in sec. 1.3. Unstable combustion in power generating gas turbines, as well as airborne turbines, is often associated with lean-premixed combustion, discussed in sec. 1.4.

Even at a lower level – when there is no direct mechanical threat to the combustion system itself – the vibrations can disturb sensitive equipment or people in the vicinity. Additionally they can lead to an increase in pollutants. Currently the main concern is the restrictions that possible instabilities impose on the flexibility of operation for power producing gas turbines.

Figure 1.1: Gas turbine parts – a connecting piece (left) and a burner assembly (right) – damaged by combustion induced oscillations; courtesy of Laborelec/GDF–Suez.

This research is part of the Marie Curie initial training network (ITN) 'LIMOUSINE', which is introduced in sec. 1.5. Active control of combustion instabilities will be introduced in sec. 1.6. The introduction will be concluded by an outline of this thesis in sec. 1.7.

1.1 Discovery of the 'chemical harmonica'

Ueda[279] is probably the first to document an example of thermoacoustics. In a ghost story, he mentions a divinatory cauldron. Its roar was considered an omen for good fortune:

> 「巫子祝詞をはり。湯の沸上るにおよびて。吉祥には釜の鳴音牛の吼るが如し。凶きは釜に音なし。」

This roughly translates to:

> 'The temple maiden recites a prayer and instigates the water to boil. For good fortune, the howl of the cauldron would resemble that of cattle. To misfortune, the cauldron would remain silent.'

Although ghosts can safely be assumed fictional, the described ritual is real, and is still performed at the Kibitsu Shrine in Okayama.[132] The phenomenon is used in Japan to introduce children to thermoacoustics.[133] Figure 1.2 shows the cauldron in cross section.
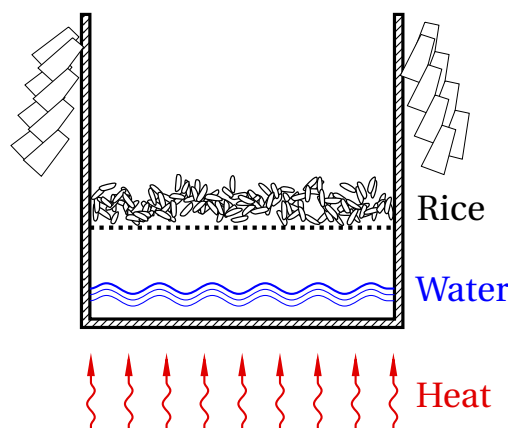
Figure 1.2: Schematic, cross-sectional view of the cauldron of Kibitsu, with lid removed.[132, 133] Paper streamers are connected to the top for spiritual purposes.

Higgins[113] might be the first to investigate this phenomenon scientifically. Clearly pleased by this curious source of sound, he writes (in 1802, when the long s was still used in mainstream typesetting):

> 'It was in the year 1777, that I firſt exhibited the experiment you mention, and produced ſeveral ſweet tones, [. . .]'

As soon as 1795 (before Higgins published his article), Chladni[44] mentions various pioneers working in the field of thermoacoustics, and proposes that this new phenomenon could be used to construct a 'chemical organ'. As with a normal organ, the pitch of the tone can be controlled by the length of the pipes. Many publications follow, discussing the conditions under which flames may produce sound. Wheatstone[287] used flames and a rotating mirror to visualise sound. This showed that flames do not only *produce* sound, amplified by a surrounding pipe, but flames *respond* to sound as well.

Non-linear effects were found as well. Tyndall[277] noted that the oscillation state of flames can show *hysteresis*. That is, stable flames can be triggered to sing if they are 'close' to instability. After damping the sound, by blocking the airflow with a finger, the flame is silent again. A strong instability can even extinguish the flame.[240] LeConte[148] noted flames can pulse to the beat (amplitude fluctuation) of music, i.e. the *average* shape of an unstable flame is not the same as its stable shape.

Rijke[230] devised a set-up which allowed him to investigate thermoacoustics without the presence of a flame. This was an important step forward, since it was a clear demonstration that movement of the flame or chemistry for instance are no necessity for thermoacoustic phenomena. This device, nowadays known as the 'Rijke tube' consists of a straight tube with a heated metal gauze situated in the upstream half, as in fig. 1.3. The mean flow is caused by natural convection when the tube is held vertically. The gauze can be heated by a gas flame or electricity, although gathering enough electrical power posed a considerable challenge in 1859.

Rijke found that the temperature difference between the gauze and the surroundings were driving the oscillation and that the experiment works best with a cold tube. Upon this, Riess[228] showed that a cold gauze in a tube with hot flow flowing through can radiate sound as well. Best results were obtained with a water-cooled tube.[229] The Rijke tube has been a very popular set-up to investigate thermoacoustics ever since.[223]

By 1878, Rayleigh[265] formulated his famous criterion:

> '[. . .] If heat be given to the air at the moment of greatest condensation, or taken from it at the moment of greatest rarefaction, the vibration is encouraged. On the other hand, if heat be given at the moment of greatest rarefaction, or abstracted at the moment of greatest condensation, the vibration is discouraged. [. . .]'
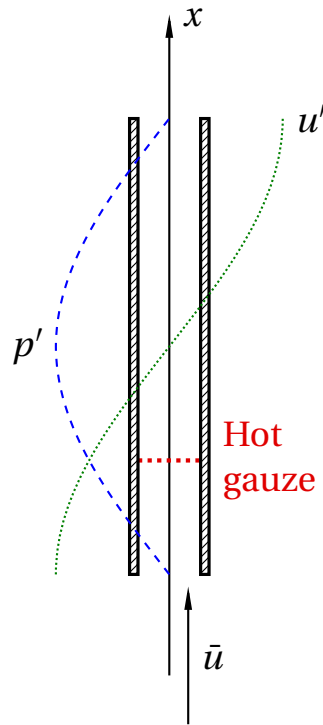
Figure 1.3: Rijke's thermoacoustic resonator tube; The distribution of pressure fluctuating p' and velocity fluctuation u' are indicated as function of position x.

The working of the Rijke tube can now be analysed as follows: the pressure at the gauze is highest after the fluctuating flow was directed into the tube at both sides. During inflow, the fluctuating flow at the gauze is in the same direction as the mean flow due to free convection. The fluctuating heat release by convection comes slightly later, due to dynamic boundary layer development, as argued by Lighthill.[157] Since the pressure is slightly higher when the heat release is greatest, a thermoacoustic oscillation develops.

1.2 Thermoacoustics in rockets and ramjets

During the Second World War, or maybe even earlier, combustion instabilities appeared in the newly developed solid and liquid-fuelled rockets. Culick,[56: Ch.1] Harrje and Reardon,[99] and Wimpress[290] give a very decent overview of the subject. During the 1960s, the liquid-fuelled F-1 rockets, used on the prestigious Apollo missions, suffered from thermoacoustic instabilities which led to great

research interest. With around 10 GW of power* concentrated in less than a cubic meter, even relatively small fluctuation can have disastrous results.[56: p.1-1] And since especially solid-fuelled rockets can be fired only once, a good theoretical understanding of the matter was crucial. Nowadays, the trend towards larger payloads requires larger engines which in turn allow for more modes of oscillation for a given frequency range. The use of new, cleaner fuels also requires new models to predict their stability.[236, 250, 283]

Starting at a similar time (WW II and after), jet powered aircraft were developed. Like rocket engines, their combustion chambers were susceptible to thermo-acoustic oscillations. Most notably the problem emerged on ramjets[82, 159] and afterburners.[23, 151, 180] Since these combustion systems had much larger resonant volumes – while their construction was much lighter – in comparison to piston engines, combustion instabilities became more likely to cause structural damage. In the case of ramjets, there is the added risk that longitudinal oscillations can disturb the inlet shock system, leading to engine stall in the worst case.

1.3 Power generating gas turbines

Undesired instabilities arise in a wide range of combustion systems. IfTA has traditionally concentrated on active control solutions for land based, electric power generating gas turbines. The possible applications of the research discussed here are, however, by no means restricted to these systems. Nonetheless, explicitly or implicitly, application on power generating gas turbines may be assumed.

Turbine is the ablative case of *turbo*, the Latin word for whirlwind. Contrary to an Otto engine, which uses a piston in a cylinder to compress and expand air, a gas turbine uses rotating (whirling) aerofoils for the same purpose. Figure 1.4 gives a simple overview of a gas turbine. The main parts are the *compressor*, shown on the left, where the incoming air is compressed. Fuel is added to the compressed air and combusted in the *combustion chamber*. At a constant pressure, the temperature increase leads to an increase in volume. After leaving the combustion chamber, the gas mixture comes in the actual turbine, the

---

* The worlds largest nuclear power plant had an output capacity of 8.2 GW,[269] while currently the world's largest gas turbine (9HA.02 by General Electric) currently has a thermal power of 0.77 GW and a maximum output of 0.47 GW.[89]

namesake of the complete device. In the turbine, now more volume of air is expanded than was compressed in the compressor. This delivers more power than was needed to drive the compressor and the surplus energy can be used to generate electricity.
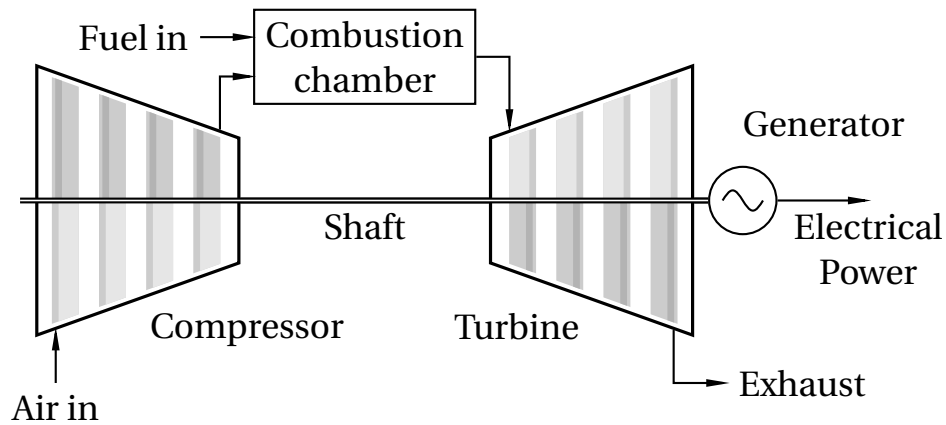
Figure 1.4: Overview of a single-cycle, single-shaft gas turbine for power generation.

A *gas* turbine is a system where – contrary to a steam turbine or water turbine – mechanical labour is extracted from a throughflow of gas, mostly air. This does not imply the *fuel* has to be gaseous.

Power generating gas turbines are typically much larger in size – compared to aero-engines for instance – while production series are small. Figure 1.5 gives an impression of typical dimensions. The large dimensions and smaller series make it hard to use prototypes to thoroughly check power generating gas turbines for thermoacoustical issues. As a result, the demand is high for predictive tools, and postfix solutions in case the predictions fail.

Power generating gas turbines are operated for many thousands of hours without maintenance or overhaul. Due to these long running times, acceptable amplitudes of pressure oscillations are much lower than for other combustion systems.[155]
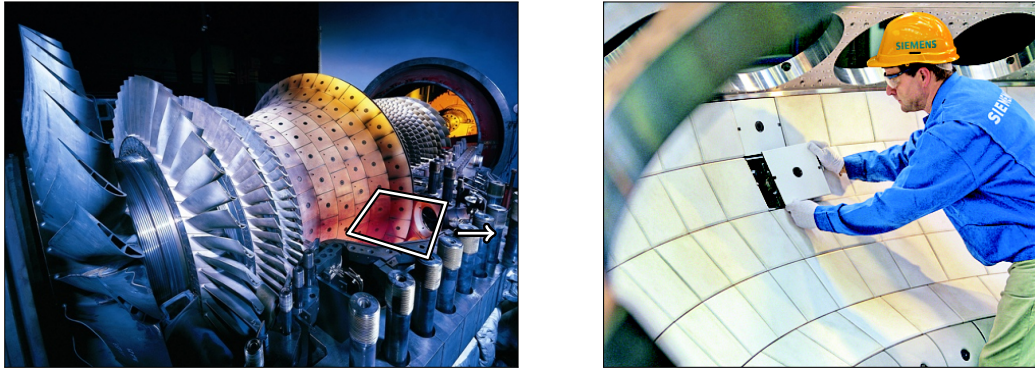
Figure 1.5: Left: An opened gas turbine shows its inner parts: the compressor in the background, the combustion chamber in the middle and the turbine expander in the foreground. Right: An engineer installs ceramic heat shields to the outer combustion chamber wall. The approximate location in the total assembly is indicated by the white quadrangle in the left figure; Courtesy of Siemens AG.[249, 292]

1.4 Lean-premixed combustion

Thermoacoustics in airborne and stationary gas turbines became a concern more recently, when restrictions on emissions increased. In the European Union for instance, these regulations can be found in the Large Combustion Plants (LCP) Directive by the European Comission.[74] The restrictions on emission of NO_x have had the greatest impact on gas turbine engineering.

According to the Zel'dovich mechanism,[293] NO_x production increases rapidly with temperature. A too cold flame on the other hand produces CO. To keep both emissions low and keep the flame temperature within the required window, *lean-premixed* combustion is required, which unfortunately leads to an increased risk of instability as well.[239: p.36-4]

Traditionally, the firing temperature of gas turbines has been as high as possible without causing thermal damage to the turbine blades, to increase efficiency.[234] Film cooling of turbine blades and combustor liners allowed for a high firing temperature, whilst keeping the temperature of the mechanical parts of the gas turbine relatively low. A pleasant side-effect of these cooling systems was the damping effect they had on acoustics.

The formation of NO_x increases exponentially with the local flame temperature,[293] so the emissions depend disproportionally on hot spots in the combustion process. Cold spots on the other hand promote the formation of CO,

another unwanted combustion product. To reduce these emissions, whilst keeping the efficiency high, it is important to have a firing temperature which does not vary too much in space and time. To achieve this goal, modern gas turbines guide as much as possible of the available air through the primary flame region, giving rise to the term 'lean-premixed combustion'.[239]

Unfortunately, for lean flames, the combustion characteristics depend especially strongly on fluctuations of the local equivalence ratio.[156, 299] Due to the premixing, there is less geometrical definition in the gradients of the equivalence ratio. Therefore flammability becomes more sensible to acoustic fluctuations, and more susceptible to instability. The reduction of cooling air aggravates this tendency, which has made modern gas turbines more susceptible to instabilities.[131]

For proprietary reasons, little information has been published about combustion instabilities in commercial gas turbines of either kind.[56: p.1-17] In some cases this information would be published only much later, such as for instance in the case of the research by Dowling.[68]

Renewable sources of energy, such as solar and wind power, are on the rise, but can not guarantee a delivered output. Traditional sources of energy, such as gas turbines, are required to flexibly compensate for shortfalls in renewable output. Gas turbines are increasingly operated at partial load and as a result, stable operation is required for an increased range of operating points, while conforming to ever stricter emission guidelines. This is expected to increase thermoacoustic problems in both stationary and airborne gas turbines.[7, 10, 65] Varying (bio) fuel composition influences the combustion behaviour as well and can lead to additional, unexpected instability issues.[154]

1.5 Project 'LIMOUSINE'

The EU-funded Marie Curie ITN 'LIMOUSINE' (Limit cycles of thermoacoustic oscillations in gas turbine combustors) aims to strengthen the fundamental scientific work in the field of thermoacoustic instabilities in combustion systems. The project partners, situated in various European countries, as shown in fig. 1.6, have done analytical, numerical and experimental research to reach this goal.

For comparability of results between project partners, especially validation of analytical work, a model combustor was devised. This combustor, which

1. Keele University
2. ANSYS UK
3. Imperial College London
4. University of Twente
5. Laborelec/GDF–Suez
6. Siemens Power Generation (Fossil Power Division)
7. DLR (Institute of Combustion Technology)
8. IfTA GmbH
9. Brno University of Technology
10. University of Zaragoza
11. CERFACS

Figure 1.6: Partners of the project 'LIMOUSINE', and their location within the European Union.

will be analysed in detail in chapter 4, comprises of a rectangular resonator tube with a bluff-body stabilised, partially premixed flame. A great deal of the development of this combustor, including the production of prototypes, was done at the University of Twente.[134, 233] Besides, early in the project another prototype combustor was developed at IfTA, which was used for this research as well.[136]

Both combustors exhibit a loud low-frequency thermoacoustic oscillation, often referred to as *humming*. For brevity, the model combustor used throughout the LIMOUSINE project will be called the 'Limousine' test rig. The prototype constructed at IfTA is longer and has a lower resonant frequency as a result. It will therefore appropriately be named the 'Hummer'. Figure 1.7 gives a first impression of the combustors. Both will be discussed in more detail in chapter 4.

Roughly half the numerical work done in the scope of the project 'LIMOUSINE' and all analytical and experimental work concerned the Limousine combustor or one of its variants, while the other half of the numerical research was dedicated to industrial gas turbine combustors.

This thesis describes the work done in sub-project '4.1: Active control of model combustor'. AIC was successfully applied to the Hummer test rig. AIC was attempted on the Limousine rig as well, but was not effective at damping the instability. Both burners are simulated in ANSYS CFX, leading to an explanation for this difference in effectiveness of AIC between both burners, discussed in sec. 6.2.
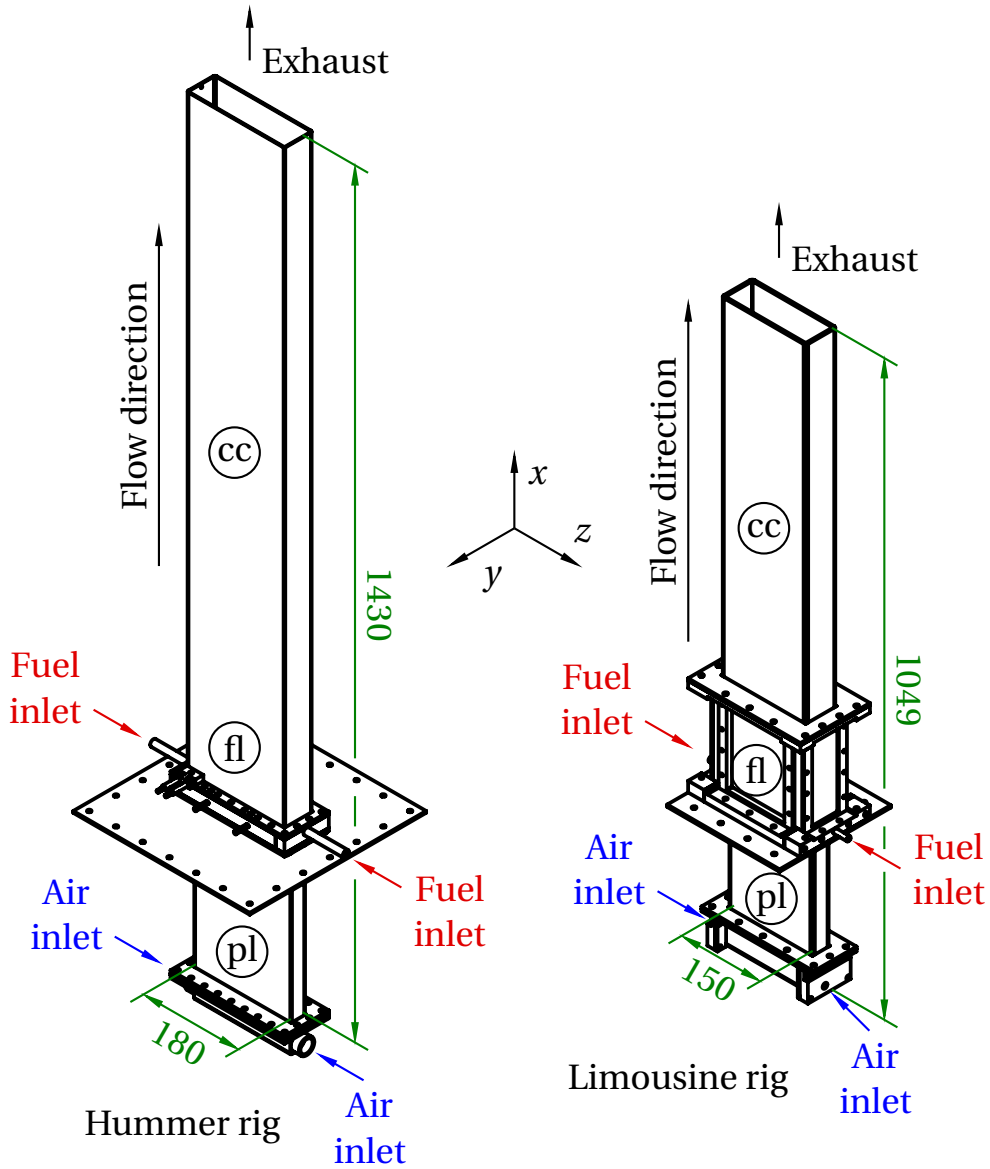
Figure 1.7: Comparison of the Hummer and Limousine test rigs, with inner dimensions in mm. The plenum ('pl') is 25 mm wide (in y-direction) for both burners, while the combustion chamber ('cc') is 50 mm wide. The flame region is indicated as 'fl'.

1.6 Passive and active damping, and control authority

Combustion instabilities can be solved by passive or active measures, which will be discussed in greater detail in sec. 3.1 and sec. 3.2 respectively. In the case of *passive damping*, the amplitude of the instability is reduced without the use of electronics. The combustion system is changed so that the source of the instability is reduced, fluid-dynamic damping is increased, or the feedback mechanism is disrupted. *Active damping* on the other hand involves an electronic control loop with fast moving actuation and one or more sensors to continuously measure the instability.

Formally, the term *active control* is broader than *active damping*, since the goal of control is not necessarily damping. However, in thermoacoustic literature the terms are generally used interchangeably. In this thesis as well, unless explicitly stated otherwise, active control refers to active damping.

From a gas turbine developer's the point of view, it is usually cheaper, and considered more elegant, to solve instability issues by passive means. If, after development, a combustion system shows unexpected instabilities in operation, it can however be simpler or more effective to apply an active damping system to solve problems on a running system.

Besides, due to the size of typical power generating gas turbines, instabilities can occur at frequencies which are impractical to damp by passive resonators, since their size increases with decreasing frequency as well. In this case as well, active control can be a more practical solution. Last, but not least, active control can damp instabilities at varying frequencies, or multiple frequencies at once, while passive solutions are often tailored to address a specific, immutable frequency range.[256] This added flexibility can be an argument to install active control on a combustion system, even if no concrete instability issues are predicted.

There are numerous examples of successful active suppression of combustion instabilities in literature.[58] Section 3.2 will give a more thorough introduction. There is however little material in literature documenting unsuccessful control, or material predicting the effectiveness of active control on a given combustion system a priori.[58, 108] This thesis investigates the effectiveness of active control in terms of the *control authority*, i.e. the extent to which the control actuation is able to influence the dynamical state of the system.

The current research investigates control authority for active damping of combustion instabilities. The effectivity of AIC will be investigated for both combustors introduced in sec. 1.5, using either a direct dive valve (DDV) or a loudspeaker as actuator. The experimental results are compared to, and explained with the help of analytical models and numerical simulations.

1.7 Outline of this thesis

Chapter 2 will introduce and explain some concepts required as a theoretical background to the rest of this thesis. The chapter will cover analytical and numerical methods used in *fluid dynamics* and *thermodynamics,* as well as the mathematical background of *spectral analysis* and *low-order modelling.*

Chapter 3 gives an overview of possible solutions to unstable combustion, separated into passive and active measures. The possibilities to use low-order modelling in the context of thermoacoustics will be discussed in sec. 3.3. The Limousine combustor is modelled in the acoustic network modelling package taX, developed at the Fachgebiet Thermodynamik of the Technische Universität München (TUM).[147] The main challenges in modelling the current combustor are the description of the valve used as an actuator, and the prediction of the response of the flame to fluctuation of the equivalence ratio through active control. These issues are addressed in chapter 5 and sec. 6.2 respectively.

The results of measurements on both combustors without control are given in Chapter 4.

The valve used for this research has been used for the active damping of combustion instabilities in the past,[112, 238] but also for the active suppression of dynamic compressor stall.[115, 149] In chapter 5, an acoustic model will be formulated and compared to experimental results.

Chapter 6 describes the effect of AIC on both combustors. Section 6.1 describes the experimental part, while sec. 6.2 describes the corresponding numerical simulation. The results of the simulation are used to investigate the response of the flame to active control. To this end, the Limousine combustor and the prototype Hummer are modelled in the *computational fluid dynamics* (CFD) package CFX. The convective time delay between the fuel injection and the flame is evaluated, and identified as a decisive factor causing the difference in controllability between these combustors.

2 Theoretical background

This chapter gives an overview of the basic theoretical models used in the remainder of this thesis. Analytical fluid models, including thermodynamics and combustion will be discussed in sec. 2.1. In the set-ups investigated in this thesis, solid boundaries are generally much stiffer than the fluid flow, so that no elastic solid modelling is required.

Especially the equations for *fluid dynamics* are too complex to solve analytically for all but the simplest situations. Therefore practical situations are usually investigated using numerical techniques. *Computational fluid dynamics* (CFD) is introduced in sec. 2.2.

In vibrating systems, the quantities that vary in space and time can often be described more conveniently as the product of a *mode shape*, which is a function of space only, and a harmonic function of time. If a system can be described by N modes of vibration, a fluctuating quantity $X(\vec{x}, t)$ can be expressed as

$$X(\vec{x}, t) = \sum_{i=0}^{N} \Re\left(\hat{X}_i(\vec{x}) \, \mathrm{e}^{\mathrm{i}\omega_i t} \right) ,$$

where $\omega_0 = 0$ and $\hat{X}_0(\vec{x})$ is the mean value, also written as $\bar{X}(\vec{x})$. Consecutive ω_i are the *frequencies* of the ith modes. If these are real-valued, the mode is constant in amplitude. A positive imaginary part $\Im(\omega_i)$ signifies a damped mode, decreasing in amplitude, while a negative imaginary part of the frequency indicates a mode that grows in amplitude. The complex-valued spatial field $\hat{X}_i(\vec{x})$ is known as the mode shape of X at the ith mode. Information concerning these modes are found through frequency analysis, explained in sec. 2.3.

Although physical systems theoretically have infinite modes, an analysis of a limited number of the lower-frequency modes suffices for engineering applications. This observation is used to reduce computational complexity in *low-order modelling*, introduced in sec. 2.4. Low-order *acoustic network modelling*, and its application to *thermoacoustics* will be described in chapter 3.

2.1 Analytical fluid modelling

2.1.1 Fluid dynamics: The Navier–Stokes equations

In fluid mechanics, conservation of *mass, momentum* and *energy* is expressed by the *Navier–Stokes equations*.[*][193, 260, 261] The equations will be given in integral form – for a fluid moving through a control volume V, bounded by the surface ∂V – and in *partial-differential-equation* (PDE) form.

2.1.1.1 Mass conservation

For a fluid moving through a control volume V, bounded by the surface ∂V, mass conservation (the continuity equation) can be written in *integral conservation form* as

$$\partial_t \iiint_V \rho \, \mathrm{d}V + \iint_{\partial V} \rho \, (\vec{u} - \vec{u}_{\partial V}) \cdot \vec{n} \, \mathrm{d}A = 0 \,, \tag{2.1a}$$

where t is time, ρ is density and $\vec{n}$ is the unit vector normal to ∂V, pointing outward. $\vec{u}_{\partial V}$ is the velocity of the bounding surface ∂V, so for a stationary control volume $\vec{u}_{\partial V} = \vec{0}$. The factor $\vec{u} - \vec{u}_{\partial V}$ is the difference between the velocity of the fluid and the boundary of the control volume, neither of which is required to be zero.

Mass conservation can be written in various other useful forms, derived from the integral conservation form. With help of the *divergence theorem*[139: p.120]

$$\iint_{\partial V} \vec{X} \cdot \vec{n} \, \mathrm{d}A = \iiint_V \vec{\nabla} \cdot \vec{X} \, \mathrm{d}V \,,$$

the surface integral can be rewritten as volume integral over the divergence of the *momentum* $\rho \, \vec{u}$. Divergence is written using the *nabla* symbol $\vec{\nabla}$, which represents the vector of all spatial derivatives $(\partial_x, \partial_y, \partial_z)^{\mathrm{T}}$. The resulting equation is valid as long as this divergence is defined – that is, in the absence of discontinuities such as shock-waves for instance. Taking a fixed control vol-

---

[*] The forms given here are from Hoeijmakers.[118]

ume ($\vec{u}_{\partial V} = \vec{0}$) and removing the volume integral gives the equation for mass conservation in the *PDE conservation form*:

$$\partial_t \iiint_V \rho \, \mathrm{d}V + \iiint_V \left(\vec{\nabla} \cdot \left(\rho \, \vec{u} \right) - \cancel{\vec{\nabla} \cdot \left(\rho \, \vec{u}_{\partial V} \right)} \right) \mathrm{d}V = 0$$

$$\partial_t \rho + \vec{\nabla} \cdot \left(\rho \, \vec{u} \right) = 0 \,. \qquad \text{(2.1b)}$$

The *material* derivative or *Lagrangian* derivative $\mathrm{D}_t \circ \equiv \partial_t \circ + \vec{u} \cdot \vec{\nabla} \circ$ expresses the rate of change of quantities as experienced by particles travelling along path lines. This is especially useful when this rate of change can be argued to be negligible. Mass conservation in PDE form, using the material derivative is given by

$$\mathrm{D}_t \rho + \rho \vec{\nabla} \cdot \vec{u} = 0 \,. \qquad \text{(2.1c)}$$

This equation implies that for divergence-free flow ($\vec{\nabla} \cdot \vec{u} = 0$), density is constant along particle path lines.

For internal flows where quantities can be assumed constant over openings (*homogeneous plug flow*), eq. (2.1a) reduces to a simple summation over inlets and outlets:

$$\partial_t m + \sum_i \rho_i \, \vec{u}_i \cdot \vec{n}_i \, A_i = 0 \,. \qquad \text{(2.1d)}$$

2.1.1.2 Momentum conservation

Momentum conservation (a three-dimensional vector equation) is written as

$$\partial_t \iiint_V \rho \, \vec{u} \, \mathrm{d}V + \iint_{\partial V} \rho \, \vec{u} \, ((\vec{u} - \vec{u}_{\partial V}) \cdot \vec{n}) \, \mathrm{d}A = \cdots$$

$$- \iint_{\partial V} p \, \vec{n} \, \mathrm{d}A + \iint_{\partial V} \bar{\bar{\tau}} \, \vec{n} \, \mathrm{d}A + \iiint_V \rho \, \tilde{\vec{F}} \, \mathrm{d}V \,, \quad \text{(2.2a)}$$

where p is (static) pressure, $\bar{\bar{\tau}}$ is the viscous stress tensor, and $\tilde{\vec{F}}$ represents *external* (i.e. not fluid-dynamical) body forces, such as gravity or magnetism, for instance. The relation between and p, ρ and other thermodynamic quantities are given by the *equations of state*, introduced in sec. 2.1.2. Using the

divergence theorem as before, momentum conservation can be stated in PDE form:

$$\partial_t \left(\rho \, \vec{u} \right) + \vec{\nabla} \cdot (\rho \, \vec{u} \otimes \vec{u}) = -\vec{\nabla} p + \vec{\nabla} \cdot \bar{\bar{\tau}} + \rho \, \tilde{\vec{F}} \, , \qquad (2.2\text{b})$$

or, taking advantage of the expression for mass conservation,

$$\rho \, \mathrm{D}_t \vec{u} = -\vec{\nabla} p + \vec{\nabla} \cdot \bar{\bar{\tau}} + \rho \, \tilde{\vec{F}} \, . \qquad (2.2\text{c})$$

The formulation using the material derivative can be interpreted as Newton's *second law of motion*[196: p.12], expressed for an infinitesimally small volume of fluid.

Newton's law of viscosity[196: p.373] states that shear stresses in a fluid are proportional to the rate of shear. This 'law' is not a fundamental law of nature, and as such only describes so-called *Newtonian fluids*. Fortunately, gases and many common liquids can be considered Newtonian under normal conditions. The three-dimensional form of Newton's law of viscosity is known as *Stokes' hypothesis.*[260, 261] With $\bar{\bar{I}}$ the identity tensor:

$$\bar{\bar{\tau}} = \mu \left(\vec{\nabla} \otimes \vec{u} + \left(\vec{\nabla} \otimes \vec{u} \right)^{\mathrm{T}} - \tfrac{2}{3} \bar{\bar{I}} \vec{\nabla} \cdot \vec{u} \right) \, . \qquad (2.3)$$

The relative magnitude of inertia $\left(\rho \, \vec{u} \right)$ in comparison to $\bar{\bar{\tau}}$ is of great importance to fluid dynamics. It is quantified by the non-dimensional *Reynolds number*[225] $Re \equiv \rho \, u \, L_{\text{ref}} / \mu$, evaluated at some predefined reference point in the flow field under consideration. Since $\rho = 1.3 \, \text{kg/m}^3$ and $\mu = 17 \cdot 10^{-6} \, \text{kg/(m s)}$ for air at $101.3 \cdot 10^3 \, \text{Pa}$ and $0 \, ^\circ\text{C}$, the Reynolds number can easily become very large. In such situations, neglecting viscosity is a common simplification.

The Navier–Stokes equations without viscosity are known as the *Euler equations*[73] of fluid dynamics. In the case of steady flow ($\partial_t \circ = 0$), the momentum equation (eq. 2.2b) without viscosity becomes

$$\mathrm{D}_t \vec{u} = \frac{-\vec{\nabla} p}{\rho} + \tilde{\vec{F}} \, .$$

If furthermore $\tilde{\vec{F}}$ represents a potential force – for instance gravity – the equation can be integrated along a streamline, yielding

$$\frac{|\vec{u}|^2}{2} + \int\limits_{p}^{p_{\text{st}}} \frac{1}{\rho \left(\breve{p} \right)} \mathrm{d}\breve{p} - \int \tilde{\vec{F}} \mathrm{d}\vec{x} = p_{\text{st}} \, .$$

When the flow is brought to rest $\left(\vec{u} = \vec{0}\right)$, the pressure will be p_{st}, the *total* or *stagnation* pressure. In the case of incompressible flow, this can be written as

$$\frac{\rho}{2}\,|\vec{u}|^2 + p - \int \tilde{\vec{F}} \cdot \mathrm{d}\vec{x} = p_{\text{st}}\,, \tag{2.4}$$

which is known as *Bernoulli's principle*.[18]

2.1.1.3 Energy

The *first law of thermodynamics* states that the increase of energy in a system is equal to the sum of *work* and *heat* added to the system.[51, 129, 169] With $\tilde{E}_{\text{st}} = \tilde{E} + \frac{1}{2}\,\vec{u}^2$ as specific stagnation energy (in J/kg), energy conservation (in watt) for a fluid in a moving control volume can be written in integral form as

$$\partial_t \iiint\limits_V \rho\,\tilde{E}_{\text{st}}\,\mathrm{d}V + \iint\limits_{\partial V} \rho\,\tilde{E}_{\text{st}}\,(\vec{u} - \vec{u}_{\partial V}) \cdot \vec{n}\,\mathrm{d}A = \dots$$

$$\iiint\limits_V \rho\,\tilde{\vec{F}} \cdot \vec{u}\,\mathrm{d}V - \iint\limits_{\partial V} p\,(\vec{u} - \vec{u}_{\partial V}) \cdot \vec{n}\,\mathrm{d}A + \iint\limits_{\partial V} \left(\bar{\bar{\tau}} \cdot (\vec{u} - \vec{u}_{\partial V})\right) \cdot \vec{n}\,\mathrm{d}A \dots$$

$$+ \iiint\limits_V \rho\,\dot{\check{Q}}\,\mathrm{d}V - \iint\limits_{\partial V} \vec{J}_Q \cdot \vec{n}\,\mathrm{d}A\,. \tag{2.5a}$$

The terms in the second line – containing inner products with $\vec{u}$ – represent mechanical work added to the system, while those on the last line represent heat. In PDE form, energy conservation is expressed as

$$\partial_t\left(\rho\,\tilde{E}_{\text{st}}\right) + \vec{\nabla} \cdot \left(\rho\,\vec{u}\,\tilde{E}_{\text{st}}\right) = \rho\,\tilde{\vec{F}} \cdot \vec{u} - \vec{\nabla} \cdot p\,\vec{u} + \vec{\nabla} \cdot \left(\bar{\bar{\tau}} \cdot \vec{u}\right) + \rho\,\dot{\check{Q}} - \vec{\nabla} \cdot \vec{J}_Q \tag{2.5b}$$

or

$$\rho\,\mathrm{D}_t\tilde{E}_{\text{st}} = \rho\,\tilde{\vec{F}} \cdot \vec{u} - \vec{\nabla} \cdot p\,\vec{u} + \vec{\nabla} \cdot \left(\bar{\bar{\tau}} \cdot \vec{u}\right) + \rho\,\dot{\check{Q}} - \vec{\nabla} \cdot \vec{J}_Q\,, \tag{2.5c}$$

2.1.1.4 Enthalpy

For practical considerations of open systems, the pressure term on the right-hand side of the energy equations can be inconvenient. Instead it is often more helpful to consider *enthalpy H* instead of energy, where $\tilde{H}_{\text{st}} = \tilde{E} + \frac{1}{2}\vec{u}^2 + p/\rho$.

$$\partial_t \iiint_V \rho\,\tilde{H}_{\text{st}}\,\mathrm{d}V + \iint_{\partial V} \rho\,\tilde{H}_{\text{st}}\,(\vec{u} - \vec{u}_{\partial V}) \cdot \vec{n}\,\mathrm{d}A = \iiint_V \partial_t p\,\mathrm{d}V + \iiint_V \rho\,\vec{\tilde{F}} \cdot \vec{u}\,\mathrm{d}V \cdots$$

$$+ \iint_{\partial V} \left(\bar{\bar{\tau}} \cdot (\vec{u} - \vec{u}_{\partial V})\right) \cdot \vec{n}\,\mathrm{d}A + \iiint_V \rho\,\dot{\tilde{Q}}\,\mathrm{d}V - \iint_{\partial V} \vec{J}_Q \cdot \vec{n}\,\mathrm{d}A. \quad (2.6a)$$

The PDE form becomes:

$$\partial_t \left(\rho\,\tilde{H}_{\text{st}}\right) + \vec{\nabla} \cdot \left(\rho\,\vec{u}\,\tilde{H}_{\text{st}}\right) = \partial_t p + \rho\,\vec{\tilde{F}} \cdot \vec{u} + \vec{\nabla} \cdot \left(\bar{\bar{\tau}} \cdot \vec{u}\right) + \rho\,\dot{\tilde{Q}} - \vec{\nabla} \cdot \vec{J}_Q, \quad (2.6b)$$

or

$$\rho\,\mathrm{D}_t \tilde{H}_{\text{st}} = \partial_t p + \rho\,\vec{\tilde{F}} \cdot \vec{u} + \vec{\nabla} \cdot \left(\bar{\bar{\tau}} \cdot \vec{u}\right) + \rho\,\dot{\tilde{Q}} - \vec{\nabla} \cdot \vec{J}_Q. \quad (2.6c)$$

For steady ($\partial_t \circ = 0$), adiabatic ($\vec{J}_Q = \vec{0}$, $\dot{\tilde{Q}} = 0$) processes with negligible viscous losses ($\bar{\bar{\tau}} = \bar{\bar{0}}$) and external forces ($\vec{\tilde{F}} = \vec{0}$), eq. (2.6c) states that enthalpy is constant along particle tracks, which makes enthalpy a very useful quantity to consider. For internal flows where quantities can be assumed constant over openings (homogeneous plug flow), eq. (2.6a) reduces to a simple summation over inlets and outlets:

$$\sum_i \rho_i\,\tilde{H}_{\text{st},i}\,\vec{u}_i \cdot \vec{n}_i\,A_i = 0. \quad (2.6d)$$

2.1.2 Thermodynamics

Leaving out kinetic energy and viscous dissipation, conservation of (specific) energy can be written in a much simpler form:

$$\mathrm{d}\tilde{E} = -p\,\mathrm{d}\tilde{V} + T\,\mathrm{d}\tilde{s}. \quad (2.7)$$

$\tilde{E}$ is the specific internal energy of the fluid. $-p\,\mathrm{d}\tilde{V} \equiv \mathrm{d}\tilde{W}$ is work added to the fluid, where the specific volume $\tilde{V} \equiv 1/\rho$. The heat added to the fluid is $T\,\mathrm{d}\tilde{s} \equiv \mathrm{d}\tilde{Q}$, with $\tilde{s}$ the specific *Entropy*.

In terms of enthalpy, this equation is

$$\mathrm{d}\tilde{H} = \tilde{V}\,\mathrm{d}p + T\mathrm{d}\tilde{s}\,. \tag{2.8}$$

The *heat capacity* of a material determines how much the temperature will rise on an addition of heat. For a material kept at a constant volume

$$\tilde{C}_V \equiv \left[\partial_{\tilde{Q}}T\right]_V\,. \tag{2.9}$$

If the material is kept under a constant pressure instead,

$$\tilde{C}_p \equiv \left[\partial_{\tilde{Q}}T\right]_p\,. \tag{2.10}$$

Gases expand when heated under constant pressure ($\mathrm{d}\tilde{V} > 0$). This means some energy is lost to the environment in the form of work ($\mathrm{d}\tilde{W} < 0$), which will have to be compensated for by the addition of some more heat, so that $\tilde{C}_p > \tilde{C}_V$. For ideal gases, a simple proportionality exists between pressure, density and temperature:[33, 50, 87, 88]

$$p = \rho\,\tilde{R}\,T\,. \tag{2.11}$$

The constant $\tilde{R}$ depends on the gas (mixture) and is related to its molar weight $\underline{m}$ as $\tilde{R} = \underline{R}/\underline{m}$, where $\underline{R}$ is the *universal gas constant*.[13] Combining this gives the *ideal gas law*

$$p\,\underline{m} = \rho\,\underline{R}\,T\,. \tag{2.12}$$

According to Mayer,[170,153] for ideal gases, the difference between the heat capacities is $\tilde{R}$:

$$\tilde{C}_p = \tilde{C}_V + \tilde{R}\,. \tag{2.13}$$

In the case of acoustics, air is compressed *adiabatically*, i.e. without the addition of heat. Biot and Laplace argued that this implies that the temperature is increased, instead of remaining constant.[79] In the case of adiabatic compression, density is found by Poisson's relation[212] for calorically perfect gases

$$p \propto \rho^{\gamma}\,, \tag{2.14}$$

where $\gamma = \tilde{C}_p/\tilde{C}_V$ is the ratio of the heat capacities.

In a gas turbine the compression stage is in first approximation adiabatic, for example as shown in fig. 1.4. Density increases according to eq. (2.14), and

temperature can be found by the perfect gas law. In the combustion chamber pressure remains approximately constant while the temperature rises. The expansion in the turbine is again approximately adiabatic. This cycle is known as the *Brayton cycle*.[37]

The amount of work $\tilde{W} = \int p \, \mathrm{d}\tilde{V}$ delivered per unit of mass, can be found in the $p, \tilde{V}$-diagram a by integration of the area underneath the curve, as in fig. 2.1. The heat still available in the exhaust gases can be converted into additional mechanical work, for example in a steam turbine.
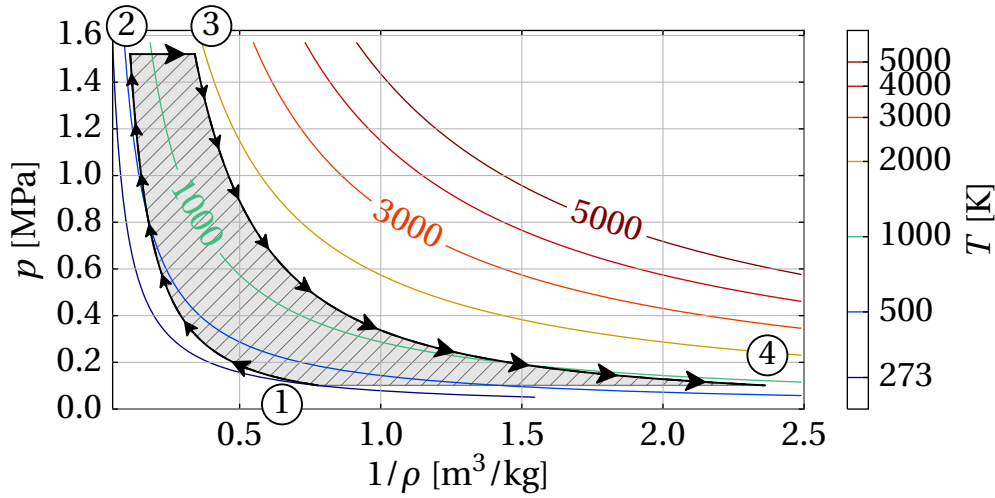
Figure 2.1: Example of an ideal Brayton cycle,[37] showing adiabatic compression $(1 \to 2)$, isobaric heat addition $(2 \to 3)$, and adiabatic expansion $(3 \to 4)$. The hatched area represents the work delivered.

It should be noted that Rayleigh published his criterion only six years after the Brayton cycle was patented, which is very similar in concept.

Chu[46, 47] reformulated the Rayleigh criterion in a more quantitative manner; integrating $p' \dot{Q}'$ over a cycle to quantify their correlation[46] and comparing this source term to a loss term,[47] to conclude whether or not a thermoacoustic mode will be unstable. Dowling[69] rewrote this inequality in the dimension of energy:

$$\frac{\gamma - 1}{\bar{\rho} c^2} \int_C \int_V p' \rho \dot{Q}' \, \mathrm{d}V \, \mathrm{d}t > \int_C \int_A p' u' \, \mathrm{d}A \, \mathrm{d}t \, .$$

2.1.3 Combustion modelling

The combustors discussed in this thesis are fuelled with *methane* (CH_4). Oxygen (O_2) is supplied in the form of air, which is assumed to be a mixture of 21 % oxygen and 79 % nitrogen (N_2). This reaction forms water (H_2O) and carbon dioxide (CO_2). The required amount of oxygen per mole of methane is expressed by the *stoichiometric equation*

$$CH_4 + 2 O_2 \longrightarrow 2 H_2O + CO_2 . \tag{2.15}$$
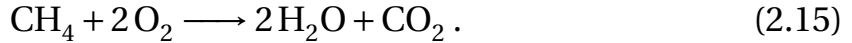
For technical and environmental reasons, generally more air is led through the combustion chamber than would be necessary according to the stoichiometry of eq. (2.15). This is expressed by the equivalence ratio Φ, which is the stoichiometrically required mole inflow of oxygen $\dot{n}_{O_2,\text{in}}$ divided by the actual amount. Alternatively, the air excess ratio Λ, is frequently used, which is $1/\Phi$. In the case of methane combustion (using the stoichiometric coefficients from eq. (2.15)):

$$\Phi = \frac{2\,\dot{n}_{CH_4,\text{in}}}{\dot{n}_{O_2,\text{in}}} \qquad\qquad \Lambda = \frac{\dot{n}_{O_2,\text{in}}}{2\,\dot{n}_{CH_4,\text{in}}} . \tag{2.16}$$

If $\Phi < 1 < \Lambda$, the combustion is limited by the amount of fuel available. This situation is referred to as *lean* combustion. In the case of *rich* combustion, where the amount of oxidiser is limiting, $\Phi > 1 > \Lambda$.

The heat generated by this process is expressed by the *lower heating value* of methane $\underset{\sim}{LHV}_{CH_4}$. 'Lower' refers to the assumption that the water produced by the combustion leaves the combustor in gaseous form, so its condensation heat is lost. The lower heating value can be determined by comparing the formation enthalpies $\overset{\star}{\underset{\sim}{H}}$ of the reactants on the left hand side of eq. (2.15), and the products on the right (see tbl. A.2). By definition, the formation enthalpy is zero for elements in their most stable mono-atomic form, such as oxygen in O_2.

$$\begin{aligned}
\underset{\sim}{LHV}_{CH_4} &= \overset{\star}{\underset{\sim}{H}}_{CH_4} + 2\,\overset{\star}{\underset{\sim}{H}}_{O_2} - 2\,\overset{\star}{\underset{\sim}{H}}_{H_2O} - \overset{\star}{\underset{\sim}{H}}_{CO_2} \\
&= -74.87 \cdot 10^6 + 0 - \left(-241.83 \cdot 10^6\right) - \left(-393.52 \cdot 10^6\right) \\
&= 802.31 \cdot 10^6 \,\text{J/kmol} . \tag{2.17}
\end{aligned}$$

The mass-based value is found as

$$\widetilde{LHV}_{CH_4} = \frac{\underline{LHV}_{CH_4}}{\underset{\sim}{m}_{CH_4}}$$

$$= \frac{802.31 \cdot 10^6}{16.03}$$

$$= 50.05 \, J/kg \, . \tag{2.18}$$

The speed of combustion can be limited, amongst others, by mixing of fuel and oxidiser, chemistry, or the speed of flame propagation. Here, the chemical time scales are assumed to be much shorter than those associated with flame propagation and turbulent mixing. This leads to a very thin flame or *flamelet*, which can be modelled as one or more surfaces A_{fl} travelling through the flow at a relative speed S_{fl}. The heat released by the flame, in the lean case, can be expressed as

$$\dot{Q} = \int_{A_{fl}} \rho \, \widetilde{LHV}_F \, \mathcal{Y}_F \, S_{fl} \, dA \, .$$

2.2 Computational fluid dynamics (CFD)

CFD is a flexible way to find approximate solutions to the equations introduced so far in this chapter for engineering situations. To this end, the geometry for which the equations need to be solved is split into small elements, for which the solution of the equation is assumed to be sufficiently close to a known analytical solution, expressed as *shape function*, with limited degrees of freedom. The error introduced by this discretisation is estimated, and minimised via an iterative approach.[231, 232]

Since this approach gets more costly (from a computational point of view) as the number of elements increases, it is important to increase the element size in less complex regions of the flow and decrease the size of elements in the directions where greatest gradients in the solution are expected.

2.2.1 Turbulence

Reynolds[226] noted that flow at higher Reynolds numbers flows more chaotically than at lower Reynolds numbers, while frictional losses get higher than would

be expected from Newton's law of viscosity or Stokes' hypothesis (eq. 2.3). This phenomenon is known as *turbulence*. The statistical properties of turbulent flow can be analysed by decomposing the variables in the Navier–Stokes equations (e.g $\vec{u}$) into an *ensemble-averaged* value ($\bar{\vec{u}}$) plus a *fluctuation* ($\vec{u}''$) as in

$$\vec{u} = \bar{\vec{u}} + \vec{u}'' \, . \tag{2.19}$$

The resulting system of equations is known as the *Reynolds-averaged Navier–Stokes* (RANS) equations. In the case of compressible flow, the averaging is weighted by density (*Favre averaging*). The equations for the averaged quantities look very similar to the original system. However, products of components of the fluctuating velocity appear, which do not vanish in the averaging process. Statistically, these products can be treated as an addition to the stress tensor in eq. (2.3):

$$\bar{\bar{\tau}}_{\mathrm{T}} = \rho \, \overline{\vec{u}'' \otimes \vec{u}''} \, . \tag{2.20}$$

The components of the tensor $\bar{\bar{\tau}}_{\mathrm{T}}$ are collectively known as *Reynolds stresses* and have to be estimated by semi-empirical means. The CFD simulations discussed in this thesis uses the *shear stress transport* (SST) model by Menter.[173]

This approach can only be justified if the features which need to be resolved in the simulation (e.g. the relevant acoustic modes of the system) can be represented meaningfully by the ensemble-averaged quantities. This is the case when the resolved features have significantly lower frequencies than the frequency of turbulent fluctuations modelled by the Reynolds stresses.[69: p.4]

For situations where these frequency ranges are too close to each other to use RANS, another approach, known as *large eddy simulation* (LES), was developed by Smagorinsky,[251] Deardorff,[63] and Schumann,[244] amongst others. In this approach, the decomposition of eq. (2.19) is replaced by a filtering of the flow field by length scale. The larger length scales are resolved, while the smaller ones are modelled.

LES performs best in free flow, away from boundaries. Near solid boundaries it becomes computationally expensive to resolve the flow by LES, while RANS gives sufficiently accurate results with much less effort. To combine the benefits of both, the *scale-adaptive simulation* (SAS) model was introduced by Menter and Egorov.[174] The SAS model can transition between LES behaviour in regions where the turbulence structure is well resolved, and the SST model (RANS) where the unsteady flow is modelled instead of resolved.

2.2.2 Combustion

Combustion is simulated by the *burning velocity model* (BVM), a flamelet model developed by Müller et al.,[185] Polifke et al.,[214] and Zimont et al.[295] A new, and currently not well-documented refinement on this model option is used in ANSYS CFX, for improving accuracy for non-premixed flames.[80] BVM performs well on predicting the flame position for partially premixed flames, as present in the combustors investigated in this research. This property will be of great importance in sec. 6.2 ('Analysis in CFD'), since the exact flame position has great influence on the feedback loop leading to thermoacoustic (in)stability.

A practical advantage of BVM in CFX is that the volumetric heat release is readily available for post-processing. In sec. 6.2, this information will be used in an investigation of the performance of active control.

2.3 Frequency (spectral) analysis

As mentioned in the introduction of this chapter, field quantities in dynamic systems are often described as a summation over N mode shapes $\hat{X}_i(\vec{x})$, oscillating at frequencies ω_i, so that an arbitrary variable $X(\vec{x}, t)$ can be expressed as

$$X(\vec{x}, t) = \sum_{i=0}^{N-1} \Re\left(\hat{X}_i(\vec{x}) \, \mathrm{e}^{\mathrm{i}\omega_i t}\right).$$

These mode shapes and their corresponding frequencies are found by frequency analysis. For simplicity, this discussion will start from a simple, steadily oscillating signal:

$$X(t) = \left|\hat{X}\right| \cos\left(\varphi + \omega t\right),$$

where $\left|\hat{X}\right|$ is the *amplitude* of the fluctuation, φ defines the *phase offset*, and the *angular frequency* is ω (expressed in rad/s for clarity). The *angular* frequency is related to the *ordinary* frequency f (expressed in Hz) as $\omega = 2\pi f$.

The previous equation is equivalent to

$$X(t) = \left|\hat{X}\right| \Re\left(\mathrm{e}^{\mathrm{i}\left(\omega t + \varphi\right)}\right),$$

which can be written more compactly, introducing the *phasor* $\hat{X}$ as a generalisation of the amplitude into the complex plane, where the complex argument represents the phase offset:

$$\hat{X} = \left|\hat{X}\right| e^{i\varphi},$$

$$X(t) = \Re\left(\hat{X} e^{i\omega t}\right). \tag{2.21}$$

2.3.1 The continuous Fourier transform

Laplace[142, 143] and Fourier[81] realised some differential equations are easier solved when the variables involved are rewritten as sums of harmonic functions, or integrals over distributions of harmonic functions, referred to as *frequency domain representations* or *spectra*. Depending on the situation, different formulations are used to transform signals into or back from the frequency domain. Although the original formulation by Fourier was written in terms of sines and cosines, under Laplace's influence, the following definition will be used for the *Fourier transform* in this dissertation:

$$\mathfrak{F}(X,f) = \int_{t_1}^{t_2} X(t)\, e^{-2\pi i t f}\, dt, \tag{2.22a}$$

where the frequency $f = N/(t_2 - t_1)$ for $N \in \mathbb{N}_0$. When $t_1 = -\infty$ or $t_2 = \infty$ or both, the result of the Fourier transform, provided it converges, becomes a function of continuous frequency. The *inverse* Fourier transform is then given by

$$X(t) = \int_{-\infty}^{\infty} \mathfrak{F}(X,f)\, e^{2\pi i t f}\, df. \tag{2.22b}$$

The closely related *Laplace transform* is defined as

$$\mathfrak{L}(X,s) = \int_{0}^{\infty} X(t)\, e^{-st}\, dt,$$

where s is the angular frequency, generalised into the complex plane $\mathbb{C}$ as $s = i\omega = 2\pi i f$.

Some advantages of handling quantities in the Laplace or frequency domain, are that differentiation simplifies to multiplication by s in the frequency domain, and integration becomes division by s. Convolution of two functions in the time domain becomes a simple multiplication in the frequency domain.

2.3.2 Analytical signals

Since $\cos(\varphi + \omega\, t) = \left(e^{i(\varphi + \omega\, t)} + e^{-i(\varphi + \omega\, t)}\right)/2$, the Fourier and Laplace transforms will split real valued harmonic signals into two peaks in the frequency domain: one with a positive frequency, and one with a negative frequency, opposite phase, and both with half the original amplitude. In such situations, it is common practice to introduce *analytical signals*. Analytical signals are defined complex-valued, such they have no negative frequency components, and the real part is equal to the original signal.

In the case of a signal with only one frequency, such as $X(t) = \mathfrak{R}\left(\hat{X}\, e^{i\omega\, t}\right)$ in eq. (2.21), the analytical version is simply $X_{\mathrm{an}}(t) = \hat{X}\, e^{i\omega\, t}$. In the frequency domain this can easily be extended to the general case:

$$
\hat{X}_{\mathrm{an}}(f) = \begin{cases} \hat{X}(f) + \hat{X}(-f) & \text{if } f > 0 \\ \hat{X}(f) & \text{if } f = 0 \\ 0 & \text{if } f < 0\,. \end{cases} \tag{2.23}
$$

In the time domain, for general signals, the *Hilbert transform*[114] ($\mathfrak{H}$) gives the imaginary part which has to be added to real-valued signals to get the analytical equivalent:[98]

$$
X_{\mathrm{an}}(t) = X(t) + i\,\mathfrak{H}\,X(t)\,. \tag{2.24}
$$

The Hilbert transform is given by

$$
\mathfrak{H}\,X(t) = \frac{1}{\pi}\int_{-\infty}^{\infty} \frac{X(\check{t})}{t - \check{t}}\mathrm{d}\check{t}\,. \tag{2.25}
$$

In the remainder of this thesis, spectra of real-valued signals will be presented in their analytical form, to get the amplitudes in their more intuitive form. The subscript 'an' will be dropped from here on.

2.3.3 The discrete Fourier transform (DFT)

In reality, measurement data are *sampled* (discrete in time), and have finite length. If the amplitudes or frequencies present in the signal change over time, it can be more interesting to analyse short sections of the signal, and see how these spectra evolve over time. The results are often presented as a false colour plot, displaying amplitude as a function of time and frequency, called a *spectrogram.* Since this technique was developed by Gabor,[86] the short-time Fourier transform is sometimes known as the *Gabor transform.*

Since the Fourier transform can not be used in the *continuous* form introduced in eq. (2.22), the *discrete Fourier transform* (DFT) is used instead:

$$\mathfrak{F}(X)_k = N\,\hat{X}_k = \sum_{j=0}^{N-1} X_j\, e^{-2\pi i \frac{k}{N} j}\,. \tag{2.26a}$$

Note that in this equation, $i = \sqrt{-1}$ is the imaginary unit while j and k are indices. f_{sm} is the sampling frequency of the signal X. The frequency corresponding to the index k is $\omega_k = 2\pi\,(k/N)\,f_{sm}$ or equivalently $f_k = (k/N)\,f_{sm}$. and the physical time of sample j is $t_j = j/f_{sm}$. The signal X consists of N samples. The inverse transform is given by

$$\mathfrak{F}^{-1}(N\hat{X})_j = X_j = \frac{1}{N} \sum_{k=0}^{N-1} N\,\hat{X}_k\, e^{2\pi i \frac{k}{N} j}\,. \tag{2.26b}$$

The DFT represents the signal X as a sum of harmonic *base functions* of the form $e^{2\pi i (k/N) j}$. Using Lagrange's trigonometric identities,[184] it can be shown that

$$\sum_{j=0}^{N-1} e^{2\pi i \frac{k_1}{N} j}\, e^{-2\pi i \frac{k_2}{N} j} = \sum_{j=0}^{N-1} e^{2\pi i \frac{j}{N} (k_1 - k_2)}$$

$$= \begin{cases} N & \text{if } (k_1 - k_2)\bmod N = 0 \\ \dfrac{1 - e^{2\pi i (k_1 - k_2)}}{1 - e^{2\pi i \frac{k_1 - k_2}{N}}} & \text{else} \end{cases}$$

$$= \begin{cases} N & \text{if } (k_1 - k_2)\bmod N = 0 \\ 0 & \text{else, if } (k_1 - k_2) \in \mathbb{N}_1\,. \end{cases}$$

This illustrates some important characteristics of the DFT:

1. The projection of a base function onto itself (i.e. $k_1 = k_2 \in \mathbb{N}_1$) is N.

   a) The base functions are *not normalised* (in which case the projection of a base function onto itself would be unity).

   b) The inverse DFT has to contain a factor $1/N$.

2. The projection of one base function onto another one (i.e. $k_1 - k_2 \in \mathbb{N}_1$) is zero, i.e. the base functions form an *orthogonal basis*.

3. The results for k are the same as for $k + N$, a phenomenon known as *aliasing*.

4. When $k_1 \notin \mathbb{N}_0$, the signal does not have an integer number of cycles within the signal X. in this case the energy of the original signal is distributed over all frequencies. This phenomenon is known as *spectral leakage*. For a large N, this distribution tends to

$$\frac{1 - e^{2\pi i (k_1 \bmod 1)}}{2\pi i \frac{k_1 - k_2}{N}} ,$$

   which has its peak where $\mathrm{abs}(k_1 - k_2)$ has its minimum, so the distribution is still centred around the original signal frequency. Figure 2.2 shows a spectrum with spectral leakage.

Spectral leakage is related to the weighting or *windowing function* used to extract the section of data used for the DFT. In fig. 2.2 all data points have a weighting of unity, while those outside of the section had weight zero. This corresponds to a *boxcar* function, which is unity in a certain interval, and zero outside. The shape of the spectral leakage, known as the *instrument function*, is the Fourier transform of the windowing function.

Identifying the flanks of the boxcar function as the main culprit, Bartlett[15] multiplied the sampled data by a triangular window. After that, various other windowing functions were introduced, optimised for different criteria. This research uses the *Blackman window*, which was 'not very seriously' [sic] proposed by Blackman and Tukey.[22: p.98]

For the special case where $\log_2 N \in \mathbb{N}$, Cooley and Tukey[53] developed an efficient computational algorithm, known as *fast Fourier transform* (FFT). Due to the efficiency of this algorithm and its successors, this DFT with signal length equal to an integer power of two has become a very popular tool in research and engineering.
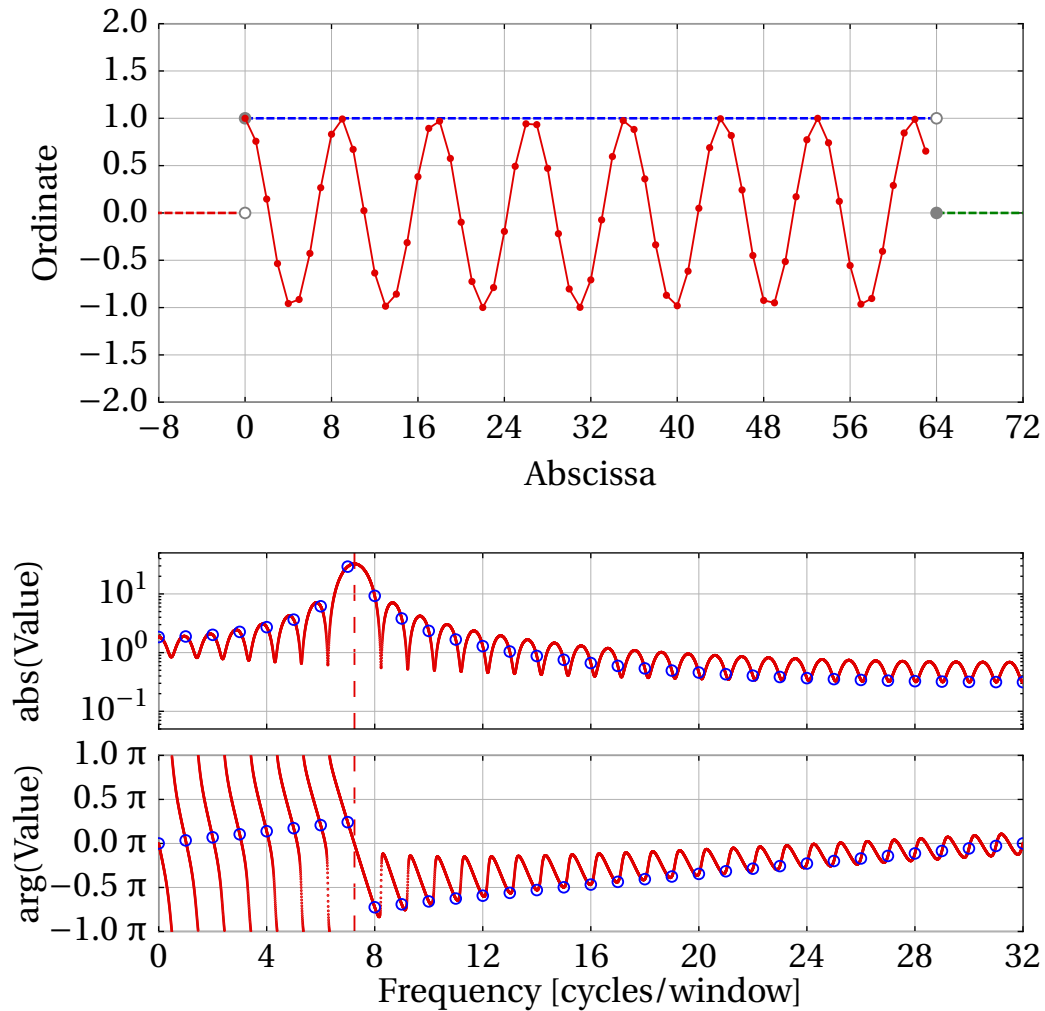
Figure 2.2: A short signal (above) and its DFT (below), demonstrating spectral leakage. The boxcar function is shown dashed behind the original signal. The rings on the spectrum indicate the results from the (orthogonal) DFT. The line connecting them indicated the components of intermediate frequencies, as would be found by the continuous Fourier transform.
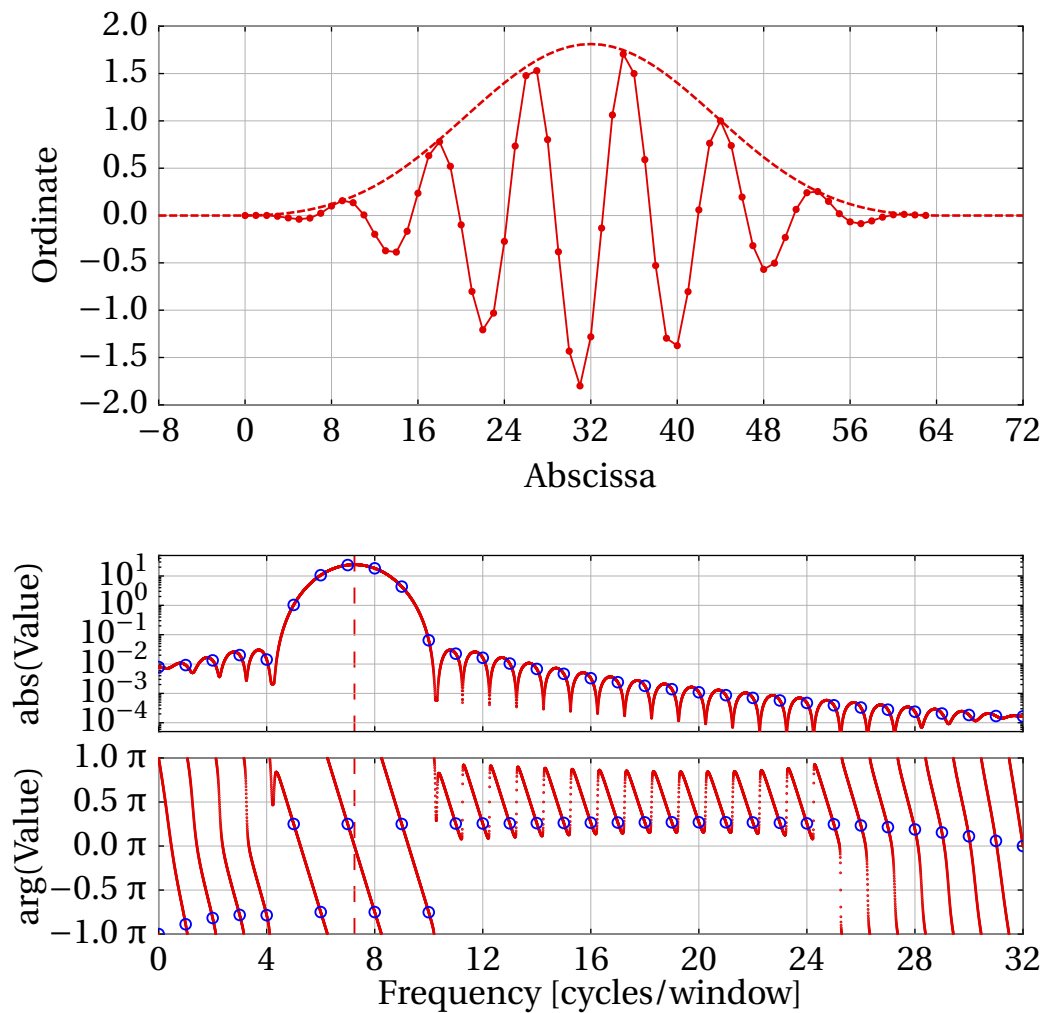
Figure 2.3: A short, Blackman-windowed signal (above) and its DFT (below), demonstrating much less spectral leakage. The Blackman window is shown dashed behind the original signal. Note the difference in scaling of the absolute axis on the right, compared to fig. 2.2.

Real-valued signals are split into positive and negative frequencies, as is the case with the continuous Fourier transform. These negative frequency components are found in the second half of the transformed array:

$$\mathfrak{F}(X)_k = -\mathfrak{F}(X)_{N-k} .$$

As a result, only $N/2$ distinct frequencies can be represented by the spectrum, the highest being half the sampling frequency. This observation is known as the *Nyquist–Shannon sampling theorem*[248].

The frequency resolution of the DFT, $f_k - f_{k-1} = f_{\mathrm{sm}}/N$, is inversely proportional to the length of the signal. When a signal is divided into short sections to generate a spectrogram, a trade-off has to be made between spectral resolution, requiring long sections of signal, and temporal resolution, requiring short sections.

Fourier spectra of real measurement signals often have a very noisy appearance, which needs to be smoothed to generate readable plots. Bartlett[16] proposed an averaging of the squared magnitude of the subsequent spectra of a spectrogram. This saves considerable computational cost compared to Fourier-transforming the signal in full length, but implicitly reduces the spectral resolution, which might be problematic if disturbing narrow peaks (e.g. mains hum) need to be filtered out from the spectrum.[35] The result of Bartlett's method is the *auto-spectral density* (*ASD*) of the measured signal:

$$ASD_{X,j} = \frac{1}{N} \sum_{k=0}^{N-1} \hat{X}_{j,k}^* \, \hat{X}_{j,k} \qquad\qquad \in \mathbb{R} .$$

The value of k refers to one windowed block, j distinguishes the samples within the block. The square root of $ASD_{X,j}$ is the k-wise *root mean square* (RMS) of $\hat{X}_{j,k}$. Welch[286] improved upon this method, by applying windowing functions to the individual blocks of data, and using *overlapping* blocks, to make better use of the samples at the ends of the blocks.

It is assumed that measured signals are the sum of a 'well behaved' part $\hat{X}'$ due to dynamic behaviour of the system under investigation, and some additive, uncorrelated noise $\hat{X}''$:

$$\hat{X} = \hat{X}' + \hat{X}'' .$$

The auto-spectral density can now be worked out as

$$ASD_{X,j} = \frac{1}{N} \sum_{k=0}^{N-1} \left(\hat{X}' + \hat{X}'' \right)^*_{j,k} \left(\hat{X}' + \hat{X}'' \right)_{j,k}$$

$$= \frac{1}{N} \sum_{k=0}^{N-1} \mathrm{abs} \left(\hat{X}'_{j,k} \right)^2 + 2 \underbrace{\Re \left(\hat{X}'^*_{j,k} \hat{X}''_{j,k} \right)}_{\to 0} + \mathrm{abs} \left(\hat{X}'' \right)^2_{j,k} .$$

Averaging over consecutive windows k will converge to a consistent over-prediction of $\mathrm{abs} \left(\hat{X}' \right)^2$.

2.3.4 Cross-spectral (correlation) analysis

A usual idealisation in system identification or *low-order modelling* (discussed in sec. 2.4), is to assume the system under consideration to be *linear* and *time-invariant.* This means that if an *output* $\hat{Y}$ depends on *inputs* $\hat{X}_i$, the total output can be written as a sum of linear *responses*:

$$\hat{Y}(\omega) = \sum_i \mathcal{G}_i(\omega) \, \hat{X}_i(\omega) ,$$

where the *transfer function* $\mathcal{G}$ is a function of frequency ω only. It does not change in time ($\partial_t \mathcal{G} = 0$) and is independent of the amplitude of the oscillation ($\partial_{|\hat{X}|} \mathcal{G}(\omega) = 0$). Non-linear systems can be *linearised* for small fluctuations around an mean state. Assuming $Y(t)$ can be written as a non-linear function of $X(t)$, first both are split into a mean value, indicated by an over-bar ($\bar{\circ}$) plus a perturbation, indicated by a prime ($\circ'$):

$$X(t) = \bar{X} + X'(t)$$

$$Y(t) = \bar{Y} + Y'(t)$$

The linearised relation between both variables is given by the first two terms of the Taylor[267: p.23] series expansion:

$$Y(t) \approx \bar{Y} + \underbrace{[\partial_X Y]_{\bar{X}} \, X'(t)}_{Y'(t)}$$

In this simple example (without frequency dependence)

$$\hat{Y}(\omega) \approx \mathcal{G} \, \hat{X}(\omega) ,$$

with

$$\mathcal{G} = [\partial_X Y]_{\bar{X}}.$$

Frequency dependence is introduced when $Y(t)$ depends on time-wise derivatives and integrals of $X(t)$, which are written in the frequency domain as $(i\omega)^N \hat{X}(\omega)$. In the case of weak linearity, or slow variation in time, this approach can be used as an approximation, writing $\mathcal{G}(t, |\hat{X}|, \omega)$ for instance.

Transfer functions can be found from measurement data by *cross-spectral analysis*. This analysis makes use of the *ASD* defined in the end of sec. 2.3.3, and the *cross-spectral density* (*CSD*), which defined in a similar manner, but uses two simultaneously measured signals:

$$CSD_{X,Y,j} = \frac{1}{N} \sum_{k=0}^{N-1} \hat{X}_{j,k}^* \hat{Y}_{j,k} \qquad \in \mathbb{C}.$$

Working this out like the auto-spectral density before shows that the *cross-spectral density* (*CSD*) converges to the noise-free product $\hat{X}'^* \hat{Y}'$:

$$CSD_{X,Y,j} = \frac{1}{N} \sum_{k=0}^{N-1} \left(\hat{X}' + \hat{X}'' \right)_{j,k}^* \left(\hat{Y}' + \hat{Y}'' \right)_{j,k}$$

$$= \frac{1}{N} \sum_{k=0}^{N-1} \hat{X}_{j,k}'^* \hat{Y}_{j,k}' + \hat{X}_{j,k}'^* \hat{Y}_{j,k}'' + \underbrace{\hat{X}_{j,k}''^* \hat{Y}_{j,k}' + \hat{X}_{j,k}''^* \hat{Y}_{j,k}''}_{\to 0}.$$

The auto-spectral density and the *cross-spectral density* (*CSD*) together can be used to investigate linear correlation between the signals X and Y. Two estimates of the transfer function $\mathcal{G}_{X,Y} = \hat{Y}'/\hat{X}'$ relating both signals can be formulated:

$$\mathcal{G}_{X,Y,j}^- = \frac{CSD_{X,Y,j}}{ASD_{X,j}} \qquad \in \mathbb{C}$$

$$\mathcal{G}_{X,Y,j}^+ = \frac{ASD_{Y,j}}{CSD_{X,Y,j}^*} > \mathcal{G}_{X,Y,j}^- \qquad \in \mathbb{C}.$$

The (real-valued) ratio between the estimates is a measure for the level of correlation between X and Y, known as the coherence *Coh*. If the signals X and Y are fully correlated and there is no measurement noise, the transfer function estimates will be identical, and the coherence will be unity:

$$\frac{\mathcal{G}_{X,Y,j}^-}{\mathcal{G}_{X,Y,j}^+} = \frac{\left| CSD_{X,Y,j} \right|^2}{ASD_{X,j}\, ASD_{Y,j}} = Coh_{X,Y,j} \qquad \in [0,1] \subset \mathbb{R}.$$

If there is noise on one of the signals, say X, this will only influence ASD_X. As a result, only $\mathcal{G}_{X,Y}^+$ will converge to the true transfer function, while $\mathcal{G}_{X,Y}^-$ will be less. If on the other hand only Y is noisy, $\mathcal{G}_{X,Y}^-$ will not be influenced, while $\mathcal{G}_{X,Y}^+$ gives an overestimation.[107]

The inverse Fourier transform of $\mathcal{G}_{X,Y}\left(f\right)$ is known as the impulse response $\mathcal{H}_{X,Y}\left(\tau\right)$. Since multiplication in the frequency domain corresponds to convolution in the time domain, $Y(t) = \int_{-\infty}^{\infty} X(t-\tau)\,\mathcal{H}_{X,Y}(\tau)\,\mathrm{d}\tau$. If there is a *causal* relation between the signals, such that X causes Y, then $\mathcal{H}_{X,Y}(\tau) = 0$ for all $\tau < 0$.

2.3.5 Other transforms

The Fourier transform does not remove any information from the original signal. The temporal variation of the analysed signal is however severely obfuscated. Short-time Fourier transforms (Gabor[86] transform) can show spectral information combined with evolution over time.

There is a trade-off between the spectral and temporal resolution of the short-time Fourier transform. This trade-off is not optimal for all applications, which gave rise to the development of other time-frequency representations.

Wavelet analysis uses longer signal sections to investigate lower frequencies and shorter signal sections to investigate higher frequencies. As a result, spectral resolution is greater for lower frequencies, while higher frequencies have better temporal resolution. This approach was first proposed by Haar[96: Ch.3] in 1910. The method became popular only during the latter half of the last century, with major contributions by Morlet et al.[182] and Daubechies.[62]

The Hilbert transform[98, 114] can be used to form an analytical signal X_{an}. If the signal is assumed to contain only one frequency, varying in time, the momentary amplitude of the oscillation is found as the absolute value $|X_{\mathrm{an}}|(t) = \sqrt{X_{\mathrm{an}}^* X_{\mathrm{an}}}$. The momentary frequency can be found as the time-derivative of the momentary phase or argument $\omega(t) = \partial_t \arg X_{\mathrm{an}}(t)$. Figure 2.4 compares this approach to the Fourier transform.

The *Wigner quasi-probability distribution* is also known as the *Wigner–Ville distribution*.[284, 289] This time–frequency representation is given by

$$\mathfrak{W}\, X_{\mathrm{an}}(t,\omega) = \int_{\mathbb{R}} X_{\mathrm{an}}\left(t + \frac{\tau}{2}\right) X_{\mathrm{an}}^*\left(t - \frac{\tau}{2}\right) \mathrm{e}^{-2\mathrm{i}\pi\omega\tau}\,\mathrm{d}\tau\,.$$
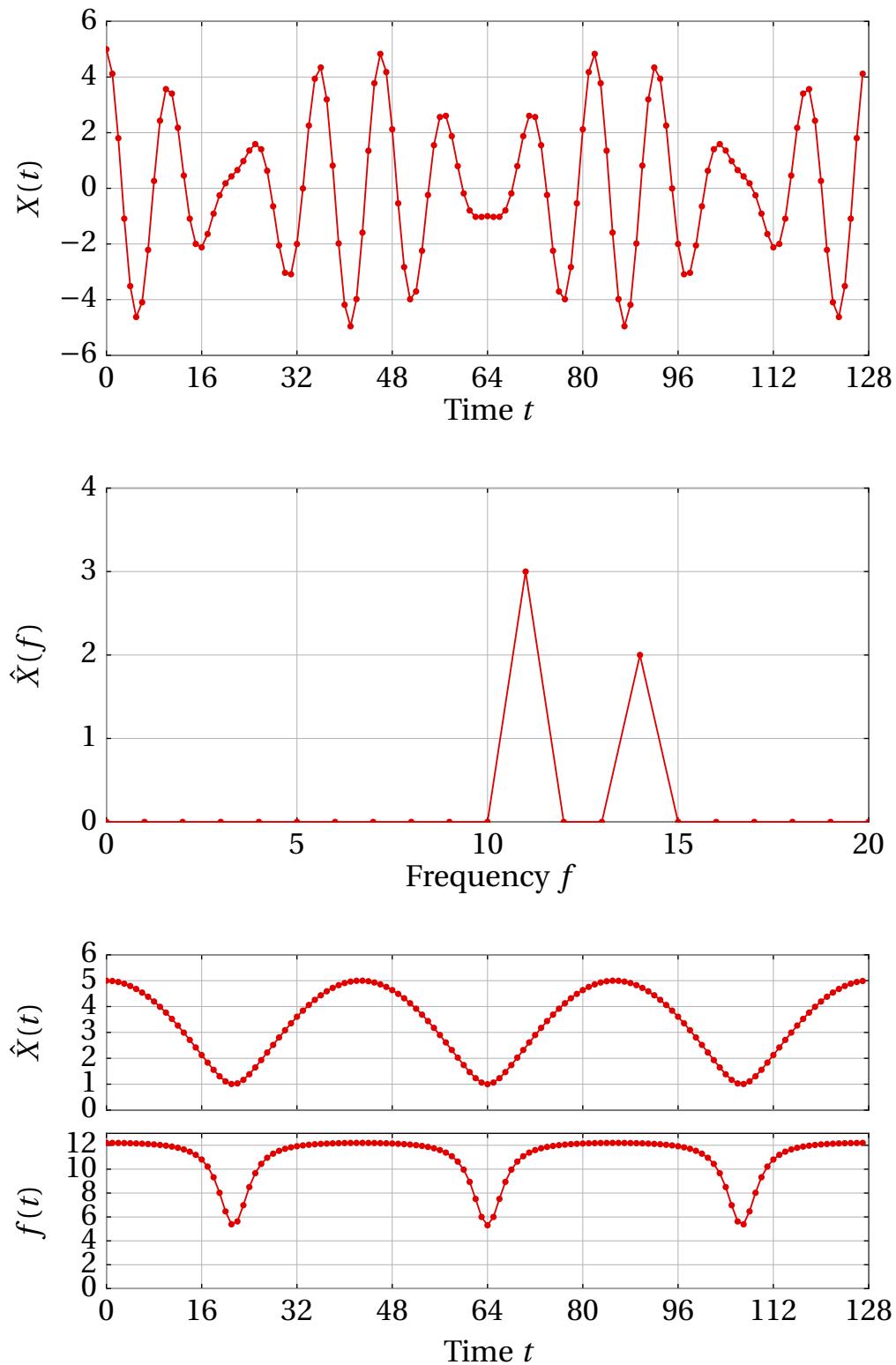
Figure 2.4: A pulsating signal (top) and its Fourier spectrum (middle). The pulsations are more intuitively represented by the amplitude and momentary frequency of the corresponding analytical signal (bottom). The maximum amplitude $\max(\hat{X}(t)) = \sum \hat{X}(f)$, appears where both frequency components are in phase.

The Wigner–Ville distribution, seemingly violating the uncertainty principle, gives sharper images than the short-time DFT, but this comes at the cost of interferences. Chiollaz and Favre[43] introduced a smoothing procedure, which is being successfully applied to the analysis of rapidly changing spectra.[258, 221: p.130–139]

In this research, the systems under consideration are assumed to be in a quasi-constant state, and no variations over excessively short times are considered. In this situation, the DFT is a very adequate tool to investigate the spectral information.

2.4 Low-order modelling

In *feedback systems*, the dynamic modes of greatest interest are usually found at relatively low frequecies, at least compared to the highest frequencies that could theoretically be modelled. *Low-order modelling* is the practice of concentrating the analysis of a system on a relatively low number of relevant modes.

The *Helmholtz resonator* in fig. 2.5 will be discussed as a example. A Helmholtz resonator consists of a *cavity* (subscript 'ca'), connected to the environment by a *neck* (subscript 'nk'). Since the cross-sectional area of the neck is much smaller than that of the cavity, the flow velocity is much higher in the neck than in the rest of the system. As a result, the effect of inertance is most significant inside the neck, while it can be neglected elsewhere. The volume of the neck is in turn much smaller than that of the cavity, so that the compliance of the fluid in the neck can be neglected, compared to that of the fluid in the cavity.[106: §10] For illustrative purposes, the cavity has been equipped with a microphone, whose output signal is compared to a reference, amplified, delayed and fed to a loudspeaker (subscript 'ls').
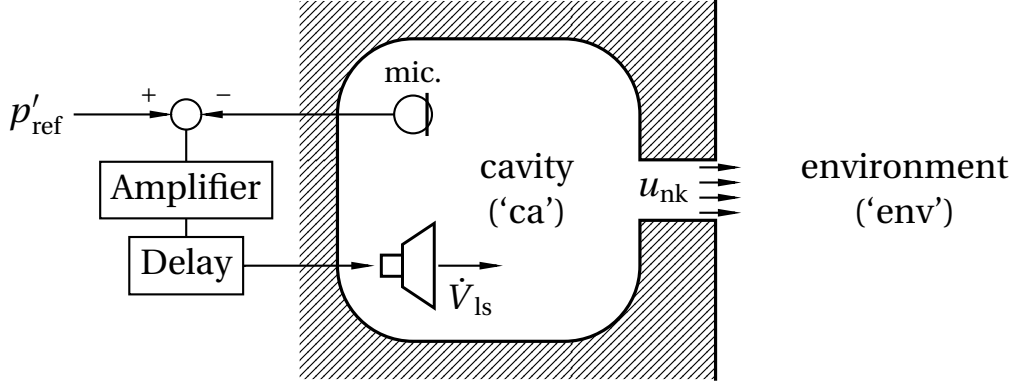
Figure 2.5: Helmholtz resonator with a minimalistic control system

The governing equations are:

Mass conservation (eq. 2.1) for a fixed volume (the cavity), with flow entering at the loudspeaker and through the neck only:

$$\partial_t \iiint_V \rho \, \mathrm{d}V + \iint_{A_{nk}} \rho \, \vec{u} \cdot \vec{n} \, \mathrm{d}A + \iint_{A_{ls}} \rho \, \vec{u} \cdot \vec{n} \, \mathrm{d}A = 0 \,.$$

The *lumped form* is found by assuming plug flow through the neck, and homogeneous density in the cavity, since internal pressure differences are negligible compared to the pressure drop over the neck:

$$V_{ca} \partial_t \rho = - A_{nk} \left(\rho \, u \right)_{nk} + \rho_{ca} \, \dot{V}_{ls} \,.$$

In linearised form, leaving out terms of the order of fluctuations squared, this becomes

$$V_{ca} \partial_t \rho'_{ca} = - A_{nk} \bar{\rho} \, u'_{nk} - A_{nk} \rho' \, \bar{u}_{nk} + \bar{\rho} \, \dot{V}'_{ls} \,, \tag{2.27a}$$

where the second term on the right hand side disappears since $\bar{u}_{nk} = 0$.

One-dimensional momentum conservation (eq. 2.2), for a fixed volume without viscous dissipation or external forces:

$$\partial_t \iiint_V \rho \, \vec{u} \, \mathrm{d}V + \iint_{\partial V} \rho \, \vec{u} \, \vec{u} \cdot \vec{n} \, \mathrm{d}A = - \iint_{\partial V} p \, \vec{n} \, \mathrm{d}A \,.$$

The one-dimension, lumped formulation describing the fluid in the neck is:

$$A_{nk} L_{nk} \partial_t (\rho \, \vec{u})_{nk} + A_{nk} \left(\rho_{env} u_{env}^2 - \rho_{ca} u_{ca}^2 \right) = -A_{nk} \left(p_{env} - p_{ca} \right) ,$$

$$\partial_t (\rho \, u)_{nk} + \frac{\rho_{env} u_{env}^2 - \rho_{ca} u_{ca}^2}{L_{nk}} = \frac{-\left(p_{env} - p_{ca} \right)}{L_{nk}} ,$$

after linearisation, this becomes:

$$\bar{\rho} \, \partial_t u'_{nk} = \frac{p'_{ca} - \bar{p}}{L_{nk}} . \tag{2.27b}$$

Poisson's adiabatic relation (eqs. 2.14)

$$p_{ca} \propto \rho_{ca}^{\gamma} ,$$

linearised as:

$$\frac{\mathrm{d} p'_{ca}}{\bar{p}} = \gamma \frac{\mathrm{d} \rho'_{ca}}{\bar{\rho}} . \tag{2.27c}$$

The controller action is given by

$$\dot{V}_{ls} = \left(p_{ref} - p_{ca} \right) X_{amp} \, e^{-i \omega \tau} , \tag{2.27d}$$

where X_{amp} is the amplification factor and τ is a delay.

2.4.1 Matrix representation

The system can be expressed in the form of matrix equations:

$$\mathrm{d}_t \begin{bmatrix} p'_{ca} \\ u'_{nk} \end{bmatrix} = \overbrace{\begin{bmatrix} -X_{amp} \, e^{-i \omega \tau} \, \frac{\bar{\rho}}{V_{ca}} c^2 & -A_{nk} \frac{\bar{\rho} c^2}{V_{ca}} \\ \frac{1}{L_{nk} \bar{\rho}} & 0 \end{bmatrix}}^{\mathbf{A}} \begin{bmatrix} p'_{ca} \\ u'_{nk} \end{bmatrix} + \overbrace{\begin{bmatrix} X_{amp} \, e^{-i \omega \tau} \, \frac{\bar{\rho}}{V_{ca}} c^2 \\ 0 \end{bmatrix}}^{\mathbf{B}} p'_{ref} .$$

A is the *system matrix,* describing the temporal evolution of the state variables p'_{ca} and u'_{nk}. **B** is the *input matrix,* describing the influence of the input p'_{ref} on the system.

The output p'_ca is related to the state variables and input by the *output matrix* **C** and *feedthrough matrix* **D**. In this case the expression is rather trivial:

$$
p'_\text{ca} = \overbrace{\begin{bmatrix} 1 & 0 \end{bmatrix}}^{\textbf{C}} \begin{bmatrix} p'_\text{ca} \\ u'_\text{nk} \end{bmatrix} + \overbrace{\begin{bmatrix} 0 \end{bmatrix}}^{\textbf{D}} p'_\text{ref} .
$$

Without controller action or external excitation ($X_\text{amp} = 0$, and $\textbf{B} = \vec{0}$), the system simplifies to

$$
\text{d}_t \begin{bmatrix} p'_\text{ca} \\ u'_\text{nk} \end{bmatrix} = \begin{bmatrix} 0 & -A_\text{nk}\dfrac{\bar{\rho}\, c^2}{V_\text{ca}} \\ \dfrac{1}{L_\text{nk}\bar{\rho}} & 0 \end{bmatrix} \begin{bmatrix} p'_\text{ca} \\ u'_\text{nk} \end{bmatrix} .
$$

In the frequency domain, the differential operator is replaced by a factor $(\mathrm{i}\omega)$, so that the eigenvalues of the matrix can be interpreted as frequencies for which the system can oscillate without excitation, multiplied by i. The current matrix has an *eigenvalue* $\mathrm{i}\omega_\text{R} = \mathrm{i}c\sqrt{A_\text{nk}/(L_\text{nk} V_\text{ca})}$ for the (right) *eigenvector* $[\mathrm{i}\omega_\text{R} L_\text{nk}\bar{\rho}, 1]^\text{T}$:

$$
\mathrm{i}c\sqrt{\frac{A_\text{nk}}{L_\text{nk} V_\text{ca}}} \begin{bmatrix} \mathrm{i}\omega_\text{R} L_\text{nk}\bar{\rho} \\ 1 \end{bmatrix} = \begin{bmatrix} 0 & -A_\text{nk}\dfrac{\bar{\rho}\, c^2}{V_\text{ca}} \\ \dfrac{1}{L_\text{nk}\bar{\rho}} & 0 \end{bmatrix} \begin{bmatrix} \mathrm{i}\omega_\text{R} L_\text{nk}\bar{\rho} \\ 1 \end{bmatrix} .
$$

Where the eigenvalue of the matrix corresponds to the *eigenfrequency* of the system, the eigenvector corresponds to the *eigenmode*. Currently the eigenmode involves only the discrete state variables p'_ca and u'_nk, oscillating at a constant amplitude and a frequency of $\omega = \omega_\text{R}$. Modes with increasing or decreasing amplitude will be discussed in the remainder of this section. In sec. 3.3, the spatial mode shapes of the Hummer combustor are modelled in taX.

Having a system response in the absence of input means that the absolute value of the transfer function is infinity at that (complex) frequency. These points in the complex plane are referred to as *poles*. Frequencies for which there is no response to a certain complex frequency, are known as *zeros*.

The eigenfrequency of the Helmholtz resonator derived above is purely real, which means that the resonator would keep humming endlessly. This is not physical, and in reality the oscillation will decay due to various effects:

- Viscous dissipation in the neck could be added to the left-hand side of eq. (2.27b) as a term depending on u'_{nk} instead of $\partial_t u'_{nk}$.

- Radiation of sound could be modelled by replacing $\bar{p}$ on the right-hand side of eq. (2.27b) by a more appropriate expression including u'_{nk}.

- Pressure loss by flow separation, in case of higher amplitudes, which is a non-linear effect which could be modelled similar to sound radiation, with some amplitude dependence, for instance as a term including u'^2_{nk}.

For simplicity's sake, these terms are left out of the analysis in this section.

König[135] used the frequency response of Helmholtz resonators to visualise sound, split up in different frequency ranges. His spectral analyser, shown in fig. 2.6, consists of an array of Wheatstone's apparatuses, mentioned in sec. 1.1.
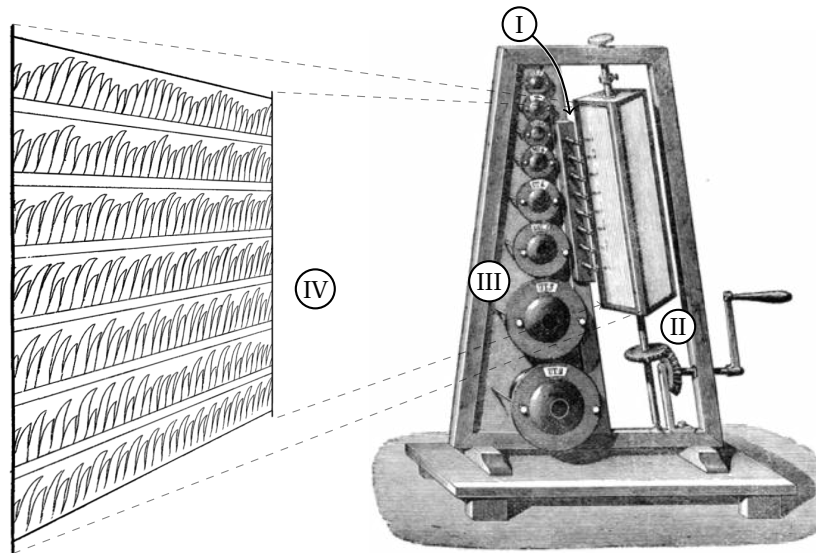
Figure 2.6: This acoustic spectral analyser by König[135] uses flames (I) and a rotating mirror (II) to visualise resonance in a series of Helmholtz resonators (III). The resulting projections are traced, as shown on the left (IV).[235]

2.4.2 Block diagram

When the system gets more elaborate, it is hard to keep an overview of the system matrix. To get a grasp on more complicated systems, feedback systems

are often displayed in *block diagrams*, such as fig. 2.7. The diagram includes the resonator and the controller with feedback loop. The influence of an external disturbance (p'_{env}) and measurement errors are indicated for completeness of the graph.
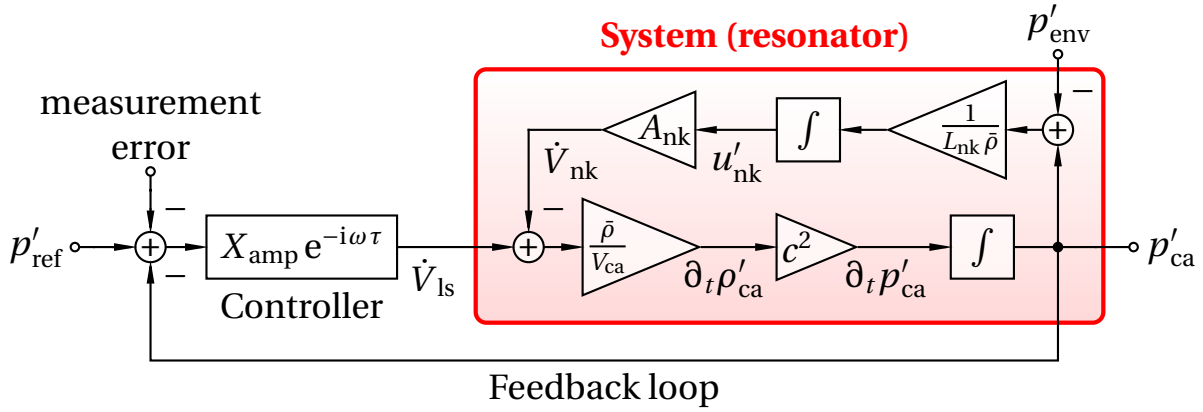
Figure 2.7: Block diagram, describing the Helmholtz resonator with controller as shown in fig. 2.5.

Multiplications by real numbers are indicated by triangles, additions are round nodes, and all other operations are drawn as rectangles. Feedback systems with loops can be simplified. Taking p'_{ca} as output and $\dot{V}_{ls}$ as input, the forward path is a multiplication by $(\bar{\rho}/V_{ca}) c^2/(i\omega)$, and the return path is a multiplication by $-1/(L_{nk} \bar{\rho} i\omega) A_{nk}$, so that

$$\text{output} = \text{forward path} (\text{input} + \text{return path} \cdot \text{output})$$

$$= \frac{\text{forward path}}{1 - \text{forward path} \cdot \text{return path}} \text{input} ,$$

and in this specific case

$$p'_{ca} = \frac{\bar{\rho}/V_{ca} \; c^2 \; 1/i\omega}{1 + \bar{\rho}/V_{ca} \; c^2 \; 1/(i\omega) \; 1/(L_{nk} \bar{\rho}) \; 1/(i\omega) \; A_{nk}} \dot{V}_{ls}$$

$$= \frac{\bar{\rho}/V_{ca} \; c^2}{i\omega + c^2 \; A_{nk}/(L_{nk} V_{ca}) \; 1/(i\omega)} \dot{V}_{ls}$$

$$= \frac{\bar{\rho} \, c^2/V_{ca}}{i\omega + \omega_R^2/(i\omega)} \dot{V}_{ls} .$$

This expression has a pole ($p'_{ca} / \dot{V}_{ls}$ becomes infinite) for $\omega = \omega_R$, so even if this frequency is not present in the input signal, it can exist in the output. If on the other hand this frequency is constantly present in the input signal, the amplitude will grow indefinitely. Poles with a negative imaginary part of ω (in the left-hand half of the s-plane) represent damped eigenmodes of the system. In the absence of excitation their amplitude goes down. Poles with a positive imaginary part of ω (in the right half of the s-plane) represent unstable modes, which start growing in amplitude at the slightest disturbance, even there is no further excitation at the corresponding frequency.

Very little controller action is needed to move the poles of the Helmholtz resonator to the left-hand side of the s-plane. With

$$X_{amp} = \frac{V_{ca}}{\bar{\rho} \, c^2} \, n$$

and

$$\tau = 0 \,,$$

the transfer function can be worked out as

$$p'_{ca} = \frac{n}{i\omega + \omega_R^2 / (i\omega) + 1 \cdot 10^{-6}} \, p'_{ref} \,.$$

This transfer function has a pole when the denominator becomes zero at

$$i\omega = \frac{-1 \cdot 10^{-6} \pm \sqrt{n^2 - 4\omega_R^2}}{2}$$

$$\Re\,(i\omega) < 0 \,,$$

so the system is stable for any (arbitrarily small) positive n.

2.4.3 The Nyquist criterion

As systems become more complicated, it becomes impractical to find all poles of the transfer function individually, and determine where they are situated in the s-plane. Nyquist[200] realised that the question of stability for a system could be answered by investigation of the *open-loop transfer function* (OLTF or $\mathcal{G}_{OL}$).

In fig. 2.7, the OLTF relates the output p'_{ca} to the input p'_{ref}, after removal of the arrow labelled 'Feedback loop', i.e.

$$\mathcal{G}_{\text{OL}} = X_{\text{amp}}\, e^{-i\omega\tau}\, \frac{\bar{\rho}\, c^2 / V_{\text{ca}}}{i\omega + \omega_{\text{R}}^2 / (i\omega)}\;.$$

The Nyquist criterion states:

> Plot plus and minus the imaginary part of $A\,J(i\omega)$ against the real part for all frequencies from 0 to ∞. If the point $1 + i0$ lies completely outside this curve the system is stable; if not it is unstable.

The quantity $A\,J(i\omega)$ as used by Nyquist is in fact $-\mathcal{G}_{\text{OL}}$, so that in a 'modern' analysis $\mathcal{G}_{\text{OL}} = -1$ implies a pole in the *closed-loop transfer function* (CLTF or $\mathcal{G}_{\text{CL}}$):

$$p'_{\text{ca}} = \mathcal{G}_{\text{CL}}\, p'_{\text{ref}} = \frac{\mathcal{G}_{\text{OL}}}{1 + \mathcal{G}_{\text{OL}}}\, p'_{\text{ref}}\,,$$

and the number of encirclements of $(-1 + 0i)$ determine whether the system is stable.

The Nyquist criterion only guarantees stability for a controller applied to an otherwise stable system. An unstable system can appear to be stabilised when an unstable pole coincides with a zero in the controller transfer function. In this case the mode has only become uncontrollable instead of being stabilised. Furthermore the Nyquist criterion assumes that unstable modes are manifested in the output. If the sensor position is chosen unfortunately, the system may seem stable, although there are unobservable modes.

This criterion can now be used to evaluate the stability of the actively controlled Helmholtz resonator. Three cases are tested, with controller settings listed in tbl. 2.1. Compared to case A, case B has an increased gain, while the delay was increased for case C.

Figure 2.8 shows the corresponding *Nyquist plots* on top. For case A, the point $(-1 + 0i)$ lies outside the contour, so this case is stable. The other contours lie around $(-1 + 0i)$, so the corresponding cases are unstable. This representation does however have a few drawbacks:

- Due to the pole in the OLTF (at ω_{R}), the contours do not fit in the plot area. It is however important to know how the different curves in the plot are connected to determine whether $(-1 + 0i)$ lies inside the contour.

Case	X_{amp}	τ	Stability
A	$2\,V_{ca}/\left(\bar{\rho}\,c^2\right)$	$\pi/\left(6\,\omega_R\right)$	Yes
B	$5\,V_{ca}/\left(\bar{\rho}\,c^2\right)$	$\pi/\left(6\,\omega_R\right)$	No
C	$2\,V_{ca}/\left(\bar{\rho}\,c^2\right)$	$\pi/\left(4\,\omega_R\right)$	No

Table 2.1: Three sets of controller settings and their resulting stability according to the Nyquist criterion.

- It can not be seen what point on a curve corresponds to a certain frequency. Labels could be added along the curve, but this would further clutter the plot.

- It is unclear how the controller action has influenced the transfer function, and as a consequence, it is hard to design a controller in a structured way.

Bode[25, 26] found a solution to these shortcomings, by plotting the absolute value and the argument of the OLTF in two separate plots as a function of frequency. The plot at the bottom of fig. 2.8 shows an example. In this plot, the point $(-1+0\mathrm{i})$ corresponds to the values 1 on the absolute-value axis, and $-\pi$ on the argument axis. The system is stable if the absolute value of the OLTF drops below 1 before the argument drops below $-\pi$.

The plot shows show clearly that changing X_{amp} (between case A and B) only changes the absolute value of the transfer function, while changing the delay τ (between case A and C) influences the (derivative of the) argument only. The instability of case C lies just over $2\,\omega_R$, which is shown much more clearly in the *Bode plot*.

The Bode plot can, however, be harder to read in some cases, for instance when the OLTF approaches $(-1+0\mathrm{i})$, but does not cross the real axis,[213: §4.3.1] or when the absolute value of the OLTF stays below unity for all frequencies. In those situations, the Nyquist plot can be more conclusive.

For systems with real-valued inputs and outputs, the transfer function for negative frequencies is the conjugate of that for positive frequencies:

$$\mathcal{G}\left(-\omega\right) = \mathcal{G}\left(\omega\right)^{*}.$$
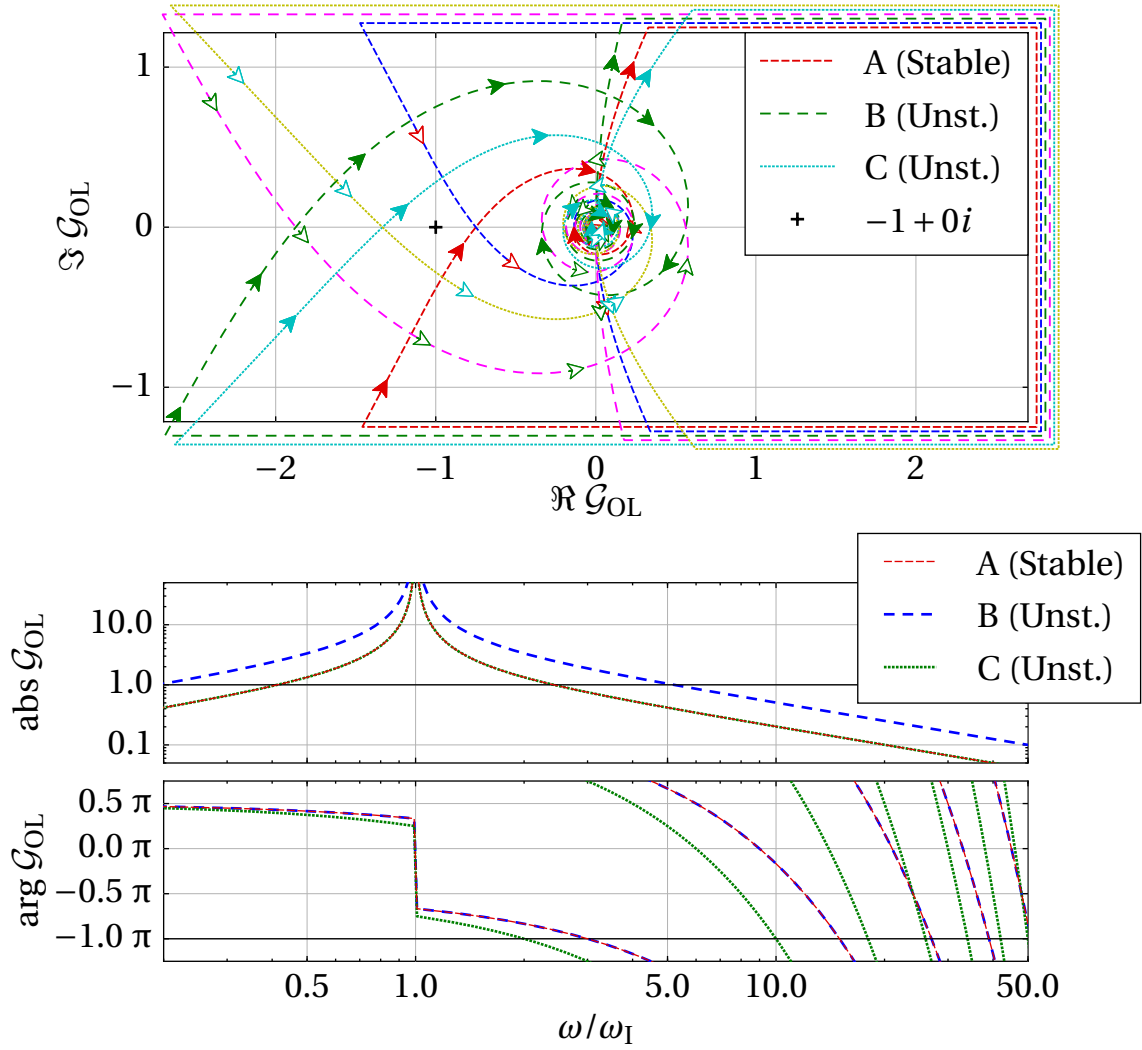
Figure 2.8: Nyquist plot (above) describing the system with control. The arrowheads in the Nyquist plot indicate the direction of increasing frequency. Empty arrowheads correspond to negative frequencies, solid arrowheads correspond to positive frequencies. The Bode plot (below) corresponds to the same system. Note the absolute value for case A is identical to the absolute value of case C. The argument of case A is identical to that of case B.

Therefore. Nyquist plots including the curve for negative frequencies (such as fig. 2.8) are symmetric around the real axis. To reduce clutter, without loss of information, the curve for negative frequencies will be left out of the Nyquist plots from here on.

2.4.4 Non-linearities and limit cycles

Of course, unstable modes mentioned before would not lead to truly infinite-amplitude oscillations in physical situations. In reality, the assumptions on which the linearised formulation was founded will lose their validity, and non-linear effects will emerge. In the current Helmholtz resonator example, some fluid-dynamical non-linear effects might be:

- At higher velocity fluctuations, shape drag proportional to the square of the velocity will become significant.

- At larger pressure fluctuation, the linearisation of Poisson's (eq. 2.27c) will lose its validity.

Neither of these have a damping effect on the pressure fluctuation inside the cavity, so the amplitude will probably only stop increasing due to clipping in the feedback loop. This could occur when the pressure rises outside of the measurement range of the microphone, of when the amplifier or the suspension of the loudspeaker becomes a limiting factor.

As the signal rises above the clipping level, the first harmonic (i.e. the component at the original signal frequency) saturates, with a limit of $4/\pi$, while odd higher harmonics are introduced, as shown in fig. 2.9.
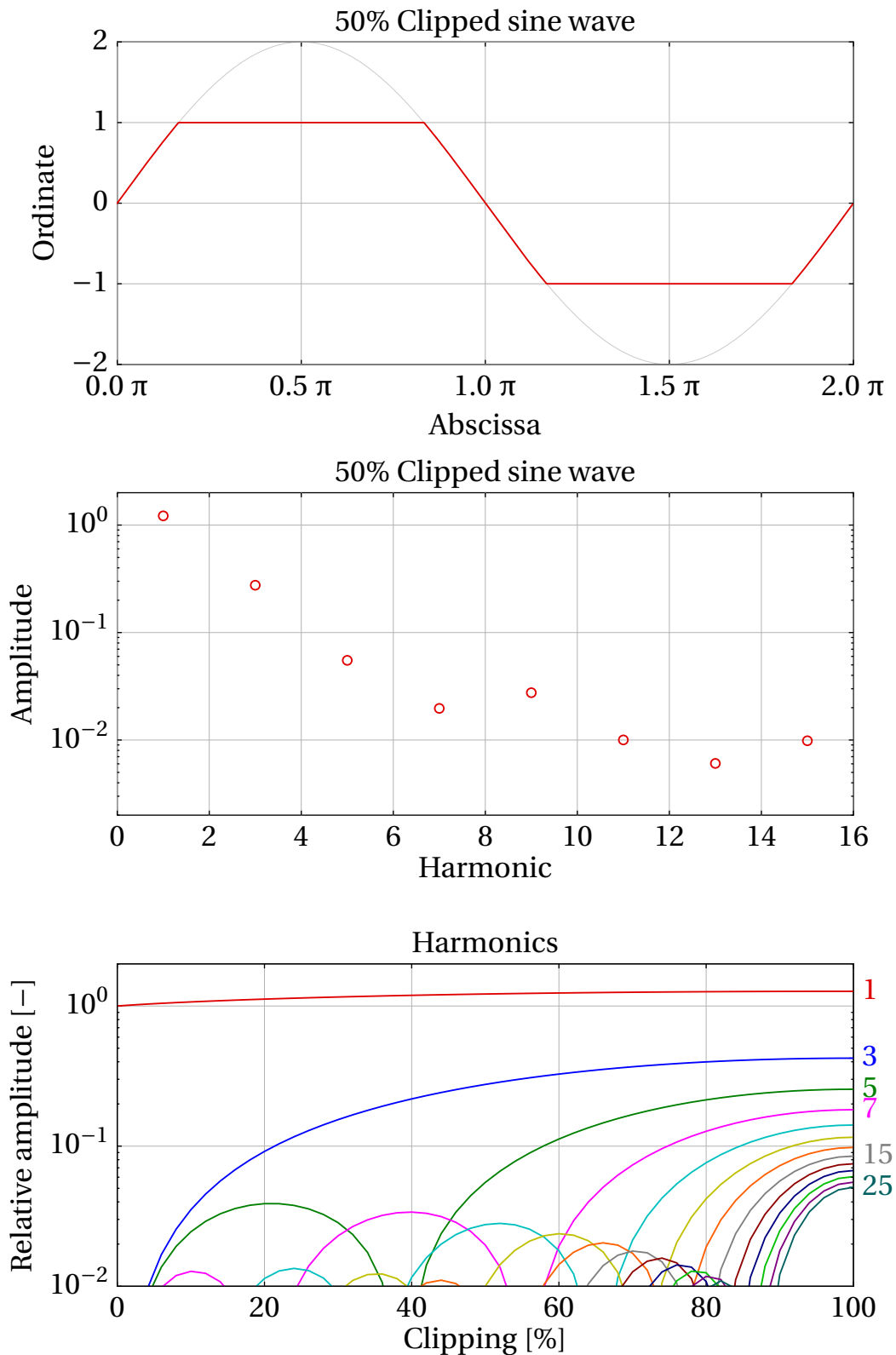
Figure 2.9: Introduction of higher harmonics by clipping of a harmonic signal. The limit of 100% clipping corresponds to a square wave, which can be expanded as $\mathrm{sgn}\,\sin(\omega\,t) = 4/\pi \sum_{k=1}^{\infty} \sin\left((2\,k-1)\,\omega\,t\right)/(2\,k-1)$.

3 Mitigation of combustion instabilities

This chapter will discuss the possible solutions to combustion instabilities. *Passive* and *active* control will be discussed in sec. 3.1 and sec. 3.2 respectively. Section 3.3 introduces the low-order network modelling tool 'taX', and demonstrates the network modelling of *active instability control* (AIC) on the unstable Hummer combustor.

Combustion instabilities can be damped in various ways. In this section, a division will be made between two mayor groups:

Passive control, where damping is achieved by fluid-dynamical means, without the use of electronics or actuators, and

Active control, where a sensor and an actuator are used in a closed control loop to counter-act the oscillation at the same frequency.

Most damping strategies fit well in either of these groups. A few intermediate cases exist though. In the case of *operating point control* for example, a sensor warns when an instability develops, or ideally shortly before. Consequently, the operating point is changed away from the instability. This form of control prevents damage to the turbine, but hardly improves operational flexibility.

In the case of *semi-active control*, a sensor is used in a control loop to tune passive measures according to the vibration at hand. The actuator moves with the operating point changes, and is not required to move at the frequency of the instability. In this section semi-active control will be discussed as a special case of passive control.

For uncorrelated actuation, also known as *open loop control*, the actuator is actuated at another frequency than the oscillation to be damped. This form of control does not fit the definition of active control stated above very well, especially since the control loop does not necessarily need to be closed. From an actuation point of view though, this strategy is more similar to active than passive control, and as a consequence, it will be regarded here as a case of active control.

3.1 Passive control

Figure 3.1 gives a simple overview of the feedback loop leading to unstable combustion. Passive control can disturb this feedback loop in various ways. According to Culick,[56: p.8-1] passive control of combustion instabilities can be divided into three operating principles:

- decrease of the source term,
- increase in damping, and
- change of the combustion chamber response.
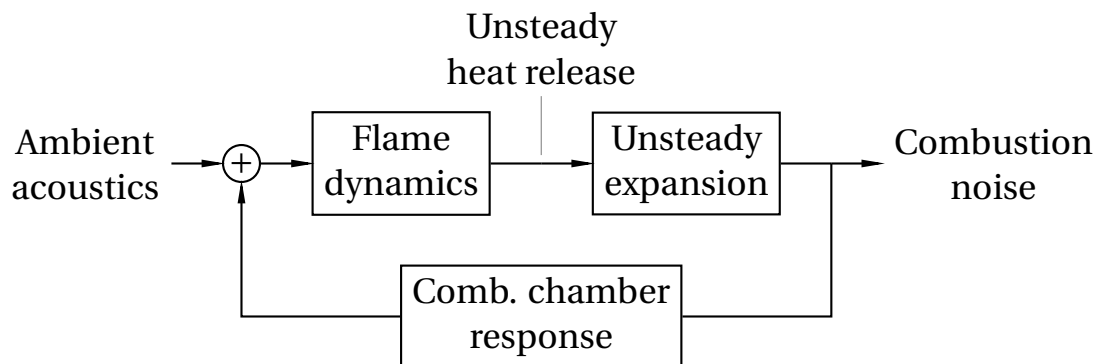
Figure 3.1: A very simple overview of the relevant phenomena in combustion instabilities.

3.1.1 Reduction of the source term

Wimpress[290] wrote one of the earliest discussions on the reduction of unstable combustion in rocket engines. Chapter 9 of his book describes the influence of the fuel grain shape of solid fuel rockets on combustion stability.

Other means are needed for stabilising gas flames. Brande[34] found that steady flames react to an electric field. Abrukov et al.[2] used both steady and alternating electric fields to damp an oscillation in a simple laboratory combustor. Hammer et al.[97] investigated the feasibility of this concept under pressure, with the possible aims of application in gas turbine combustors. The electric field not only influenced the stability of the flame, but the emission of CO and NO_x as well.

The shape of the burner or the flame holder has influence on the stability of the combustor as well. Blackman[20] showed on small-scale combustors that

screech can be eliminated by properly spacing the flame holders relative to the combustor walls. Polifke et al.[215] describe how a burner can be made more stable, by either changing the vortical structure after the fuel nozzle, or by lengthening the flame in stream-wise direction. Bazarov[17] gives an overview of similar considerations, leading to more stable operation of rocket fuel injection systems.

Thiruchengode et al.[272] describe a semi-active approach where the ratio of fuel delivered to the pilot flame is increased when instability is imminent. The pilot flame is usually more stable than the lean-premixed mean flame. Increasing the pilot fuel flow has a detrimental effect on emissions and efficiency, but can be justified to stabilise the flame in transient operation.

3.1.2 Change in combustor response

A resonance can be attenuated effectively, without explicit addition of damping or removal of excitation, if some form of coupling in the feedback loop can be disrupted. In the case of the combustion systems, where the feedback loop usually depends on a combination of acoustic and convective delays, this can most often be achieved by the variation of some characteristic length.

Since the earliest demonstrations of thermoacoustics, it has been known that the variation of a length of the combustor, or the position of the flame could make an oscillation disappear. Putnam and Dennis[218] give a structured overview of a simple burner, where variation of various lengths leads to alternating stability and instability. Zinn et al.[297] describe a semi-active control system, where the time delay between fuel injection and combustion can be dynamically tuned to avoid instability. Noiray et al.[198] describes a combustor in which several modes can become unstable, depending on the length of the chamber upstream of the flame, as well as the oscillation amplitude. Noiray et al.[198] do not refer to their investigation as being a form passive control, since their objective is to accurately describe the stability in the system, instead of damping the instabilities that arise. Goldmeer et al.[91] describe the tuning of fuel gas supply system as a solution to combustion instabilities.

Schadow[237] discusses the same mismatching procedure, but concentrates on altering the vortex shedding frequency, instead of the length of the combustion chamber.

3.1.3 Resonators and liners

Resonators were amongst the earliest examples of passive damping for combustion instabilities. Fox,[82] and Sterbentz and Evvard[259] for instance damped instabilities in ramjets by adding Helmholtz and quarter wave resonators respectively, tuned to the dominant frequency.

A perforated liner with a resonating cavity behind it, can be regarded as a collection of Helmholtz resonators, with their cavities connected. The combustion chamber walls of gas turbines traditionally had perforated lines to allow cooling air through. These liners worked as effective acoustic dampers. In rocket engines they were added specifically for this purpose.[21, 281]

Liners with throughflow do not only damp acoustics, but also cause pressure losses in the mean flow. Leaving out these liners, efficiency could be increased, and a higher turbine inlet temperature could be realised with lean combustion. A trade-off has to be made between acoustic damping and stability on one hand, and efficiency on the other. As a result the benefit of damping liners had to motivated and estimated more quantitatively.[70]

Neise and Koopmann[194] developed dynamically tuned Helmholtz resonators to damp the dominant frequency of centrifugal fan noise. This development was taken up by the combustion community and a variety of dampers was developed that could be used for semi-active control. To name a few, Zhao and Morgans[294] used adaptive Helmholtz resonators to damp an experimental combustor, Park and Sohn[207] investigated half wave resonators to damp instabilities on rocket engines, and Sun[263] described a liner where cavity depth and cross flow can be adapted to need, for application on an airborne gas turbine.

3.1.4 Baffles

Oscillation in rocket engines are often solved by mounting baffles at velocity anti-nodes, perpendicular to the mode velocity. Harrje and Reardon[99: §8.2] give an overview of longitudinal baffles, which are effective against transverse modes. In the same year, Cherry and Haymes[42] filed a patent for transverse baffles, damping longitudinal modes. In gas turbines, the choice for a cannular layout instead of an annular combustion chamber, can be seen as a variation on this theme.

3.1.5 Addition of particulate material

It has long been suspected that particulate material (e.g. rain, fog or snow) should have some influence on sound propagation, although its influence was hard to separate from other atmospheric circumstances.[66, 278] Theory describing the damping potential of suspended particles developed during the early[36, 246] and middle[45, 72] 19th century.

In solid rocket engines, the addition of aluminium particles became a popular means of damping oscillations.[119, 183, 201] Aluminium is not consumed or evaporated in the flame, and is much lighter than many other materials with this property.

Aluminium particles can not be used in gas turbines however, as they would lead to unacceptable erosion of the turbine blades downstream of the combustion chamber.

3.2 Active instability control (AIC)

Unfortunately, passive control solutions usually need to be tailor-made per combustor, and tend to work only satisfactory over a limited operating range.[298] *Active instability control* (AIC) of combustion instabilities hopes to overcome these limitations. Besides, active control allows optimisation for other objectives, such as increased thermal output[203] or reduction of pollutants.[257]

In 1936, Lueg[162] was granted a patent on *anti-sound*, where a sound field measured by a microphone is reproduced in opposite phase by a loudspeaker, leading to cancellation of the sound field. Keeping the phase of the anti-sound opposite to the original sound field is usually only possible within a certain region (see fig. 3.2). For acoustic systems with one-dimensional wave propagation however, it is conceptually relatively easy to damp sound by these means.

After a proposal by Bollay,[29] Tsien[274] analysed active control as a remedy to low-frequent oscillations in a liquid-fuelled rocket. The first laboratory-scale demonstration followed a lot later by Dines,[67] under the supervision of Ffowcs Williams.[77]

This example, where a Rijke tube was damped by a loudspeaker mounted near an open end, was investigated further by Heckl[103, 104] and patented for the
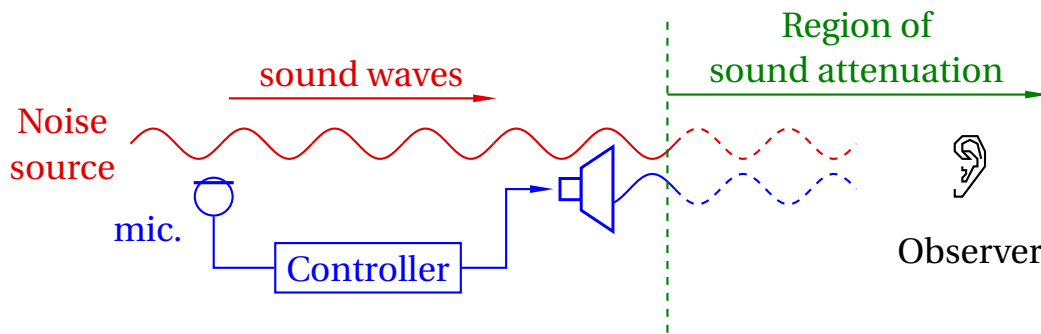
Figure 3.2: The principle of anti-sound. Note the absence of a feedback loop.

application on industrial combustion systems.[78] The patent states that the actuator can be either a diaphragm or a loudspeaker, mounted either in the fuel supply system or near to the combustion region. The figures hint that the intended application was instability of an afterburner.

Around the same time, the Technische Universität München, as well as the École Centrale Paris started applying active control on combustion instabilities. Lang et al.[140] for instance, in a collaboration between both institutes, used a loudspeaker in the plenum between fuel injection and flame, to apply active damping to a premixed propane combustor.

Langhorne et al.[141] were the first to publish on experimental control of a combustion instability by modulation of the fuel supply. Since this form of actuation requires much less energy than modulation of the air flow – or anti-sound in the conventional sense – this method of actuation is now used in virtually all applications and research.[58]

Most examples of AIC are found on a laboratory scale, with very few exceptions. Rolls-Royce demonstrated active control of afterburner rumble during the early 1990s, but published these results only much later.[180, 181] DeLaat and Chang,[64] working at NASA in cooperation with Pratt & Whitney and United Technologies Research Center (UTRS) demonstrated active control of unstable combustion at high frequencies (up to 1 kH), intended for application on aero-engines. Whether these developments were commercialised is however not known.

Hermann and Orthmann[112] did have commercial success, using a *direct dive valve* (DDV) by Moog Inc. in the fuel supply line to apply AIC on a heavy duty industrial gas turbine.

3.2.1 Actuation position

As mentioned before, the mounting position of the actuator is an important choice in the application of AIC, with great influence on the controllability. While the greatest part of recent research is dedicated to actuation of the fuel flow, a notable exception remains the 'impedance tuning' by Bothien et al., using loudspeakers[30] or valves[31] to prescribe a variable artificial boundary condition on a laboratory combustor. It must be noted that that research is not meant to be applied to commercial gas turbines, but to test how prototypes of burners behave under varying boundary conditions before they are mounted in commercial systems.

It is not always practical to modulate the complete fuel flow. Hermann and Orthmann[112] for instance only modulated the pilot fuel flow, which accounts for 10% of the total. The main premix flame did however follow the actuated pilot flame very well.

3.2.2 Actuators

Actuators for AIC should ideally be mechanically robust, work reliably in hot environments and have a great actuating action. Smaller actuators are easier to mount and require less structural modification of the combustion system.

Till now, the most popular actuators for AIC are by far loudspeakers and valves. Schuermans[242: §6.1.2] lists their relative (dis)advantages as follows:

Valves are mechanically more robust than loudspeakers. At low frequencies they are more effective than loudspeakers. Their behaviour is more complex, and not always linear. Opening or closing a valve while keeping the throughflow constant changes the acoustic behaviour.

Loudspeakers are usually a lot cheaper than valves, and perform better at higher frequencies. They are however mechanically not as robust as valves. For Hermann and Orthmann[112] this was an important reason to choose valves over loudspeakers.

Neither of these actuators works satisfactory in all applications, and selection of an actuator that delivers the desired control authority remains a challenge in the application of AIC systems.[238] As a result, many other actuators have been described in the literature.

Bloxsidge et al.[23] for instance used a mechanical shaker to open and close the inlet nozzle of the combustor, effectively this can be regarded as a custom spindle-type valve, regulating the inlet air flow.

Hermann et al.[110] used a piezo actuator to modulate the liquid fuel flow in their combustor. Although this actuator was much stronger than a loudspeaker, and much quicker than a valve, due to the small volume of fuel flow that can be modulated, this actuator is unsuitable for actuation of gaseous fuel.

Neumeier et al.[195] developed a 'liquid injector actuator' where a magneto-restrictive actuator is used to rapidly (range of kH) actuate a spindle-type valve in liquid fuel flow. The atomisation process is emphasised. The actuator is controlled in three frequency ranges: the lower range controls the mean fuel flow, the middle range damps instabilities and at the highest frequency range the atomisation process is enhanced.

Abrukov et al.[2] and Afanas'ev[4] used uncorrelated and correlated control respectively, to damp an unstable flame using an electric field over the combustion zone.

Padmanabhan et al.[203] used pulsating jets, transversal to the mean flow, to control vortex shedding at the flame holder, and thereby the combustion dynamics. Gutmark et al.[92] describe a similar actuator, combining the generation of vortices with the injection of fuel.

Gutmark et al.[94] used a spark plug, or 'flame kernel pulse actuator' to stimulate the ignition of the flame in a controlled manner.

3.2.3 Sensors

Like the actuators, sensors should ideally be small, robust and reliable, and easy to mount. Various sensors can be used to monitor the different fluctuating quantities to gain information about the oscillating state of a combustor.

Dines[67] used CH^* chemiluminescence as controller input. CH^*, and later OH^* and C_2^* chemiluminescence have remained popular sensor types for laboratory combustors.[56: p.9-31, 128, 93] Chemiluminescence has the obvious disadvantage that the sensor needs optical access to the combustion region. Especially in industrial systems it is hard to get a wide enough field of view to monitor the complete combustion region. A smaller view angle often leads to a noisy signal dominated by small-scale effects.[68] When good optical access can not

be realised, because there is no flame (as for example in an electrically heated Rijke tube), or because optical access is not economically feasible, pressure sensors are a popular choice.

The Rijke tube by Heckl[103] used a microphone to feed the controller. Microphones are however relatively sensitive to heat and water condensation, which is problematic in the vicinity of a flame.[109] Piezo transducers are much more robust from this point of view, and have been proven reliable enough for industrial application.[112]

Paduano et al.[204] used hot wire anemometers for a laboratory demonstration of active control of a compressor. Although no examples are found in literature, this could be done for unstable combustion just as well. This type of sensor is however much too sensitive for industrial applications. Dowling[68] hopes for *micro electro-mechanical system* (MEMS) solution to measure velocity fluctuations by a robust device.

The position of the sensors has to be chosen so that all modes that can occur in the system are observable. The application of control introduces new degrees of freedom to the system, and as such introduces new – and possibly unstable – modes to the system. The observability of these new modes has to be considered as well.[242: p.136] Padula and Kincaid[205] give an overview of optimisation methods for sensor placement.

If modes are close in the frequency spectrum, enough sensors should be present to differentiate between them. Hermann and Orthmann[112] used for instance 12 sensors to control a combustion chamber with 24 burners. This remains the only example of multi-channel (MIMO) AIC found in the literature.[58: p.449]

In practice, especially when control is applied as a postfix solution to an existing combustor, every new sensor access point has to be justified. From an engineering point of view it is often more feasible to add a sensor at a low-pressure position than at a position with high mean pressure. Due to the range in allowable operating temperature of sensors, these are usually placed at relatively cool positions.

3.2.4 Controllers

From a controller engineering point of view, combustion instabilities pose several special challenges. First of all combustion instabilities are non-linear, due

to the influence of quantities which cannot be negative, such as pressure and heat release, or the influence of vorticity. Combustion systems often include time delays – convection times of e.g. entropy, vorticity and mixture fluctuations – which are long compared to the dominant period of the acoustics. There is usually a high level of noise in the system and the action of control might change properties of the system, such as the time lags mentioned before.[58: p.2]

The system changes with the operating point, temperature (run time), fuel composition and other factors. There is a lot of noise due to turbulence for instance and there are many degrees of freedom and corresponding modes of oscillation, which cannot practically be measured independently.

The current research uses the controller by Hermann and Orthmann,[112] which works in the frequency domain. In simple terms, it behaves like an amplification with phase shift, which can be set according to preferences. The details of the algorithm are not disclosed.

The earliest attempts at AIC used very simple controllers. Heckl[104] for instance used only a phase shifter and amplifier to control the loudspeaker on her electric Rijke tube. Moran et al.[180] (around the same time, but published later) used a simple comparator with time lag to damp an unstable aero-engine afterburner. Poinsot et al.[210] added a filter to improve the result on a turbulent laboratory combustor.

These simple controllers worked well as a proof-of-concept for a fixed operating point, but lacked the flexibility to cope with varying operating conditions in industrial applications. In the worst case, this could lead to destabilisation of the combustor with controller. To solve this shortcoming, Billoud et al.[19] used an *least mean squares* (LMS) adaptive controller after Widrow,[288] to stabilise the controller used by Poinsot et al.[210] for varying operating conditions.

Fung et al.[85] (in a theoretical analysis) introduced a Luenberger estimator,[163] to estimate the state of a combustion system where the heat release depended on a distributed time delay. This approach was later extended for non-linear applications.[84]

Gutmark et al.[93] pioneered the use of a neural network to optimise the controller coefficients on their test rig. In a following publication,[95] the neural network optimisation was done off-line for varying operating equivalence ratio. Consequently, the optimised controller settings were used depending on the equivalence ratio – an approach known as gain scheduling.

Early adaptive controllers often caused secondary peaks[102] and could still destabilise. These issues were addressed by Hathout et al.,[100] who proposed a model-based controller using the *linear-quadratic Gaussian optimal control / loop transfer recover* (LQG/LTR) approaches. Later Annaswamy et al.[8] applied this controller to a bench-top burner, and showed that the model-based controller damped the instability quicker than the LMS-algorithm used for comparison. Chu et al.[49] used H_∞-loop shaping*[171] in an effort to develop a more robust adaptive controller.

To explicitly address the time delays present in combustion systems due to convection, Hathout et al.[101] started investigating the application of Smith controllers[254] for the suppression of combustion instabilities. These controllers, called posi-cast ('positive forecasting') controllers by Hathout et al., were developed to deal with systems with a known time delay, for instance due to convection. The original formulation by Smith dealt with stable systems. The generalisation to the control of unstable systems, still formulated in the time domain, was developed by Manitius and Olbrot.[166] Ichikawa[123] extended this method to a frequency-domain pole placement approach, which was taken as a starting point by Hathout et al.[101] The implementation in experiment followed by Park et al.[208]

Le et al.[146] investigated the merits of the *multiscale extended Kalman* (MSEK) approach, which combines a multi-scale wavelet-like analysis with an extended Kalman observer.

Schuermans[242] gives a comparison between H_∞-loop shaping controllers and a controller acquired by an evolutionary algorithm. The latter performed better in terms of suppression of the instability, while the H_∞-loop shaping controller sometimes got unstable.

For instabilities at higher frequencies, it can become challenging to find an actuator which has a cut-off frequency high enough to follow the combustion instability. Yu et al.[291] found that in such situations, the instability can be damped by actuating at a sub-harmonic of the dominant oscillation.

Perhaps even more surprising, combustion instabilities can be damped by actuation at a frequency unrelated to the dominant instability, using open loop control. Lubarsky et al.[161] damped a gas turbine combustor by fluctuating

---

∗ H_∞ refers to the objective of this loop-shaping strategy, which is to reduce the ∞-norm (the peak) of the signal in Hilbert space, i.e. its frequency spectrum. The LQG/LTR approach by Hathout et al.[100] on the other hand minimises the 2-norm of the spectrum, i.e. the total energy present over the full spectrum of the oscillation.

the fuel mass flow by an open loop controller. While a conventional controller realised a reduction of only 50% of the pressure fluctuation, the instability was damped almost completely using uncorrelated control. Uhm and Acharya[280] used an open-loop controller to modulate a high momentum air jet.

3.2.5 Outlook on the state of the art

Altogether, a lot of research effort has been invested to investigate the possibilities of AIC. The first successful lab scale demonstrations were realised more than 30 years ago, and many more have followed since. In this light, the publications on industrial applications are disappointingly scarce.

The implementation of AIC on a given gas turbine remains far from trivial, and no example is known where the effect of a certain actuator mounted on a certain position was predicted successfully. Combustion instabilities are costly matter which could embarrass gas turbine manufacturer, so unsuccessful attempts to solve instability issues are hardly ever published.

Publications concentrate on successful, but often ad hoc solutions. When these are effective enough to solve the problems at hand, research interest fades quickly. Nonetheless, it has been shown that AIC can improve the reliability and flexibility of combustion systems, and the commercialisation would benefit from the availability of more predictive models and tools.[56, 58] The current thesis will investigate and extend the possibilities of low-order acoustic network tools and CFD for this purpose.

3.3 Thermoacoustic network modelling in taX

In an *acoustic network model*, an acoustic system is represented by a collection of interconnected discrete *elements*. Network models are a very quick method to analyse a complex acoustic system, as long as the parts of the system can be described by the elements available in the network model. This modelling approach has proven useful in many fields, such as exhaust mufflers,[83, 255] loudspeaker systems[252, 270] and combustion systems.[24, 104, 175, 211]

This research uses the network modelling tool 'taX', based on the work of Polifke,[213] Leandro et al.,[147] and Huber[120] amongst others. An overview of the

newest developments during the writing of this thesis is given by Emmert et al.[71]

Figure 3.3 gives an impression what an acoustic network in taX could look like. The model consists of one-dimensional elements – in this case only the straight ducts labelled ' `Plenum`', ' `CombChamberCold`' and ' `CombChamberHot`' – and zero-dimensional (acoustically compact) elements. taX can, amongst others, be used to calculate the most unstable frequencies, resonance spectra, profiles of acoustic variables, and a transfer matrix over several elements. The formulation of the acoustical behaviour of the elements will be discussed in the following.

3.3.1 One-dimensional acoustic wave propagation

Acoustic wave propagation is governed by the mass conservation, momentum conservation (without body forces and viscous stress tensor), and Poisson's relation (eqs. 2.1b, 2.2b and 2.14):

$$\partial_t \rho + \vec{\nabla} \cdot \left(\rho \, \vec{u} \right) = 0 \,,$$

$$\partial_t \left(\rho \, \vec{u} \right) + \vec{\nabla} \cdot (\rho \, \vec{u} \otimes \vec{u}) = -\vec{\nabla} p + \underbrace{\vec{\nabla} \cdot \bar{\bar{\tau}} + \rho \, \tilde{\vec{F}}}_{\text{sources}=0} \,,$$

$$p \propto \rho^{\gamma} \,.$$

For simplicity, a quiescent steady solution will be assumed.[†] Linearisation and subtraction of the steady solution yields

$$\partial_t \rho' + \bar{\rho} \, \vec{\nabla} \cdot \vec{u}' = \mathcal{O}\left(\text{fluctuations}^2\right) \,,$$

$$\bar{\rho} \, \partial_t \vec{u}' + \gamma \frac{\bar{p}}{\bar{\rho}} \vec{\nabla} \rho' = \mathcal{O}\left(\text{fluctuations}^2\right) \,.$$

Subtracting $\bar{u}$ times the divergence of the second equation from the time derivative of the first equation, and introducing $c^2 = \gamma \, \bar{p} / \bar{\rho}$ gives

$$\partial_t^2 \rho' - c^2 \vec{\nabla} \cdot \vec{\nabla} \rho' = 0 \,, \tag{3.1a}$$

[†] A more general approach makes the identification of sources and wave propagation much more elaborate. For a more thorough introduction, the reader is referred to Lighthill,[157, 158] Culick,[57] or Candel et al.[38: §2]
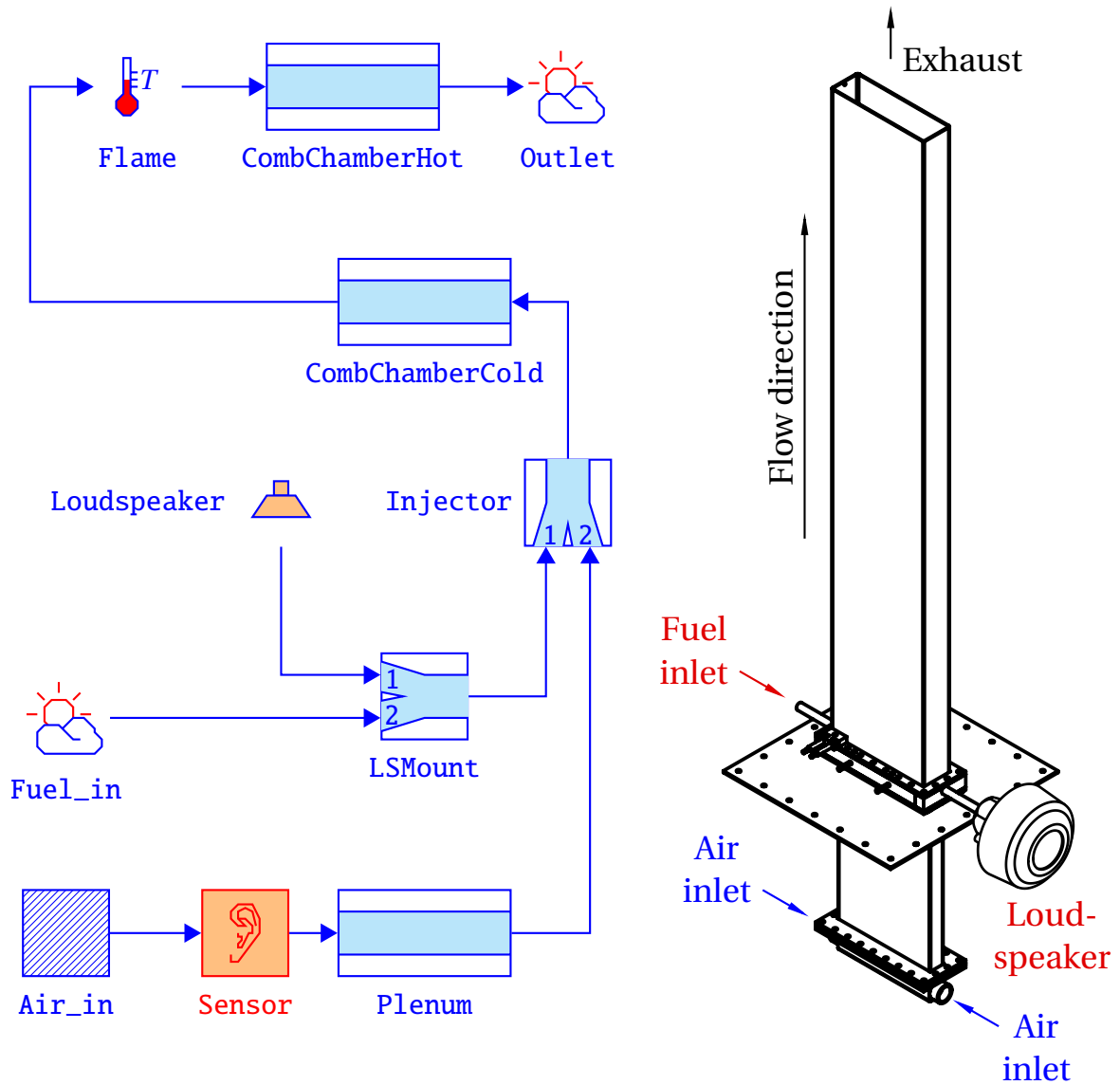
Figure 3.3: An acoustic network, as used by taX. The network on the left gives an abstract and simplified representation of the combustor on the right.

which is the acoustic wave equation for density in a quiescent medium. The wave equation for pressure eq. (3.1b) can be found with Poisson's relation (eqs. 2.14). The equation for velocity is found when switching the time derivative and spatial derivative in the second last step:

$$\partial_t^2 p' = c^2 \vec{\nabla} \cdot \vec{\nabla} p' \, , \tag{3.1b}$$

$$\partial_t^2 \vec{u}' = c^2 \vec{\nabla} \vec{\nabla} \cdot \vec{u}' \, , \tag{3.1c}$$

where the newly introduced variable c is the speed of sound:

$$c^2 = \gamma \frac{\bar{p}}{\bar{\rho}} = \gamma \tilde{R} \bar{T} \, . \tag{3.1d}$$

For the one-dimensional case, solutions to the acoustical wave equation can be written as the sum of a wave travelling in positive x-direction (f) and one travelling the other way (g):[212]

$$\frac{p'(x, t)}{\bar{\rho} c} = f(x - c\,t) + g(x + c\,t) \, , \tag{3.2a}$$

$$u'(x, t) = f(x - c\,t) - g(x + c\,t) \, . \tag{3.2b}$$

This solution is named after d'Alembert who found that the shapes of vibrating strings could be expressed in this way.[59–61]

The amplitude ratio between travelling pressure and velocity waves is known as the *characteristic impedance $Z = \bar{\rho} c$.*

Re-introducing a steady, homogeneous background velocity $\bar{u}$ (i.e. 'plug flow'), the characteristic wave amplitudes f and g are defined as follows:

$$f(x - c\,t - \bar{u}\,t) = \tfrac{1}{2} \left(\frac{p'}{\bar{\rho} c} + u' \right) , \tag{3.2c}$$

$$g(x + c\,t - \bar{u}\,t) = \tfrac{1}{2} \left(\frac{p'}{\bar{\rho} c} - u' \right) . \tag{3.2d}$$

These equations show that when $\bar{u} > c$, both waves travel in downstream direction. This changes the wave equation from elliptic to hyperbolic, and brings about a fundamental change in the flow dynamics. To stress the importance of the ratio between flow velocity and the speed of wave propagation, the background velocity is often non-dimensionalised as the Mach number[3, 164]

$$M \equiv \frac{\bar{u}}{c} \, . \tag{3.3}$$

The straight duct — In a straight (i.e. prismatic) duct, cross sectional area, density, speed of sound and Mach number are constant. In taX, these quantities are taken from the element upstream of the duct, while the length is to be defined. Neglecting damping, wave propagation in a straight duct can be modelled as a pure time delay:

$$\mathfrak{f}_{\text{out}} = \mathfrak{f}_{\text{in}} \exp\left(-\mathrm{i}\,\frac{\omega/c}{M+1}\,L\right),$$

$$\mathfrak{g}_{\text{out}} = \mathfrak{g}_{\text{in}} \exp\left(-\mathrm{i}\,\frac{\omega/c}{M-1}\,L\right).$$

For brevity, one-dimensional wave propagation is often expressed in terms of the wave numbers:

$$k_{\mathfrak{f}} = \frac{\omega/c}{M+1} \qquad \text{and} \qquad k_{\mathfrak{g}} = \frac{\omega/c}{M-1},$$

so that

$$\mathfrak{f}_{\text{out}} = \mathfrak{f}_{\text{in}} \exp\left(-\mathrm{i}\,k_{\mathfrak{f}}L\right) \qquad \text{and} \qquad \mathfrak{g}_{\text{out}} = \mathfrak{g}_{\text{in}} \exp\left(-\mathrm{i}\,k_{\mathfrak{g}}L\right).$$

Most notably, the straight duct can not be used to model the combustion chamber. Although its geometry is one-dimensional, the temperature increase at the flame causes an increase in flow velocity and speed of sound, as well as a decrease in density. This leads to a change in characteristic impedance and scattering of acoustic waves. The hot and cold sections can be modelled as separate ducts though.

3.3.2 Conventions on notation

3.3.2.1 Steady background flow

In taX, the steady background flow is defined in terms of

- the speed of sound c,
- the Mach number M,
- the (mean) density $\bar{\rho}$,
- the diameter D, which is used to describe skew (mixed longitudinal / transversal) modes in annular geometries, and

- the cross-sectional area A.

These quantities are defined at the boundaries, and handed over to the following elements in downstream direction. At discontinuities, for example at an area change, the new values of the quantities are set at the outlet of the element, as shown in fig. 3.4.
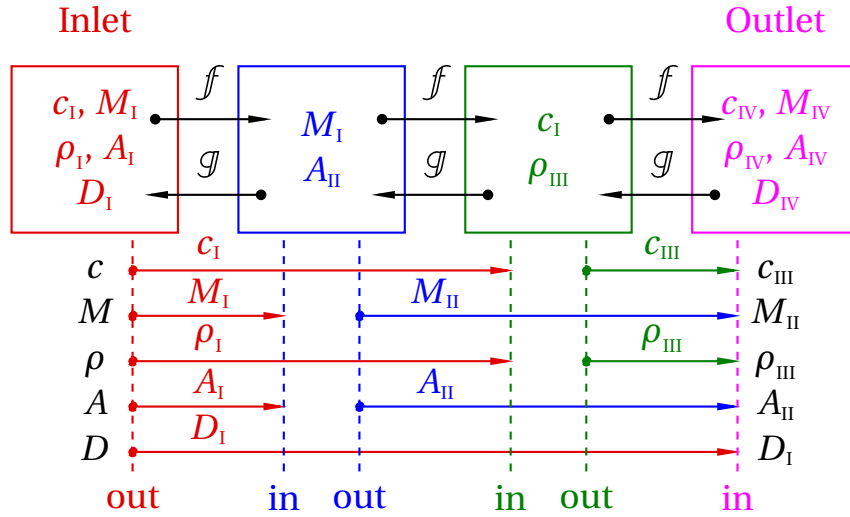
Figure 3.4: Propagation of the steady flow variables through a network in taX.

Other variables can be computed from these, although they are hardly used in the source code. The most relevant are:

- The steady pressure $\bar{p}$ is found by Poisson's adiabatic relation (eq. 2.14), and the definition of c (eq. 3.1d):

$$\bar{p} = \bar{\rho}\,\tilde{R}\,T$$

$$= \frac{c^2}{\gamma}\,\bar{\rho}\,. \tag{3.4a}$$

- The steady flow velocity, and other measures for throughflow are derived from the Mach number:

$$\bar{u} = M\,c$$

$$\dot{V} = A\,M\,c$$

$$\dot{m} = A\,M\,\bar{\rho}\,c\,. \tag{3.4b}$$

- The temperature T cannot be determined from the information given before. Either the temperature itself or the specific gas constant $\tilde{R}$ should be given additionally:

$$T\,\tilde{R} = \frac{c^2}{\gamma} = \frac{\bar{p}}{\bar{\rho}} \,. \tag{3.4c}$$

3.3.2.2 Fluctuating quantities

Fluctuations on the steady solution are expressed in terms of the characteristic wave amplitudes f and g. The definition in eq. (3.2) can be used to find p' and u'. Poisson's adiabatic relation (eq. 2.14), and definition of c (eq. 3.1d) are used to express fluctuations in the density ρ'.

$$
\begin{aligned}
\rho' &= \frac{\bar{\rho}}{\bar{p}}\,\frac{p'}{\gamma} \\[2mm]
&= \frac{p'}{c^2} \tag{3.5a} \\[2mm]
&= \frac{\bar{\rho}}{c}\left(f + g\right). \tag{3.5b}
\end{aligned}
$$

The total pressure (eq. 2.4) is expressed as

$$
\begin{aligned}
\left(p + \frac{1}{2}\rho\,u^2\right)' &= p' + \frac{1}{2}\bar{u}^2\,\rho' + \bar{\rho}\,\bar{u}\,u' + \mathcal{O}\left(\text{fluctuations}^2\right) \\[2mm]
&= p' + \bar{\rho}\,\bar{u}\,u' + \mathcal{O}\left(M^2\right) \\[2mm]
&= p' + \bar{\rho}\,M\,c\,u' \\[2mm]
&= \bar{\rho}\,c \begin{bmatrix} 1+M \\ 1-M \end{bmatrix} \cdot \begin{bmatrix} f \\ g \end{bmatrix}. \tag{3.5c}
\end{aligned}
$$

Fluctuations in the mass flow are written as

$$
\begin{aligned}
\dot{m}' &= A\left(\rho\,u\right)' \\
&= A\left(\rho'\,\bar{u} + \bar{\rho}\,u' + \mathcal{O}\left(\rho'\,u'\right)\right) \\
&= A\left(\frac{M}{c}\,p' + \bar{\rho}\,u'\right) \\
&= A\bar{\rho}\left[\begin{array}{c} M+1 \\ M-1 \end{array}\right] \cdot \left[\begin{array}{c} f\!\!f \\ g \end{array}\right].
\end{aligned}
\tag{3.5d}
$$

3.3.2.3 Nomenclature of matrices

For every element, the model has a description relating the acoustic state at either side. Several formulations exist. Some of the most common are:

The transfer matrix relates the pressure and velocity fluctuation on the downstream side of a block to those on the upstream side, with optional source/sink terms $\mathcal{S}$ modelling an actuator ('act'):

$$
\left(\begin{array}{c} \frac{p'}{\bar{\rho}c} \\ u' \end{array}\right)_{\mathrm{dn}} = \left[\begin{array}{cc} \mathsf{T}_{1,1} & \mathsf{T}_{1,2} \\ \mathsf{T}_{2,1} & \mathsf{T}_{2,2} \end{array}\right]\left(\begin{array}{c} \frac{p'}{\bar{\rho}c} \\ u' \end{array}\right)_{\mathrm{up}} + \left(\begin{array}{c} \mathcal{S}_p \\ \mathcal{S}_u \end{array}\right) X'_{\mathrm{act}}.
$$

This formulation was used by Fukuda[83] in 1963 to model exhaust mufflers. Elements based on mass and momentum conservation are often formulated in terms of p' and u', giving succinct expressions for the matrix coefficients.

The scattering matrix expresses leaving characteristic wave amplitudes $f\!\!f_{\mathrm{dn}}$ and g_{up} as a linear combination of the incoming waves. This formulation is currently used in taX. The elements of the scattering matrix represent the reflection ($\mathcal{R}$) and transmission ($\mathcal{T}$) coefficients of the acoustic element:

$$
\left(\begin{array}{c} g_{\mathrm{up}} \\ f\!\!f_{\mathrm{dn}} \end{array}\right) = \left[\begin{array}{cc} \mathcal{R}_{\mathrm{up}} & \mathcal{T}_{g} \\ \mathcal{T}_{f\!\!f} & \mathcal{R}_{\mathrm{dn}} \end{array}\right]\left(\begin{array}{c} f\!\!f_{\mathrm{up}} \\ g_{\mathrm{dn}} \end{array}\right) + \left(\begin{array}{c} \mathcal{S}_{\mathrm{up}} \\ \mathcal{S}_{\mathrm{dn}} \end{array}\right) X'_{\mathrm{act}}.
$$

The scattering transfer matrix combines properties of the transfer matrix and the scattering matrix. Downstream characteristic wave amplitudes are expressed in terms of those on the upstream side.

$$
\begin{pmatrix} f \\ g \end{pmatrix}_{\mathrm{dn}} = \begin{bmatrix} \mathbf{S}_{1,1} & \mathbf{S}_{1,2} \\ \mathbf{S}_{2,1} & \mathbf{S}_{2,2} \end{bmatrix} \begin{pmatrix} f \\ g \end{pmatrix}_{\mathrm{up}} + \begin{bmatrix} 1 & 0 \\ -\mathbf{S}_{2,1} & -\mathbf{S}_{2,2} \end{bmatrix} \begin{pmatrix} \mathcal{S}_{\mathrm{up}} \\ \mathcal{S}_{\mathrm{dn}} \end{pmatrix} X'_{\mathrm{act}} \, .
$$

This formulation allows sequential elements to be combined by simply multiplying their matrices, but including source terms is less elegant.

Other formulations are possible as well. A previous version of taX for instance used a formulation expressing the sources as a function of the system state.

$$
\begin{bmatrix} X_{1,1} & X_{1,2} & X_{1,3} & X_{1,4} \\ X_{2,1} & X_{2,2} & X_{2,3} & X_{2,4} \end{bmatrix} \begin{pmatrix} f_{\mathrm{up}} \\ g_{\mathrm{up}} \\ f_{\mathrm{dn}} \\ g_{\mathrm{dn}} \end{pmatrix} = \begin{pmatrix} \mathcal{S}_{\mathrm{Impulse}} \\ \mathcal{S}_{\mathrm{Volume}} \end{pmatrix} X'_{\mathrm{act}} \, .
$$

3.3.3 Compact (zero-dimensional) elements

In regions which are small compared to the wavelength, the phase of the acoustic waves can considered constant. This property – acoustic compactness – is quantified by the Helmholtz number He, which is required to be small:

$$
He = \frac{\omega \, L_{\mathrm{max}}}{c} \ll 1 \, .
$$

Panton and Miller[206] for instance mention that the resonant frequency of a Helmholtz resonator is independent of the shape of the cavity, as long as $L < \lambda/16$ in all directions, which corresponds to $He \lesssim 0.4$.

Formulations for simple discontinuities in the background flow (e.g. area or temperature discontinuities) are found directly by applying mass conservation, and equating pressure before and after the discontinuity according to eq. (3.5). A smooth jump in cross sectional area – without loss in total pressure – is for instance given by mass conservation:

$$
\left[\frac{p'}{c^2} M c + \bar{\rho} \, u' \right]_{\mathrm{in}}^{\mathrm{out}} = 0 \, ,
$$

and equal stagnation pressure before and after the discontinuity:

$$\left[\frac{p'}{\bar{\rho}\,c} + M\,u'\right]_{\text{in}}^{\text{out}} = 0\,.$$

Lumped mass — The lumped mass represents an acoustical inertance. In equivalent electrical circuits, it would be a self-inductance. It can be used to describe sections of the domain where compressibility can be neglected, but inertia can not. A typical example would be the neck of a Helmholtz resonator. No mass is stored or generated, so mass inflow and outflow are identical. In the style of eq. (3.5d):

$$\left[\frac{p'}{c^2}\,M\,c + \bar{\rho}\,u'\right]_{\text{in}}^{\text{out}} = 0\,.$$

There is a jump in the dynamic pressure, due to acceleration of the mass. The element makes no changes in the background flow. Using eq. (3.5c):

$$A\left[p' + \bar{\rho}\,M\,c\,u'\right]_{\text{in}}^{\text{out}} = -m\,\partial_t u'$$

$$A\left[p' + \bar{\rho}\,M\,c\,u'\right]_{\text{in}}^{\text{out}} = -A\,L_{\text{eq}}\,\bar{\rho}\,\mathrm{i}\,\omega\,u'$$

$$\left[\frac{p'}{\bar{\rho}\,c} + M\,u'\right]_{\text{in}}^{\text{out}} = -\frac{\mathrm{i}\,\omega\,L_{\text{eq}}}{c}\,u'\,.$$

The mass can be given directly, in the form of an (equivalent) volume or the equivalent length L_{eq}.

The element can be set as well to represent the end correction at a pipe exit; 0.6133 times the radius for an flangeless end according to Levine and Schwinger[150] or 0.82159 time the radius for a flanged end, according to Norris and Sheng.[199]

The end correction as computed by the element is based on the radius for a round cross section, i.e. $\sqrt{A/\pi}$. For an rectangular duct with a high aspect ratio (or an annular geometry) this would give unrealistic results. For example, a very long slit, of small width, would give $L_{\text{ec}} \to \infty$ as $A \to \infty$. The hydraulic radius D_{H} will be used instead to solve this issue. This is the radius of a circle with the same ratio between area and perimeter: $D_{\text{H}} = L_y\,L_z/\left(L_y + L_z\right)$.

Lumped volume — The lumped volume is an acoustic compliance, equivalent to an electric capacitor or a spring in the mechanical domain. The mass equation is given by the relation between pressure fluctuation and mass accumulation as expressed by eq. (2.27c). Rewritten in the style of eq. (3.5d), this becomes

$$\left[\dot{m}'\right]_{\text{in}}^{\text{out}} = -\partial_t m'$$

$$\left[A\left(\frac{M}{c}p' + \bar{\rho}\,u'\right)\right]_{\text{in}}^{\text{out}} = -\mathrm{i}\omega\,A\,L\,\frac{p'}{c^2}$$

$$\left[\left(\frac{M}{\bar{\rho}\,c}p' + u'\right)\right]_{\text{in}}^{\text{out}} = -\frac{\mathrm{i}\omega\,L}{c}\,\frac{p'}{\bar{\rho}\,c}\,.$$

Since there is no loss in total pressure,

$$\left[\frac{p'}{\bar{\rho}\,c} + M\,u'\right]_{\text{in}}^{\text{out}} = 0\,.$$

Either the volume or the equivalent length can be set.

Closed end / loudspeaker — Boundary conditions are mostly – but must necessarily – formulated as compact elements. The closed end, as well as the loudspeaker as currently implemented in taX, are compact boundary elements, representing an acoustically stiff boundary. The only difference is the absence of the source term u'_{ls} at the closed end. A non-zero Mach number can be set, to use the element to represent a choked inlet. Acoustical stiffness implies that mass flow fluctuations are independent of pressure fluctuation:

$$\frac{M}{\bar{\rho}\,c}p' + u' = u'_{\text{ls}}\,.$$

Open end / far field excitation — At an open inlet, the flow field is irrotational, so that according to Bernoulli's principle[18] (eq. 2.4) the total pressure is constant along streamlines. Therefore, the total pressure inside the duct is equal to the ambient pressure. For a simple open outlet the ambient pressure is constant, while it fluctuates for the element 'far field excitation':

$$\frac{p'_{\text{in}}}{c\,\bar{\rho}} + M\,u'_{\text{in}} = \frac{p'_{\infty}}{c\,\bar{\rho}}\,. \tag{3.6}$$

The reflection coefficient at the inlet is

$$\mathcal{R}_{\text{in}} = \frac{f}{g} = \frac{M-1}{M+1} \, .$$

At an outlet, there is flow separation along the perimeter of the duct. The dynamic pressure in the resulting jet is not recovered. Instead the static pressure is constant over the shear layer around the jet, so that the pressure inside the duct is equal to the ambient static pressure:

$$\frac{p'_{\text{out}}}{c\,\bar{\rho}} = \frac{p'_{\infty}}{c\,\bar{\rho}} \, .$$

The reflection coefficient at the outlet is simply minus unity:

$$\mathcal{R}_{\text{out}} = \frac{g}{f} = -1 \, .$$

Heckl[105] proposed a formulation which takes the frequency-dependence of radiation into account, where higher frequencies are radiated more efficiently (i.e. reflected less efficiently). Leaving out the non-linear effects, for consistency with the other elements, her expression becomes:

$$\mathcal{R} = -\frac{1 - A/(4\pi)\,(\omega/c)^2}{1 + A/(4\pi)\,(\omega/c)^2} \, , \tag{3.7}$$

Except for the following example of an Helmholtz resonator, this expression will be used throughout this research.

It has been shown by Rayleigh[266]‡ that applying this boundary condition directly at the end of the pipe does not give a realistic result. Continuity dictates that the oscillation continues into the air outside of, but in the close vicinity of the pipe exit. This effect can be modelled well, by adding an 'end correction' to the length of the pipe. Rayleigh gave values for this end correction, which were very close to values found later by more refined models.

For an flangeless, round exit, Levine and Schwinger[150] found $\Delta L_{\text{ec}} = 0.6133\sqrt{A/\pi}$. The case of a round, flanged exit was elaborated much later by Norris and Sheng,[199] who found $\Delta L_{\text{ec}} = 0.82159\sqrt{A/\pi}$.

---

‡ Chapter 16 and appendix A

3.3.4 The Helmholtz resonator as simple example

The elements can be combined to form systems of arbitrary topology. Figure 3.5 shows a Helmholtz resonator, as it could be modelled in taX. The resonator is excited by an external pressure field labelled 'FarField'.

ClosedEnd   LumpedVolume   AreaChange   Observer   LumpedMass   FarField
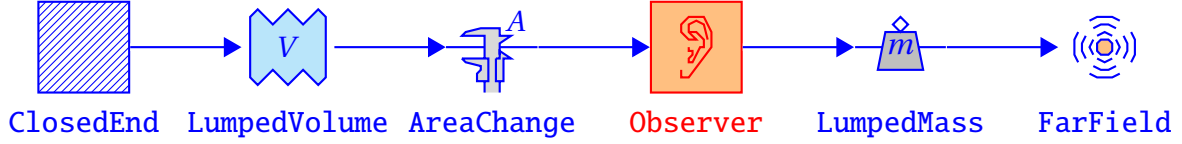
Figure 3.5: A Helmholtz resonator, exited by a varying external pressure field.

The following settings are set at the inlet 'ClosedEnd':

- Forcing amplitude $p'_\infty = 100\,\mathrm{Pa}$
- Speed of sound $c = 340\,\mathrm{m/s}$
- Mach number $M = 0$
- Density $\rho = 1.2\,\mathrm{kg/m^3}$
- Diameter $D = 0\,\mathrm{m}^\S$
- Area $A = 0.1^2\,\mathrm{m^2} = 1\,\mathrm{dm^2}$

The lumped volume is $V_{\mathrm{ca}} = 0.1^2 \cdot 0.1\,\mathrm{m^3} = 1\,\mathrm{dm^3}$. The exit of the area change is $A_{\mathrm{nk}} = 0.01^2\,\mathrm{m^2} = 1\,\mathrm{cm^2}$ and the lumped mass is set by the equivalent length $L_{\mathrm{nk}} = 1 \cdot 10^{-1}\,\mathrm{m}$. The resonant frequency of a Helmholtz resonator is given by

$$f_{\mathrm{I}} = \frac{c}{2\pi}\sqrt{\frac{A_{\mathrm{nk}}}{V_{\mathrm{ca}}\,L_{\mathrm{nk}}}}\,,$$

which is currently

$$\frac{340}{2\pi}\sqrt{\frac{0.01^2}{0.1^3 \cdot 0.1}} = 340\,\mathrm{rad/s}$$

$$\approx 54.11\,\mathrm{Hz}\,.$$

taX can determine the eigenfrequencies of the system directly. The output is as expected:

---

§ The 'diameter' parameter in taX is intended to describe annular geometries.

```
Approximate Solution found with Det(S) = 2.6e-16.
Eigenvalues:
Angular frequency:        340 - i 8.783e-13 [rad/s]
Frequency:             54.11 [Hz]          Growth rate: 0.000
```

Alternatively, taX can give the frequency response of the system for a certain excitation, evaluated at observer blocks. Either p', u', $\mathcal{f}$ or $\mathcal{g}$ can be chosen as output. Applying a forcing amplitude of $p'_\infty = 100\,\mathrm{Pa}$ at 'FarField', the response of the Helmholtz resonator is as plotted in fig. 3.6.
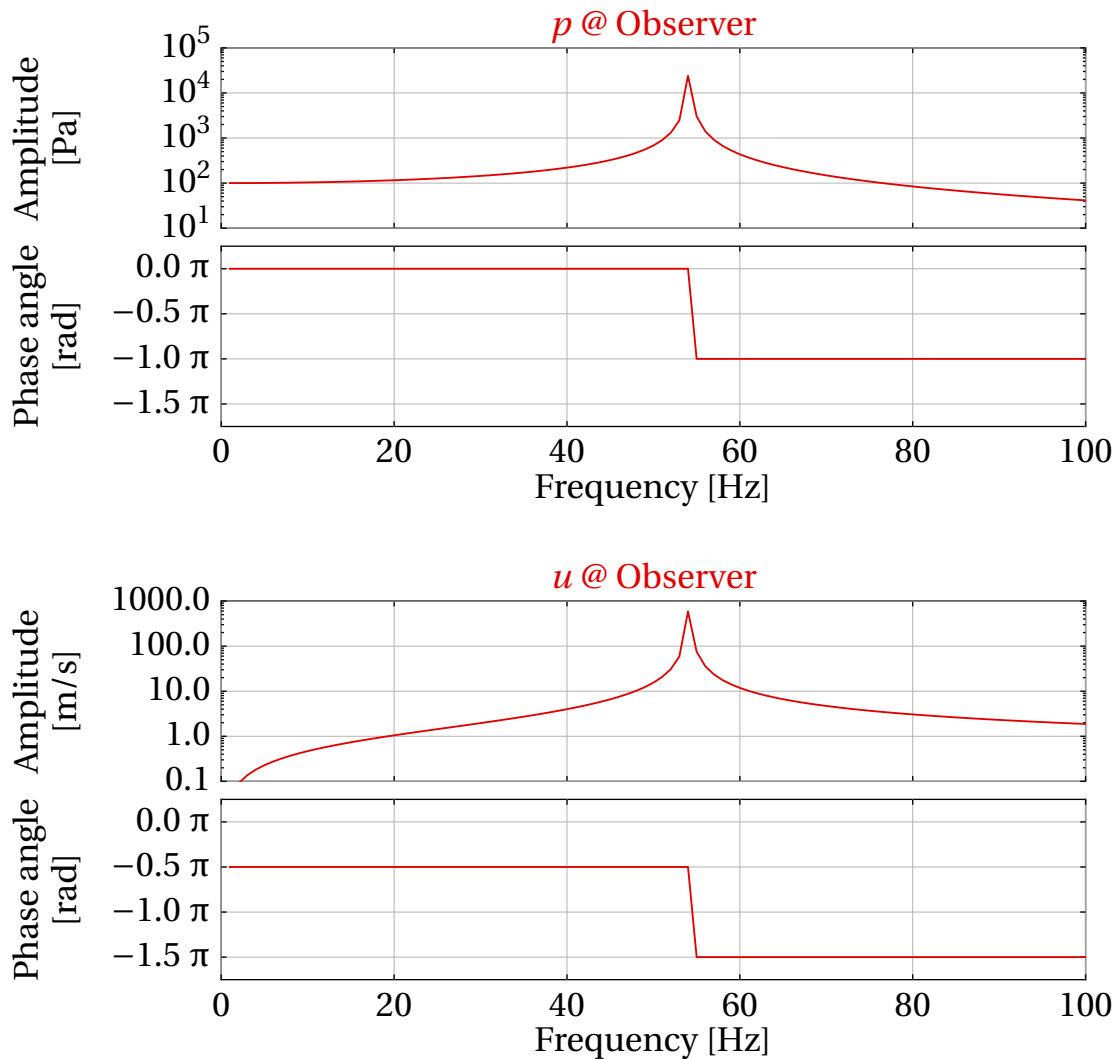
Figure 3.6: Acoustic pressure p' (above) and velocity u' (below) at the observer indicated in fig. 3.5, for an external pressure fluctuation of $100\,\mathrm{Pa}$.

The decision how a system should be divided into elements is somewhat arbitrary, and depends amongst other factors on what elements could be useful in the future. If one for instance expects to use Helmholtz resonators often, a new element can be formulated that models the impedance of a Helmholtz resonator in between two other elements. Figure 3.7 shows a system based on such an element, leading to the same results as found before.
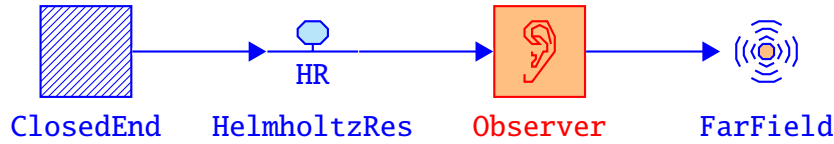
Figure 3.7: A Helmholtz resonator, implemented as a single element.

Alternatively, the Helmholtz resonator can be modelled by two short ducts, separated by an area change, as shown in fig. 3.8. For small values of L and at low frequencies, the system behaves like the lumped Helmholtz resonator. The cross sectional areas are defined in terms of L, so that the properties are the same as for the resonator discussed before. As L increases, the first resonant frequency decreases, and higher harmonics appear. For $L = 2\,\mathrm{m}$, the area change disappears, and the system becomes a quarter-lambda resonator, with a first resonant frequency at $c/L/4 = 42.5\,\mathrm{Hz}$.

3.3.5 Modelling active control in taX

Figure 3.9 shows a thermoacoustic resonator with a loudspeaker for active control. The network represents a tube, 1 m long, with an acoustically closed inlet and an open outlet.

The fluid enters the domain at the loudspeaker. The settings at this element are:

- $c_{\mathrm{cld}} = 340\,\mathrm{m/s}$
- $M_{\mathrm{cld}} = 0.02$
- $\rho_{\mathrm{cld}} = 1.2\,\mathrm{kg/m}^3$

- $A = 0.01\,\mathrm{m}^2$
- Active control and / or excitation depend on situation

The reference and observer are set to monitor pressure p. The ducts are both 0.5 m long. The block labelled 'NyqDummy' is a dummy element to investigate
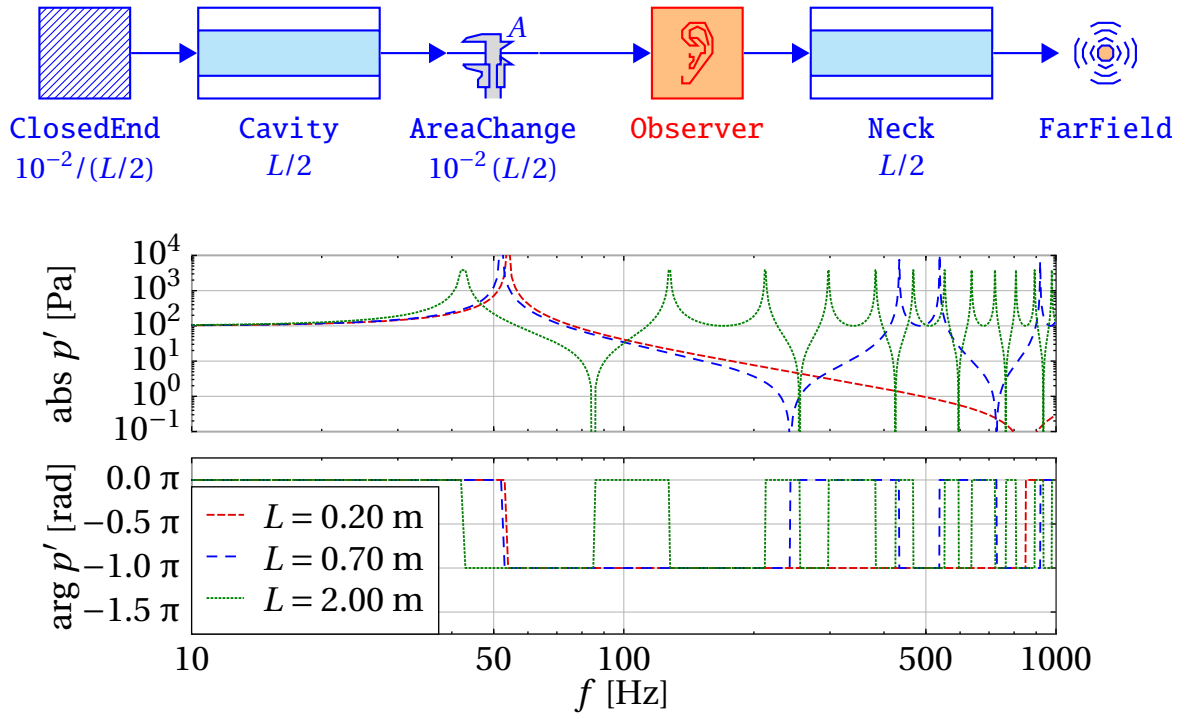
Figure 3.8: A resonator formed by two ducts (above) with pressure responses for various values of length L (below). For small values of L and at low frequencies, the system behaves like a Helmholtz resonator. For $L = 2\,\mathrm{m}$, the area change disappears, and the system becomes a quarter-lambda resonator, with a first resonant frequency at $c/(4L) = 42.5\,\mathrm{Hz}$.
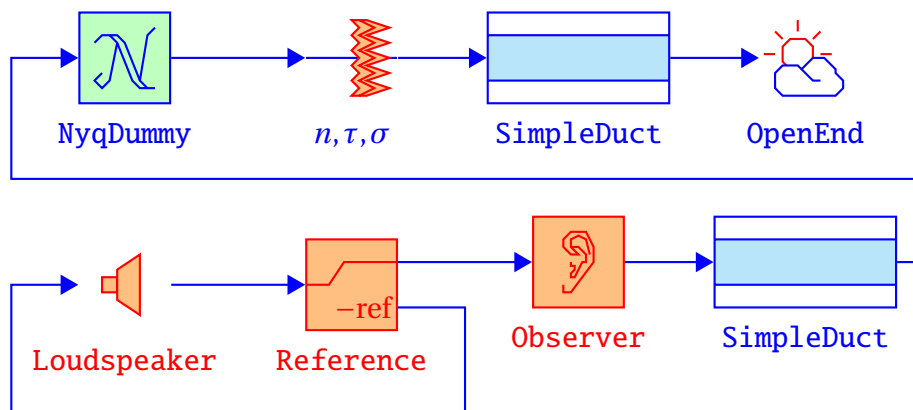
Figure 3.9: A thermoacoustic resonator with active control represented in taX.

the Nyquist criterion. It emits a unit wave in downstream direction and monitors the incoming wave on the upstream side, representing the open loop transfer function of the system.

The block labelled 'n, τ, σ' models the heat release and its acoustic effect according to the n, τ-model developed in the 1950s and described for instance by Crocco and Cheng.[55] The heat release influences the acoustics as a fluctuating volume source, described quantitatively by Chu.[48] The nominal interaction index $n_{\mathrm{nom}} = T_{\mathrm{out}}/T_{\mathrm{in}} - 1$. The additional variable σ is a measure for the temporal dispersion of the response of the heat release to velocity perturbations.[145, 243] The implementation in taX is by Temmler.[268] The flame increases the temperature by 60%, so that

- $n = n_{\mathrm{nom}}$
- $\tau = 0.7 \cdot 10^{-3}\,\mathrm{s}$
- $\sigma = 0.4 \cdot 10^{-3}\,\mathrm{s}$

- $c_{\mathrm{hot}} = \sqrt{1.6}\,c_{\mathrm{cld}}$
- $M_{\mathrm{hot}} = 1.6\,M_{\mathrm{cld}}$
- $\rho_{\mathrm{hot}} = 1.6\,\rho_{\mathrm{cld}}$

The end '`OpenEnd`' uses Heckl's[105] boundary condition, given in eq. (3.7). For increasing frequency, the reflection losses increase due to sound radiation. Together with the parameter σ in the flame element, these losses prevent the appearance of infinitely many unstable modes.

The Open-loop transfer function (OLTF), without actuation, as found by the Nyquist dummy is shown in fig. 3.10. There is one unstable mode, corresponding to the 3/4 wave form. The crossings of π by the phase in the Bode plot correspond to $(1 + 2N)/4$ wave forms for $N \in \mathbb{N}_1$. These higher modes are stable in the uncontrolled case.

Although the OLTF given by the Nyquist dummy provides information on the stability of the system, it is not obvious how a certain controller action would influence the stability of the system. For the sake of controller engineering, it gives more insight to open the control loop between sensor and controller, as was done in secs. 2.4.2 and 2.4.3. In the latter case, the controller action acts multiplicatively on the OLTF.

Figure 3.12 shows the open-loop transfer function found by opening the system between sensor and controller, when applying proportional control of $1 \cdot 10^{-4}\,\mathrm{m/s/Pa}$.

The unstable mode shows itself in this new Nyquist plot as a counter-clockwise loop, not containing the critical point $(-1 + 0\,\mathrm{i})$. This mode becomes stable
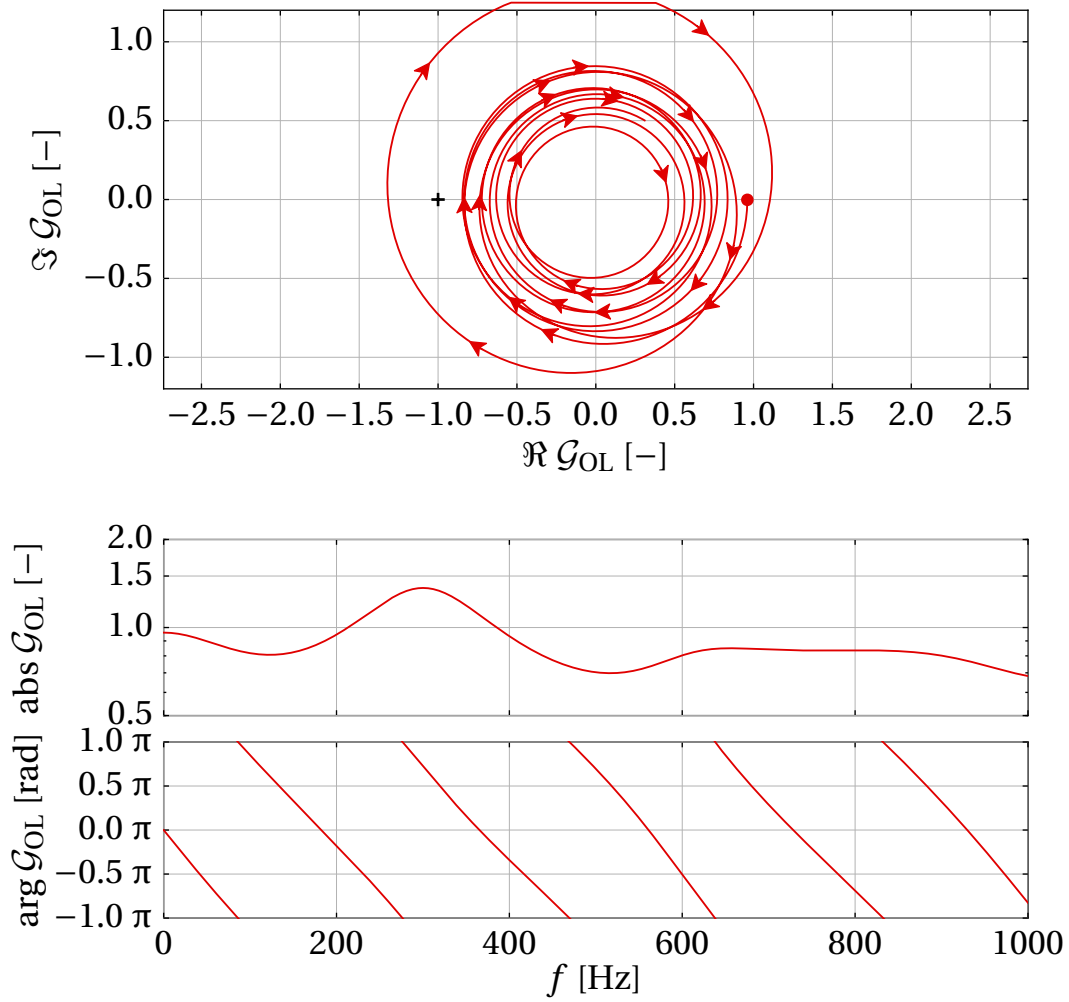
Figure 3.10: Open-loop transfer function (OLTF) of the system in fig. 3.9, as seen by the 'NyqDummy'. The Nyquist plot, (above, negative frequencies dashed) shows that the system is unstable. The Bode plot (below) indicates this unstable mode exists near 280 Hz.
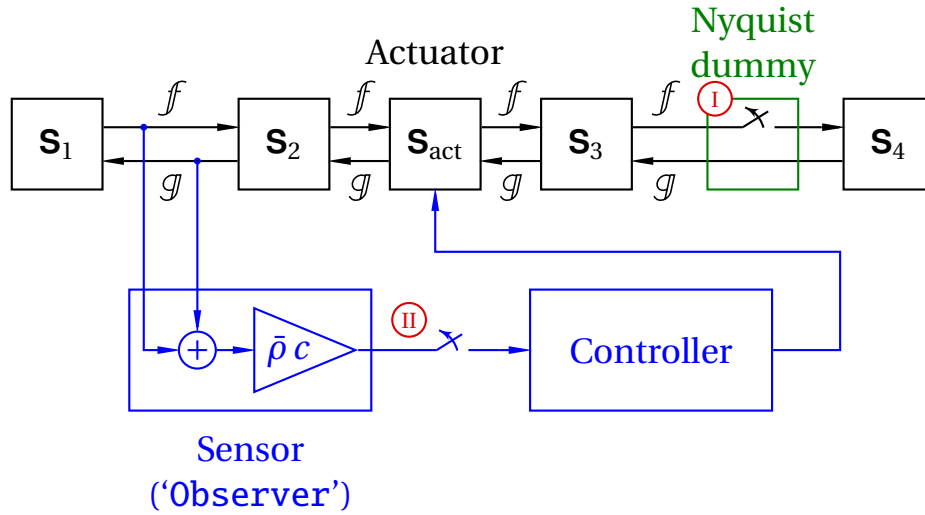
Figure 3.11: Two OLTFs are discussed in this section. They are found either by opening the acoustic system at the Nyquist dummy (I) or by opening the control loop between sensor and controller (II).

when the controller action is increased so far that it encircles the critical point. With a proportional action of $3.3 \cdot 10^{-4}$ m/s/Pa this criterion is realised, as shown in fig. 3.13.

It can be validated that the acoustical system becomes stable as well, by analysing the open loop transfer function as seen by the Nyquist dummy block. If this step were skipped, it might be the case that the controller merely made a mode uncontrollable or unobservable instead of making it stable. Figure 3.14 however shows the system is stable as intended.

The current controller reduces the inflow of volume when pressure is highest. This behaviour can be seen as a virtual boundary condition with reduced reflection compared to a simple closed end. When the amplification factor is raised further, the damping will first increase further, after which the end will behave acoustically open. Figure 3.15 shows the OLTF for $3.3 \cdot 10^{-2}$ m/s/Pa, where the active control mimics an open end and the system is just still stable. Increasing the amplification further would cause an unstable mode, corresponding to one complete wave over the length of the resonator.
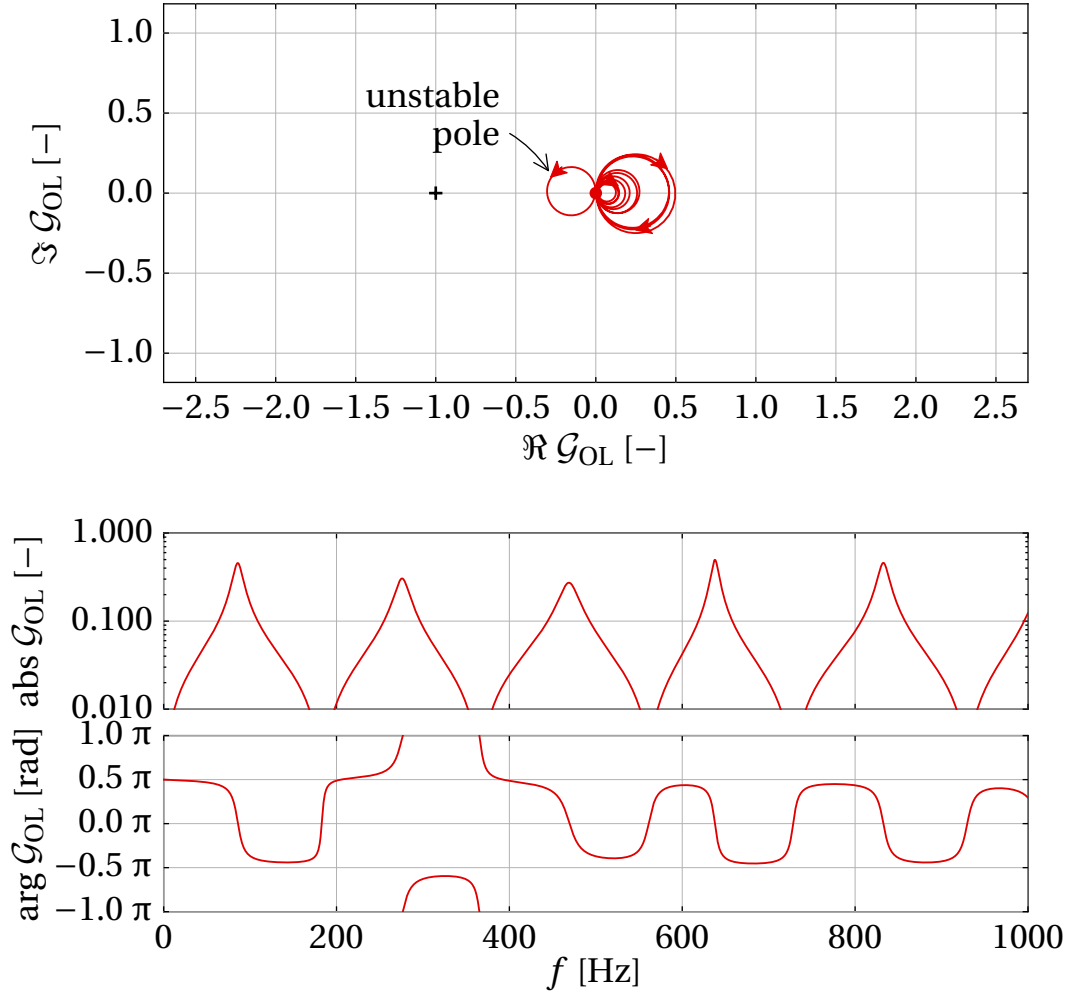
Figure 3.12: Unstable OLTF between 'Observer' and controller correspond-ing to $1 \cdot 10^{-4}$ m/s/Pa amplification, represented as Nyquist plot (above) and Bode plot (below).
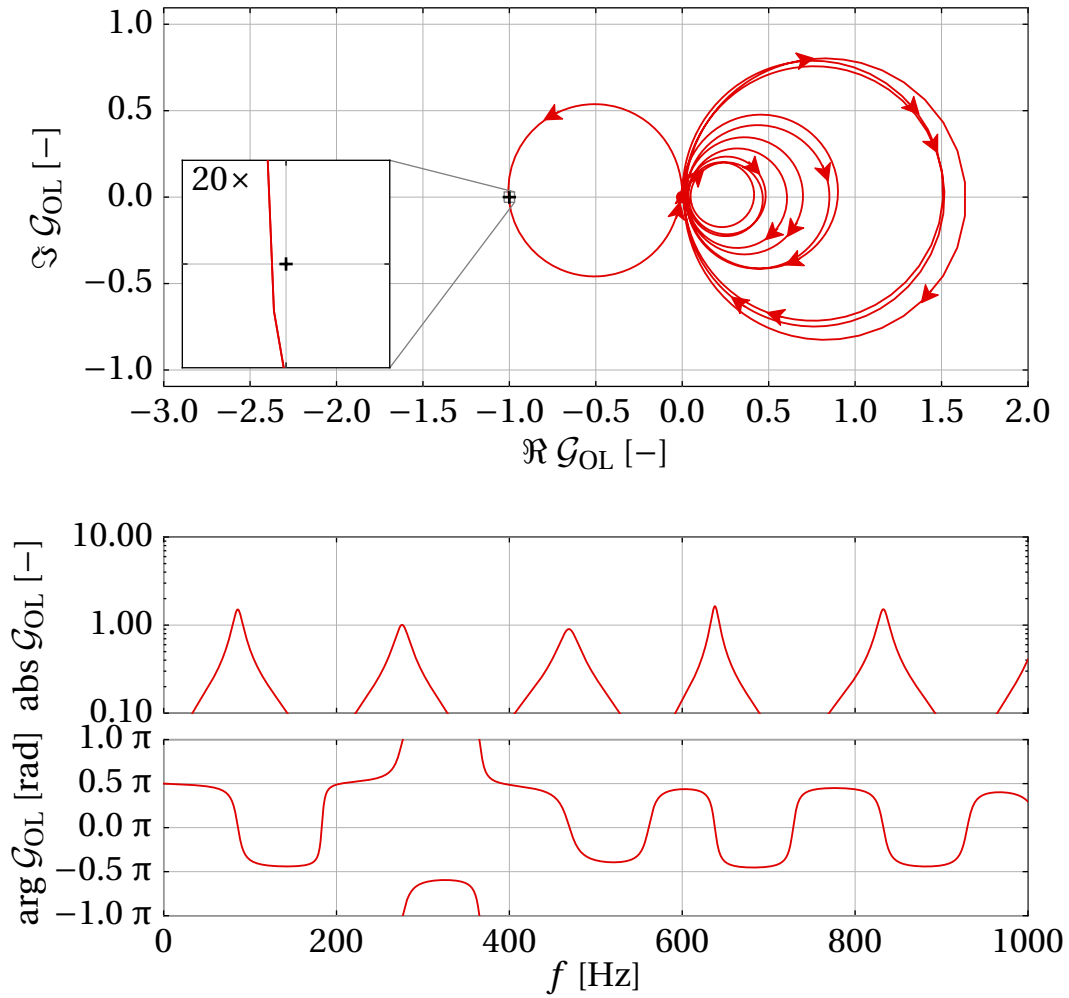
Figure 3.13: Stable OLTF between sensor and controller, corresponding to $3.3 \cdot 10^{-4}$ m/s/Pa amplification, represented as Nyquist plot (above) and Bode plot (below).
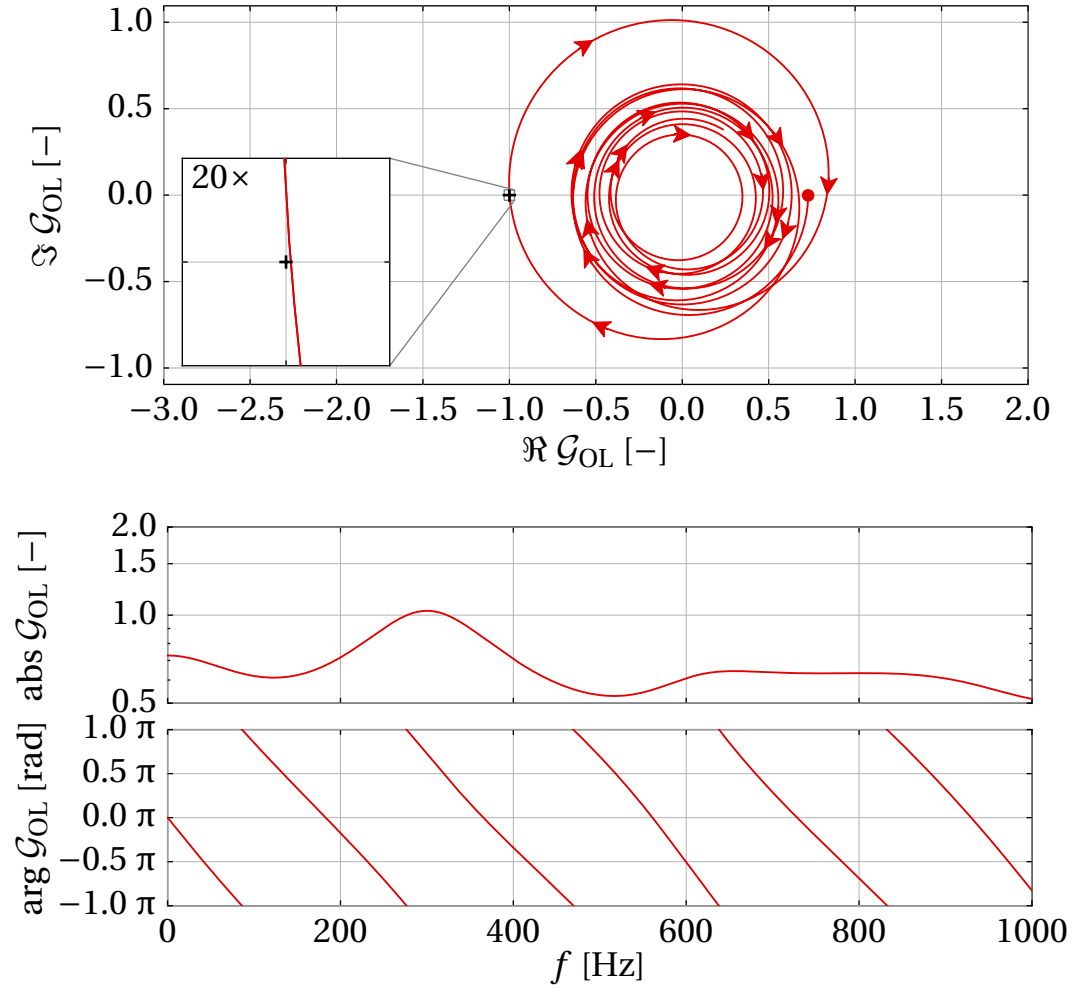
Figure 3.14: Stable OLTF seen by the Nyquist dummy corresponding to $3.3 \cdot 10^{-4}$ m/s/Pa amplification, represented as Nyquist plot (above) and Bode plot (below).
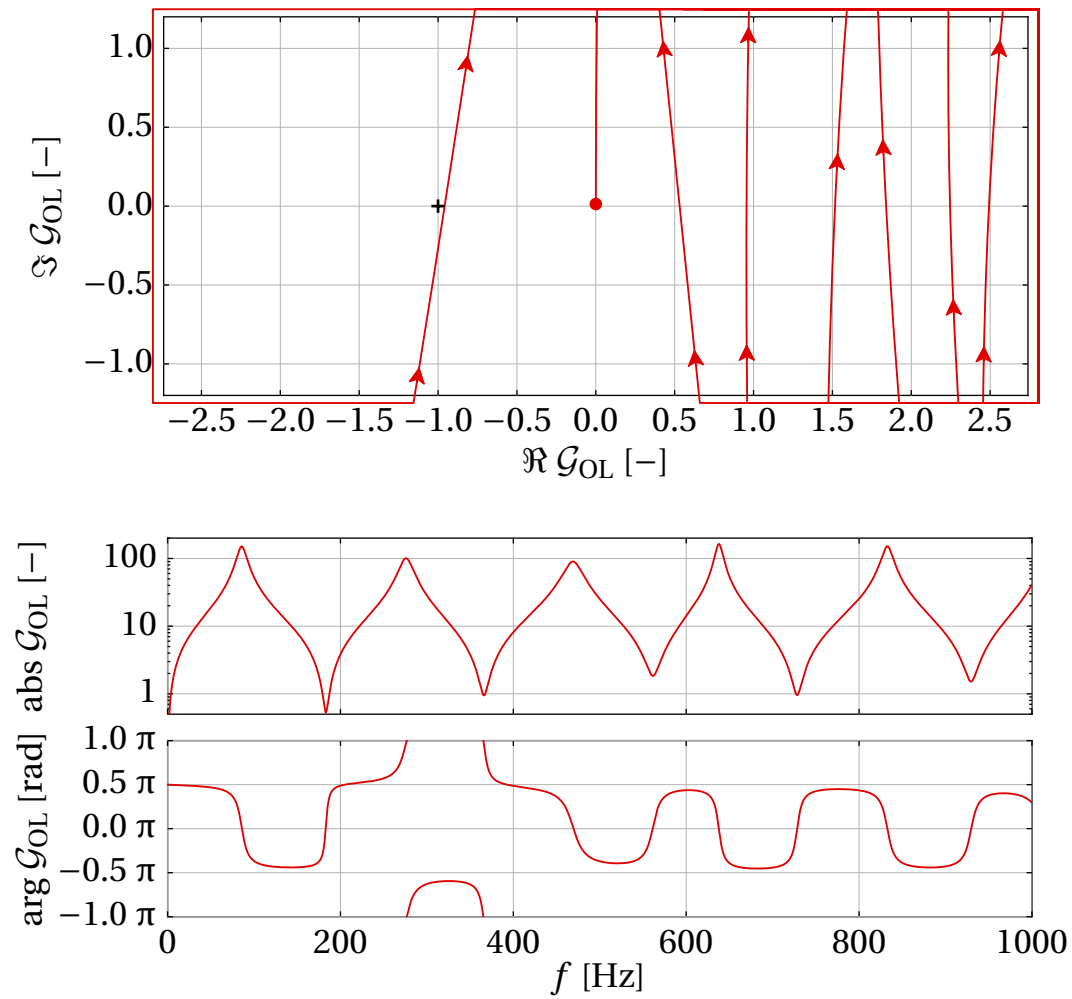
Figure 3.15: Stable OLTF between sensor and controller for $3.3 \cdot 10^{-2}$ m/s/Pa amplification, represented as Nyquist plot (above) and Bode plot (below).

4 Combustor characterisation

In this thesis, the word 'combustor' will refer to the complete test rig. 'Burner' will only refer to the flame holder and its direct vicinity. The 'plenum' is the duct between air inlet and the fuel injector, and the duct leading downstream from the burner will be called 'combustion chamber', as shown in fig. 4.1. For the combustors discussed in this thesis, the fuel injector is inside the flame holder.
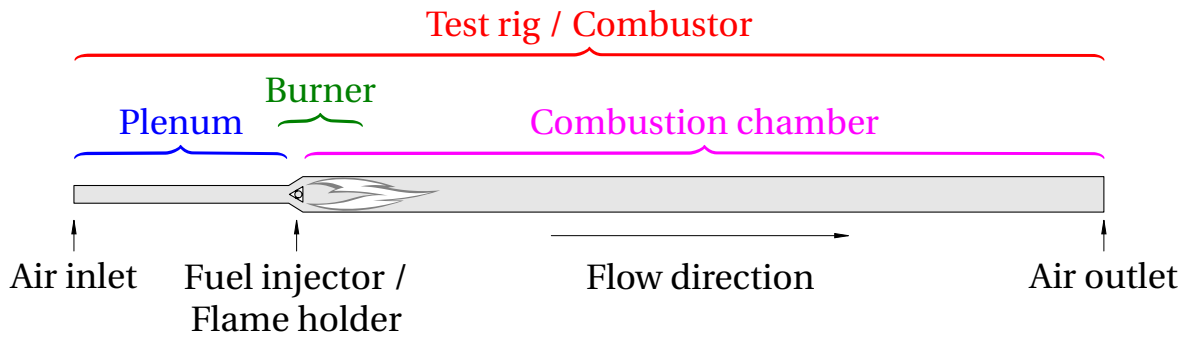
Figure 4.1: Nomenclature of combustor sections.

The measurements discussed in sec. 4.4.2 were presented as 'Stability limits and non-linear characteristics of a self-excited combustion instability' at the 19th International Congress on Sound and Vibration (ICSV19) in Vilnius, Lithuania.[186]

4.1 Description of the burners

Two combustors were used for this research. Figure 4.2 shows a photo of each test rig, as installed in the thermoacoustic laboratory at IfTA. In both combustors, the burner is situated in a duct of rectangular cross-section with closed / open acoustic boundary conditions, approximating a quarter-wave acoustic resonator. The rectangular cross section with relatively large aspect ratio leads to an approximately 2-D flow field in the x, y-plane.
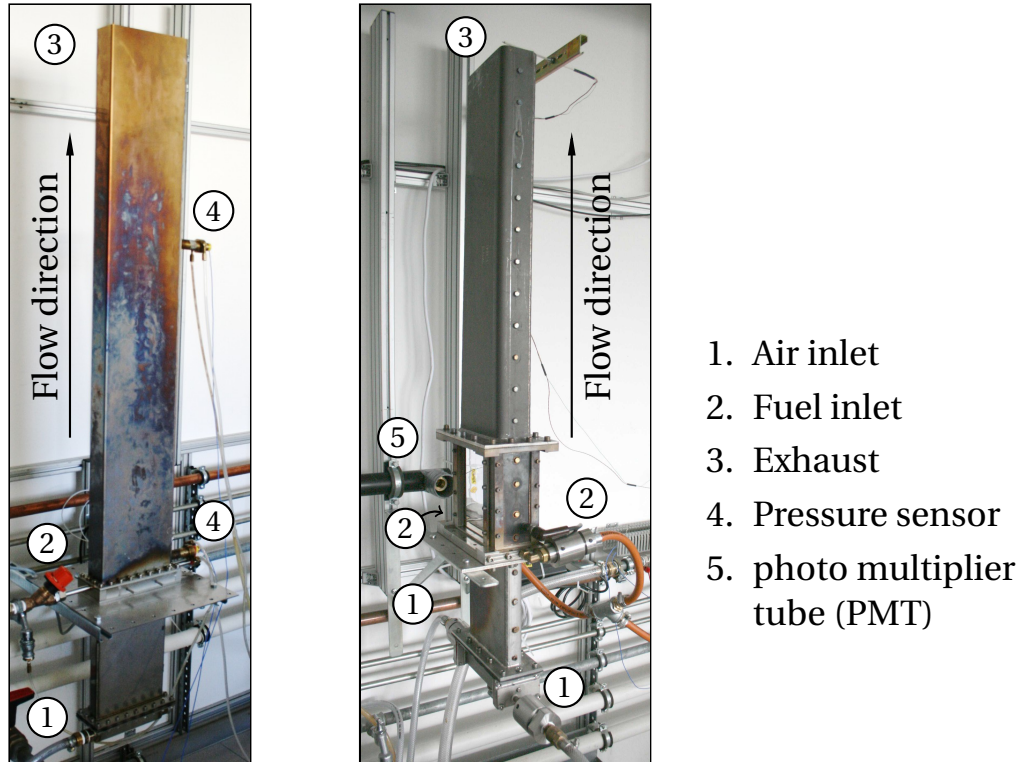
Figure 4.2: The combustors as installed in the laboratory at IfTA; the Hummer rig on the left and the Limousine rig on the right.

4.1.1 The Hummer test rig

Figure 4.3 gives the inner dimensions of the Hummer test rig. Air enters the bottom of the combustor through 66 holes in a perforated plate, forming a hard acoustical boundary condition. The flame holder rests at about a quarter of the height of the combustor. The flame holder is prismatic and triangular in cross section. A through-hole through the flame holder distributes the fuel (methane; CH_4) over the span (z-direction) of the burner. The fuel is injected into the airflow through 66 holes. A partially premixed flame forms, anchored on the top of the flame holder.

The combustion chamber is almost twice as wide (y-direction) as the plenum, so that the flow velocity is approximately the same in the plenum and the combustion chamber. (The burned gas is about half as dense as the unburned gas.) There are holes on both sides ($\pm z$-direction) of the liner for sensor access. When not in use, these are closed by brass screws. The holes are placed at 50 mm intervals or less, with the exception of the direct vicinity of the flame holder, where they could not be realised for constructional reasons.
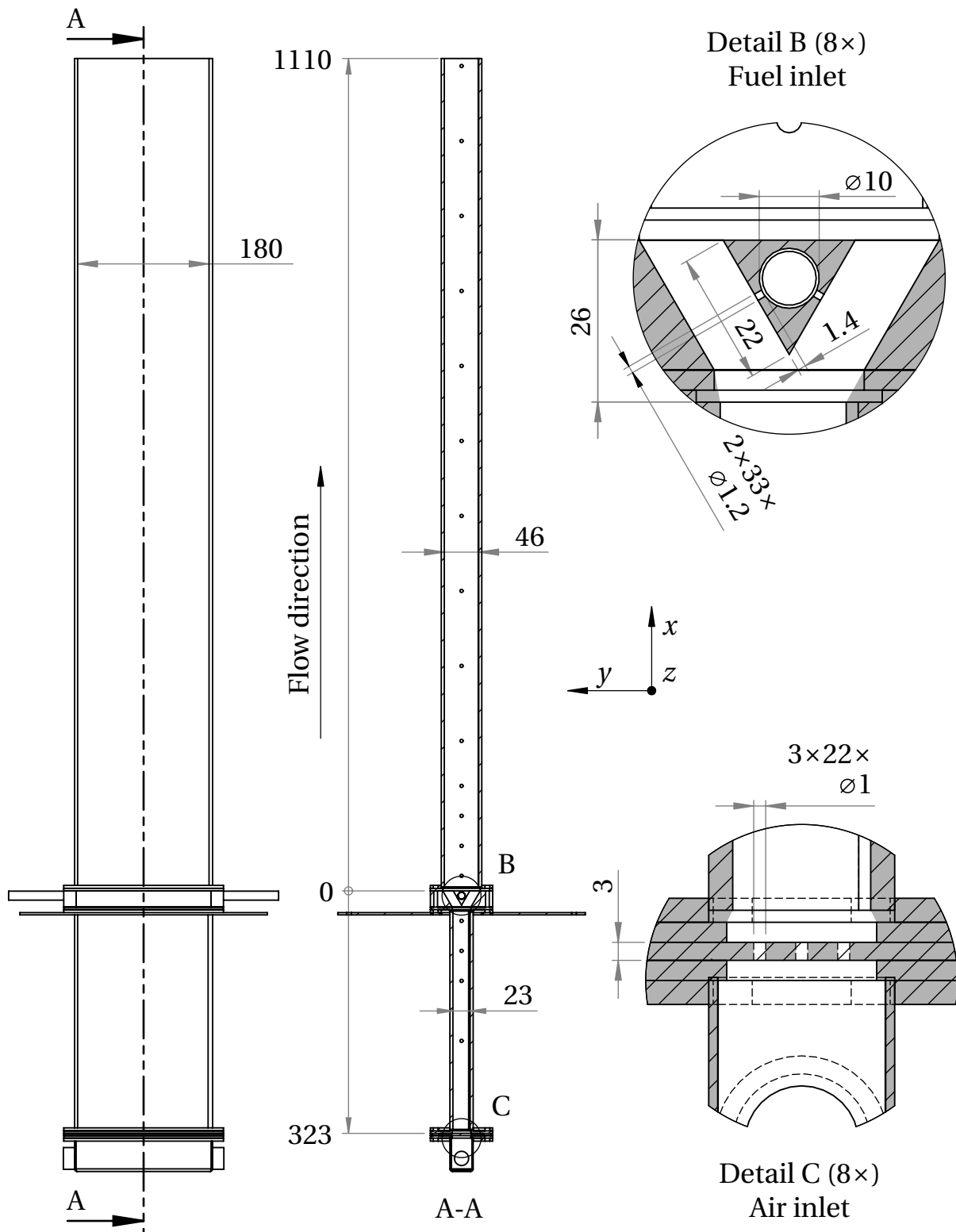
Figure 4.3: (Inner) dimensions of the Hummer test rig (in mm), with details showing fuel and air inlets.

The liner walls are all 4 mm thick. Originally, the Hummer rig had 1.5 mm liners,[136] but after these thin liners cracked repeatedly at the welds under thermal and vibration load, they were replaced with thicker ones. Since cracks introduce significant acoustic damping, crack formation compromises the reproducibility of the experiments. This problem remains in a lesser extent due to slow thermal decay of the sealings.

4.1.2 The Limousine test rig

The dimensions and cross sections of the Limousine combustor are shown in fig. 4.4. Air enters the bottom of the combustor at the front and at the back through choked orifices, which guarantees an acoustically hard boundary condition, after which perforated tubes distribute the air along the span (z-direction) of the combustor, unlike the Hummer, where the perforated plate served this purpose. The flame holder is situated at about one quarter of the height of the combustor again. Compared to the Hummer rig, the number of injection holes is reduced to 62. The holes are drilled a little bit further upstream, in an effort to increase the mixing time before the fuel is convected into the flame.

In contrast to the flame holder section in the Hummer combustor, the flow cross section contracts toward the top of the flame holder. The air enters the combustion chamber through two narrow slits. The partially premixed flame stabilises at the top of the flame holder, and on the two downstream facing steps on the outer side of the combustor. Quartz glass windows provide optical access to the flame. There are holes along the length of the front combustor wall for sensor access, which are closed by brass screws when no sensor is mounted. The holes are placed at 50 mm intervals where space allows. In the vicinity of the flame holder the holes deviate from this pattern for constructional reasons. The window in the front wall can be replaced by a steel plate to allow mounting of acoustic sensors here as well. A *photo multiplier tube* (PMT) views the flame along z-direction from the back, as in fig. 4.2. The liner thickness is 4 mm.
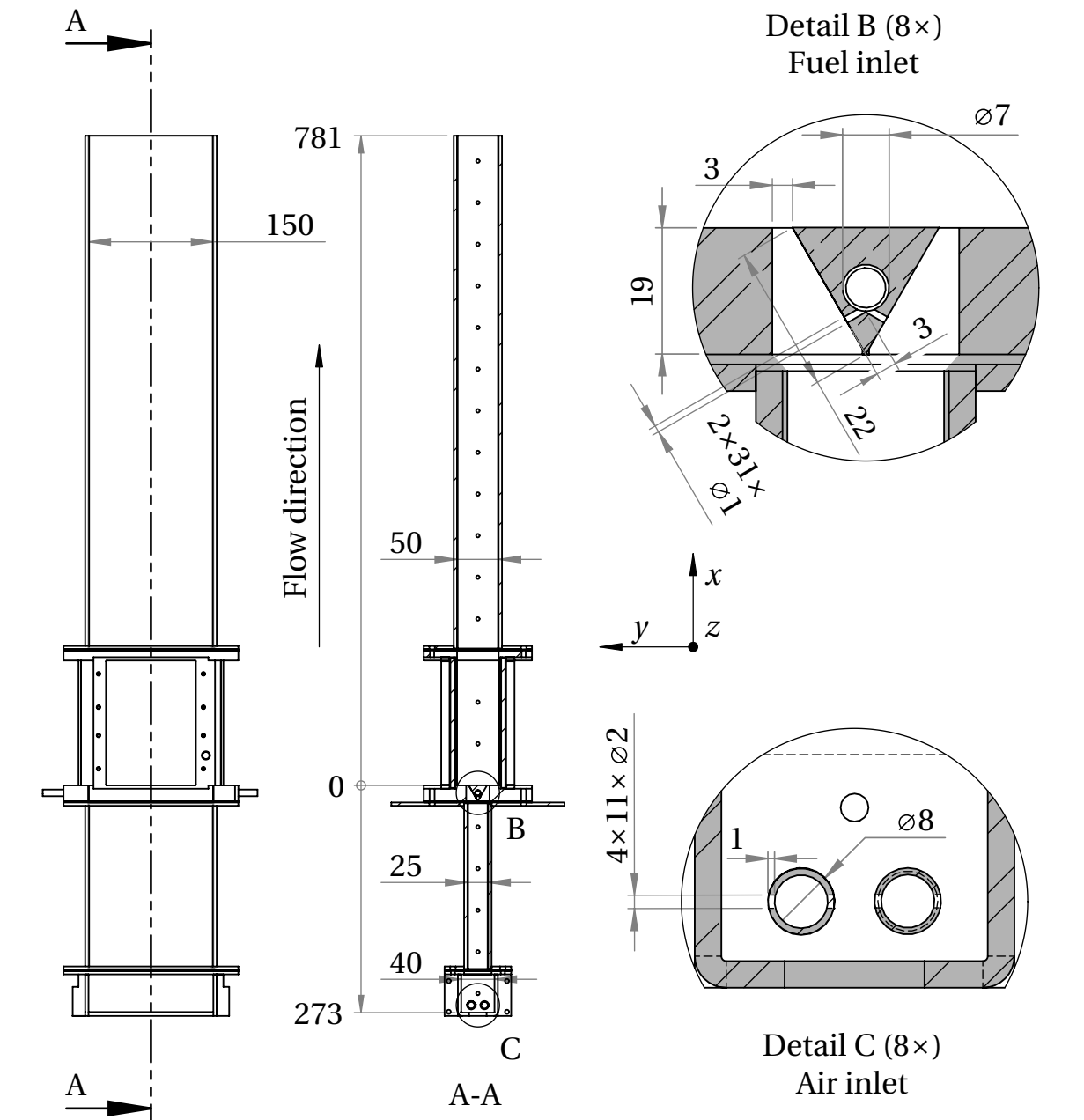
Figure 4.4: (Inner) dimensions of the Limousine test rig (in mm), with details showing fuel and air inlets

4.2 Equipment

Experiments were done at the acoustics and combustion laboratory of IfTA GmbH in Gröbenzell near München. The laboratory and equipment used for this research will be introduced in this section.

4.2.1 Fuel and air supply system

Figure 4.5 gives an overview of the fuel and air supply system at the thermo-acoustic laboratory, as far as used in this research. The signals from the individual sensors to the measurement computer are left out for clarity.

4.2.1.1 Lay-out

The methane cylinder(s), shown on the far left, are stored outside the laboratory. There are two methane supply lines entering the laboratory; a low pressure supply line, labelled (1) in the figure, and a high pressure supply line, labelled (2). The high pressure supply line was installed to facilitate this research.

The gauge pressure of the gas entering the low pressure supply line is reduced below 100 mbar before it enters the laboratory. The (volume) flow rate is measured by a positive displacement gas meter. The pulse signal delivered by the meter is converted to an analogue voltage signal, which is registered by the measurement computer. The fuel flow is set by a manually operated valve.

The high pressure gas supply line enters the laboratory at a pressure of 10 bar. The throughflow is set and monitored by a Mass-Stream D-6300 by Bronkhorst High-Tech B.V.[192] This automatic valve measures the throughflow with a *constant temperature anemometry* (CTA) sensor. The desired flow rate can be set (amongst others) by the measurement computer over an RS-232 interface.

Compressors outside of the laboratory compress ambient air to around 10 bar gauge pressure. This air is dried and stored, until it enters the laboratory at a gauge pressure of 2 bar. The temperature and absolute pressure are measured, and registered by the computer. The flow rate, which is set by a manual valve, is determined from the pressure drop over one of the available measurement orifices.
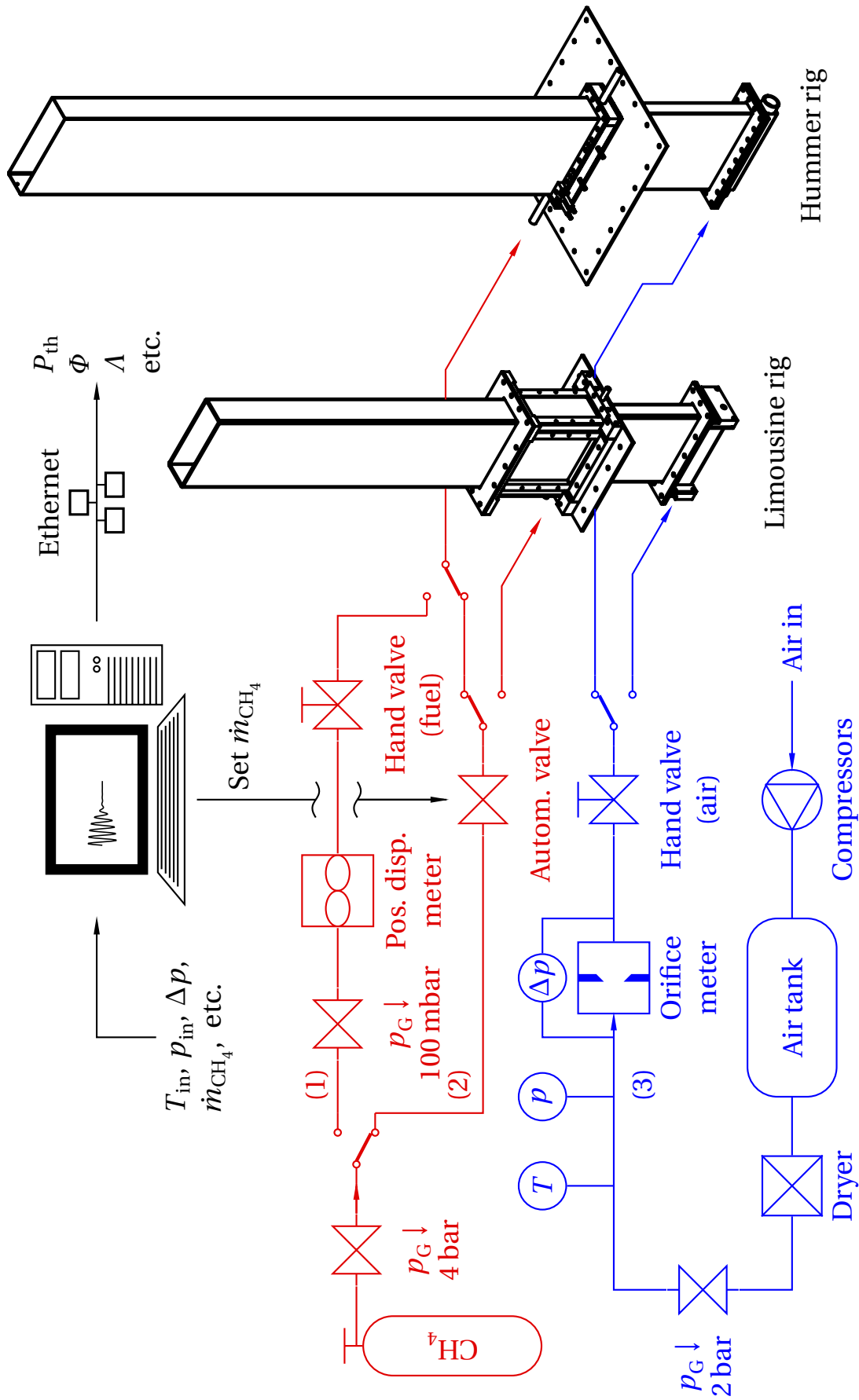
Figure 4.5: Overview of relevant air and fuel supply systems of the thermoacoustic laboratory at IfTA.

4.2.1.2 Gas flow analysis

The air flow rate is measured using a orifice meter. The air volume flow depends on the pressure drop as:

$$\dot{V}_{\text{ref}} \equiv \mathcal{C}_{\text{d}}\, A_{\text{ref}} \sqrt{\frac{2}{\rho_{\text{ref}}} \left(p_{\text{st,in}} - p_{\text{st,out}} \right)} \,,$$

where the equation for the discharge coefficient $\mathcal{C}_{\text{d}}$ is given by Reader-Harris et al.[224] This (lengthy) equation is solved by an iterative approach.

Since the velocity of the air before and after the orifice is relatively low, the drop in stagnation pressure is taken to be equal to the pressure drop Δp measured by the differential pressure meter. The mass flow is computed by the ideal gas law, using the measured values of inlet pressure and temperature.

The signal measured and computed in this way is rather noisy, especially at lower flow rates. A non-linear filter is implemented to improve the usability. The filtered mass flow, $\dot{m}_{\text{ft},i}$ depends on the newly measured 'raw' value $\dot{m}_{\text{rw},i}$, the filtered value for the last time step $\dot{m}_{\text{ft},i-1}$ and a filtering coefficient $X_{\text{ft},i}$ as

$$\dot{m}_{\text{ft},i} = \left(1 - X_{\text{ft},i} \right) \dot{m}_{\text{ft},i-1} + X_{\text{ft},i}\, \dot{m}_{\text{rw},i} \,.$$

The general form is similar to a conventional *exponential moving average* (EMA) filter. The coefficient $X_{\text{ft},i}$ is however not constant, but depends on the difference between the measured and filtered mass flow as

$$X_{\text{ft},i} = \min \left(\text{abs} \left(\ln \left(\frac{\dot{m}_{\text{ft},i}}{\dot{m}_{\text{rw},i}} \right) \right), 1 \right) \,.$$

This way, the filtered signal quickly follows the real signal when the discrepancy is large, i.e. when the operating point is changed on purpose, but it realises better noise suppression at a constant operating point. To tune the filter, the quotient could be raised to an arbitrary power, but the presented form performed very satisfactory for the current application.

The fuel gas, the gas supply line and the flow meter currently in use have to be set manually in the measurement programme. The automatic fuel valve is operated using the software provided by Bronkhorst High-Tech B.V.

With this information provided, the programme determines the operating conditions such as thermal power (P_{th}) and equivalence ratio (Φ). Together with the raw data, and some unit conversions for convenience, these are shared over ethernet with the Argus system.

4.2.2 The Argus system

The experiments described in this thesis were conducted with the help of various products from the Argus product family developed at IfTA.[124]

The signal processing rack: The hardware for signal processing is gathered in a $19''$ rack. Various cards can be added to suit the needs of the user. The following cards were used for this research:

> **Argus DSP:** The *digital signal processor* (DSP) is the core of the Argus platform. It organises measurement data per $19''$ rack and, depending on the loaded programme, applies various kinds of hardware accelerated analyses. The rack can hold various input and/or output cards. The following DSP programmes were used for this research:
>
>> **Argus OMDS:** The *Oscillation Monitoring and Diagnostic System* (OMDS) performs, amongst others, spectral analysis with up to 12 800 spectral lines. Windowing functions and their overlapping can be selected to reduce the effect of spectral leakage. Multi-channel spectral and correlation analysis can be performed.
>>
>> **Argus AIC** runs the controller for AIC. The programme supports multiple input and output signals (MIMO), but this research only used one sensor and one actuator at a time (SISO).
>
> **Argus AD-4** is a four-channel *digital–analogue* (AD) converter card with a maximum sampling frequency of 51.2 kHz. This input card is predominately used for this research. It can deal with voltage or current signals and *integrated electronics piezoelectric* (IEPE) or *integrated-circuit piezoelectric* (ICP) sensors. The analogue input signal is low-pass filtered to avoid aliasing effects in the digital spectral analysis.
>
> **Argus DA-8** is an eight-channel *digital–analogue* (DA) converter card. This output card is used to control the actuator in the case of active control.

Argus Host collects data from the various measurement systems. For systems with long running times, such as in industry, Argus Host can flexibly aggregate and store data. It is also used to communicate with the DSP to configure sensors and to set analysis preferences per channel.

Argus Trend is used to visualise, import and export real-time (on-line) as well
as saved data. It has highly dynamic plotting capabilities, and offers a
possibility to implement additional computations in the Java-extendible
calculator module. Several such calculations were written in the context
of this research.

Figure 4.6 gives an overview of the set-up as used for this research. Two Argus
systems are used: one running OMDS and one running the AIC programme.
The system running OMDS was used in all experiments to acquire measure-
ment data from the sensors. The data were analysed on-line on a PC running
Argus Host and Argus Trend. On this PC, Argus Host also collected the data
generated by the system running AIC, and the data generated by the gas flow
analysis PC. A dedicated micro PC was used to communicate with the system
running AIC. The PC running Argus Trend was used to control the micro PC
by a remote desktop connection.
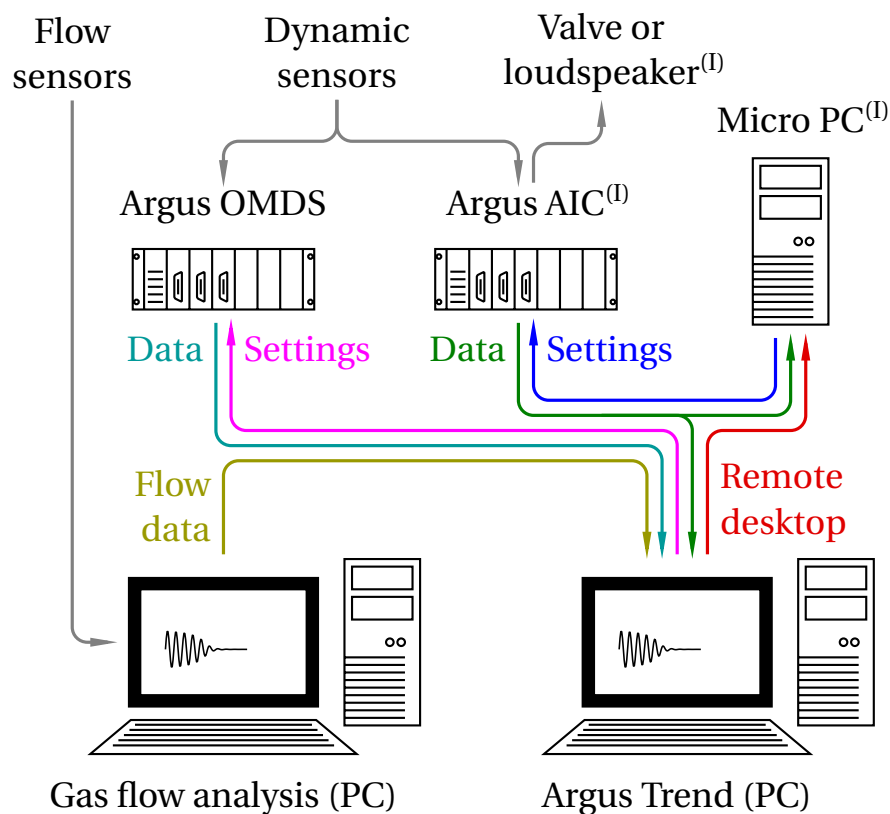
(I) The actuator, 19″ AIC rack and the micro PC are only used for experiments with active control.

Figure 4.6: Overview of the flow of experimental data.

4.2.3 Sensors

The sensors in this research can be divided in two groups. Dynamic sensors are those which can measure fluctuating quantities with frequencies into the kilohertz range. These signals can be used for spectral analysis. Other sensors measure only slowly varying signals. The sensors used for the monitoring of the gas flows (see sec. 4.2.1) fall in the latter category, but will not be repeated here.

4.2.3.1 Dynamic sensors

Voltage (within $\pm 20\,\mathrm{V}$) and current (within $\pm 20\,\mathrm{mA}$) can be measured directly by the Argus AD-4s. Higher values have to be reduced, for instance by a voltage divider. This was for instance used to quantify the actuation by loudspeaker.

The valves used as actuator for active control have build-in *linear variable differential transformers* (LVDTs) to monitor the spool position.

During some experiments, a *photo multiplier tube* (PMT) was used to measure OH* chemiluminescence. With some reservations,[144] this signal can be assumed to be proportional to the heat release at the flame.[56: 9-31] The phase relationship between the OH* chemiluminescence signal and the pressure fluctuation measured at the flame, can thus be interpreted as a qualitative measure for the Rayleigh index.

Where possible, dynamic pressure signals were measured using $1/4''$ condenser microphones, type MK301 by Microtech Gefell GmbH.[176] These sensors have a high sensitivity, but are not mechanically robust enough for measurements on a combustor. High temperatures, or condensed water from exhaust gases, could damage these microphones.

Piezo transducers were used for thermally or mechanically more demanding pressure measurements. For application on the hot liner wall downstream of the flame, these sensors were placed in water-cooled adapters, as used by Hermann.[109]

4.2.3.2 Static sensors

Neither microphones nor piezo transducers can be used to measure a constant pressure or pressure differences. For this purpose anemometers GDH-07-AN, GDH-13-AN and GDH-14-AN by GHM Messtechnik GmbH[90] were used.

Temperatures were measured with NiCr–Ni (type K) thermocouples. Unlike other sensors, these were not connected to an Argus AD-4 measurement card. Instead, the digital thermometer HH506RA by OMEGA Engineering inc.[202] was used. The log file created by the complementary software can be imported by Argus Trend.

Direct voltage and current measurements by the Argus AD-4, as well as the valve spool position measured by the LVDTs can be used for static measurements as well.

4.3 Two-microphone wave decomposition

The pressure measured by a microphone is composed of sound waves travelling in different directions, and other sources of pressure fluctuations, such as vorticity and turbulence.

In the case of one-dimensional sound propagation in a straight duct with uniform throughflow, the two characteristic wave amplitudes f and g can be determined by a two-microphone measurement. Figure 4.7 gives an overview of the set-up.

Two microphones measure pressure oscillations, which, in the noiseless case are composed of the contributions by the upstream and downstream travelling waves as $p'(x, t) = \rho c \left(f(x - (c + \bar{u}) t) + g(x + (c - \bar{u}) t) \right)$. Taking into account the travelling time of the waves, the pressure at the microphones can be related to the wave amplitudes at a reference position x_{ref}. This reference position is often, but not necessarily, the position of a physical feature under investigation. For compactness of the formulation, the wave numbers are defined as

$$k_f = \frac{\omega/c}{M+1} \qquad \text{and} \qquad k_g = \frac{\omega/c}{M-1} = \frac{M+1}{M-1} k_f.$$
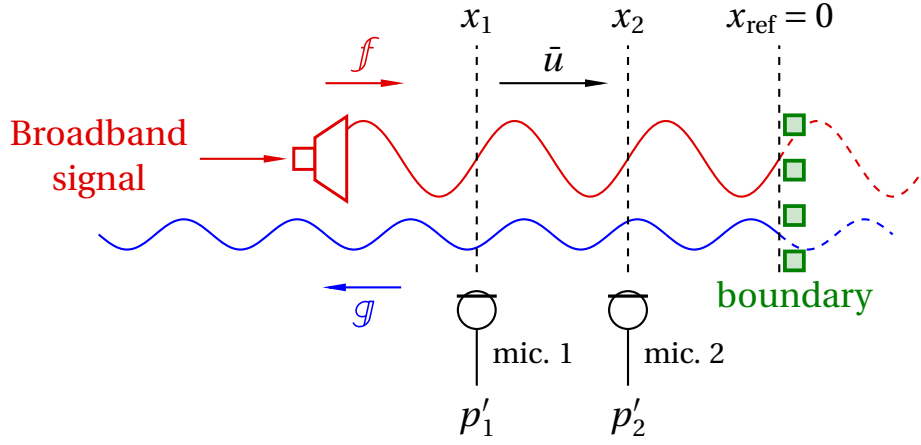
Figure 4.7: Measurement set-up for two-microphone wave decomposition.

In the frequency domain, the delays can be expressed as

$$
\mathcal{f}\left(x - (c + \bar{u})\, t\right) = \tfrac{1}{2}\left(\frac{p'}{\rho\, c} + u'\right)
$$

$$
= \mathcal{f}_0 \exp\left(-\mathrm{i}\,\frac{\omega/c}{M+1}\, x\right) \exp(\mathrm{i}\omega\, t)
$$

$$
= \mathcal{f}_0 \exp\left(-\mathrm{i}\, k_{\mathcal{f}}\, x\right) \exp(\mathrm{i}\omega\, t)\,,
$$

and

$$
\mathcal{g}\left(x + (c - \bar{u})\, t\right) = \tfrac{1}{2}\left(\frac{p'}{\rho\, c} - u'\right)
$$

$$
= \mathcal{g}_0 \exp\left(-\mathrm{i}\,\frac{\omega/c}{M-1}\, x\right) \exp(\mathrm{i}\omega\, t)
$$

$$
= \mathcal{g}_0 \exp\left(-\mathrm{i}\, k_{\mathcal{g}}\, x\right) \exp(\mathrm{i}\omega\, t)\,.
$$

The pressures at the microphones, expressed in matrix form, are

$$
\begin{bmatrix} p'_1 \\ p'_2 \end{bmatrix} = \rho\, c \begin{bmatrix} \exp\left(-\mathrm{i}\, k_{\mathcal{f}}\, x_1\right) & \exp\left(-\mathrm{i}\, k_{\mathcal{g}}\, x_1\right) \\ \exp\left(-\mathrm{i}\, k_{\mathcal{f}}\, x_2\right) & \exp\left(-\mathrm{i}\, k_{\mathcal{g}}\, x_2\right) \end{bmatrix} \begin{bmatrix} \mathcal{f} \\ \mathcal{g} \end{bmatrix}_{x=0}.
$$

The ratio between the two wave amplitudes is found by taking the inverse of the 2×2 matrix. When the reference plane is a boundary, this ratio would be its reflection coefficient.

$$X^{-1} = \frac{1}{\det X} \begin{bmatrix} X_{2,2} & -X_{1,2} \\ -X_{2,1} & X_{1,1} \end{bmatrix}$$

$$\rho c \begin{bmatrix} f \\ g \end{bmatrix}_{x=0} = \frac{1}{\det \dots} \begin{bmatrix} \exp\left(-\mathrm{i}\, k_g\, x_2\right) & -\exp\left(-\mathrm{i}\, k_g\, x_1\right) \\ -\exp\left(-\mathrm{i}\, k_f\, x_2\right) & \exp\left(-\mathrm{i}\, k_f\, x_1\right) \end{bmatrix} \begin{bmatrix} p_1' \\ p_2' \end{bmatrix}$$

$$\left(\frac{f}{g}\right)_{x=0} = \frac{\exp\left(-\mathrm{i}\, k_g\, x_2\right) - \left(p_2'/p_1'\right)\exp\left(-\mathrm{i}\, k_g\, x_1\right)}{-\exp\left(-\mathrm{i}\, k_f\, x_2\right) + \left(p_2'/p_1'\right)\exp\left(-\mathrm{i}\, k_f\, x_1\right)}.$$

Expressions for the individual wave amplitudes are found after working out the determinant of the matrix:

$$\det X = \left(X_{1,1}\, X_{2,2} - X_{1,2}\, X_{2,1}\right)$$

$$\det \dots = \exp\left(-\mathrm{i}\, k_f\, x_1\right)\exp\left(-\mathrm{i}\, k_g\, x_2\right) - \exp\left(-\mathrm{i}\, k_g\, x_1\right)\exp\left(-\mathrm{i}\, k_f\, x_2\right),$$

so that

$$\rho c f = p_1' \frac{\exp\left(-\mathrm{i}\, k_g\, x_2\right) - \left(p_2'/p_1'\right)\exp\left(-\mathrm{i}\, k_g\, x_1\right)}{\exp\left(-\mathrm{i}\, k_f\, x_1\right)\exp\left(-\mathrm{i}\, k_g\, x_2\right) - \exp\left(-\mathrm{i}\, k_g\, x_1\right)\exp\left(-\mathrm{i}\, k_f\, x_2\right)}$$

$$= p_1' \frac{\exp\left(-\mathrm{i}\, k_g\, (x_2 - x_1)\right) - \left(p_2'/p_1'\right)}{\exp\left(-\mathrm{i}\, (k_f - k_g)\, (x_1 - x_2)\right) - 1}\, \exp\left(\mathrm{i}\, k_f\, x_2\right),$$

and

$$\rho c g = p_1' \frac{-\exp\left(-\mathrm{i}\, k_f\, x_2\right) + \left(p_2'/p_1'\right)\exp\left(-\mathrm{i}\, k_f\, x_1\right)}{\exp\left(-\mathrm{i}\, k_f\, x_1\right)\exp\left(-\mathrm{i}\, k_g\, x_2\right) - \exp\left(-\mathrm{i}\, k_g\, x_1\right)\exp\left(-\mathrm{i}\, k_f\, x_2\right)}$$

$$= p_1' \frac{-1 + \left(p_2'/p_1'\right)\exp\left(-\mathrm{i}\, k_f\, (x_1 - x_2)\right)}{\exp\left(-\mathrm{i}\, (k_f - k_g)\, (x_1 - x_2)\right) - 1}\, \exp\left(\mathrm{i}\, k_g\, x_1\right).$$

Seybert and Ross[247] described this technique, and used random excitation to generate the required pressure fluctuations. In the case of a calibration, or

two-microphone measurement with excitation by a loudspeaker, there is very little noise on the input signal, so that (using the definitions from sec. 2.3)

$$\mathcal{G}^-_{U_{\text{in}},p'_1} = \frac{CSD_{U_{\text{in}},p'_1}}{ASD_{U_{\text{in}}}} \Rightarrow \frac{U_{\text{in}}{}^* p'_1}{U_{\text{in}}{}^* U_{\text{in}}} = \frac{p'_1}{U_{\text{in}}}$$

$$\mathcal{G}^+_{U_{\text{in}},p'_1} = \frac{ASD_{p'_1}}{CSD^*_{U_{\text{in}},p'_1}} \Rightarrow \frac{p'_1{}^* p'_1}{p'_1{}^* U_{\text{in}}} = \frac{p'_1 + \text{noise}}{U_{\text{in}}}$$

$$\mathcal{G}^\pm_{U_{\text{in}},p'_1} = \sqrt{\mathcal{G}^+_{U_{\text{in}},p'_1} \mathcal{G}^-_{U_{\text{in}},p'_1}}\,.$$

Now the noiseless transfer function between the noisy signals p'_1 and p'_2 can be determined as

$$\mathcal{G}^{\langle U_{\text{in}}\rangle}_{p'_1,p'_2} = \frac{\mathcal{G}^-_{U_{\text{in}},p'_2}}{\mathcal{G}^-_{U_{\text{in}},p'_1}} \Rightarrow \frac{p'_2}{p'_1}$$

$$\mathcal{G}^-_{p'_1,p'_2} < \mathcal{G}^{\langle U_{\text{in}}\rangle}_{p'_1,p'_2} < \mathcal{G}^+_{p'_1,p'_2}\,.$$

If all is well, the argument of this new transfer function should be identical to the average phase difference measured between the two output signals.

Bodén and Åbom[1, 27] investigated the errors that can be made with this two-microphone measurement. Most notably, this method breaks down when:

- Assumptions for its derivation are invalid, for instance when

    - there is too much damping in the duct

    - there is a change in cross-sectional area

- There is no damping at either end of the duct, leading to standing modes

- The pressure fluctuation at one of the microphones is close to zero

- There is no mean flow, and the distance between the microphones is $N\lambda/2$ for $N \in \mathbb{N}_0$.

These shortcomings can be solved by either traversing one microphone[127] or using multiple microphones,[126] and fitting the wave pattern to the data measured at the most reliable positions.

Bothien et al.[32: §3] developed an on-line (time-domain) version of this procedure.

4.4 Combustors without AIC

Both combustors have strong thermoacoustic instabilities, where the first and dominant mode resembles a quarter wave. This section will discuss the occurring mode shapes, and variation of the amplitude depending on operating conditions.

4.4.1 The Hummer test rig

Operating points (thermal power P_{th} and equivalence ratio Φ) where instability occurs are identified and discussed. During limit cycle operation, the pressure amplitude of the dominant oscillation, as well as its higher harmonics, are recorded. For a reference operation point ($P_{\text{th}} = 40\,\text{kW}$ and $\Phi = 0.71$, i.e. air excess ratio $\Lambda = 1.4$), the pressure signal was measured along the length of the combustor. Pressure profiles were reconstructed from these measurements. The following mode shapes are identified: the first thermoacoustic mode, which is the dominant oscillation (I, 1), its second and third harmonic (I, 2 and I, 3) and the next two independent modes (II, 1 and III, 1). These mode shapes are discussed, as well as their phase shift compared to the heat release represented by the OH^* chemiluminescence signal from the flame.

4.4.1.1 Pressure profiles

The mode shapes of the pressure oscillation are found by traversing one microphone along the length of the combustor, while another one is kept at a constant location, preferably a location where the relevant mode shapes have significant amplitude. In this case the stationary microphone was at the second hole from the upstream end of the combustor. The modes are expected to have an anti-node at the (acoustically closed) upstream end of the combustor. The turbulent noise caused by the air injection jets was however a lot less at the second hole. The mode shapes are first determined in the form of transfer functions relating the pressure along the burner to the reference sensor, as described in sec. 2.3.4. At the frequencies corresponding to thermoacoustic modes, these transfer functions are evaluated as a function of position, and scaled by a representative amplitude.
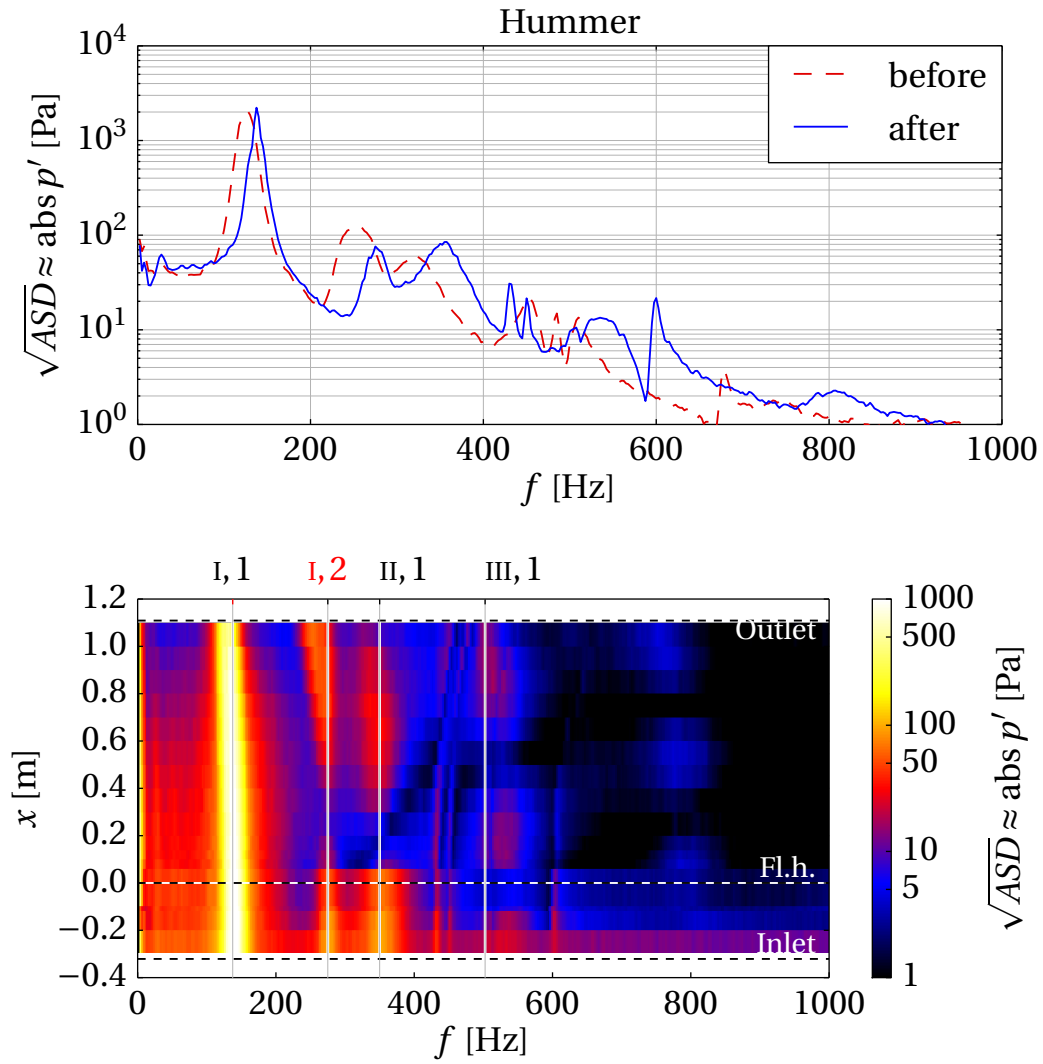
Figure 4.8: Spectrum at the reference sensor at the beginning and end of the measurement of the mode shapes in the Hummer combustor (above) and pressure amplitude as function of frequency and position (below).

Some mode shapes, and some higher harmonics of the dominant (first) mode can be identified in fig. 4.8. The first mode represents a quarter wave and dominates in terms of amplitude. Figure 4.9 shows the pressure profile.
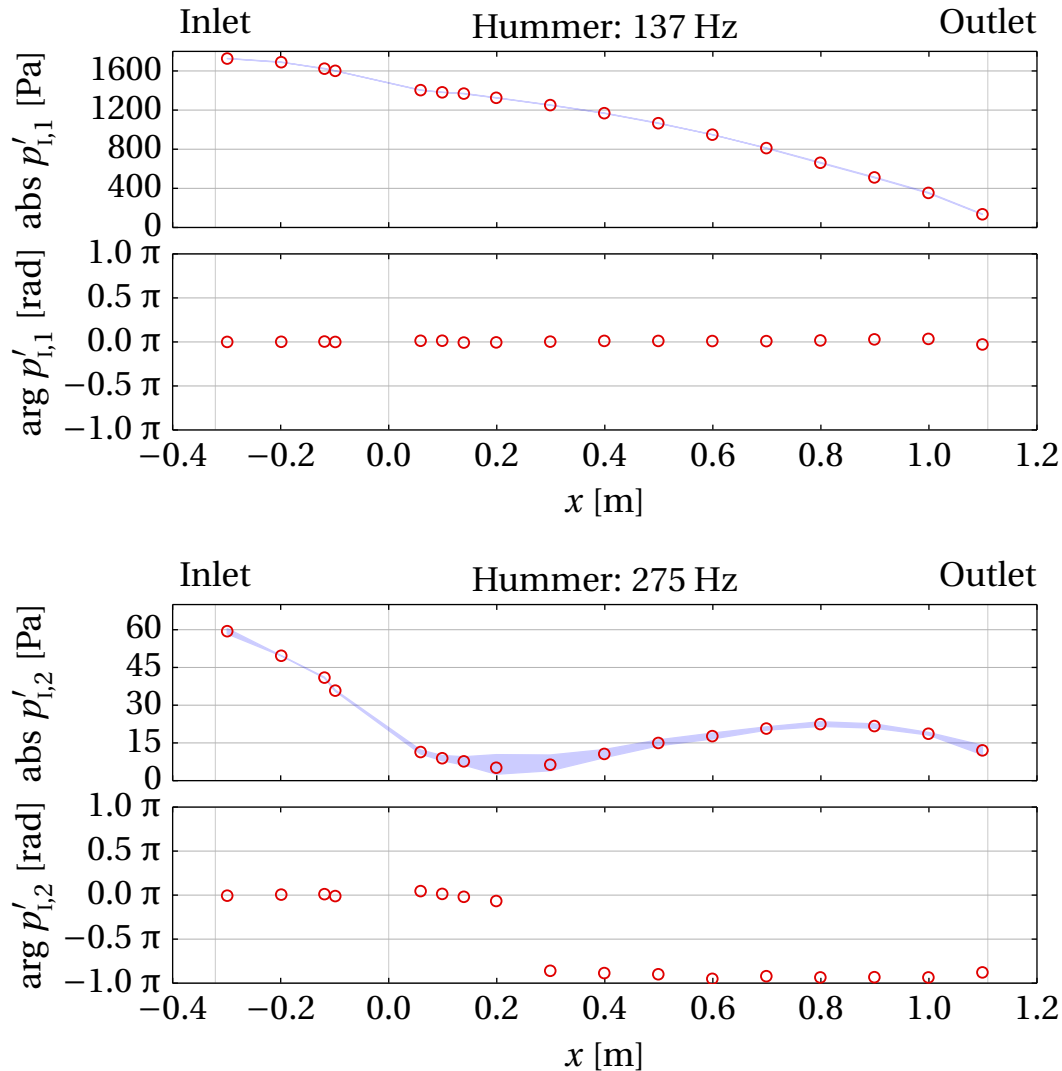
Figure 4.9: First mode of oscillation of the Hummer rig ($1/4\ \lambda$; above). The second harmonic (at twice the frequency of the first) is clearly found as well (below).

Higher modes of oscillation are much lower in amplitude, and consequently harder to measure and identify. The second and third mode can still be identified relatively well. The results are plotted in fig. 4.10.
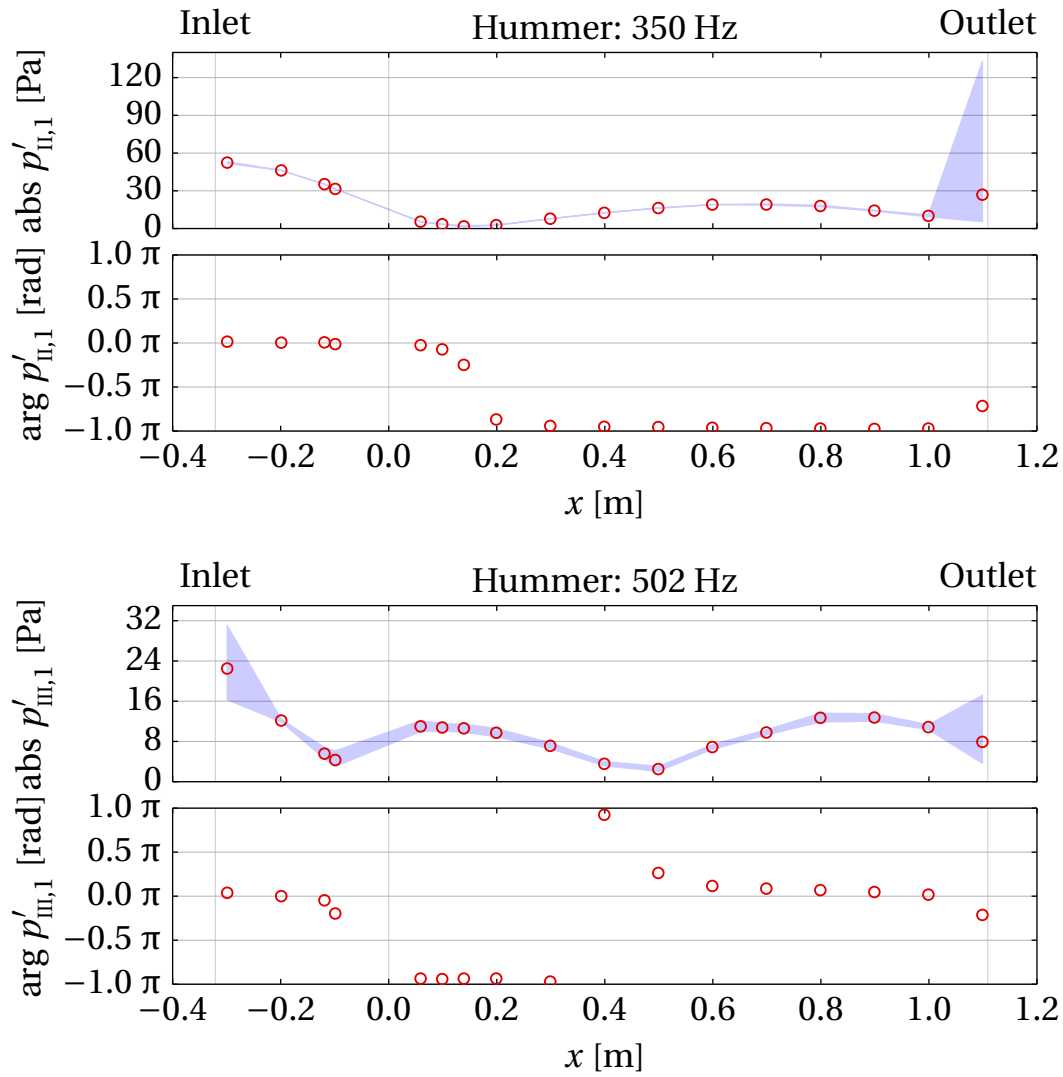
Figure 4.10: Second (3/4 λ; above) and third mode (5/4 λ; below) of oscillation of the Hummer rig.

4.4.1.2 Amplitude depending on operating conditions

Figure 4.11 shows the amplitude of the dominant oscillation, as a function of the operating conditions. To produce this graph, the burner was run at consecutive levels of increasing thermal power. For each value of thermal power, a traverse was made from high to low equivalence ratio Φ and back again. At lower thermal power, the minimum value of Φ is limited by blow-off of the flame. At higher power, the limiting factor is the air supply.
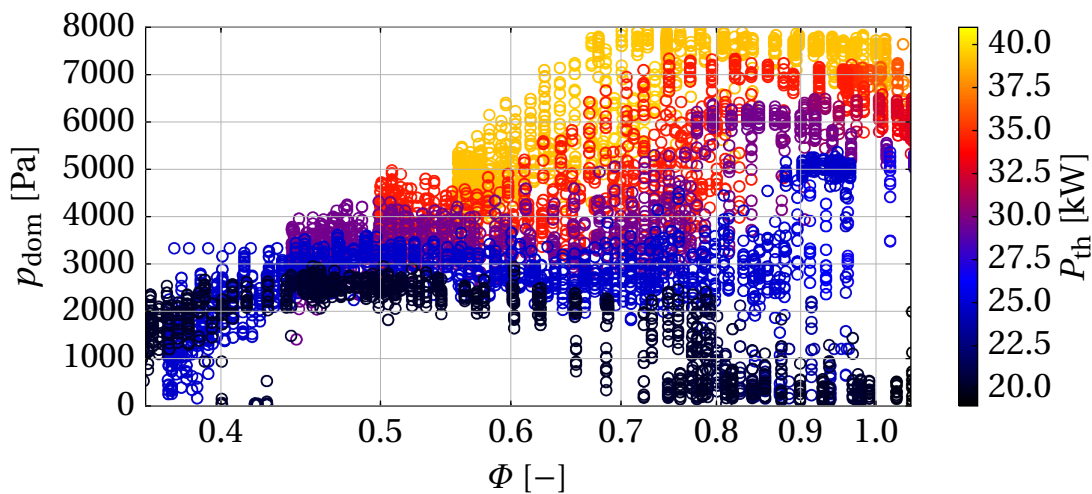
Figure 4.11: Amplitude of the dominant ('dom') oscillation in the Hummer rig for varying operating conditions.

The oscillation becomes stronger for increasing thermal power. Also, the amplitude measured at $P_{\mathrm{th}} = 40\,\mathrm{kW}$ and $\Phi = 0.71$ is a lot larger than found during the measurement of the mode shape described before. The reason for this cannot be given with certainty. It is expected that the state of the sealings between different parts of the combustor assembly plays a role, as well as long-term transient effects of liner heating.

4.4.2 The Limousine test rig

The measurements discussed in this section were presented as 'Stability limits and non-linear characteristics of a self-excited combustion instability' at the 19th International Congress on Sound and Vibration (ICSV19) in Vilnius, Lithuania.[186]

Operating points (thermal power P_{th} and equivalence ratio Φ) where instability occurs are identified and discussed. During limit cycle operation, the pressure amplitude of the dominant oscillation, as well as its higher harmonics, are recorded. For a reference operation point ($P_{th} = 40\,\text{kW}$ and $\Phi = 0.71$), the pressure signal was measured along the length of the combustor. Pressure profiles were reconstructed from these measurements. The following mode shapes are identified: the first thermoacoustic mode (I, 1), which is the dominant oscillation, its second and third harmonic (I, 2 and I, 3) and the next two independent modes (II, 1 and III, 1). These mode shapes are discussed, as well as their phase shift compared to the heat release represented by the OH* chemiluminescence signal from the flame.

4.4.2.1 Pressure profiles

The mode shapes of the pressure oscillation are determined for the Limousine combustor in the same way as described for the Hummer rig before. The Limousine combustor does however have a PMT measuring the overall OH* chemiluminescence of the flame from the back of the combustor. The phase shift between this signal and the local pressure is used as a qualitative measure of the modal Rayleigh index $RI(f) = \Re\bigl(p'(f)\,\dot{Q}'(f)^*\bigr)$. If $RI(f) > 0$, the flame acts as an acoustic source for frequency f. The heat release rate in the frequency domain $\dot{Q}'(f)$ is represented by the PMT signal. $\dot{Q}'(f)^*$ denotes its complex conjugate.[144, 245]

The measurements are conducted at $P_{th} = 40\,\text{kW}$ and $\Phi = 0.74$. Before the measurements started, the combustor had been running at constant operating conditions for 10 min to reduce the effect of transient heating. One pressure sensor was positioned at the most upstream hole ($x_{ref} = -200\,\text{mm}$) while the other one traversed along the length of the combustor (going downstream along the combustion chamber first, followed by the plenum). To construct the pressure profiles in the Limousine combustor, the correlation quantities were calculated in real time by Argus OMDS.

Figure 4.12 gives an overview of the pressure fluctuation against position and frequency $p'(f, x)$. The plotted intensity shows the square root of the *ASD* of the pressure signal per sensor access hole, which is the L^2 norm (averaged over the analysis segments) of the absolute value of the Fourier transformed pressure signal. The signal is clipped between 1 and 1000 Pa to adequately show the weaker resonances.
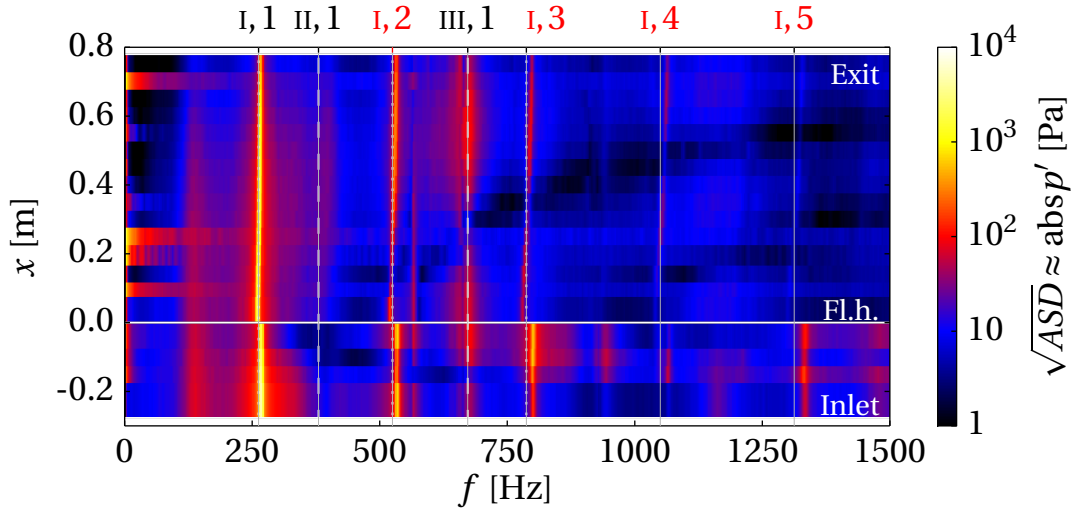
Figure 4.12: $\sqrt{ASD_p(f,x)}$ is the L^2 norm of the Fourier transformed pressure signal, per frequency bin, averaged over 200 cycles.[222] The plot gives an overview of the amplitude of the pressure fluctuation as a function of frequency and position at the operating conditions $P_{\text{th}} = 40\,\text{kW}$ and $\Phi = 0.74$.

The plot shows two phenomena clearly. Firstly, vertical bright lines show the resonant frequencies. Drift in temperature during the experiments deforms these lines, especially at higher frequencies. Secondly, there is a pressure node at the outlet, and at integer half wavelengths upstream of the inlet. These are seen as darker hyperbolic bands. There should be a pressure anti-node at the inlet, although there are not enough measurement points to show this clearly. At a quarter wave length (plus an integer of half wave lengths) downstream of the inlet there are pressure nodes as well.

Figure 4.17 shows $\sqrt{ASD_p(f)}$ measured at the reference sensor at $x = -200\,\text{mm}$, both at start and end of the experiment. The dominant peaks are harmonics of the first mode. Contrary to the behaviour at $x = -100\,\text{mm}$, discussed in sec. 4.4.2.2, at the current position the amplitude of the second harmonic $p'_{\text{I},2}$ is higher than the third, $p'_{\text{I},3}$. The frequency of the second mode of oscillation $\text{II}, 1$ is hard to pin-point, since it is so close to $f_{\text{I},1}$. The third mode of oscillation $\text{III}, 1$ is seen as a separate peak between the first and second harmonic ($\text{I}, 2$ and $\text{I}, 3$) of the dominant mode.

4.4.2.2 Stability depending on operating conditions

For these measurements, a sensor was located at $x = -100\,$mm. Measurement at this position does not require a cooling adapter, which makes comparative measurements on burners at other laboratories easier. For three (fixed) fuel flow rates, the equivalence ratio Φ was varied ($0.5 < \Phi < 1$) by increasing and subsequently decreasing the air flow rate. The combustor had been running before the start of the experiment, and the operating conditions were changed slowly (around 2 min between $\Phi = 1$ and $\Phi = 0.5$) to reduce the effects of transient cooling and heating of the structure.

Figure 4.13 gives an overview of the amplitude and frequency of the fundamental pressure oscillation in the combustor for three discrete values of the thermal power P_{th}, while the equivalence ratio decreases and subsequently increases. The edge colour of the markers indicate the thermal power, the marker orientation and filling differentiate between increasing or decreasing equivalence ratio. Generally, for a given equivalence ratio Φ, higher power will lead to a higher amplitude and higher frequency. There is a difference in amplitude and frequency between the oscillation during decreasing and increasing Φ. Possible causes are path dependence (hysteresis) of the flame stability state, but also transient heating of the combustor.[76, 262] The heat capacity of the combustor causes the temperature to react slowly to the operating conditions, which sec. 4.4.2.1 will discuss as well.

The combustion is stable at lower equivalence ratios. For all but the lowest thermal powers, the transition from stable to unstable combustion, or vice versa, takes place very abruptly ($\approx 0.1\,$s) between $\Phi = 0.5$ and 0.6. As a result, the left side of fig. 4.13 shows just a few points between 1000 and 2000 Pa. Between $\Phi = 0.6$ and 0.7 the amplitude remains approximately constant. For higher equivalence ratios there is again a trend to higher amplitudes. In the case of $P_{\text{th}} = 40\,$kW more than 5000 Pa are reached. For $P_{\text{th}} = 20\,$kW, the transition between stable and unstable combustion or vice versa, is much smoother. There is no trend to higher amplitudes near $\Phi = 1$.

The dominant frequency $f_{\text{I},1}$ depends on thermal power, where higher power leads to higher frequency due to a higher temperature of combustion products. The dependence on Φ is not monotonic, with a maximum around $\Phi = 0.8$. For lower values of Φ, the excess air reduces the adiabatic flame temperature, leading to a lower speed of sound. For $\Phi > 0.8$ slow mixing could cause a lower temperature in the flame region.
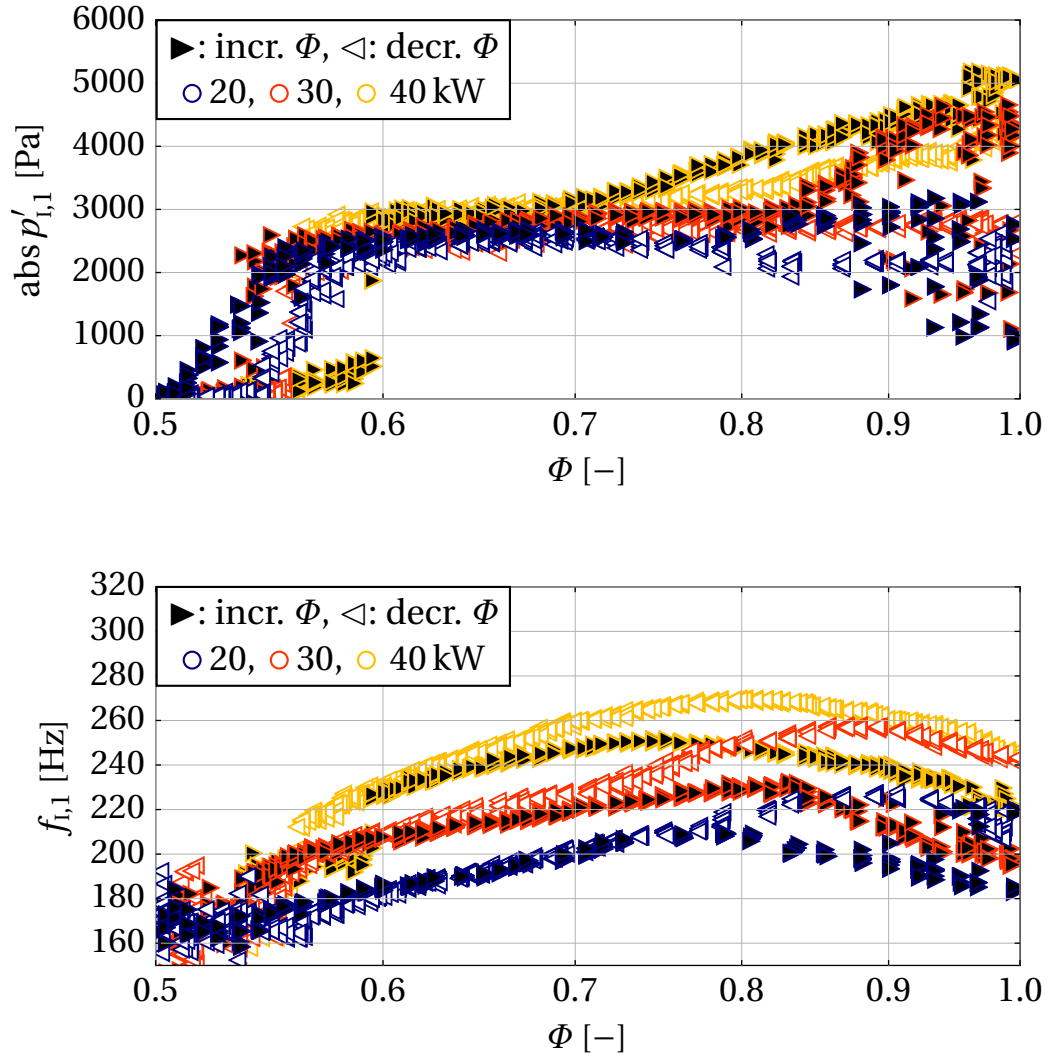
Figure 4.13: Amplitude abs $p'_{I,1}$ (above) and frequency $f_{I,1}$ (below) of the dominant mode for various thermal powers, plotted against equivalence ratio. Marker edge colour indicates thermal power P_{th}. Filling and orientation differentiate increasing versus decreasing equivalence ratio Φ. Sensor location $x_S = -100\,\text{mm}$.

Increasing versus decreasing equivalence ratio Φ — Figure 4.14 shows two intensity plots, showing the influence of the equivalence ratio Φ on the spectrum of the pressure signal at $x = -100\,\mathrm{mm}$ for $P_{\mathrm{th}} = 40\,\mathrm{kW}$. The transition between stable oscillation and limit cycle is seen as a sharp line near the bottom of both plots, at $\Phi \approx 0.56$ and $\Phi \approx 0.60$ respectively. Again, path dependence (hysteresis) of the flame stability state as well as transient heating of the combustor could cause this difference. Both effects were observed on the Limousine combustor.

Besides the Φ-dependent curves, there are two straight vertical lines in fig. 4.14, around 570 Hz and 680 Hz respectively. Their apparent temperature-independence suggests these modes are structural, or originate in cold sections of the set-up. The third fundamental mode (III, 1) in sec. 4.4.2.1 corresponds to a mode at 672 Hz whose pressure profile describes half a wave in the (cold) plenum, which likely causes this peak. Altunlu et al[6] (discussing another burner by the same design) mention a structural mode at 673 Hz as well, but none near 570 Hz.

Relative amplitudes of the higher peaks — Besides the fundamental frequency, the higher harmonics of the dominant oscillation mode are clearly visible as an equidistant array of peaks. Looking at the raw time signal of the pressure fluctuation, these higher harmonics are (for most operating points) phase-locked to the fundamental oscillation, leading to a relatively constant wave form over time.

The amplitudes of the first two harmonics, relative to the fundamental amplitude, $\mathrm{abs}\left(p'_{\mathrm{I},2}/p'_{\mathrm{I},1}\right)$ and $\mathrm{abs}\left(p'_{\mathrm{I},3}/p'_{\mathrm{I},1}\right)$ respectively, are shown in fig. 4.15. As these plots show, the first harmonic is rather small in amplitude, while the second harmonic can reach significant amplitudes. It tends to be stronger at higher equivalence ratios, but depending on thermal power, the exact location of the peak varies without obvious trend.

Plotting the relative amplitudes of the harmonics against their respective frequencies on the other hand, does show a clear trend. Irrespective of thermal power, the higher harmonics are stronger when their frequency is either close to 570 Hz or 680 Hz. These are the same frequencies as noted in sec. 4.4.2.2 and do not depend on the operating point.
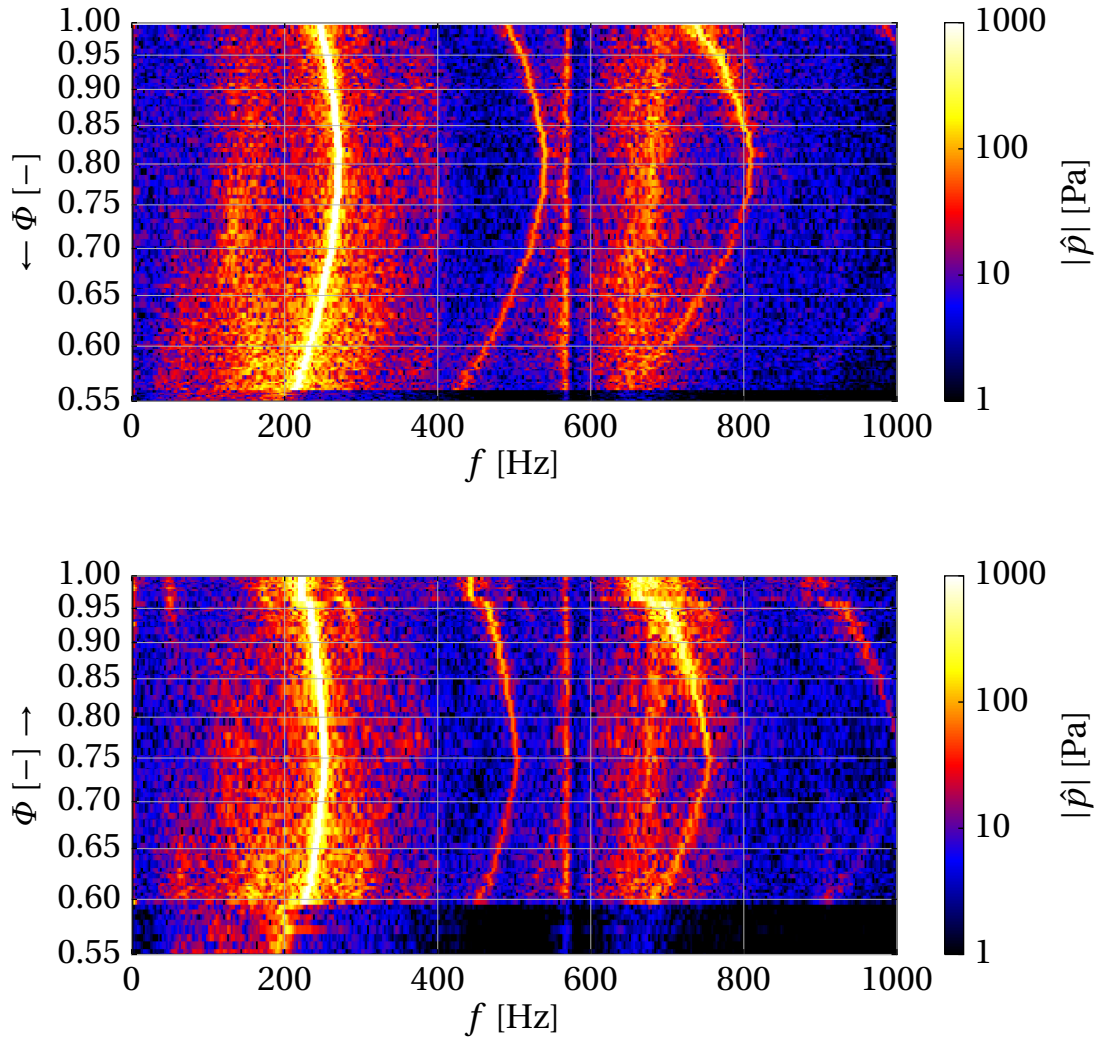
Figure 4.14: Spectral intensity for changing equivalence ratio, at $P_{\text{th}} = 40\,\text{kW}$. Decreasing equivalence ratio Φ shown above, increasing Φ shown below. The onset of instability shows hysteresis, so that the combustion becomes stable at a lower value of Φ, while it becomes unstable at higher Φ. Sensor location $x_{\text{S}} = -100\,\text{mm}$.
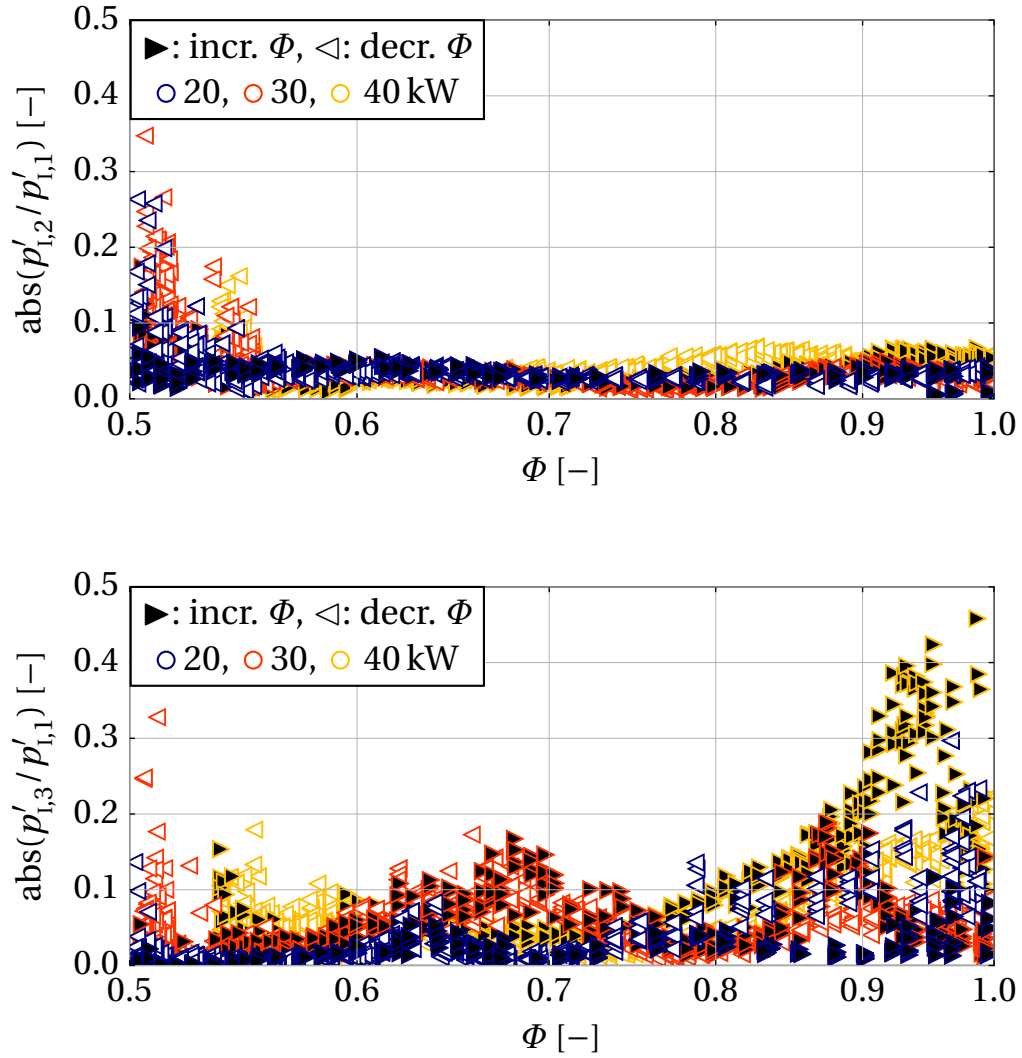
Figure 4.15: Relative amplitude of the second (I, 2 above) and third (I, 3 below) harmonic of the first mode for various powers plotted against equivalence ratio. Marker edge colour indicates thermal power P_{th}. Filling and orientation differentiate increasing versus decreasing equivalence ratio Φ. Sensor location $x_{\text{S}} = -100\,\text{mm}$.
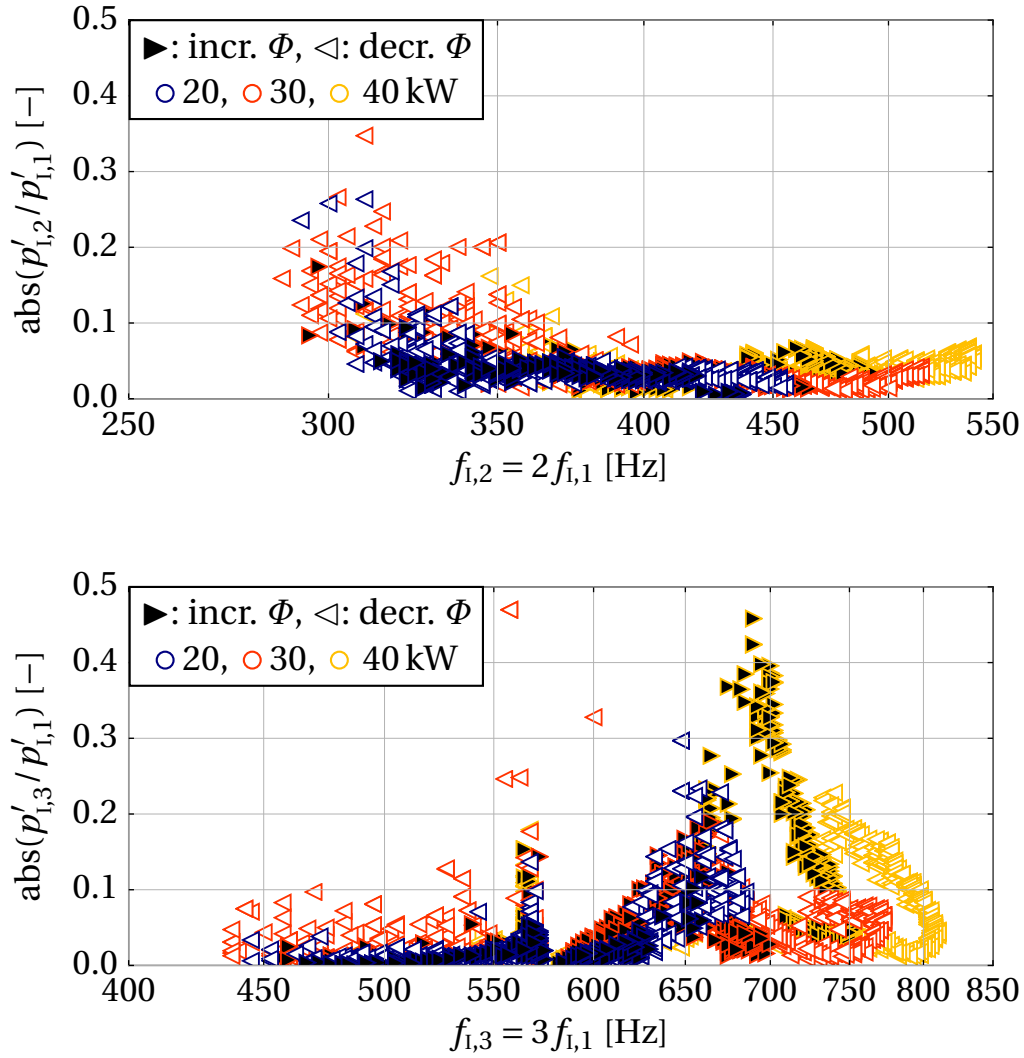
Figure 4.16: Relative amplitude of the second (I, 2 above) and third (I, 3 below) harmonic of the first mode for various powers plotted against frequency. Marker edge colour indicates thermal power P_{th}. Filling and orientation differentiate increasing versus decreasing equivalence ratio Φ. Sensor location $x_{\text{S}} = -100\,\text{mm}$.

Since proximity to these two frequencies has such a strong influence on the amplitudes of the higher harmonics, it is hard to identify other influences, such as those of thermal power or equivalence ratio.

4.4.3 Pressure profiles

The pressure profiles are presented in the form of amplitude and phase plots, based on the correlation data as discussed in sec. 2.3. The amplitude at $x_{\text{ref}} = -200\,\text{mm}$ is based on the average between the peaks of the two spectra in fig. 4.17. At the other positions the amplitude is determined via the transfer functions calculated by Argus OMDS. The rings in fig. 4.18 and onward indicate the estimated transfer function $\mathcal{G}^{\approx} = \sqrt{\mathcal{G}^{-}\mathcal{G}^{+}}$, while the range between $\mathcal{G}^{-}$ and $\mathcal{G}^{+}$ is shaded. The phase plots show the pressure signal as rings as well, relative to OH^* chemiluminescence indicated by a green asterisk.
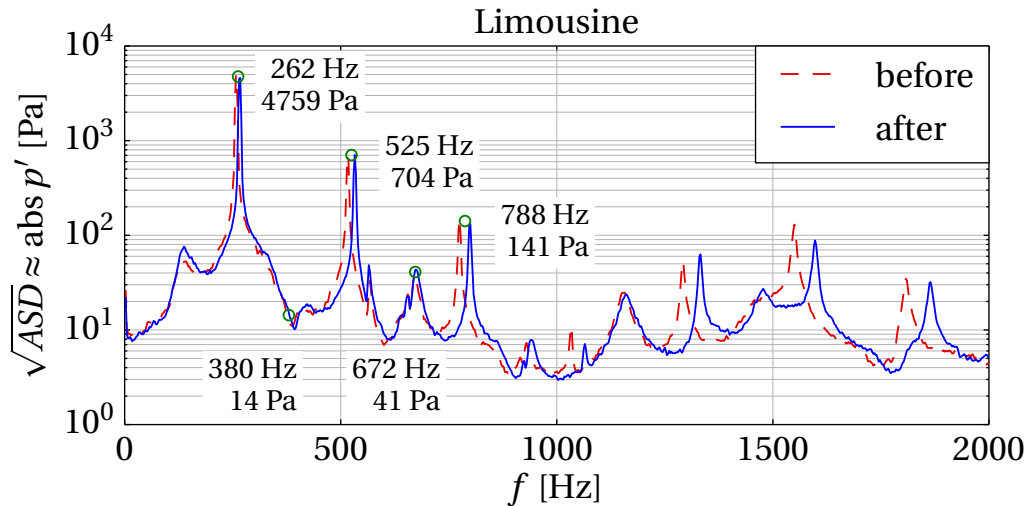
Figure 4.17: Pressure spectrum $\sqrt{ASD(f)}$ at the first and last analysis run of the experiment (around 10 respectively 30 minutes after ignition of the combustor). Peaks corresponding to the mode shapes plotted in the following figures are indicated. Sensor location $x_{\text{S}} = -200\,\text{mm}$.

The 1/4 wave pressure profile of the dominant mode of oscillation is shown in fig. 4.18. The discontinuity in cross section at the flame holder and the acoustic effect of the flame cause a cusp in the profile, deeper than it was for the Hummer rig. The OH^* signal has a small phase shift compared to pressure, indicating the thermoacoustic interaction of the flame with the

dominant mode generates acoustic energy, in agreement with the Rayleigh index ($RI_{I,1} > 0$).
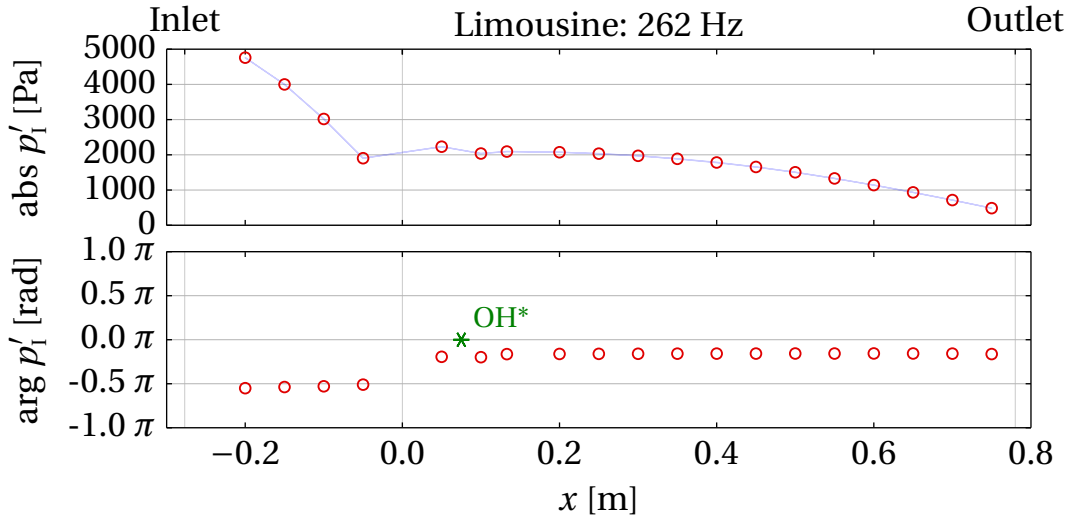
Figure 4.18: Pressure profile of the dominant mode of oscillation (I, 1) of the Limousine combustor at $P_{\text{th}} = 40\,\text{kW}$ and $\Phi = 0.74$.

Figure 4.19 shows the profiles associated with the second and third harmonic of the dominant mode. Both profiles show standing waves obeying the zero pressure fluctuation boundary condition around $x = 800\,\text{mm}$, i.e. near 0.3 times the hydraulic diameter behind the outlet.[150] The profile shape in the upstream section and the behaviour at the flame holder are harder to interpret. The phase difference between OH* signal and pressure is more than $\pi/2$, which indicates that these harmonics, although forced by higher-order, harmonic components of the non-linear flame response, dissipate fluctuation energy due to their negative modal Rayleigh indices $RI_{I,2} < 0$ and $RI_{I,3} < 0$.

The geometry of the combustor suggests the existence of 3/4 wave, 5/4 wave and higher modes as well. A profile reminiscent of 3/4 wave is found around $f_{II,1} \approx 380\,\text{Hz}$. At $x = -200\,\text{mm}$ its peak is hidden by spectral leakage of the dominant oscillation, but at locations further downstream it is seen more clearly. This mode is shown on the left in fig. 4.20. For this mode, there is a pressure node close to the location of the flame, which might explain why this mode has such a low amplitude. Also, the pressure node at the flame holder means a velocity anti-node. The energy of this mode is likely dissipated efficiently by aerodynamic resistance of the bluff body flame holder.

The 5/4 wave mode $f_{III,1}$, discussed by Tufano et al.,[276] has its peak around 670 Hz. The profile, on the right in fig. 4.20, shows a pressure anti-node, and
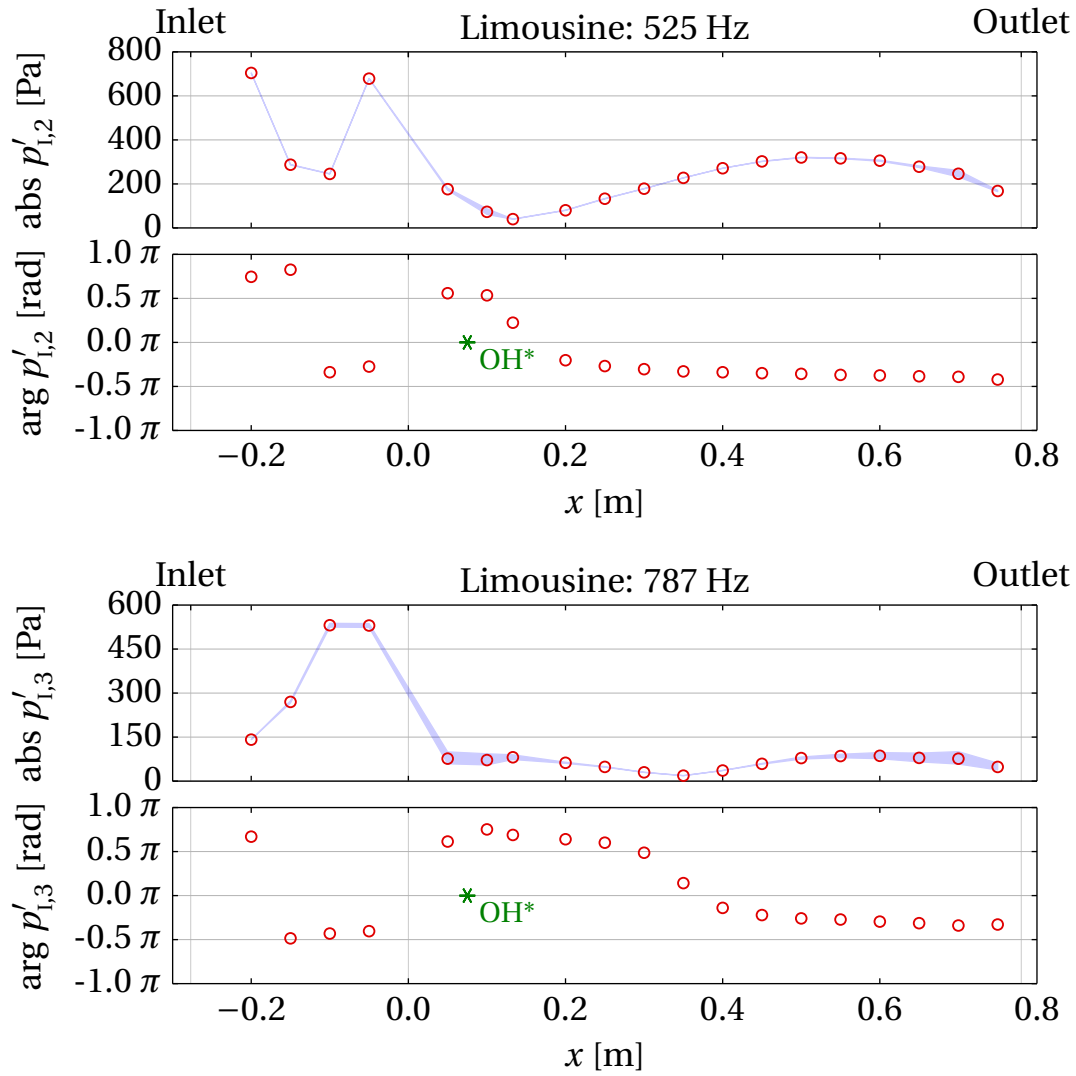
Figure 4.19: Pressure profile of the second and third harmonic of the first mode (I, 2 above and I, 3 below) of the Limousine combustor at $P_{\text{th}} = 40\,\text{kW}$ and $\Phi = 0.74$.
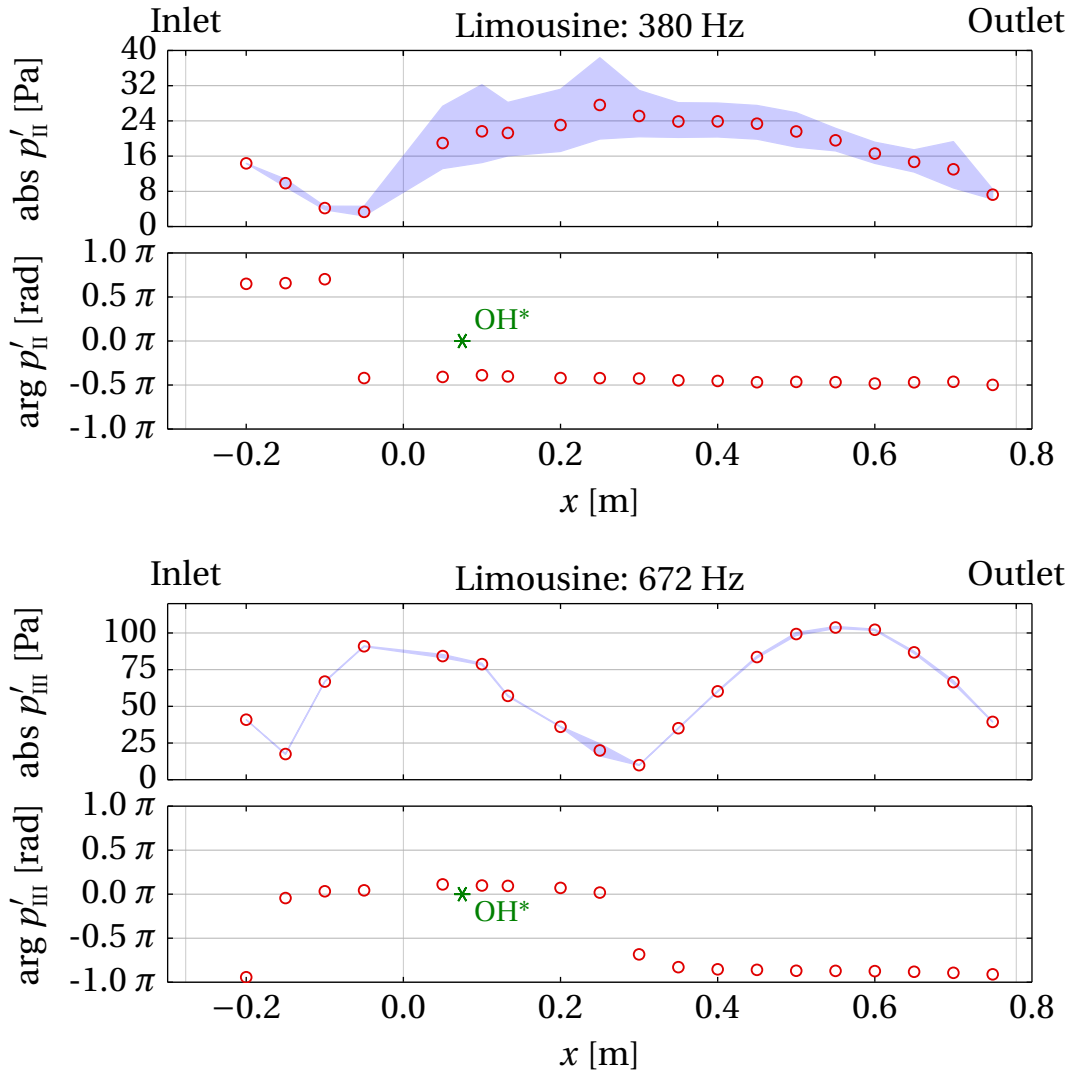
Figure 4.20: Pressure profiles of the second and third fundamental mode. II, 1: 3/4 wave above and III, 1: 5/4 wave below. $P_{th} = 40\,kW$ and $\Phi = 0.74$.

therefore a velocity node at the flame holder. Following the reasoning before, the relatively high amplitude of this mode seems reasonable. For $\text{II}, 1$ and especially $\text{III}, 3$, the phase shift between the OH* and pressure signals is small again, indicating a positive Rayleigh index for these frequencies; $RI_{\text{II},1} > 0$ and $RI_{\text{III},1} > 0$.

4.5 Modelling in taX

Figure 4.21 shows the representation of the Hummer test rig in taX. The elements making up this model have been introduced in sec. 3.3, except for the flame describing element (labelled 'Flame'). This element and the parametrisation of the others will be discussed in the coming subsections. After that, the results from the network simulation are presented.

4.5.1 n, τ, σ, Φ flame model

This flame element is a generalisation of the model proposed by Polifke et al.[216] The original element by Polifke et al. described fluctuation of the heat release due to an equivalence ratio fluctuation, in turn caused by a variation of the air flow velocity and pressure (subscript 'air') at the fuel injector:

$$\frac{\dot{Q}_\Phi(t)}{\bar{\dot{Q}}} = -\frac{1}{2} \frac{p'_{\text{air}}(t - \tau)}{p_{\text{F}} - p_{\text{air}}} - \frac{u'_{\text{air}}(t - \tau)}{\bar{u}_{\text{air}}} .$$

The first term describes a fluctuation of the equivalence ratio due a variation of the pressure of the air flow at the injector (p'_{air}) compared to the pressure drop over the fuel injector ($p_{\text{F}} - p_{\text{air}}$). The second term describes a fluctuation of the equivalence ratio due to variation in the air flow past the injector (u'_{air}). Pressure is constant over the flame, while the increase in volume is related to the heat release by the interaction index $n = T_{\text{out}}/T_{\text{in}} - 1$, where subscripts 'in' and 'out' refer to flow entering and leaving the flame:

$$[p']_{\text{in}}^{\text{out}} = 0$$

$$[u']_{\text{in}}^{\text{out}} = n \exp(-i\omega\tau)\, u'_{\text{air}} .$$
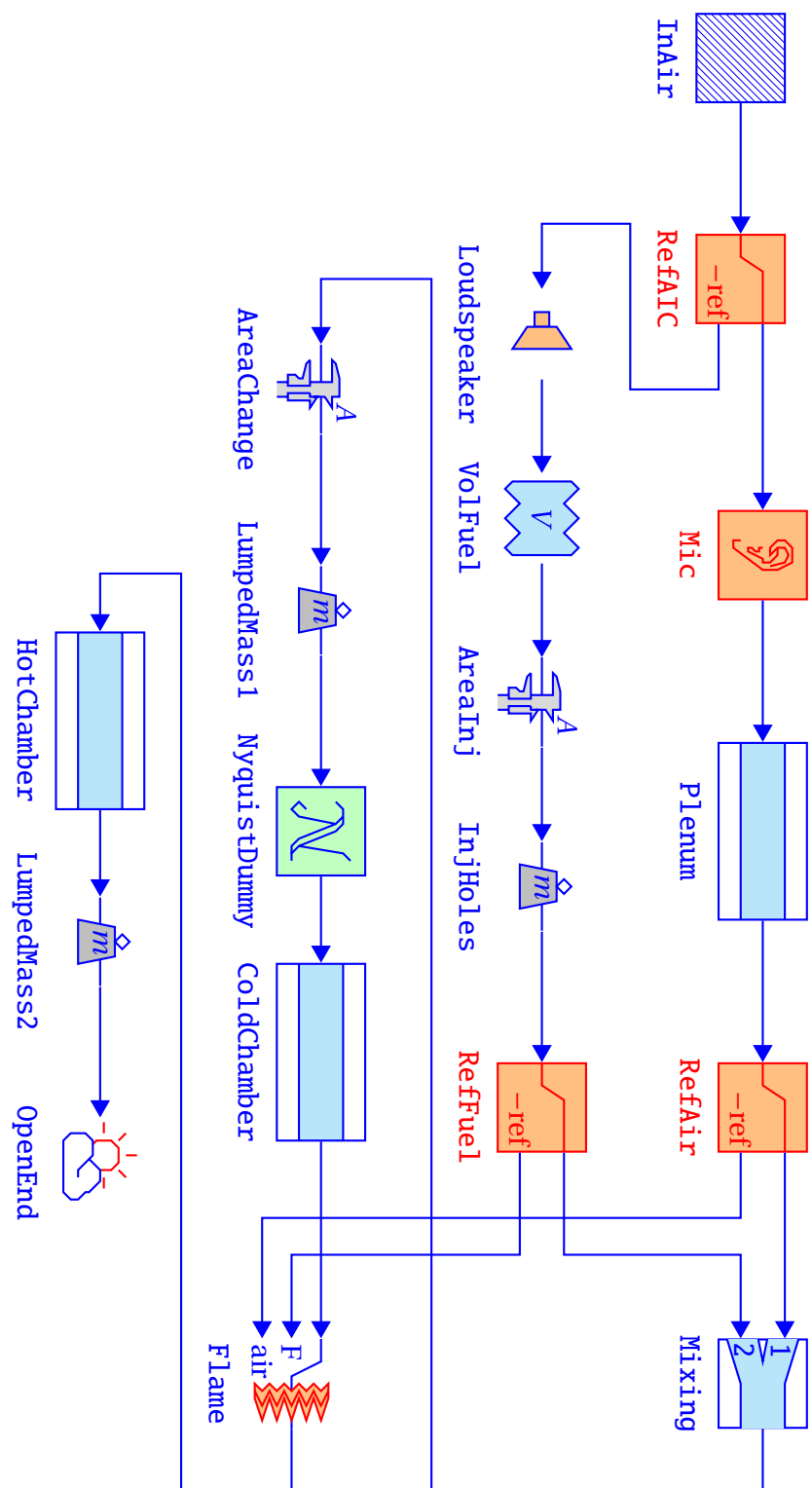
Figure 4.21: Representation of the Hummer test rig in taX.

In the current model, the fuel inflow is computed by taX along with all other acoustic quantities, leading to (similar to Auer et al.[11: eq.2])

$$\frac{\dot{Q}_\Phi(t)}{\bar{Q}} = \frac{u'_\mathrm{F}(t-\tau)}{\bar{u}_\mathrm{F}} - \frac{u'_\mathrm{air}(t-\tau)}{\bar{u}_\mathrm{air}} \; .$$

Where subscript 'F' refers to the fuel flow at the fuel injector. Furthermore, the time delay τ can have a dispersion σ, damping higher frequencies in the sense of Polifke et al.,[215] so that

$$[u']_\mathrm{in}^\mathrm{out} = n \exp\left(-\mathrm{i}\omega\tau - \sigma^2\omega^2/2\right) u'_\mathrm{F} \; .$$

Currently these values are based on results of the simulations presented in sec. 6.2. $\tau = 8\,\mathrm{ms}$, which is the average time delay between fuel injector and flame. $\sigma = 2\,\mathrm{ms}$, which is slightly less that the simulated standard deviation of the delay, so that the system is slightly less stable. For engineering purposes it would be very useful to have an estimation approach that requires less computational effort.

According to Kosztin et al.,[137] the temperature downstream of the flame (discussed in sec. 4.5.4) can be taken to be a representative constant temperature along the length of the combustor, without introducing too severe errors. The interaction index $n = T_\mathrm{out}/T_\mathrm{in} - 1$ is set according to the same temperature.

4.5.2 Geometry

Figure 4.3 gave an overview of the relevant sizes of the Hummer combustor. For reference the values used in taX are repeated in tbl. 4.1.

The flame holder section of the Limousine combustor is convergent in the flow direction. Section 5.3.2.2 will describe how such a geometry can be modelled.

4.5.3 Throughflow and flow composition

The temperature and velocity inside the burner are closely related and dependent on the operating conditions. The required amounts of gases to operate the burner determine the velocities upstream of the flame. At the flame the fuel and part of the oxygen (assuming lean combustion) are consumed, and

	Length L_x mm		Width L_y mm	Breadth L_z mm
Air injection[I]	3		$3 \cdot 33 \cdot \varnothing 2$	
Plenum	323		23	180
Flame holder	19	$2 \cdot$	14	142
Combustion chamber	779		50	150
Main fuel duct[II]	75		$2 \cdot \varnothing 6$	
Fuel injection[III]	3		$2 \cdot 31 \cdot \varnothing 1$	

(I)   Modelled acoustically stiff
(II) Modelled as pure compliance
(III) Modelled as pure inertance

Table 4.1: Geometry of the Hummer combustor.

replaced by the combustion products; water vapour and carbon dioxide in this case. The temperature is raised by the combustion process, leading to a lower density and higher velocities as well.

The amount of methane needed to operate the burner at the reference point of $P_{th} = 40\,\text{kW}$ can be determined from the mole-based LHV of CH_4 according to the National Institute of Standards and Technology (NIST)[197]:

$$
\begin{aligned}
\dot{n}_{CH_4,in} &= \frac{P_{th}}{LHV} \\
&= \frac{40 \cdot 10^3}{802.310 \cdot 10^6} \\
&= 49.86 \cdot 10^{-6}\,\text{kmol}_{CH_4}/\text{s}\,.
\end{aligned}
$$

The required amount of oxygen follows from the stoichiometric relation and the definition of the equivalence ratio $\Phi = 0.71$ or equivalently air excess ratio $\Lambda = 1.4$:

$$CH_4 + 2\,O_2 \longrightarrow CO_2 + 2\,H_2O \tag{4.1}$$

$$\dot{n}_{O_2,\text{in}} = 2\,\dot{n}_{CH_4,\text{in}}/\Phi$$

$$= 139.6 \cdot 10^{-6}\,\text{kmol}_{O_2}/\text{s}\,.$$

The oxygen is supplied in the form of dried air, which can well be approximated by 21% O_2 and 79% N_2 by volume. Nitrogen is the third and last of the inflowing gases:

$$\dot{n}_{N_2,\text{in}} = \frac{\mathcal{X}_{N_2,\text{in}}}{\mathcal{X}_{O_2,\text{in}}}\,\dot{n}_{O_2,\text{in}}$$

$$= \frac{0.79}{0.21}\,139.6 \cdot 10^{-6}$$

$$= 525.2 \cdot 10^{6}\,\text{kmol}_{N_2}/\text{s}\,.$$

Assuming complete combustion, the gas flows after combustion can readily be determined from eq. (4.1) and the definition of Φ:

$$\dot{n}_{N_2,\text{out}} = \dot{n}_{N_2,\text{in}}$$

$$= 525.2 \cdot 10^{6}\,\text{kmol}_{N_2}/\text{s}\,,$$

$$\dot{n}_{CH_4,\text{out}} = \max\left(1 - \frac{1}{\Phi}, 0\right)\dot{n}_{CH_4,\text{in}}$$

$$= 0\,\text{kmol}_{CH_4}/\text{s}$$

and

$$\dot{n}_{O_2,\text{out}} = \max\left(1 - \Phi, 0\right)\dot{n}_{N_2,\text{in}}$$

$$= 39.88 \cdot 10^{-6}\,\text{kmol}_{O_2}/\text{s}\,.$$

Table 4.2 lists the resulting flow rates.

| | $\dot{n}_{in}$ | $\dot{m}_{in}$ | $\dot{n}_{out}$ | $\dot{m}_{out}$ |
	10^{-6} kmol/s	10^{-3} kg/s	10^{-6} kmol/s	10^{-3} kg/s
CH_4	49.86	0.799	—	—
O_2	139.60	4.467	39.88	1.276
N_2	525.12	14.713	525.12	14.713
CO_2	—	—	49.86	2.194
H_2O	—	—	99.71	1.797
Total	714.60	19.979	714.60	19.979

Table 4.2: Flow rates at the reference operating conditions: $P_{th} = 40$ kW and $\Phi = 0.71$ ($\Lambda = 1.4$).

4.5.4 Exhaust temperature

As a first estimate for the temperature downstream of the flame, the adiabatic flame temperature is computed. The adiabatic flame temperature is the temperature downstream of the flame, where the enthalpy is assumed to be identical to the enthalpy of the inflowing gases. Using the Shomate equations given by NIST[197] for the gases in tbl. 4.2, the enthalpy of these inflowing gases for ambient conditions ($T_{env} = 293.15$ K) can be found. The temperature found at the same enthalpy for the outflowing gases, – i.e. the adiabatic flame temperature – is found to be 1868 K, as shown in fig. 4.22.

Due to heat loss over the combustor wall, the real temperature will be lower. The temperature of the exhaust gases was measured (at $z = 600$ mm downstream of the flame holder) using a type K thermocouple. The thermocouple measures the temperature of the chromel–alumel junction at the end of the probe held in the hot flow. The temperature of the probe is however not equal to the temperature of the gas surrounding it.[40]

Especially at higher temperatures, there is significant heat transfer by radiation from the sensor to the combustor liner, leading to a sensor temperature below that of the surrounding fluid, as depicted schematically in figs. 4.23 and 4.24.
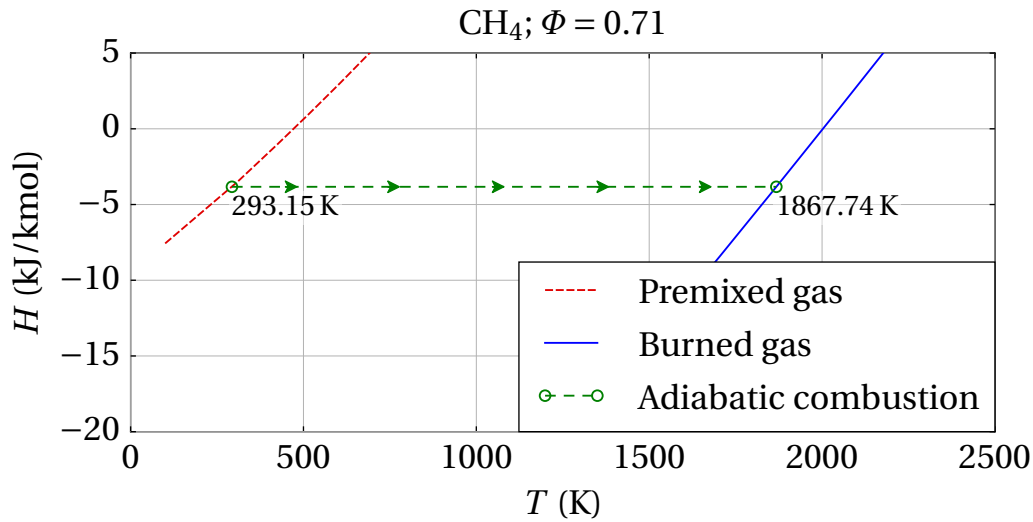
Figure 4.22: The adiabatic flame temperature at reference air excess ratio $\Phi = 0.71$ and $T_{\text{in}} = 293.15\,\text{K}$ is $1868\,\text{K}$.
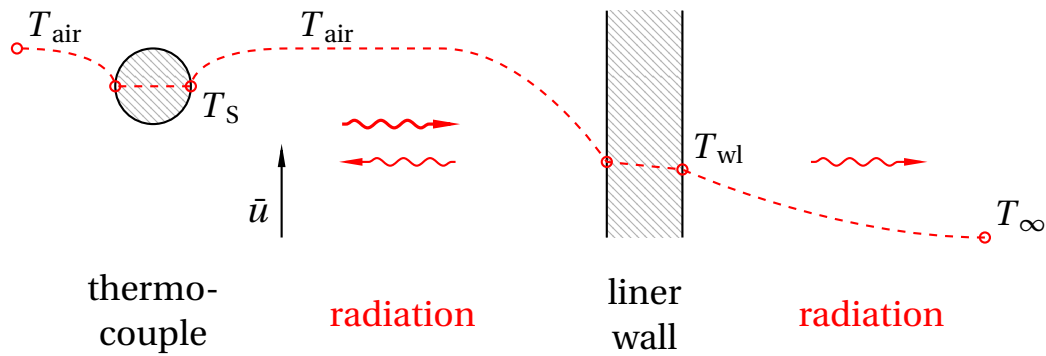
Figure 4.23: Impression of the temperature profile due to convection and radiation, inside the combustor, the sensor (drawn in cross section) and the liner wall, seen from the side.
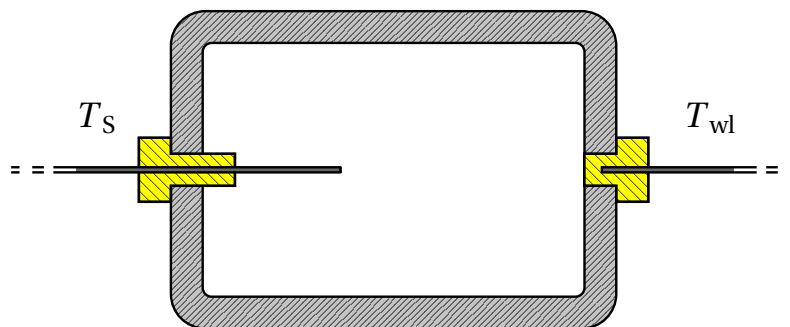
Figure 4.24: Overview (not to scale) of the sensor mounting ($z = 600\,\text{mm}$), seen from the above.

In the stationary situation, the net heat flow to the sensor is zero. Neglecting conduction through the sensor, the sensor is heated and cooled by *convective heat transfer* as well as *radiation*:

$$\sum \dot{Q}_S = \dot{Q}_{S,cv} + \dot{Q}_{S,rd} = 0 \, .$$

The convective heat transfer is expressed in terms of the heat transfer co-efficient $h_{cv} = \dot{Q}_{cv} / (A \Delta T)$, non-dimensionalised as the Nusselt number $Nu_S = h_{cv} D_S / k_{cd,air}$. Lienhard and Lienhard,[152: eq.7.66] give an expression for the Nusselt number for a cylinder in low Reynolds number ($Re_S = \rho \, \bar{u} \, D_S / \mu < 4000$) cross-flow[*]:

$$Nu_S = 0.3 + \frac{0.62 \, Re_S^{1/2} \, Pr_{air}^{1/3}}{\left(1 + (0.4/Pr_{air})^{2/3}\right)^{1/4}} \, .$$

According to Lienhard and Lienhard[152: p.299] $Pr_{air} = 5/7$, so

$$Nu_S = 0.3 + \frac{0.62 \, Re}{1 + 0.4^{2/3}} \, .$$

The product $\rho \, \bar{u}$ in the Reynolds number depends on the operating point and the burner geometry, but is independent of temperature.

$$\begin{aligned}
\rho \, \bar{u} &= \frac{\dot{m}}{A_{cc}} \\
&= \frac{0.0200 \, \text{kg/s}}{0.18 \, \text{m} \, 0.05 \, \text{m}} \\
&= 2.220 \, \text{kg/s} \, \text{m}^2 \, .
\end{aligned}$$

The diameter of the sensor is $D_S = 1 \cdot 10^{-3} \, \text{m}$, so that

$$Re_S = \frac{D_S}{\mu(T)} 2.220 \, \text{kg/s} \, \text{m}^2 \, ,$$

where $\mu(T)$ is given by Sutherland[264]:

$$\mu(T) = \mu_{Suth,air} \frac{T_{Suth,air} + X_{Suth,air}}{T + X_{Suth,air}} \left(\frac{T}{T_{Suth,air}}\right) \, ,$$

---

[*] The current Reynolds number is in the order of magnitude of 100.

with $T_{\mathrm{Suth,air}} = 273.15\,\mathrm{K}$, $\mu_{\mathrm{Suth,air}} = 1.716 \cdot 10^{-5}\,\mathrm{Ns/m^2}$ and $X_{\mathrm{Suth,air}} = 110.4\,\mathrm{K}$. The temperature T is be found by iteration.

The last quantity needed for the determination of the heat transfer coefficient h_{cv} is the thermal conductivity of air, $k_{\mathrm{cd,air}}$. This was found by evaluating the function

$$k_{\mathrm{cd,air}}(T) = 1.5207 \cdot 10^{-11}\, T^3 - 4.8574 \cdot 10^{-8}\, T^2 + 1.0184 \cdot 10^{-4}\, T - 0.00039333 \,,$$

(4.2)

given by Patel[209: eq.C-23] and checked against Lienhard and Lienhard.[152: p.714, tbl.A.6]

Heat transfer by radiation is expressed as[152: ch.10]:

$$\dot{Q}_{\mathrm{S,rd}} = A_{\mathrm{S}}\, \epsilon_{\mathrm{S}}\, \sigma_{\mathrm{SB}} \sum_i F_{\mathrm{S},i}\left(T_{\mathrm{S}}^4 - T_i^4\right),$$

where T_i refers to the temperature of surface i in line of sight from the sensor, and $F_{\mathrm{S},i}$ is the form factor, declaring to what extent surface i encapsulates the sensor. Since the liner of the combustion chamber almost fully encapsulates the sensor, this simplifies to

$$\dot{Q}_{\mathrm{S,rd}} = A_{\mathrm{S}}\, \epsilon_{\mathrm{S}}\, F_{\mathrm{S,wl}}\, \sigma_{\mathrm{SB}}\left(T_{\mathrm{S}}^4 - T_{\mathrm{wl}}^4\right),$$

with wall emissivity $\epsilon_{\mathrm{wl}} = 0.6$ for repeatedly heated steal.[152: p.528] The wall temperature is measured by a second thermocouple, at the same distance z downstream of the flame holder. Although the radiation of visible light by the flame seems impressive, the flame radiates relatively little heat. Tien and Lee[273: figs.3&4] give an emissivity of less than a percent for flames of the current size, temperature and pressure, which is negligible compared to the influence of the liner. The results of the above computations converge in a few iterations. The result are plotted in fig. 4.25. Based on these results, the flow downstream of the flame will be taken to 1550 K in taX.

4.5.5 Flow conditions

The speed of sound is determined from eq. (3.1d): $c = \sqrt{\gamma \tilde{R} T}$. To determine this value, the heat capacity ratio $\gamma = \bar{C}_p/\bar{C}_V$, the gas constant $\tilde{R}$ and the temperature of the gas mixture need to be found.
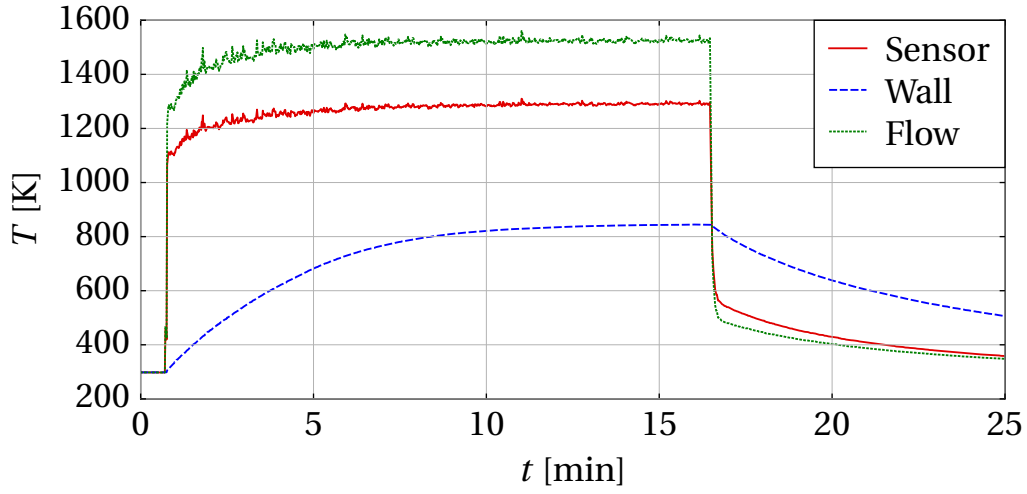
Figure 4.25: Measured temperature in flow and liner compared to the corrected flow temperature during the warming-up of the Hummer combustor.

With $\partial_T H = C_p$, the heat capacity ratio can be computed using the coefficients from the Shomate equations mentioned before. At the adiabatic flame temperature

$$\bar{\underset{\sim}{C}}_p = \sum_{i \in \text{species}} \frac{\dot{n}_i}{\dot{n}} \underset{\sim}{C}_{p,i}$$

$$= \frac{28.265}{714.60 \cdot 10^{-6}}$$

$$= 39.553 \cdot 10^3 \, \text{J}/(\text{kmol K}) \,.$$

$$\bar{\gamma} = \frac{\bar{\underset{\sim}{C}}_p}{\bar{\underset{\sim}{C}}_V}$$

$$= \frac{\bar{\underset{\sim}{C}}_p}{\bar{\underset{\sim}{C}}_p - \tilde{R}_{\text{abs}}}$$

Which gives

$$\gamma_{\text{out}} = 1.417 \,.$$

Apparently, to good approximation $\gamma = 1.4$ can be used to compute the speed of sound for all flows throughout the combustor, except for unmixed methane, which has $\gamma_{CH_4} = 1.3$ according to Air Liquide.[5]

From tbl. 4.2 (as well as eq. 4.1) it can be seen the number of molecules, as well as the mass stays the same. This means the average molar mass, as well as the specific gas constant $\tilde{R} = \tilde{R}_{abs}/m$ are not altered by the combustion process. To compute the speed of sound in various parts of the burner, with the exception of the fuel supply system, the specific gas constant for air can be used: $\tilde{R}_{air} = 286.9\,J/(kg\,K)$.

As a sidestep, the bulk velocities of the gas though the burner can be computed from the mole flow, the ideal gas law and the burner cross section:

$$\dot{V} = \frac{\dot{n}\,\tilde{R}_{abs}\,T}{p}$$

$$u = \frac{\dot{n}\,\tilde{R}_{abs}\,T}{p\,A} \ .$$

From tbl. 4.2, $\dot{n} = 664.72 \cdot 10^{-6}\,kmol/s$ upstream to the flame holder and $714.60 \cdot 10^{-6}\,kmol/s$ after. The fact that the Limousine test rig is an atmospheric burner gives the last required quantity: $\bar{p} = 101\,325\,Pa$, from which the velocities throughout the burner can be determined.

4.5.6 Results from taX

The eigenvalues and eigenmodes found by taX correspond to the $(1 + 2\,N)\,/4$ wave modes of the combustor. Only the first mode, corresponding to the pressure profile in fig. 4.26, is unstable, and hence the imaginary part of its eigenfrequency is negative. The pressure mode shapes of the higher modes are shown in fig. 4.27. Since a linear model is used, unlike in experiment, no higher harmonics are found.

This instability can also be investigated using the Nyquist dummy (see fig. 4.28). The unstable mode shows up as clockwise loop around the critical point $(-1 + 0\,i)$, or – in terms of Bode's form of presentation – a downward crossing of $\pm\pi$ by the argument, while the absolute value of the OLTF is greater then unity.
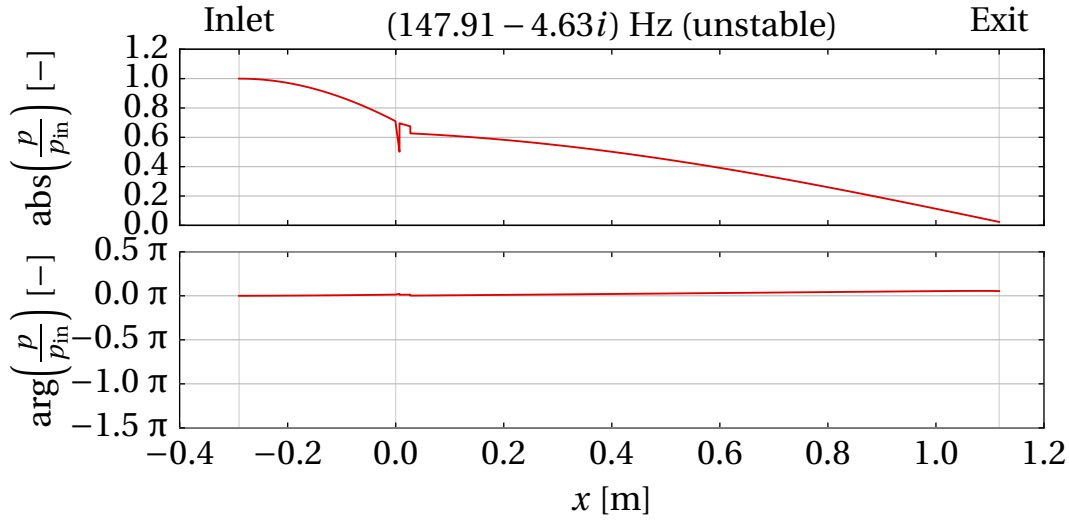
Figure 4.26: First (unstable) mode of the Hummer rig as simulated in taX.

The same instability is also seen when analysing the OLTF between loud-speaker excitation and the pressure probed at $x = 0$ (recall fig. 3.11). Using a simple proportional controller, as described by

$$\frac{u'_{ls}}{-p'_{x=0}} = 3 \cdot 10^{-3} \, \text{(m/s)/Pa} \,, \tag{4.3}$$

the unstable mode shows itself in the Nyquist plot (fig. 4.29) as an anti-clockwise loop, not including the critical point $-1 + 0i$. In the Bode plot the instability can be recognised as a local maximum of the argument, where the absolute value decreases.[213: §4.3.1]

The system can not be stabilised by simple proportional control. This would simply scale the Nyquist plot and would not be able to move the loop corresponding to the unstable mode over the critical point. To realise this, some phase shift is needed as well, which can for instance be realised by a second order transfer function, such as

$$\frac{u'_{ls}}{-p'_{x=0}} = \frac{-3.9 \cdot 10^{-3}}{1 + i\omega/825 - \omega^2/825^2} \, \text{(m/s)/Pa} \,. \tag{4.4}$$

The amplification $(-3.9 \cdot 10^{-3})$ and frequency $(825\,\text{rad/s})$ are chosen to centre the loop corresponding to the previously unstable mode around the critical point. The Nyquist plot (fig. 4.30) shows the result.
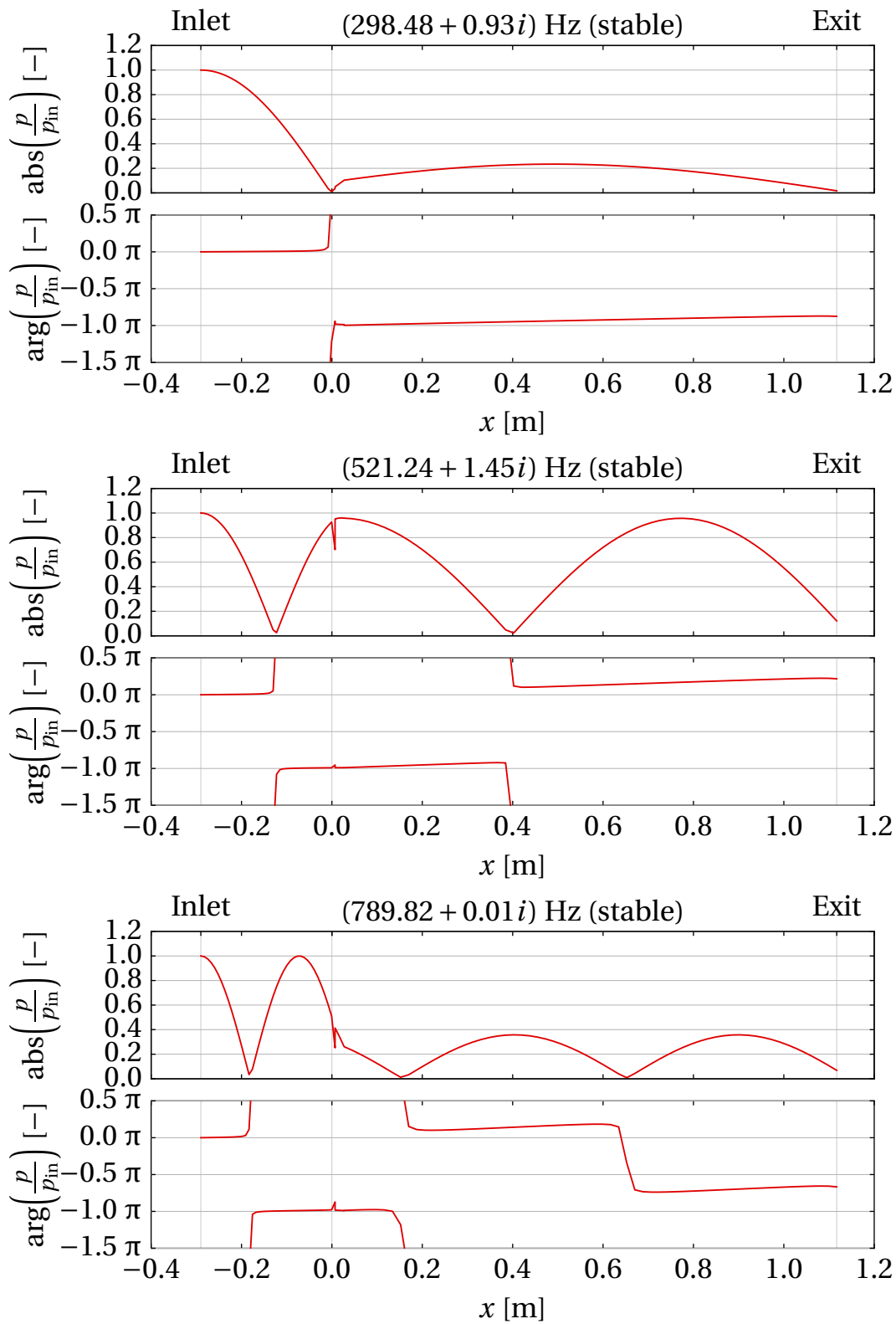
Figure 4.27: Higher (stable) modes of the Hummer rig as simulated in taX.
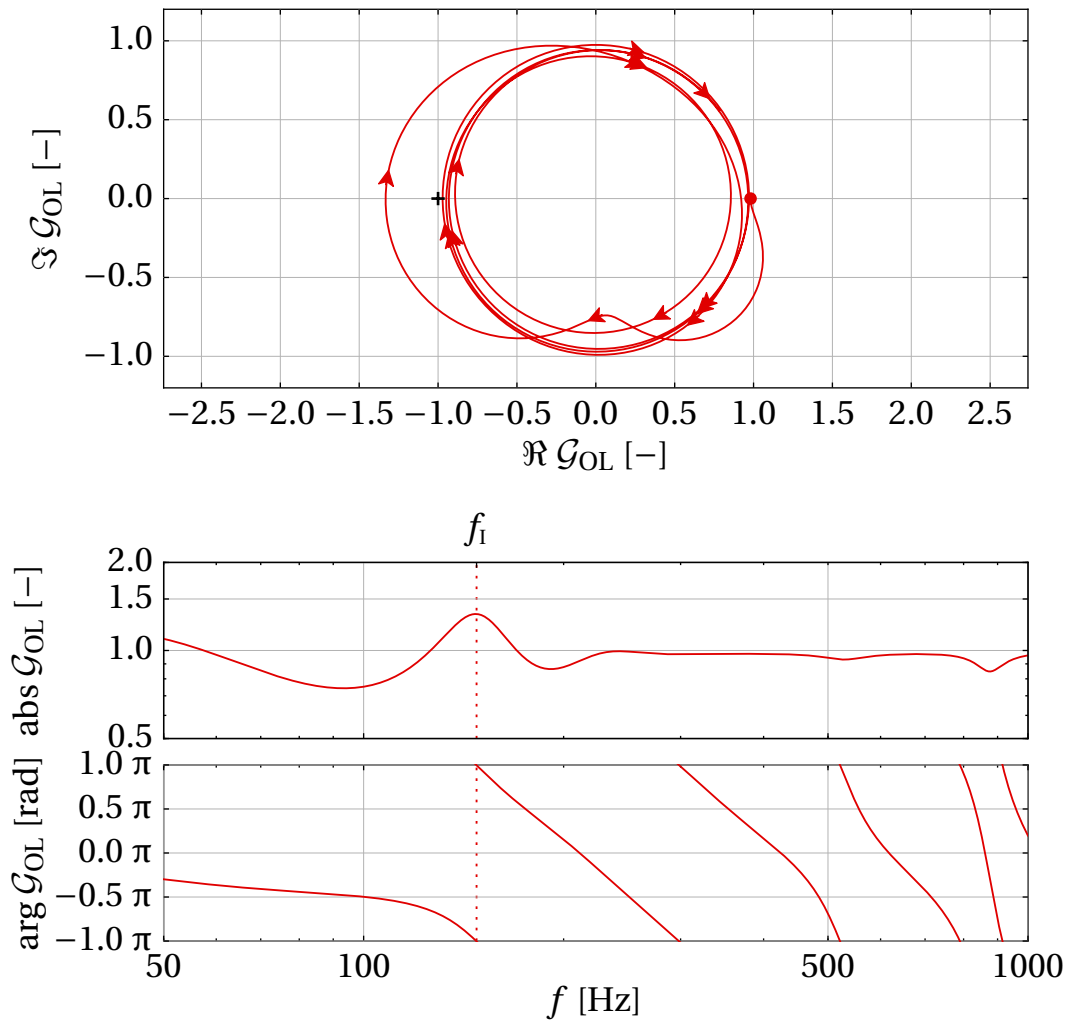
Figure 4.28: Nyquist plot (above) and Bode plot (below) of the open-loop transfer function (OLTF) of the uncontrolled system, as seen by the Nyquist dummy. The first (unstable) frequency is indicated by a vertical dashed line.
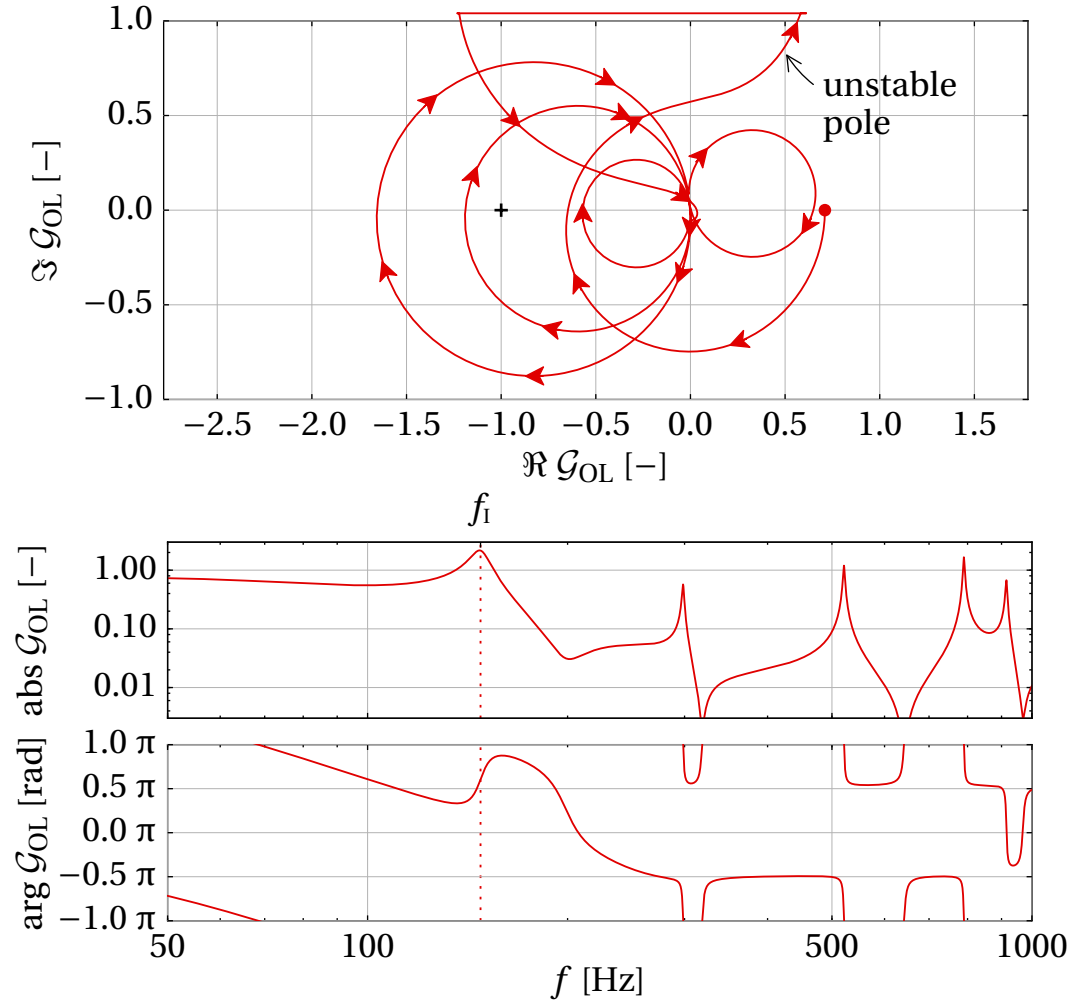
Figure 4.29: Nyquist plot (above) and Bode plot (below) of the unstable controller OLTF corresponding to eq. (4.3). The first (unstable) frequency is indicated by a vertical dashed line.
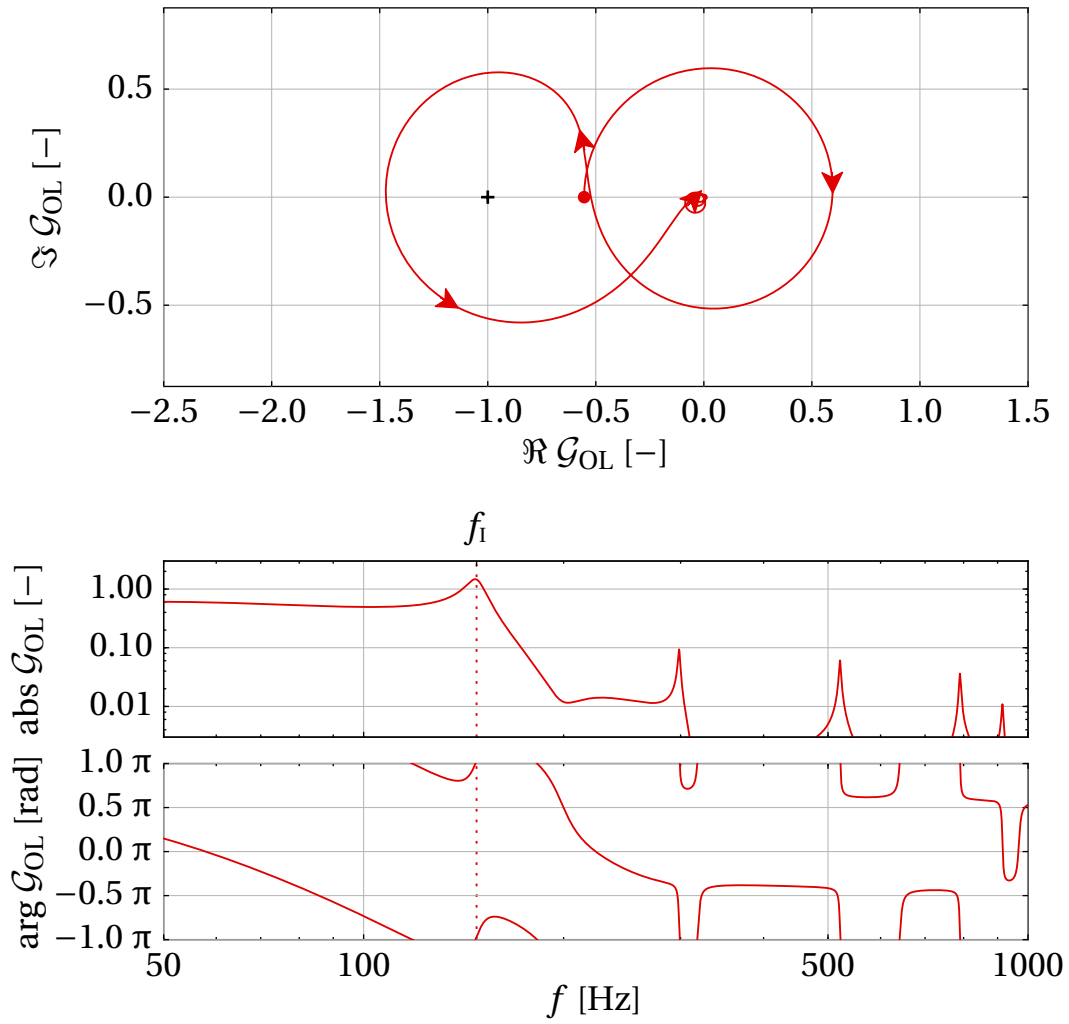
Figure 4.30: Nyquist plot (above) and Bode plot (below) of the stable controller OLTF corresponding to eq. (4.4). The first (now stabilised) frequency is indicated by a vertical dashed line.

To check that the acoustical system is stable as well, i.e. to validate that there are no uncontrollable/unobservable modes, fig. 4.31 shows the OLTF as seen by the Nyquist dummy block.
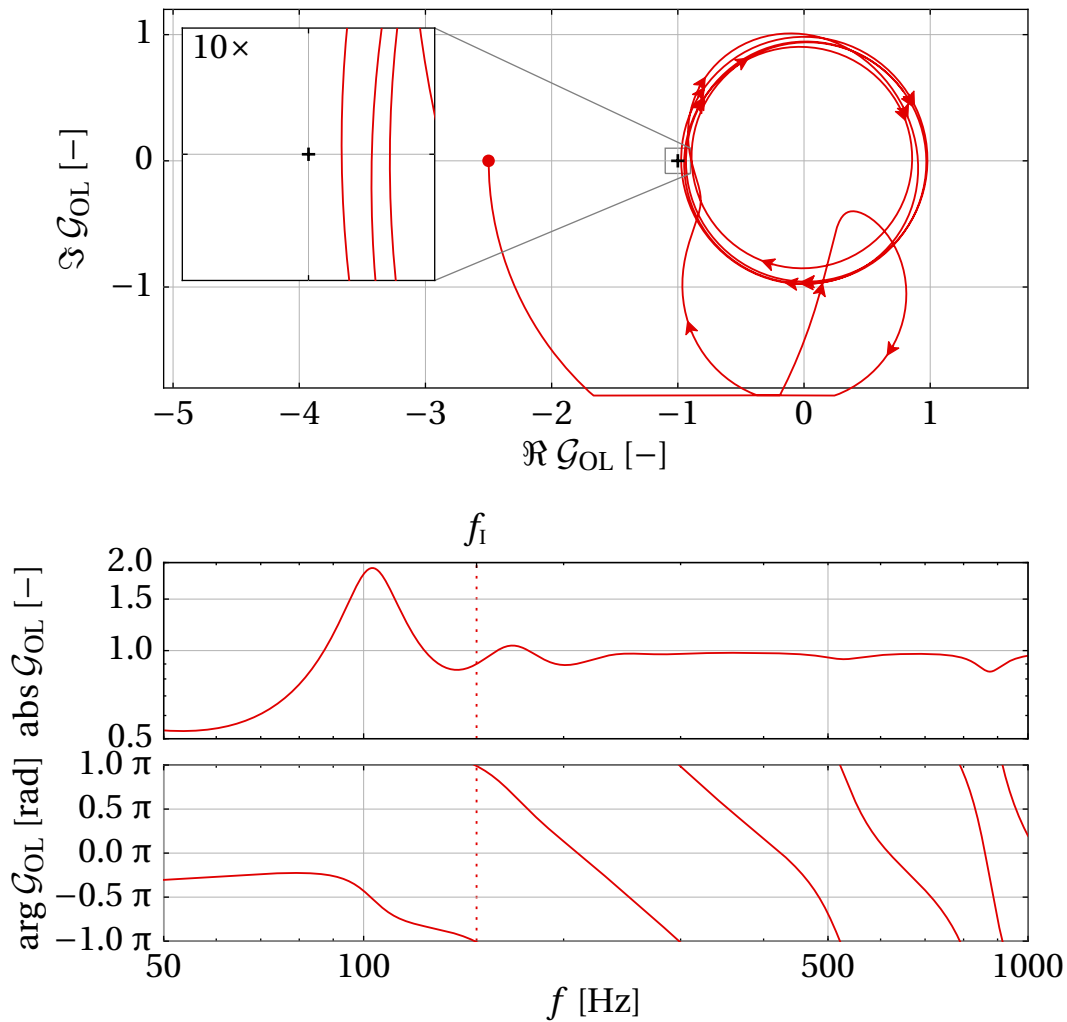
Figure 4.31: Nyquist plot (above) and Bode plot (below) of the OLTF of the controlled system, as seen by the Nyquist dummy, corresponding to eq. (4.4). The first (now stabilised) frequency is indicated by a vertical dashed line.

5 Valve model

This chapter describes a quasi-stationary, low-order model of a *direct dive valve* (DDV), used as an active element in an acoustic network model. The chapter has been submitted for publication as 'Direct drive valve model for use as an acoustic source in a network model' in the International Journal of Acoustics and Vibration (IJAV).[187]

A preliminary version of this publication was presented as 'Direct drive valve model used as an acoustic source in a network model' at the 19th International Congress on Sound and Vibration (ICSV19) in Vilnius, Lithuania.[188]

In acoustic network modelling tools, acoustic sources are often implemented as simple velocity or mass flow boundary conditions. In practice however, DDVs are not necessarily situated at the boundary of the system, and the throughflow depends on the fluctuating pressure drop over the valve. The acoustically compact model described here is based on mass conservation and a time-varying, but quasi-stationary hydraulic resistance. The resistance depends on the fluctuating valve opening. Results, in terms of acoustic wave transfer functions, are compared to experiment.

DDVs can be used as acoustic actuators in duct systems when requirements on mechanical or thermal robustness are high, e.g. for the active control of aerodynamic or combustion instabilities.

5.1 Introduction

Direct drive valves are mostly used as hydraulic (oil flow) actuators. For this application they are required to be stiff and precise, but their range of operation is restricted to frequencies below $100\,\mathrm{Hz}$.[179] Recently, they have been used as acoustic (gas flow) actuators, for instance for the active suppression of combustion instabilities or dynamic compressor stall.[112, 115, 238]

In these applications, DDVs have the advantage over loudspeakers that valves are very robust to thermal and mechanical influences. The volume flow modu-

lated by a loudspeaker is limited by its geometry, while the modulated volume for a valve is limited by the throughflow. For the applications mentioned above, this is usually to the advantage of the valve.

The implementation of control systems as described before is not trivial, and better tools are needed to predict the control authority a priori.[58] Network models are a popular tool to analyse 1-D acoustics, and could be a valuable aid when setting up new systems. However, until now no description of a valve for use in such a model is available.

No truly acoustical description of how such a valve would need to be modelled was found in the literature. Annaswamy and Ghoniem[9] for instance simply state that the throughflow is assumed to be proportional to valve opening, where the constant of proportionality depends, amongst others, on the (average) pressure drop over the valve. In reality, the throughflow depends on fluctuation of the pressure drop too. Wang et al[285] includes a description of the dynamic behaviour of the electro-mechanical subsystem of the valve, but does not discuss the resulting throughflow.

Reflection, transmission and generation of acoustic waves by a constriction at high Mach numbers has been analysed in the context of rocket exhaust nozzles. Contrary to in the current work, it is usually assumed that the geometry of the nozzle is smooth and well known, and of course constant in time. Tsien[275] for instance discusses a nozzle where the velocity u is a linear function of position x. Candel,[39] Marble and Candel,[167] and Bohn[28] generally assume smooth, conveniently defined geometries, where the only losses are caused by shock waves. For valves on the other hand, losses are dominated by flow separation at edges. Mani[165] amongst others discussed upstream reflection of free jets, but again assumes more knowledge of the flow field than is practically available for the flow through a commercial valve.

Here, a model of a DDV is formulated and implemented in a linear network model of acoustic wave propagation and scattering. The DDV is described in sec. 5.2, and the model will be formulated in sec. 5.3. This model is implemented as an active element in taX, which is an acoustic network model, developed at the TUM and implemented in MATLAB.[147] The results are compared to experimental data in sec. 5.4.

5.2 Description of the physical DDV

The valve used in this research is DDV model D633E7320 by MOOG Inc. Valve models of this type are usually used in hydraulic applications. The manufacturer mentions for example metal forming and presses, automotive testing and the timber industry.[179] The control electronics of the valve under investigation were modified for use in active instability control of combustion instabilities, increasing its frequency range up to around 500 Hz.

5.2.1 Fluid-mechanical description

Figure 5.1 gives a first impression of the outer appearance. A vessel (on top, largely outside of the picture) is connected to the inlet of the valve and functions as a decoupler, to acoustically decouple the valve from the upstream duct system. It implements, to a good approximation, an acoustically open boundary condition on the upstream side of the valve.
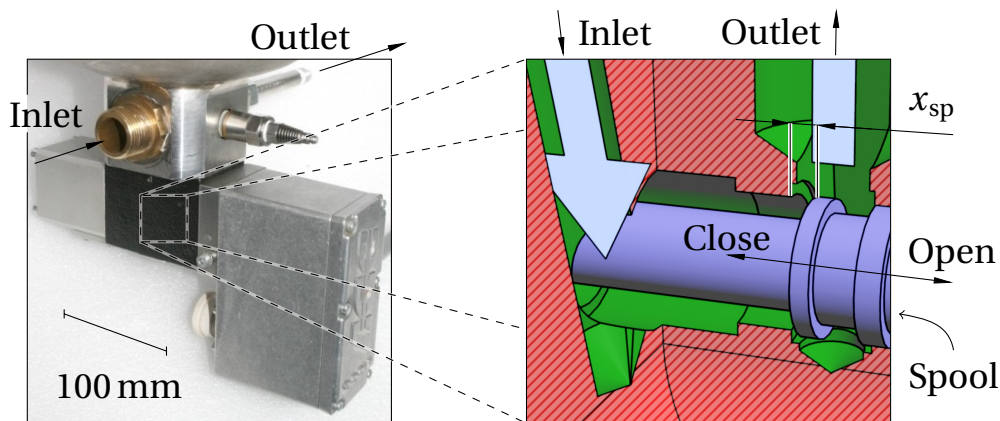
Figure 5.1: Overview of MOOG valve D633E7320 on the left. The close-up on the right shows the principle gas flow and the spool in opened position inside the bushing. Moving to the left, the spool closes the valve.

The valve itself, which is a cylinder type valve, is shown below the vessel. Only the bushing can be seen as a dark block on the photo, flanked by the linear motor on the left and the housing for electronics on the right.

The close-up on the right shows the principle gas flow and the spool in opened position. Moving the spool to the left would close the valve. The gas leaves the valve upward and then out through the exit duct, which points away from the observer.

137

5.2.2 Electro-mechanical description

The spool position follows the input voltage as a second order dynamic system. Figure 5.2 gives a graphical impression. Unfortunately, there are a few non-linearities involved, which make it impractical to model the electro-mechanical system of the valve – as was done by Wang et al.[285] – in the linear network model taX. Most notably, hysteresis due to Coulomb friction causes significant, non-linear deviation from the ideal behaviour. The movement of the spool is restricted by hard ends (see fig. 5.3). These introduce a clipping of the spool position for higher amplitudes. Since the spool position x_{sp} is monitored by a *linear variable differential transformer* (LVDT), a simpler model can be formulated using x_{sp} as input. Therefore, without loss of usability, the model will be restricted to the part indicated in the lower part of fig. 5.2, i.e. concerning fluid mechanics only.
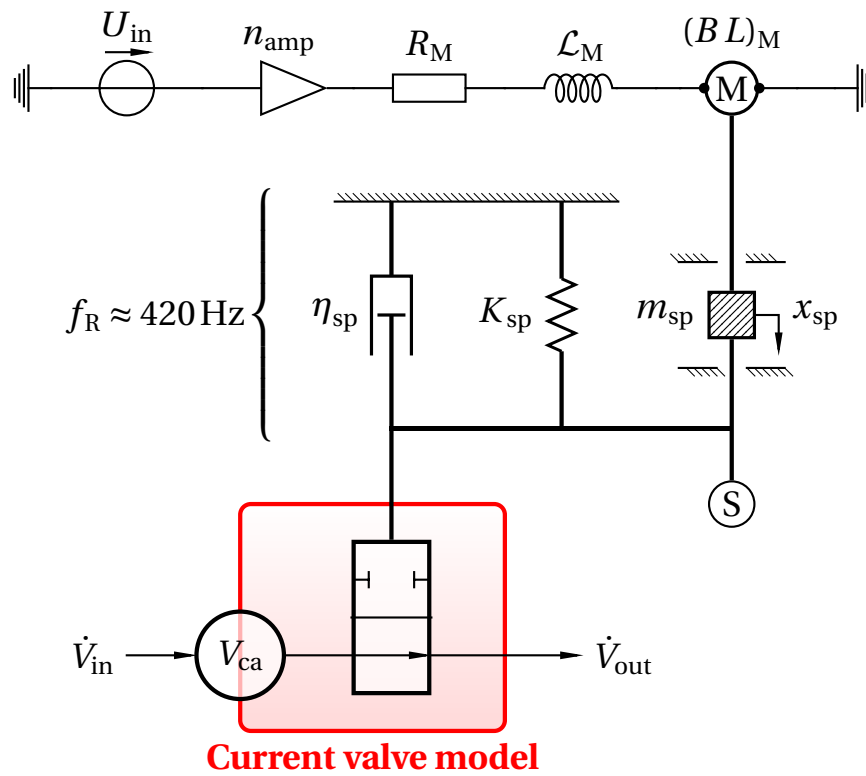
Figure 5.2: Dynamic system of the valve with non-linearities. Most notably friction (hysteresis) and hard ends limiting the movement of the spool..

In typical industrial usage as an actuator controlling combustion instability or dynamic compressor stall, the mean spool position is half open ($x_{sp} = 50\,\%$).
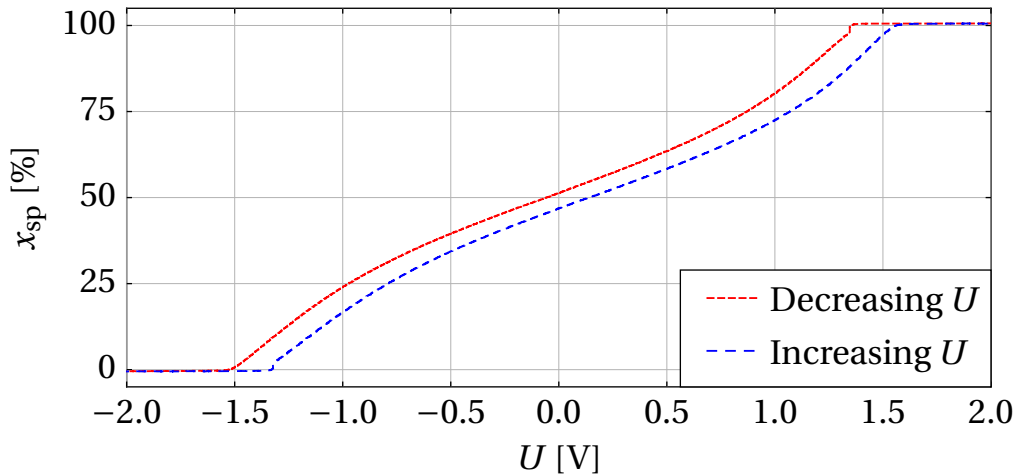
Figure 5.3: Hysteresis of (slowly varying) spool position as a function of input voltage. $x_{sp} = 0\%$ and $x_{sp} = 100\%$ are determined by the hard ends. At the $x_{sp} = 0\%$ there is still some flow possible through the valve (see sec. 5.3.2.1).

The spool oscillates harmonically around this position. The average flow is usually set by another valve in a slow feedback loop. This way, the DDV can remain half-open, independent of throughflow. Hermann and Orthmann[112] used the valve to modulate the fuel supply of the pilot flame of 24 burners in a heavy duty gas turbine. This constitutes only a relatively small fraction of the total amount of fuel burned in the gas turbine. The amplitude of the actuation of the valve depends on the instability at hand.

5.3 Linear, quasi-steady, 1-D Model

In the duct systems where DDVs are typically applied, acoustic effects can be considered quasi 1-D. Since the cross-over frequency of the DDV lies around 500 Hz, its application and the scope of the model considered here are limited to frequencies below this value. The wave lengths associated with these frequencies are of the order of (deci)metres,while the dimensions of the valve are limited to millimetres or centimetres. Therefore the valve model will be formulated as acoustically compact and – in the absence of convected effects – quasi-steady.

The network modelling package taX deals with perturbation of a flow around a mean flow state. Quantities are written as a mean value, indicated by an over-bar ($\bar{\odot}$) plus a perturbation, indicated by a prime ($\odot'$). Pressure becomes $p = \bar{p} + p'$, velocity becomes $u = \bar{u} + u'$ etc.

The frequency domain solver of taX uses models which are linear in perturbation. Therefore, the valve model as an element in taX, must be linearised. Using the ideal gas law and Poisson's relation for calorically perfect gases $\rho = \bar{\rho} + \rho' = \bar{\rho} + p'/c^2$.

5.3.1 The mass equation

In the current valve, the volume of fluid inside the valve does not change under movement of the spool. Since the valve is acoustically compact as well, no mass is accumulated in the valve and the mass flow on inlet and outlet is the same ($[\dot{m}]_{\text{in}}^{\text{out}} = \left[A\,\rho\,u\right]_{\text{in}}^{\text{out}} = 0$). Linearising and subtracting the mean equation gives[213]

$$\left[A\left(\bar{\rho}\,u' + \bar{u}\,\rho'\right)\right]_{\text{in}}^{\text{out}} = 0 + \mathcal{O}\left(\rho'\,u'\right)$$

$$\left[A\left(\bar{\rho}\,u' + \bar{u}\,\frac{p'}{c^2}\right)\right]_{\text{in}}^{\text{out}} = 0$$

$$\left[A\bar{\rho}\left(u' + M\,\frac{p'}{\bar{\rho}\,c}\right)\right]_{\text{in}}^{\text{out}} = 0\,. \tag{5.1}$$

5.3.2 The momentum equation

The volume flow rate $\bar{\dot{V}}$ in steady state is described by the discharge coefficient of the valve $\bar{\mathcal{C}}_{\text{d}}$, where the outlet is taken as a reference point:

$$\bar{u}_{\text{out}} = \frac{\bar{\dot{V}}_{\text{out}}}{A_{\text{out}}} = \bar{\mathcal{C}}_{\text{d}}\sqrt{\frac{2}{\bar{\rho}_{\text{out}}}\left(\bar{p}_{\text{st,in}} - \bar{p}_{\text{st,out}}\right)}\,. \tag{5.2}$$

5.3.2.1 Measured steady discharge coefficient

The pressure drop was measured[*] as a function of throughflow, for consecutive spool positions $x_{\text{sp}} = 10, 20, \ldots, 100\,\%$. The results, non-dimensionalised as the

---

[*] Loss in static pressure, not total pressure was measured. The difference is insignificant for the current.

discharge coefficient $\mathcal{C}_d$ and the Reynolds number Re, are plotted in the upper graph of fig. 5.4. The discharge coefficient is weakly dependent on the flow rate. Under turbulent flow conditions, it is common for valves and orifices to show a power-law relation between flow rate and pressure drop.[54: p.2-7, 227] Therefore it seems appropriate to express the variation of $\mathcal{C}_d$ as a power function of Reynolds number Re.
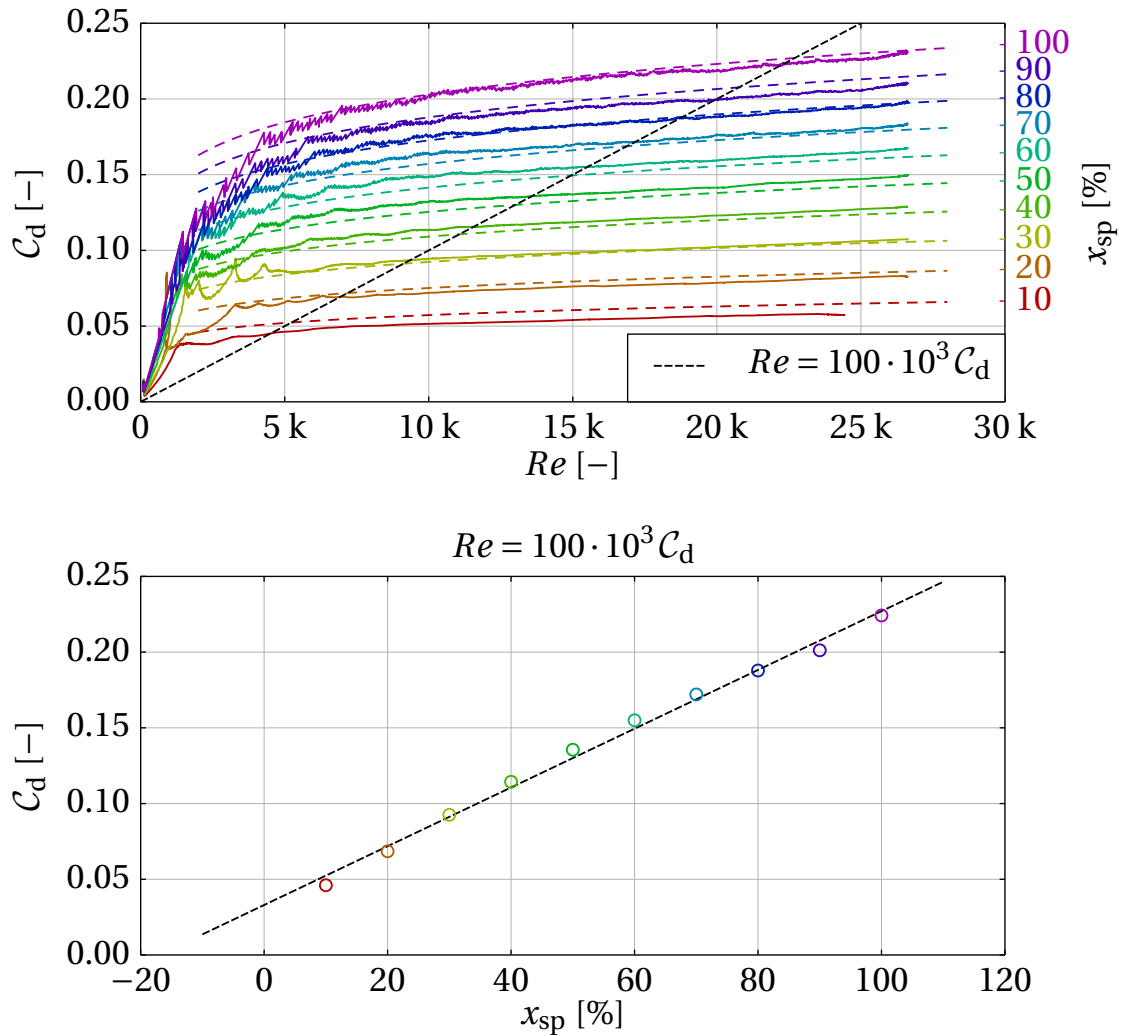
Figure 5.4: Trends of the discharge coefficient $\mathcal{C}_d$ as function of valve opening x_{sp} and throughflow, based on measurement data from Kaiser[130] (above). According to the specification by the producer, $\mathcal{C}_d$, at constant outlet pressure, should depend linearly on x_{sp}. The graph below show this is indeed the case, although there is an offset.

According to specification by the manufacturer,[179] at a constant pressure drop, the steady state mass flow rate through the valve depends linearly on the spool position x_{sp}. Constant pressure drops (where Re is proportional to $\mathcal{C}_d$) are found along lines through the origin of the axes, e.g. the diagonal dashed line in the upper graph of fig. 5.4. If the curves $\mathcal{C}_d(Re)$ for constant x_{sp} are individually curve-fitted by power-law functions, these cross the diagonal line at the points plotted in the lower graph. This plot shows indeed, that $\mathcal{C}_d$ depends linearly on the spool position x_{sp}, when the pressure drop is kept constant. Combining this linearity with the power-law behaviour gives the trend lines in the upper figure.

5.3.2.2 Unsteady momentum equation

To use the valve model in an acoustic network model, two effects need to be considered. Firstly, the spool position is allowed to oscillate around a mean value, thus the valve acts as an acoustic source. Secondly, when the valve is nearly closed, the flow accelerates through the contraction between bushing and spool, which can be modelled as a lumped acoustical inertance, after Hirschberg and Rienstra.[117] With Δp_{st} as dependent variable and adding the inertia term, rewriting eq. (5.2) leads to a formulation for the dynamic behaviour of the valve

$$\Delta p_{st} = p_{in} - p_{out} + \frac{1}{2}\rho_{out}\left(u_{in}^2 - u_{out}^2\right)$$

$$= \mathcal{C}_d^{-2}\frac{\rho}{2}u^2 + \rho L_{kin}\mathrm{d}_t u\,, \tag{5.3}$$

where $\mathcal{C}_d$ is now a quasi-steady function of time. Inertia is modelled by the term on the far right. The equivalent length L_{kin} represents the length of a duct with the same amount of kinetic energy (for a certain throughflow) as the true geometry, but with constant cross section. Assuming homogeneous density throughout the constriction, $u(x) = \dot{m}/(\rho_{ref}A(x))$. L_{kin} can now be expressed as

$$L_{kin} = \frac{\int \frac{1}{2}\rho_{ref}u(x)^2 A(x)\,\mathrm{d}x}{\left[\frac{1}{2}\rho u^2 A\right]_{ref}} = \int \frac{A_{ref}}{A(x)}\,\mathrm{d}x\,. \tag{5.4}$$

Though the form of this equation is relatively simple, it requires an expression for the cross-sectional area as a function of stream-wise coordinate x. Considering the geometry of the ducts in fig. 5.1, this expression is not obvious. To

find an approximation of L_{kin}, a simplified geometry was defined, shown in fig. 5.5.
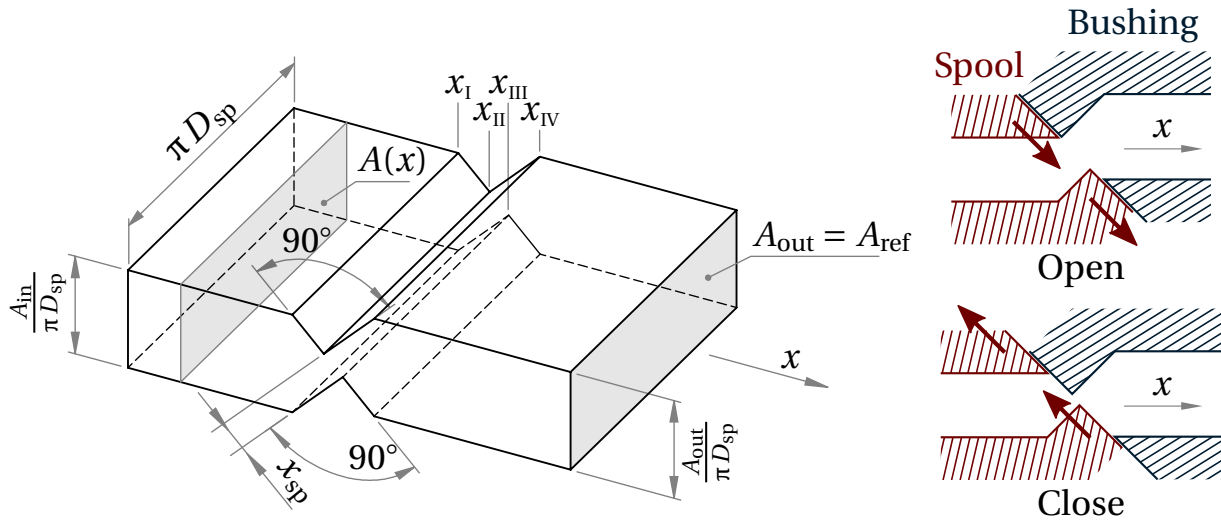
Figure 5.5: Simple geometry, used as an approximation of the fluid at the constriction of the valve. The inlet and outlet ducts (subscript 'in' and 'out') do not need to be equal in cross-sectional area.

This simplified geometry represents a 'rolled out' version of the annular constriction between the spool and the surrounding bushing. It models the basic characteristics of the flow through the aperture of the valve: the flow converges at a 90° angle, while the ridges are offset by a distance of x_{sp}. Also, opening and closing the valve does not change the volume of the fluid.

The contraction is modelled with zero volume, since the flow volume is modelled as part of the in-and outlet ducts. The additional inertia caused by the restriction, is therefore the surplus of inertia compared to that represented by the inlet and outlet ducts. Figure 5.6 expresses this concept graphically.

Closing the physical valve does not change the fluid volume. To keep the volume inside the simplified geometry constant as well, the contraction becomes longer when the valve is closed, and shorter when the valve is opened.
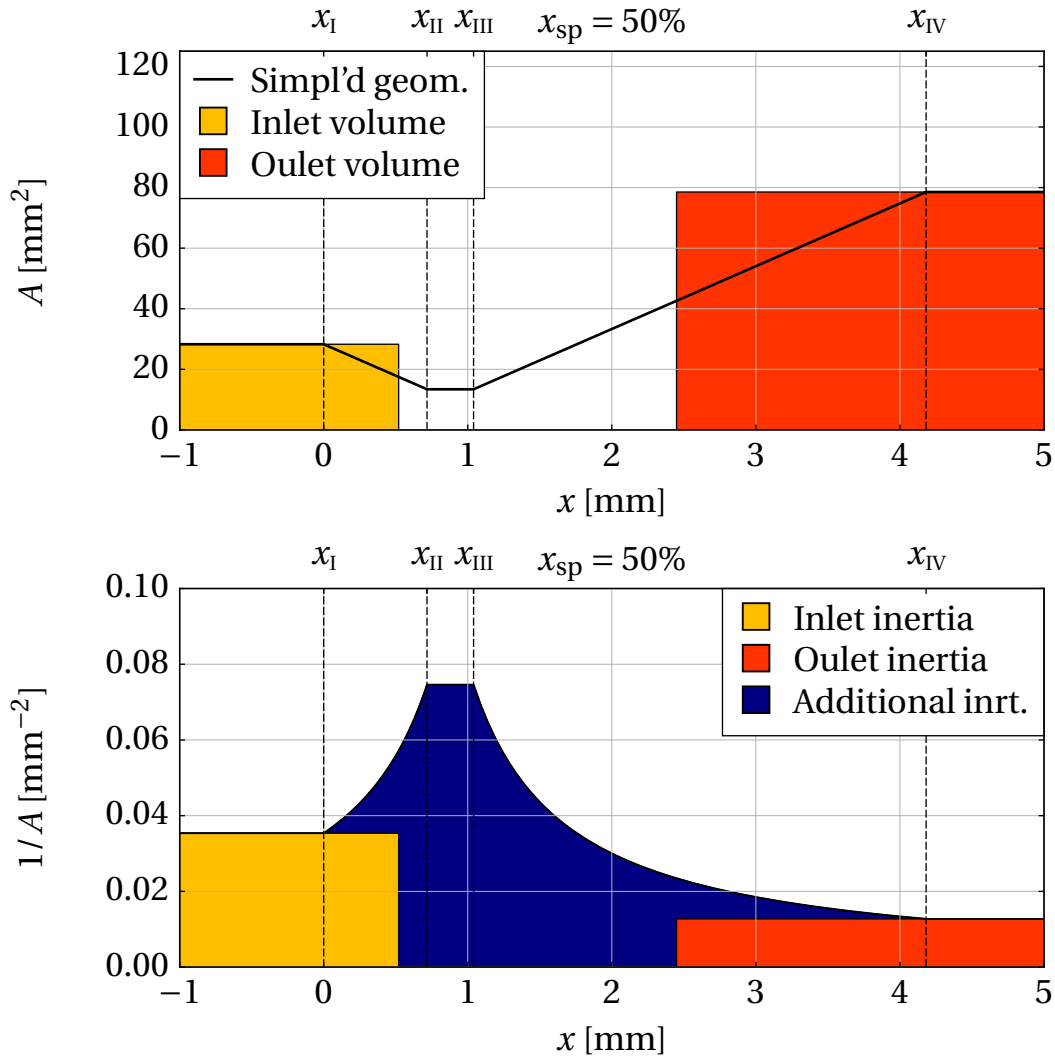
Figure 5.6: The volume of the fluid inside the inlet and outlet duct of the valve is modelled by the elements representing those ducts. The additional inertia (compared to the undisturbed inertia of the inlet and outlet ducts) due to the constriction is added in terms of an equivalent length L_{kin}. The figure on top shows how the volume of the simplified valve geometry is redistributed amongst the in- and outlet ducts. The corresponding inertia distribution is shown below. The rectangular parts on the left and right are modelled as part of inlet and outlet ducts respectively, while the blue area in the middle has to be added to the valve model explicitly.
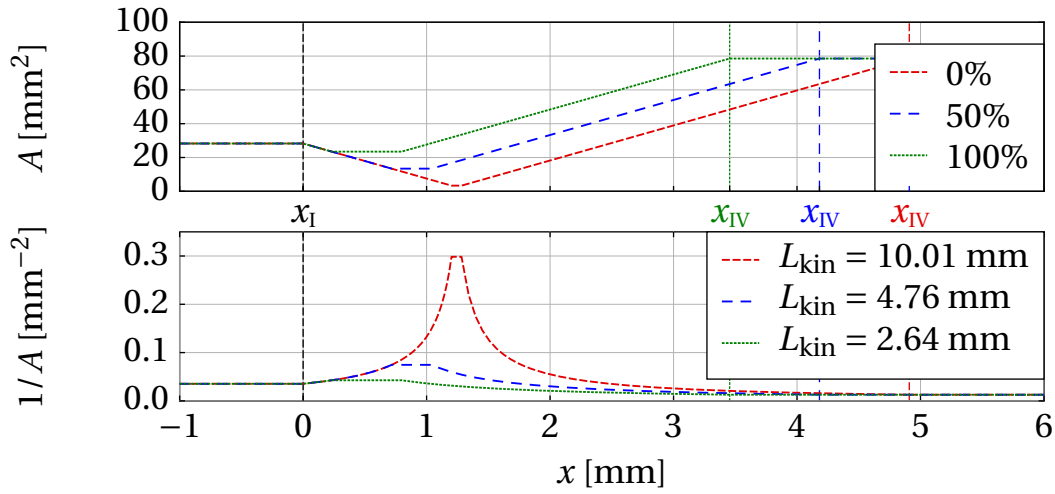
Figure 5.7: $A(x)$ and L_{kin} for different degrees of valve opening.

This is shown in fig. 5.7. The expression for the equivalent length L_{kin}, can be evaluated as

$$L_{\text{kin}} = L_{\text{kin,tot}} - L_{\text{kin,in}} - L_{\text{kin,out}}$$

$$= A_{\text{ref}} \int_{\text{I}}^{\text{IV}} \frac{1}{A(x)}\,\mathrm{d}x - \frac{x_{\text{III}} - x_{\text{I}}}{2\,A_{\text{in}}} - \frac{x_{\text{IV}} - x_{\text{II}}}{2\,A_{\text{out}}}$$

$$= \frac{A_{\text{ref}}}{2\,\pi\,D_{\text{sp}}} \ln \frac{A_{\text{in}}\,A_{\text{out}}}{A_{\text{min}}^2}\;.$$

In reality the valve will not be operated when fully closed, since then the flow could not be modulated any more. For the current DDV, L_{kin} is estimated in the order of millimetres for all practical applications. In reality L_{kin} would be somewhat larger, due to flow separation and jet formation, but still much smaller than the other relevant lengths in the system. Therefore, L_{kin} can safely be neglected. For geometries where this inertia is relevant, it can be added as a separate element in the network model.

5.3.2.3 Linearised fluctuating hydraulic resistance

taX requires its components to be linearised and formulated in terms of the characteristic wave amplitudes $f = \frac{1}{2}\left(p'/(\rho\,c) + u'\right)$ and $g = \frac{1}{2}\left(p'/(\rho\,c) - u'\right)$. Firstly, the dynamic variables are expressed in the form of a steady mean value

plus a fluctuation. This fluctuation is assumed to be small compared to the average, so that terms of the order of fluctuations squared can be neglected.

Leaving out the L_{kin} term, linearising $p = \bar{p} + p'$, $\rho = \bar{\rho} + p'/c^2$, $\mathcal{C}_{\text{d}} = \bar{\mathcal{C}}_{\text{d}} + \mathcal{C}'_{\text{d}}$ and $u = \bar{u} + u'$, and subtracting the steady solution, eq. (5.3) becomes

$$p'_{\text{in}} + \bar{\rho}_{\text{in}}\,\bar{u}_{\text{in}}\,u'_{\text{in}} = p'_{\text{out}} - \bar{\mathcal{C}}_{\text{d}}^{-2}\,\bar{\rho}_{\text{out}}\,\bar{u}_{\text{out}}^2\,\frac{\mathcal{C}'_{\text{d}}}{\bar{\mathcal{C}}_{\text{d}}} + \left(1 + \bar{\mathcal{C}}_{\text{d}}^{-2}\right)\bar{\rho}_{\text{out}}\,\bar{u}_{\text{out}}\,u'_{\text{out}}$$

$$+ \mathcal{O}\left(M^2, \text{perturbations}^2\right)$$

Dividing by $\bar{\rho}_{\text{out}}\,c_{\text{out}}$, and substituting $\bar{\mathcal{C}}_{\text{d}}^{-2} = \zeta$ and $\bar{u} = c\,M$ gives

$$\underbrace{\frac{p'_{\text{out}}}{\bar{\rho}_{\text{out}}\,c_{\text{out}}} - \frac{p'_{\text{in}}}{\bar{\rho}_{\text{out}}\,c_{\text{out}}}}_{\text{pressure difference}} + \underbrace{(1+\zeta)\,M_{\text{out}}\,u'_{\text{out}} - \frac{\bar{\rho}_{\text{in}}\,c_{\text{in}}}{\bar{\rho}_{\text{out}}\,c_{\text{out}}}\,M_{\text{in}}\,u'_{\text{in}}}_{\text{steady resistance, acceleration}} = \underbrace{\zeta\,M_{\text{out}}^2\,c_{\text{out}}\,\frac{\mathcal{C}'_{\text{d}}}{\bar{\mathcal{C}}_{\text{d}}}}_{\text{source term}}. \quad (5.5)$$

The momentum and mass equations are rewritten as a matrix equation in terms of the characteristic wave amplitudes. The resulting matrix can then be used to characterise the valve element in the network model taX.

5.4 Comparison to experiment

5.4.1 Practical restrictions

The acoustic behaviour of the valve is characterised by six transfer functions, relating two outputs – upstream and downstream outgoing waves – to three inputs – upstream and downstream incoming waves, and actuation of the valve (see the block labelled 'Valve element' in fig. 5.8). Ideally, the model formulated before would be validated against an independent measurement of all these transfer functions. Unfortunately, this is not possible with the current valve, since there is no sensor access to the duct connecting the decoupler volume to the inlet of the valve, and this duct is impractically short to accommodate such access. The best that currently can be done is a determination of the reflection and source coefficients of the system consisting of the valve combined with the inlet duct and decoupler volume. Figure 5.8 shows an overview of this system. The inlet duct is characterised by two transmission coefficients, $\mathcal{D}_f$ and $\mathcal{D}_g$,

which are assumed to be pure delays. The reflection coefficient of the volume, $\mathcal{R}_{\text{ca}}$, is assumed to be $(1-M)/(1+M)$, based on acoustical energy conservation. The total reflection and source coefficients of this acoustical subsystem will be referred to as $\mathcal{R}_{\text{sys}}$ and $\mathcal{S}_{\text{sys}}$ respectively. The model coefficients $\mathcal{T}_{f}$, $\mathcal{T}_{g}$, $\mathcal{R}_{\text{in}}$, $\mathcal{R}_{\text{out}}$, $\mathcal{S}_{\text{in}}$ and $\mathcal{S}_{\text{out}}$ are derived from the expressions derived in sec. 5.3. These coefficients are evaluated numerically, since the algebraic expressions would be unwieldily long. The full system shown in fig. 5.8 is described by the following matrix equation:

$$
\begin{bmatrix}
0 & (\mathcal{D}_{g}\mathcal{R}_{\text{ca}}\mathcal{D}_{f}) & 0 & 0 & 0 \\
\mathcal{R}_{\text{in}} & 0 & 0 & \mathcal{T}_{g} & \mathcal{S}_{\text{in}} \\
\mathcal{T}_{f} & 0 & 0 & \mathcal{R}_{\text{out}} & \mathcal{S}_{\text{out}}
\end{bmatrix}
\begin{bmatrix}
f_{\text{in}} \\
g_{\text{in}} \\
f_{\text{out}} \\
g_{\text{out}} \\
x'_{\text{sp}}
\end{bmatrix}
=
\begin{bmatrix}
f_{\text{in}} \\
g_{\text{in}} \\
f_{\text{out}}
\end{bmatrix},
$$

where f_{out} can be expressed as a function of g_{out} and x'_{sp}:

$$
f_{\text{out}} = \underbrace{\left(\frac{\mathcal{T}_{f}\mathcal{D}_{g}\mathcal{R}_{\text{ca}}\mathcal{D}_{f}\mathcal{T}_{g}}{1 - \mathcal{R}_{\text{in}}\mathcal{D}_{g}\mathcal{R}_{\text{ca}}\mathcal{D}_{f}} + \mathcal{R}_{\text{out}} \right)}_{\mathcal{R}_{\text{sys}}} g_{\text{out}} + \underbrace{\left(\frac{\mathcal{T}_{f}\mathcal{D}_{g}\mathcal{R}_{\text{ca}}\mathcal{D}_{f}\mathcal{S}_{\text{in}}}{1 - \mathcal{R}_{\text{in}}\mathcal{D}_{g}\mathcal{R}_{\text{ca}}\mathcal{D}_{f}} + \mathcal{S}_{\text{out}} \right)}_{\mathcal{S}_{\text{sys}}} x'_{\text{sp}} . \quad (5.6)
$$
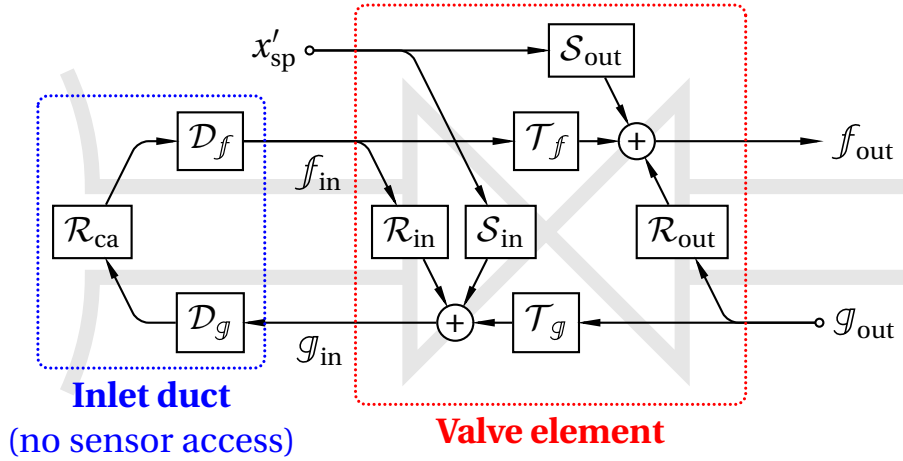
Figure 5.8: Overview of acoustic transfer functions and the three measurable signals x'_{sp}, f_{out} and g_{out}.

5.4.2 Measurement and signal analysis

The characteristic wave amplitudes are determined by the well known two-microphone method, described in sec. 4.3.[247] To separate the source term and the reflection coefficient, two independent acoustic sources are needed.[191] For this measurement an additional loudspeaker was used. Figure 5.9 shows the experimental set-up.

Introducing the superscript ('ls') to identify quantities correlated to loudspeaker excitation, and ('vl') to indicate quantities correlated to valve excitation, the two-state approach is written as

$$
\begin{bmatrix} f_{\mathrm{out}}^{(\mathrm{vl})} \\ f_{\mathrm{out}}^{(\mathrm{ls})} \end{bmatrix} = \begin{bmatrix} \mathcal{R}_{\mathrm{sys}} & \mathcal{S}_{\mathrm{sys}} & \cdot & \cdot \\ \cdot & \cdot & \mathcal{R}_{\mathrm{sys}} & \mathcal{S}_{\mathrm{sys}} \end{bmatrix} \begin{bmatrix} g_{\mathrm{out}}^{(\mathrm{vl})} \\ x_{\mathrm{sp}}'^{(\mathrm{vl})} \\ g_{\mathrm{out}}^{(\mathrm{ls})} \\ x_{\mathrm{sp}}'^{(\mathrm{ls})} \end{bmatrix} ,
\tag{5.7}
$$

where $x_{\mathrm{sp}}'^{(\mathrm{ls})} = 0$, since the valve opening x_{sp} is constant when the loudspeaker is used for actuation. Solving eq. (5.7) gives the expressions for $\mathcal{R}_{\mathrm{sys}}$ and $\mathcal{S}_{\mathrm{sys}}$ (similar to Bothien et al.[32: §2.2]):

$$
\mathcal{R}_{\mathrm{sys}} = \frac{f_{\mathrm{out}}^{(\mathrm{ls})}}{g_{\mathrm{out}}^{(\mathrm{ls})}}
\tag{5.8}
$$

and

$$
\mathcal{S}_{\mathrm{sys}} = \frac{f_{\mathrm{out}}^{(\mathrm{vl})} - g_{\mathrm{out}}^{(\mathrm{vl})} \mathcal{R}_{\mathrm{sys}}}{x_{\mathrm{sp}}'} .
\tag{5.9}
$$
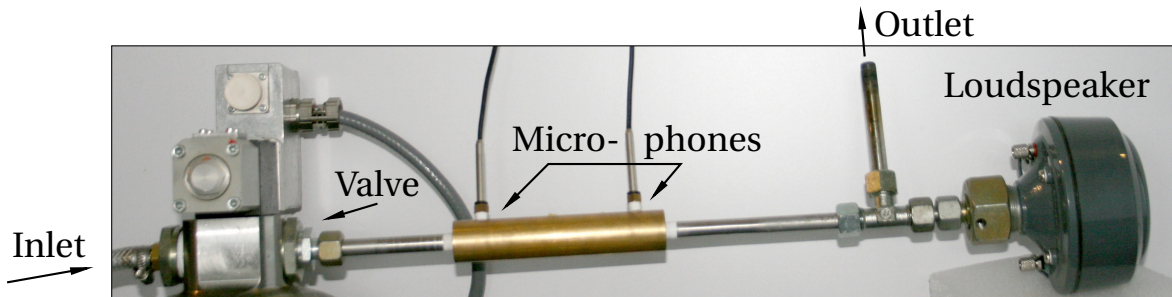
Figure 5.9: Experimental set-up for measurement of the reflection coefficient $\mathcal{R}_{\mathrm{sys}}$ and source strength $\mathcal{S}_{\mathrm{sys}}$ of the valve.

5.4.3 Experimental cases

Measurements were done with varying air throughflows, as well as with different values of valve opening, listed in tbl. 5.1. For all cases the transfer function relating pressure fluctuation to valve opening variation was determined in Pascal per percent opening fluctuation (Pa/%). Subsequently, the two-microphone method Seybert and Ross[247] was used to find the transfer function relating the characteristic wave amplitudes to valve opening variation, from which the system coefficients were determined as discussed before.

Case	$\dot{n}$ SLPM	$\dot{m}$ g/s	$\bar{x}_{sp}$	$\bar{C}_d$	Δp (Pa)	M_{out}	Re
n020-x050	20	0.33	50%	0.106	1091	0.0132	3236
n040-x025			25%	0.077	8207		
n040-x050	40	0.67	50%	0.117	3609	0.0263	6471
n040-x075			75%	0.154	2073		
n080-x050	80	1.33	50%	0.128	11940	0.0526	12943
n160-x050	160	2.67	50%	0.141	39500	0.1053	25885

Table 5.1: Overview of investigated operating conditions.

5.4.4 Low-frequency limit

In the quasi-steady limit, and with L_{kin} much smaller than relevant geometric lengths, eqs. (5.1) and (5.3) are frequency-independent. Since these equations contain no complex numbers either, the acoustical coefficients describing the valve are real functions of the steady conditions. Figure 5.10 shows how these quantities vary as a function of valve throughflow, when the valve is opened 50% on average. Figure 5.11 shows the variation as a function of valve opening, at 40 SLPM throughflow. The low frequency limits of $\mathcal{R}_{sys}$ and $\mathcal{S}_{sys}$ – the quantities which can be measured experimentally for not too low frequencies – are given for comparison.

The influence of an increase in throughflow is similar to that of a decrease in opening. In both cases the flow velocity through the constriction increases, increasing the acoustical stiffness of the valve.
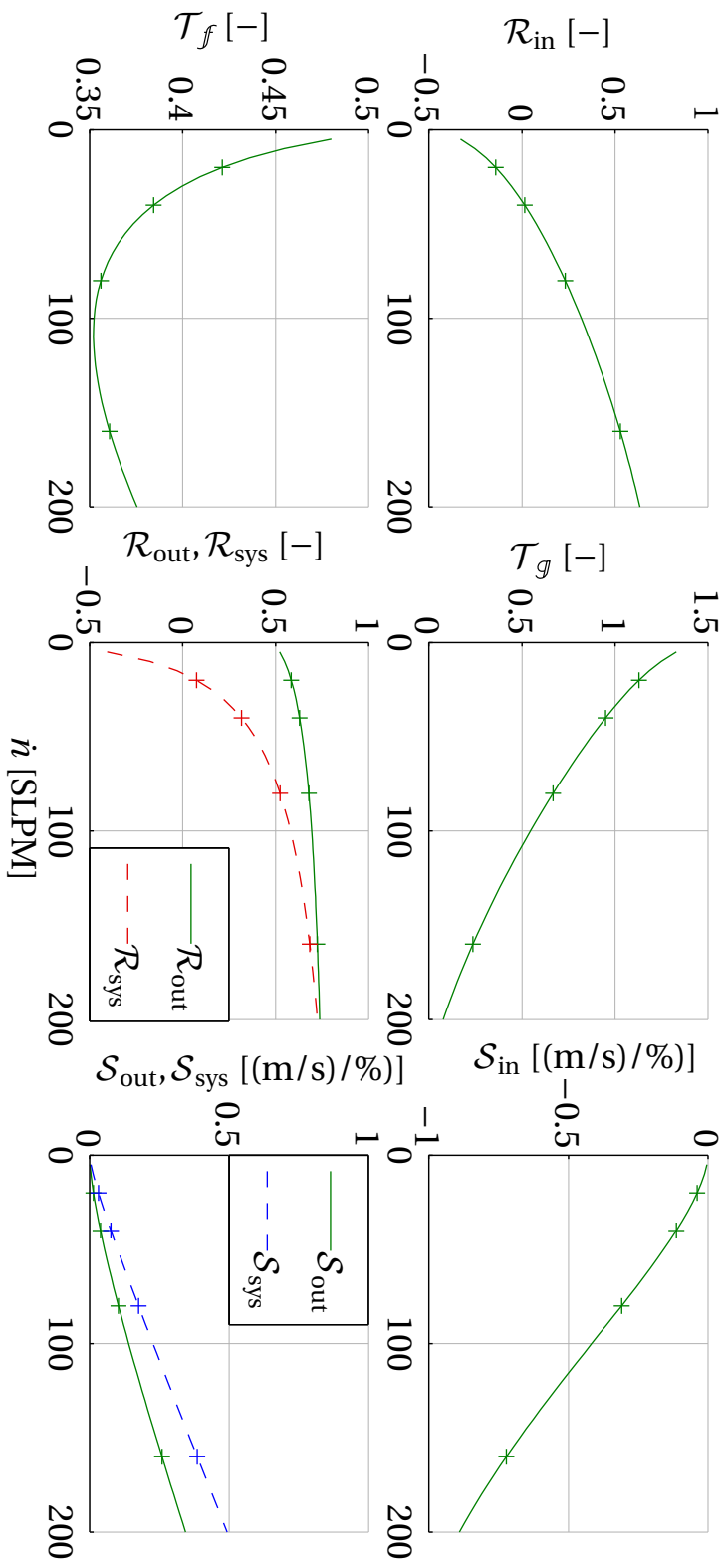
Figure 5.10: Modelled transfer functions, according to eqs. (5.1) and (5.5), as function of throughflow $\dot{n}$ in standard litre per minute (SLPM). Mean valve opening $\bar{x}_{sp} = 50\,\%$. Markers indicate operating points listed in tbl. 5.1.
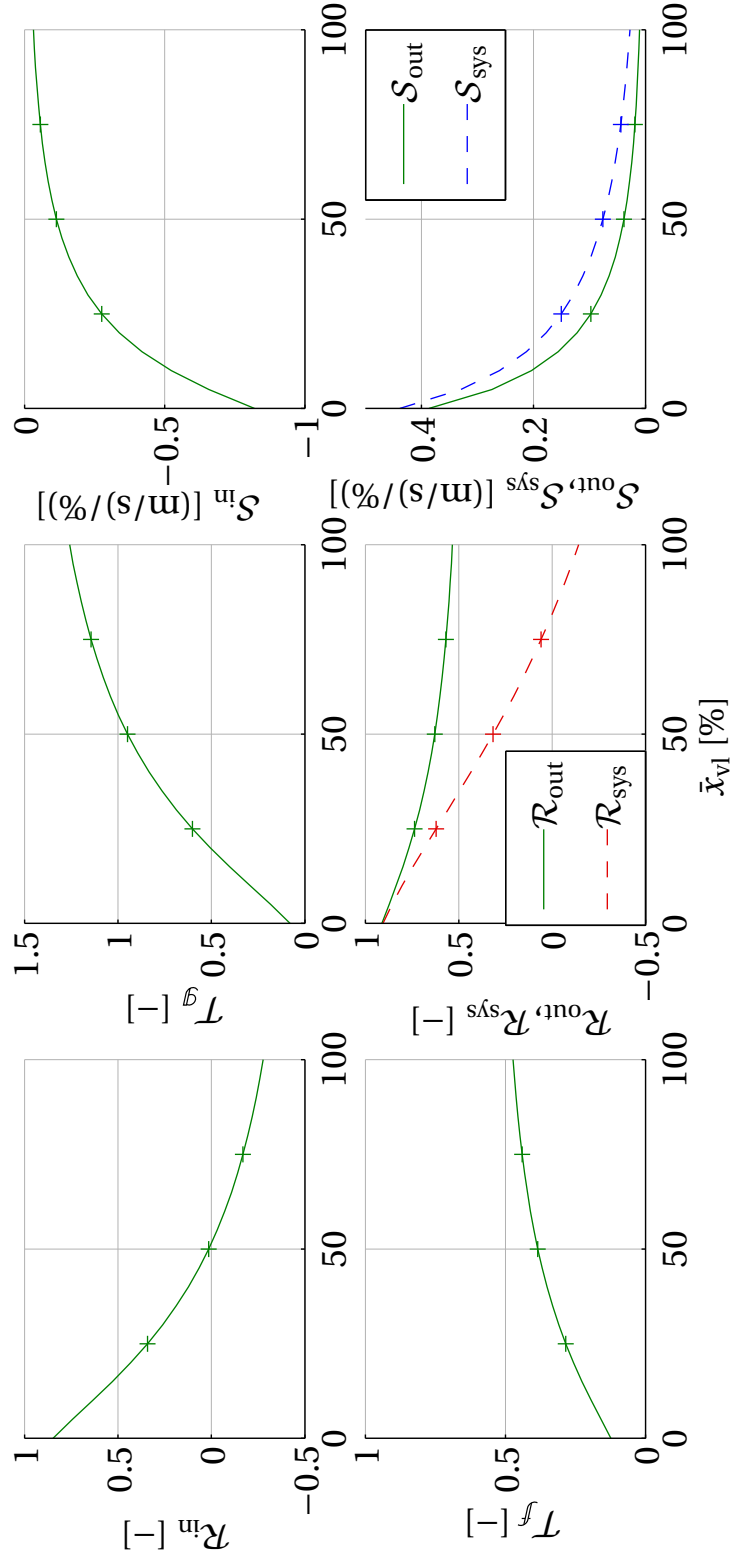
Figure 5.11: Modelled transfer functions, according to eqs. (5.1) and (5.5), plotted against mean valve opening $\bar{x}_{\mathrm{sp}}$ in percent. Throughflow $\dot{n}=40\,\mathrm{SLPM}$. Markers indicate operating points listed in tbl. 5.1.

When the inlet and outlet tubes are of the same size (i.e. $D_{in} = D_{out}$, not shown) all quantities vary between 0 and 1, except for $\mathcal{S}_{in}$ which is negative. As far as the passive coefficients are concerned, this intuitively corresponds to the valve acting like a zero-length tube, a complete acoustical blockage, or something in between. The absolute values of the source coefficients accidentally lie between 0 and 1, due to on the choice of units. The source term on the outlet side is slightly larger in absolute value.

Currently $D_{in} = 6\,\text{mm}$ and $D_{in} = 10\,\text{mm}$, so $D_{in} < D_{out}$. In this case, the valve with large opening, or little throughflow approaches the behaviour of an area discontinuity. $\mathcal{T}_g$ can for example exceed unity, and approaches 2 as D_{in}/D_{out} goes to zero.[116: §5.3] $\mathcal{R}_{in}$ can be less than zero, when the combined impedance – of the valve plus the outlet duct – is less than the impedance of the inlet duct. The source term is greater on the side with larger diameter.

5.4.5 Frequency dependence

Figure 5.12 gives an overview of the measured reflection coefficient and source term, compared to prediction. The lower limit of the frequency range for this measurement is caused by the loudspeaker, which does not excite efficiently enough below 100 Hz. The high frequency limit of the measurement is determined by the valve, which can only be operated up to around 500 Hz.

The predicted reflection starts at the positive real axis and curves up to the right for increasing frequency. Intuitively, this can be understood as direct reflection from the valve, plus a delayed open end, i.e. the reflection of the decoupler. The measured reflection coefficient shows similar trends depending on operating condition; reflection increases as the valve is closed, or as throughflow is increased. The low-frequency limit, which can be evaluated better from the bode plots in figs. 5.13 and 5.14, lie on the real axis. For cases n020-x050 and n040-x075, the reflection coefficient at low frequencies was predicted positive, while the measurements show a negative value. The phase is generally lower then predicted, and falls further for increasing frequency. The reason for this behaviour remains unknown.

The low-frequency limit of the source term is situated on the positive real axis; the flow increases when the valve is opened. Reflected waves from the decoupler have the same sign, with a small delay, and cause the curve down to the left as frequency increases. The magnitude of the source term increases
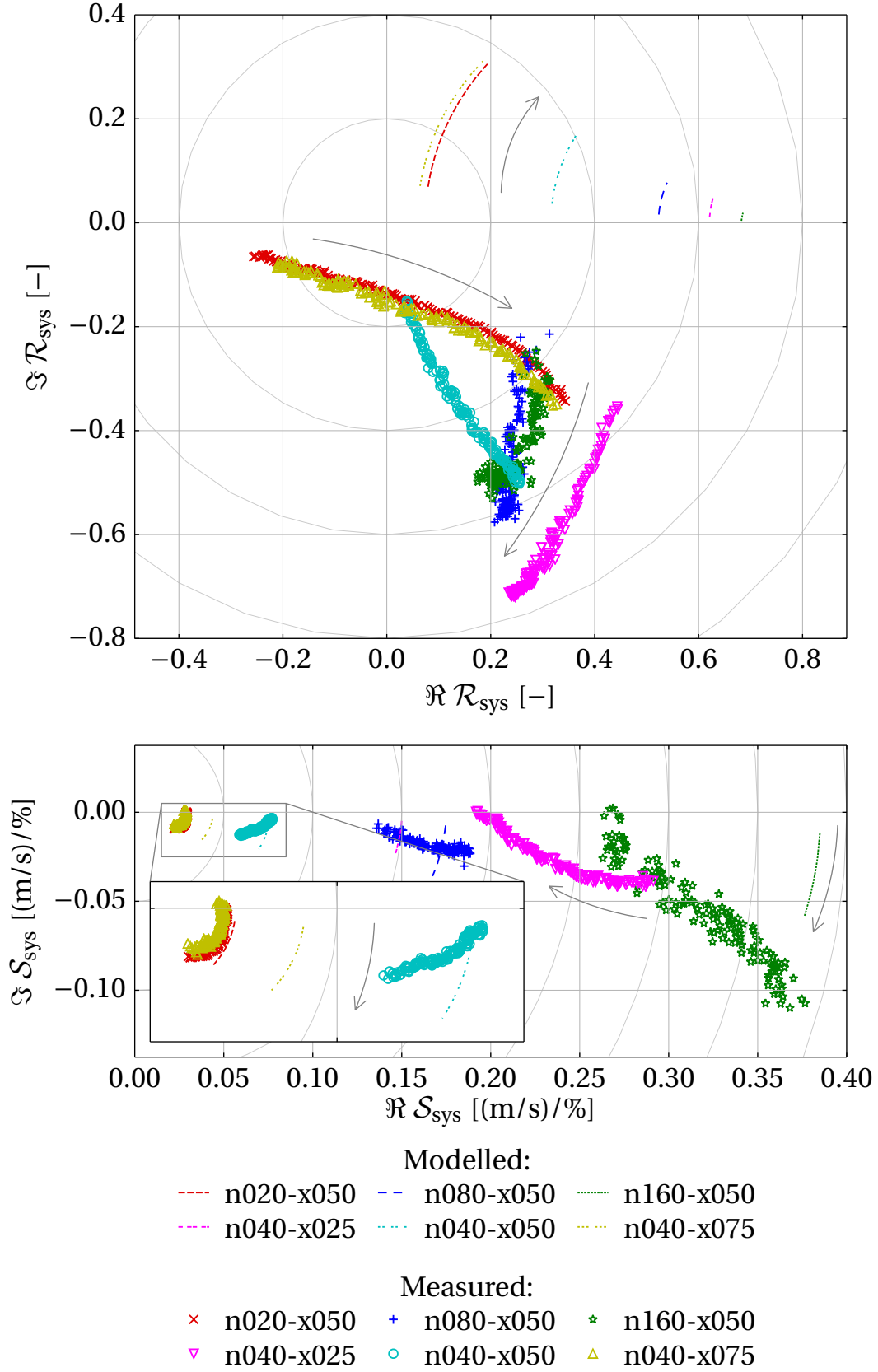
Figure 5.12: Reflection (above) and source term (below) of the system plotted in the complex plane, for frequency in the range $f \in [100, 500]$ Hz. Arrows indicate the direction of frequency dependence.

when the valve is closed, or when throughflow is increased. The predicted source term shows better agreement with experiment than the reflection coefficient. The main discrepancies are that the measured source terms show a greater dependence on valve opening, and in some cases an other behaviour for increasing frequency.
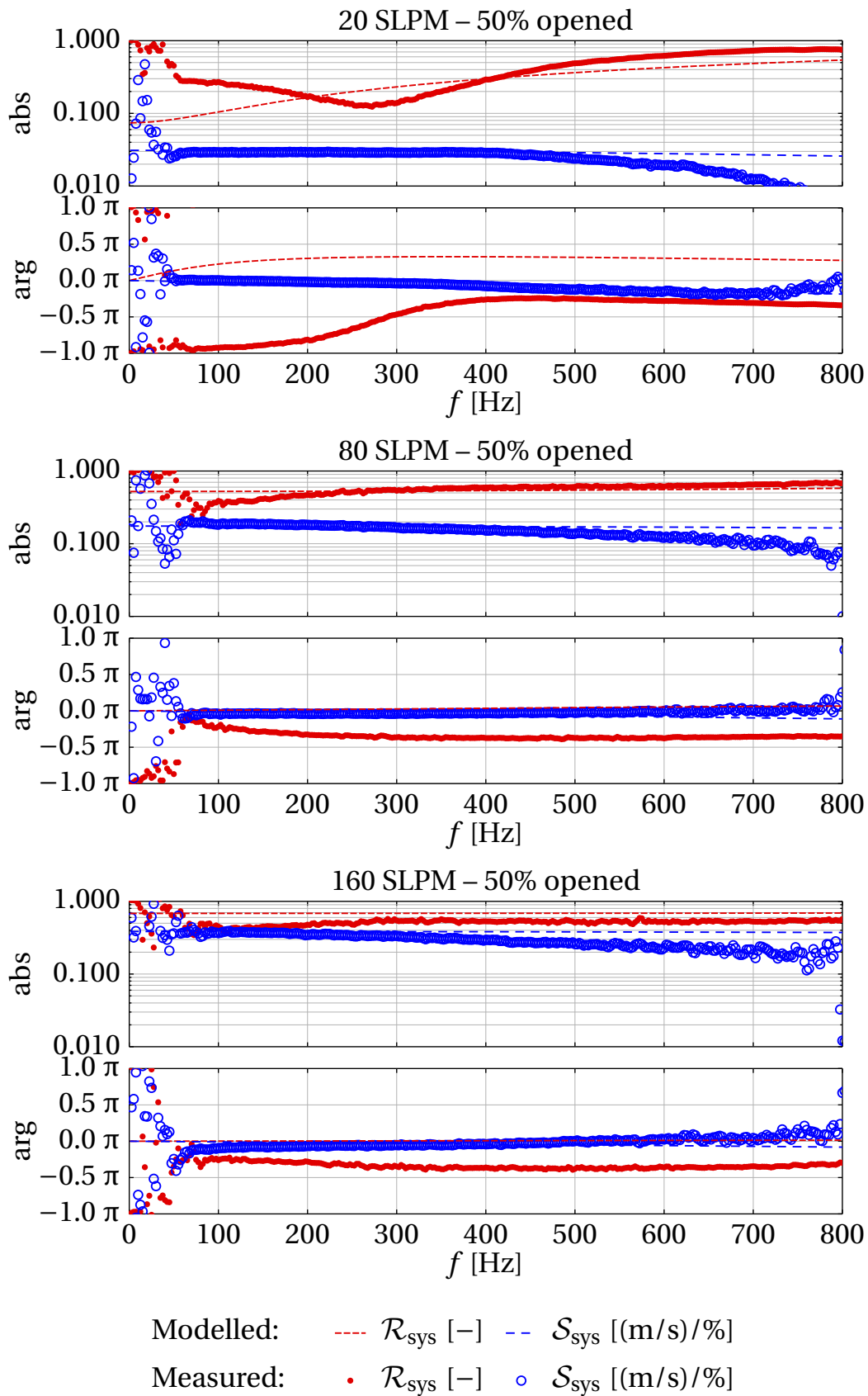
Figure 5.13: Model prediction of the transfer functions $\mathcal{S}_{\mathrm{sys}}$ and $\mathcal{R}_{\mathrm{sys}}$ of the valve, compared to measurement for various values of average through-flow in SLPM.
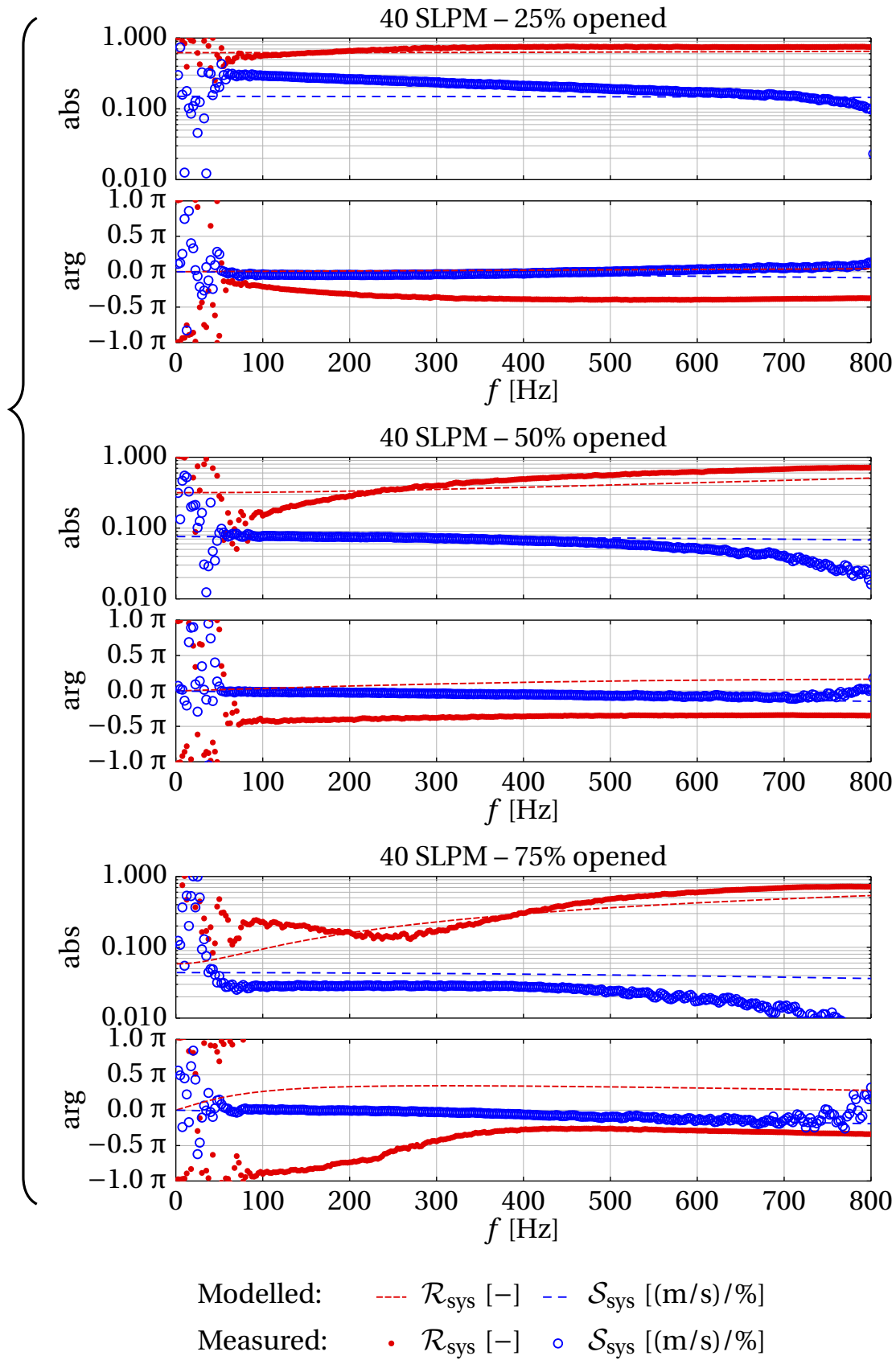
Figure 5.14: Model prediction of the transfer functions $\mathcal{S}_{\text{sys}}$ and $\mathcal{R}_{\text{sys}}$ of the valve, compared to measurement for various values of average valve opening $\bar{x}_{\text{sp}}$.

5.5 Implementation in a simplified fuel system

5.5.1 Set-up

To demonstrate the usability of the valve model in an acoustic network model, the set-up as shown in fig. 5.9 was modified. After removal of the tee-piece and the loudspeaker, what remains can be thought of as a simplified fuel system. The representation of this system in the network modelling programme taX is shown in fig. 5.15. An open inlet represents the decoupler. The valve element (labelled 'DDV') is accompanied by short ducts representing the inlet and outlet inside the bushing and decoupler. Additional inertia at the valve outlet is set to zero, as argued in sec. 5.3.2.2, but included for illustrative purposes. Ducts A, B and C together form the simplified fuel supply system. The two microphones measure the pressure fluctuation caused by the valve as before.

5.5.2 Results

The predicted and measured transfer functions are shown in figs. 5.16 and 5.17. Since the valve is predicted to behave similar to a closed end, and the exit is open, the resonances correspond to the 1/4 and 3/4 wave modes of the duct. For n020-x050 and n040-x075, where the valve, contradictory to the model, behaves more like an open end, the measured peaks in the transfer function are much more damped.

In general, the model gives a good impression of the order of magnitude of the flow modulation and pressure pulsation generated by the valve. It has to be remembered that the valve can hardly be operated above 500 Hz, so deviation from prediction at higher frequencies is not dramatic for application.

5.6 Comparison to loudspeaker

As argued in sec. 5.4.1, not all coefficients describing the valve model could be measured independently. Nonetheless, the current data suffice to make a comparison between a valve and a loudspeaker as acoustic actuators. In acoustical network modelling, loudspeakers are often assumed to behave like fluctuating volume sources, being 'much stiffer' than the medium involved,
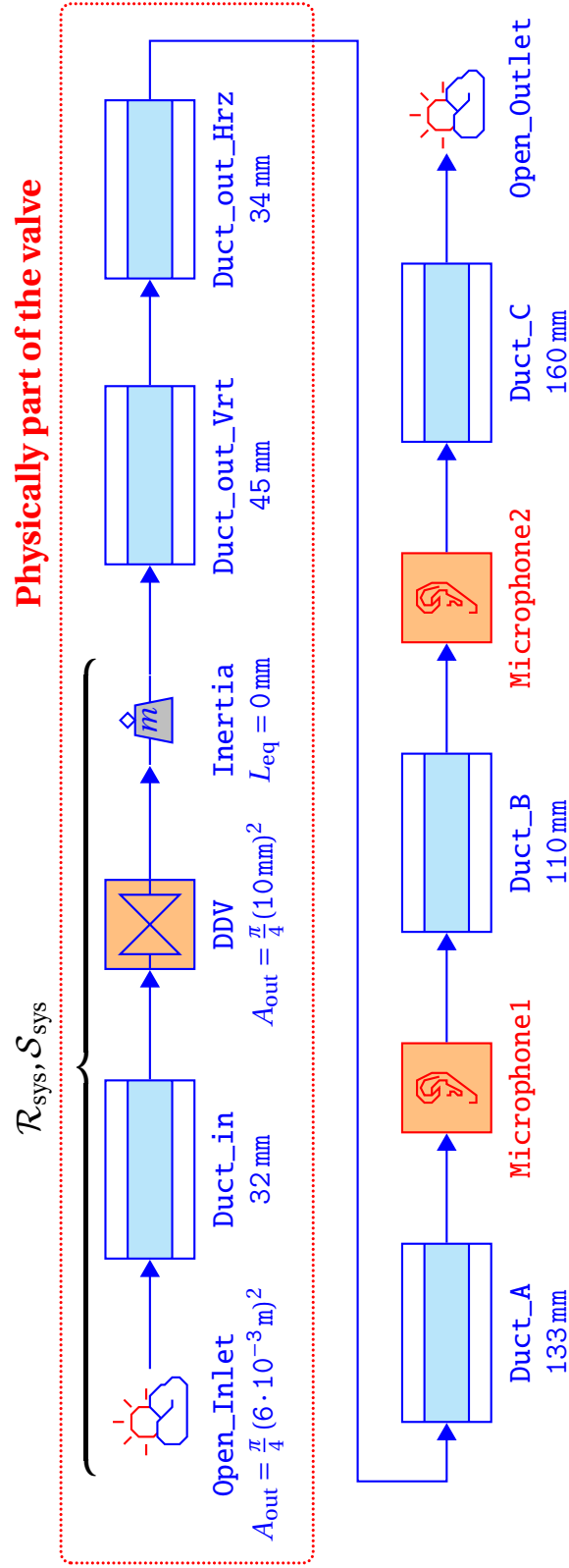
Figure 5.15: Representation of the simplified fuel system in taX: The six elements circled on the top of the taX model together represent the valve and decoupler. A simple duct with two microphones below complete this simplified fuel supply system.
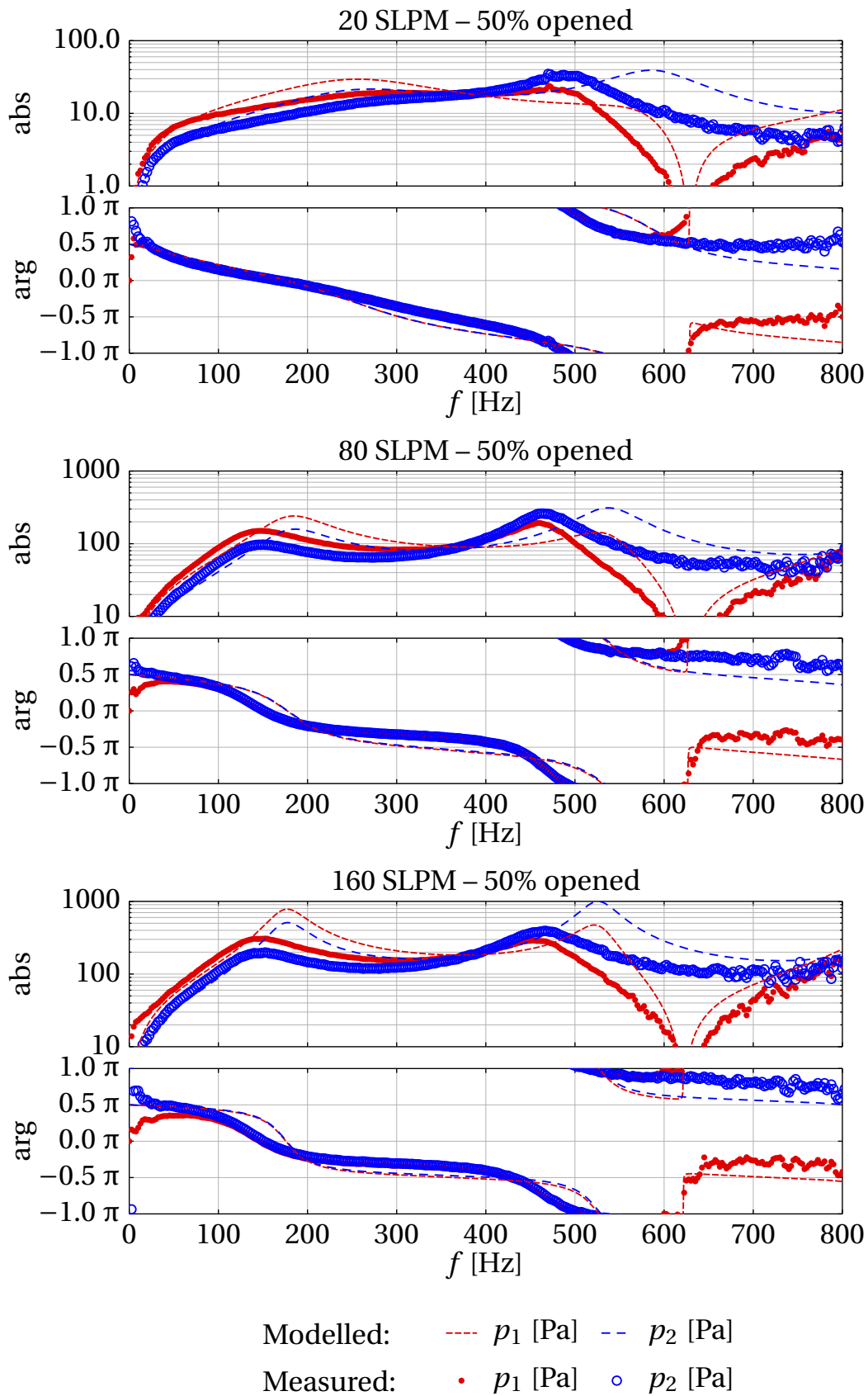
Figure 5.16: Model prediction of the pressure fluctuation caused by the valve, compared to measurement for various average flow rates $\dot{n}$ in SLPM.
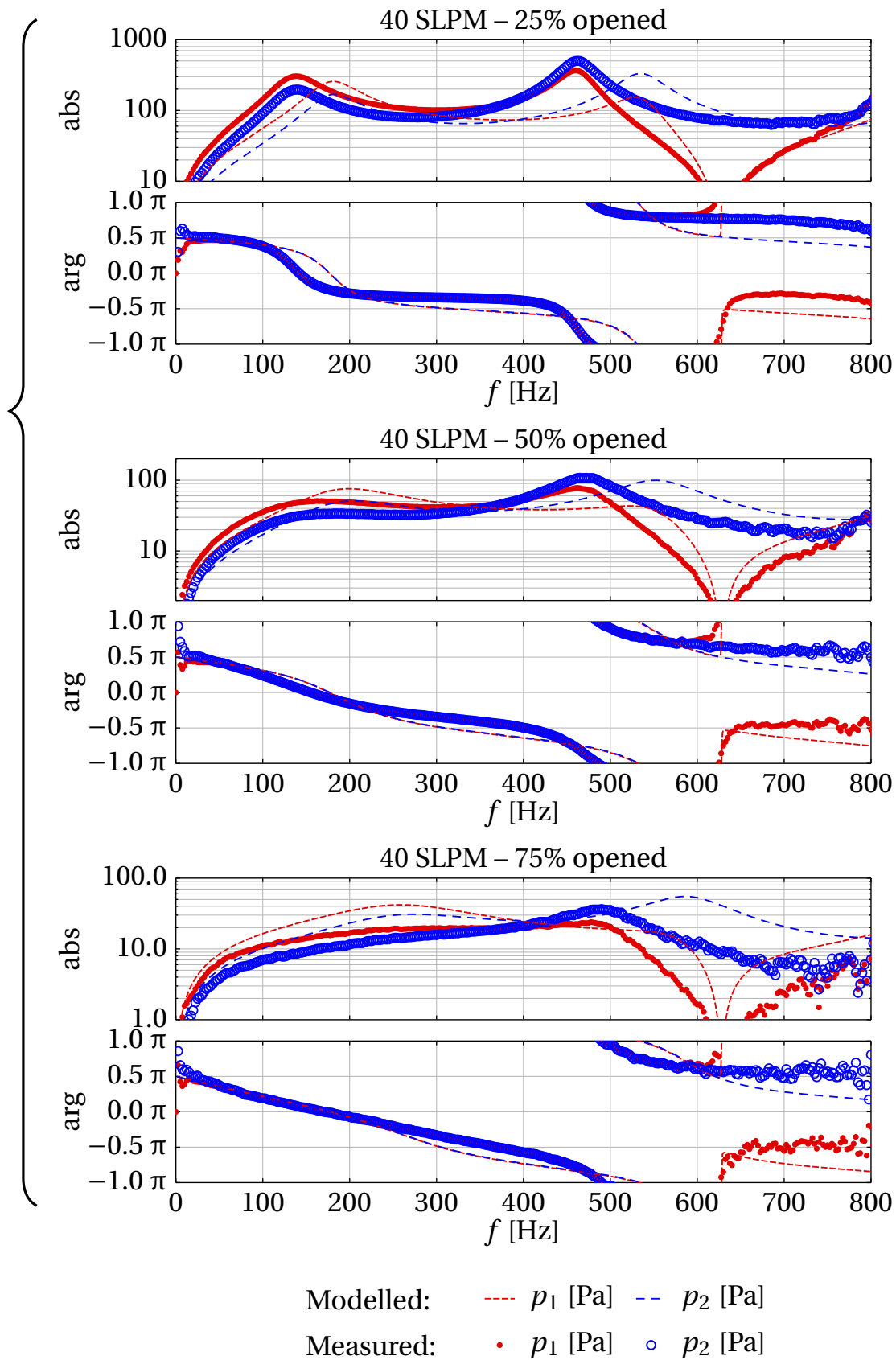
Figure 5.17: Model prediction of the pressure fluctuation caused by the valve, compared to measurement for various values of average valve opening $\bar{x}_{\mathrm{sp}}$.

and as such not reacting to pressure fluctuations.[9, 147] Although more advanced models exist,[168, 252, 270, 271] in first approximation for many relevant situations, a loudspeaker mounted at the end of a duct can be assumed to behave like a hard end and a constant source term in superposition.

The behaviour of the valve introduces much more damping. Figure 5.12 shows reflection coefficients varying between unity and zero. The measured reflection coefficient of the valve with decoupler was even negative for some operating conditions.

While the influence of the flow conditions on a loudspeaker are usually neglected, the behaviour of the valve depends strongly on these conditions. Both reflection and sound creation increase with throughflow, or reduction of the opening.

Finally, from a practical perspective, the volume modulated per cycle by a loudspeaker is limited by its geometry. For a valve on the other hand, the modulated volume is limited by its throughflow. Since throughflow per cycle increases for lower frequencies, a valve is a more effective actuator at lower frequencies.

When an upstream duct is modelled, another relevant difference between both actuators is that the loudspeaker behaves like a volume source, i.e. an acoustic monopole. The loudspeaker, on the other hand, modulates the pressure drop, and hence acts as an acoustic dipole.

5.7 Discussion and conclusion

The model presented in this chapter describes the basic characteristics of a DDV. Embedded in an acoustic network, it can give a good first prediction of the pressure amplitude caused by excitation by the valve. This can be used to predict the control authority, as introduced in sec. 1.6, of a control system using the valve as an actuator.

There remains a significant discrepancy in the prediction of the phase of the reflection coefficient $\mathcal{R}_{sys}$, shown in figs. 5.12 to 5.14. This discrepancy is largest for the low-frequency limit of the cases Q020-X050 and Q040-X075, where the absolute value of the reflection coefficient is relatively small. For other cases and frequencies the phase difference is less, but often still around $\pi/2$.

Equation eq. (5.6) gives $\mathcal{R}_{\mathrm{sys}}$ as the sum of $\mathcal{R}_{\mathrm{out}}$ and another term, involving the reflection at the decoupler, amongst others. Since both terms are nearly opposite in phase according to the model, it is to be expected that errors either one term can lead to large phase errors in $\mathcal{R}_{\mathrm{sys}}$. Which of the quantities mentioned in eq. (5.6) causes the discrepancy, can not be determined from the current measurements, since the valve assembly discussed in this paper did not allow for measurement of the acoustics upstream of the valve.

The assumption that the decoupler behaves like an open end does not cause the discrepancy. Network simulations with a Helmholtz resonator instead of an open end did not give better agreement.

Furthermore, acoustical influence of the corners and cross-sectional variation of the ducts inside the bushing of the valve is hard to predict, and harder to separate from other effects. For further improvement of the model, it would be advisable to test the model on a valve with a 'cleaner' and more accessible duct geometry.

This discussion does not differentiate between M and Re effects, since only one fluid (air) was used. The model could be improved, especially for application in fuel gas supply systems, by redoing the $\bar{\mathcal{C}}_{\mathrm{d}}$ measurements with another gas.

The (linear) model assumes the modulation of the discharge coefficient $\mathcal{C}'_{\mathrm{d}}$, which appears in the source term, to be small compared to the mean value $\bar{\mathcal{C}}_{\mathrm{d}}$. When $\mathcal{C}'_{\mathrm{d}}$ is increased to improve control authority over hard-to-control combustion instabilities, this assumption – needed for the linearisation – no longer holds.

The current model can be used in the initial stage of implementing a system for rapid flow control, and as such, speed up this phase of development.

6 Analysis of control authority

This chapter describes the results of active instability control (AIC) applied to the combustors Hummer and Limousine. In sec. 6.1 a comparison will be made between the valve and loudspeaker as actuators on the Hummer test rig. AIC was not effective on the Limousine rig.

Section 6.2 describes numerical simulations in ANSYS CFX, of both combustors with and without active control. The section has been submitted for publication as 'Control authority over a combustion instability investigated in CFD' in the International Journal of Spray and Combustion Dynamics (IJSCD).[189]

A preliminary investigation, concerning only the Limousine combustor was presented as 'CFD-based feasibility study of active control on a combustion instability' at the 20th International Congress on Sound and Vibration (ICSV20) in Bangkok, Thailand.[190] Robert Widhopf-Fenk made the controller algorithm available in a form that could be connected to CFX, and preliminary work by Constanze Temmler helped setting up the computations.

6.1 Analysis in experiment

6.1.1 Demonstration on the Hummer rig

The effect of active control was demonstrated in experiment on the Hummer combustor. To this end the test rig was equipped with actuators as shown in fig. 6.1. A direct dive valve (DDV), model D633E7320 by MOOG Inc.[179] is mounted on one side of the fuel supply, and a horn driver unit, KU-516 by Monacor International,[178] on the other. Fuel is only supplied through the valve with the average opening kept at 35 %. Only one actuator – i.e. either DDV or loudspeaker – was active at a time.

A larger valve was added to the air supply. Active control by modulation of the air flow was, however, unsuccessful, possibly due to the damping effect of the perforated plate at the bottom end of the combustor.

Fuel supply loudspeaker

Pressure sensor

Fuel supply valve

Air supply valve
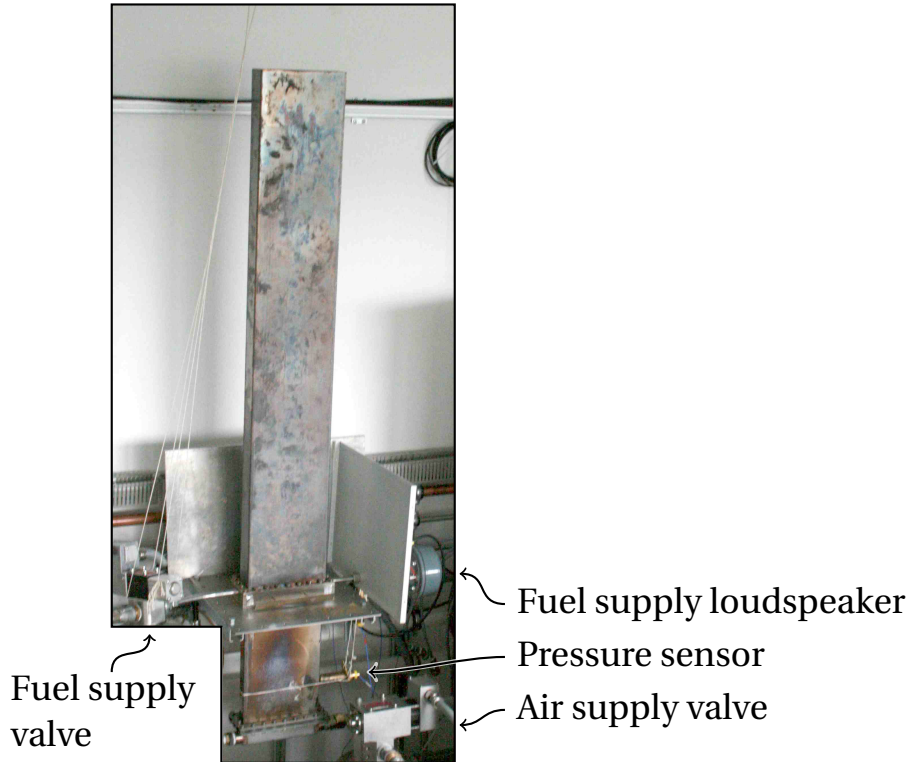
Figure 6.1: Hummer test rig with actuators mounted for active control.

The frequency-domain controller by Hermann and Orthmann[112] is used. In simple terms, it behaves like an amplification plus phase shift. Figure 6.3 shows the pressure oscillation p_S at the sensor position ($x_S = -200\,$mm) and valve spool position x_{sp} for the Hummer combustor running at thermal power $P_{th} = 25\,$kW and equivalence ratio $\Phi = 0.73$ ($\Lambda = 1.37$). AIC, by means of valve actuation, is turned on and off in alternation. The vertical lines correspond to the pressure spectra in fig. 6.2. The reduction in pressure oscillation for this case lies around a factor 20. This value is high compared to other values found in literature. Poinsot et al.,[210] Langhorne et al.,[141] Billoud et al.,[19] Zinn and Neumeier,[298] Hermann et al.,[111] and Schuermans[242] for instance report reduction of the amplitude by around a factor ten.

6.1.2 Comparison of actuators

To compare the effectiveness of the actuators over a large range of operating conditions, the fuel supply valve was set to an average opening of 25 %. Opening the valve further decreased the instability for some operating conditions,
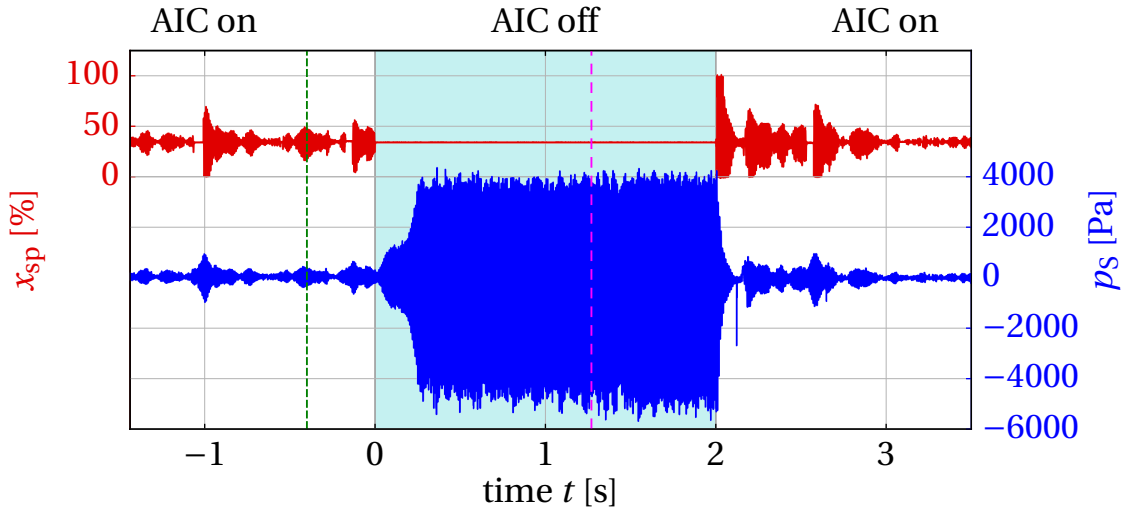
Figure 6.2: Valve spool position x_{sp} (above) and pressure sensor signal p_S (below) for the Hummer combustor running at thermal power $P_{th} = 25\,\text{kW}$ and equivalence ratio $\Phi = 0.73$ ($\Lambda = 1.37$) with AIC turned on and off in alternation. The vertical lines correspond to the spectra in fig. 6.3.
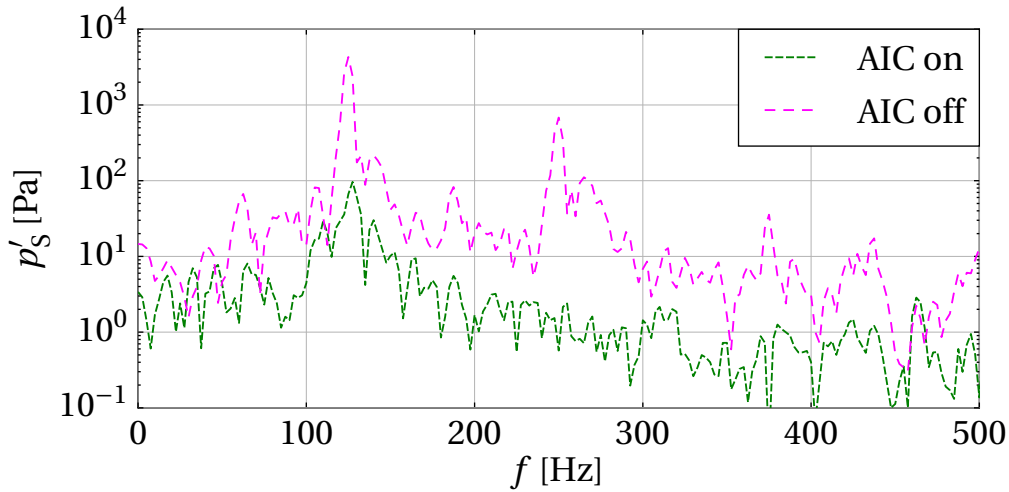
Figure 6.3: Comparison of pressure spectra at the sensor for the Hummer combustor with AIC turned on and off in alternation, corresponding to the vertical lines in fig. 6.2.

which was undesirable for the current assessment of active control. The reduction of the oscillation will, however, be less than mentioned in the last section. Again, only one actuator was active at a time.

The resulting pressure amplitudes are plotted in fig. 6.4. Figure 4.11 (showing the undamped amplitude) is reproduced for comparison. The control action, in terms of gain and phase shift at the dominant oscillation, are listed in tbl. 6.1, for both actuators at various operating conditions.

Actuator	P_{th}	Φ	Λ	Setting	Value
Valve	20	0.91	1.1	Gain	5
	20	0.48	2.1	$-''-$	2.9
	39	0.83	1.2	$-''-$	1
	39	0.63	1.6	$-''-$	0.8
	20	0.91	1.1	Phase	150°
	20	0.48	2.1	$-''-$	130°
	39	0.85	1.17	$-''-$	80°
	39	0.63	1.6	$-''-$	100°
Loudspeaker	20	0.83	1.21	Gain	10
	20	0.55	1.82	$-''-$	5
	39	0.87	1.15	$-''-$	1
	39	0.63	1.6	$-''-$	5
	20	0.83	1.21	Phase	120°
	20	0.55	1.82	$-''-$	140°
	39	0.87	1.15	$-''-$	170°
	39	0.63	1.6	$-''-$	200°

Table 6.1: Controller settings optimised for various operating conditions, for valve and loudspeaker.

The amplitude of the oscillation can be decreased by either actuator, although they are most effective in different ranges of the operating conditions. The valve is more effective for higher thermal power, even though controller gain is set significantly lower there. The effect of active control also seems to be higher for leaner flames (lower equivalence ratio Φ, higher air excess ratio Λ).
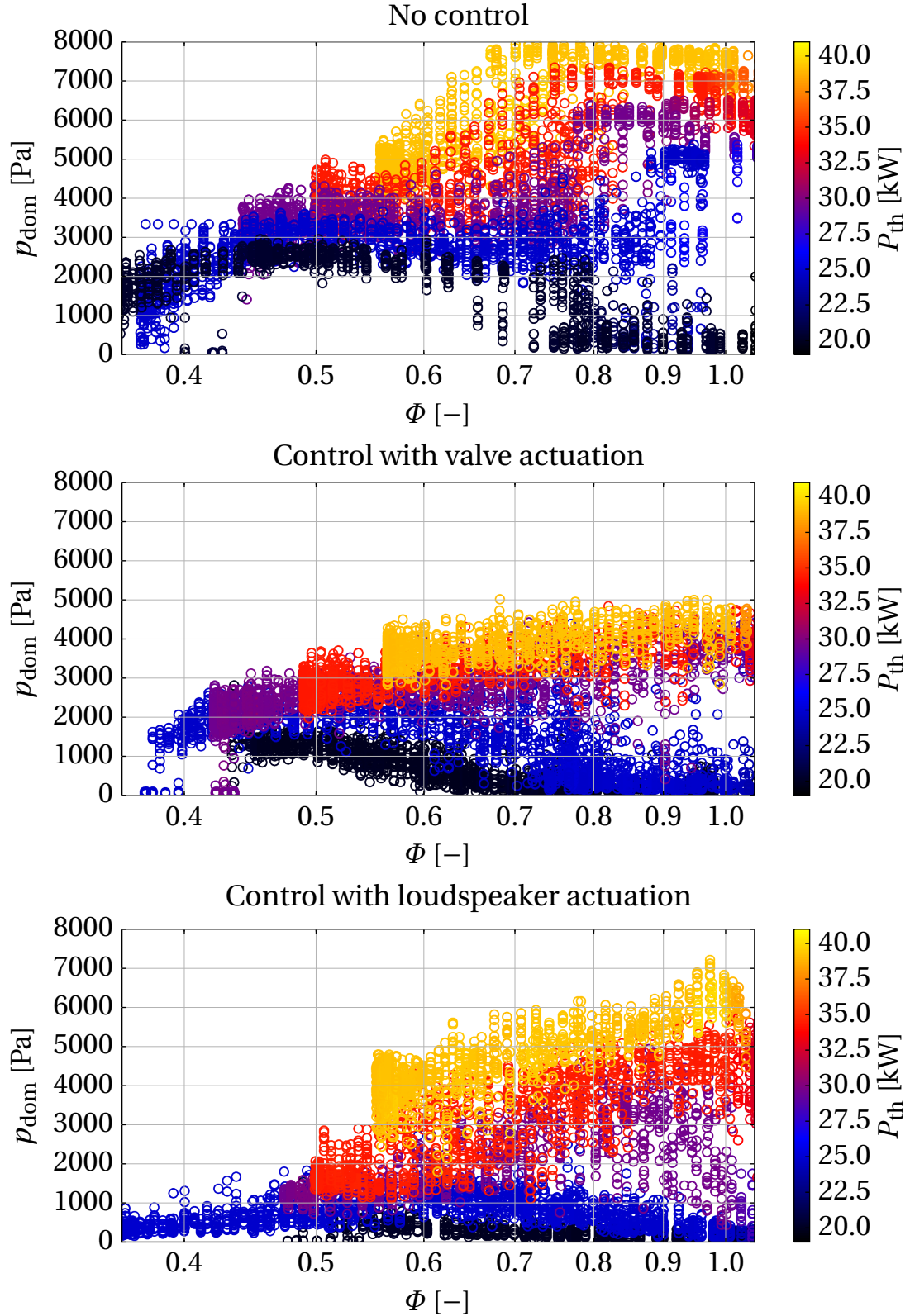
Figure 6.4: Comparison of amplitudes op the dominant ('dom') pressure oscillation as a function of air excess ratio Φ and thermal power P_{th}: without control (top, same as fig. 4.11), with active control by valve actuation (middle), and using the loudspeaker (bottom).

The reason for this might be that for richer flames, an increase in fuel mass flow does not always lead to an increase in heat release. In richer regions of the flame, an increase in fuel flow might even lead to a reduction in heat release.

The loudspeaker on the other hand is most effective for lower thermal power. This was expected. The volume modulation the valve can achieve scales with the throughflow, i.e. thermal power. At lower power the valve loses control authority. The modulated volume by loudspeaker does not scale this way, which is to its advantage at lower power.

Although the scaling of the modulated volume seems to the advantage of the valve in this discussion, the loudspeaker is scalable as an actuator. More loudspeakers can modulate more volume (see fig. 6.5), while the modulated volume for the valve is limited by the fuel throughflow.

Figure 6.5: Multiple drivers connected to a single horn increase the volume that can be modulated by loudspeaker actuation.

6.1.3 Attempt on the Limousine rig

Application of active control was attempted on the Limousine test rig as well. Interestingly, the effect was a lot less pronounced than on the Hummer rig. Figure 6.6 compares pressure spectra with AIC on and off, measured on both combustors, running at $P_{th} = 40\,\mathrm{kW}$ and $\Phi = 0.71$ ($\Lambda = 1.4$).
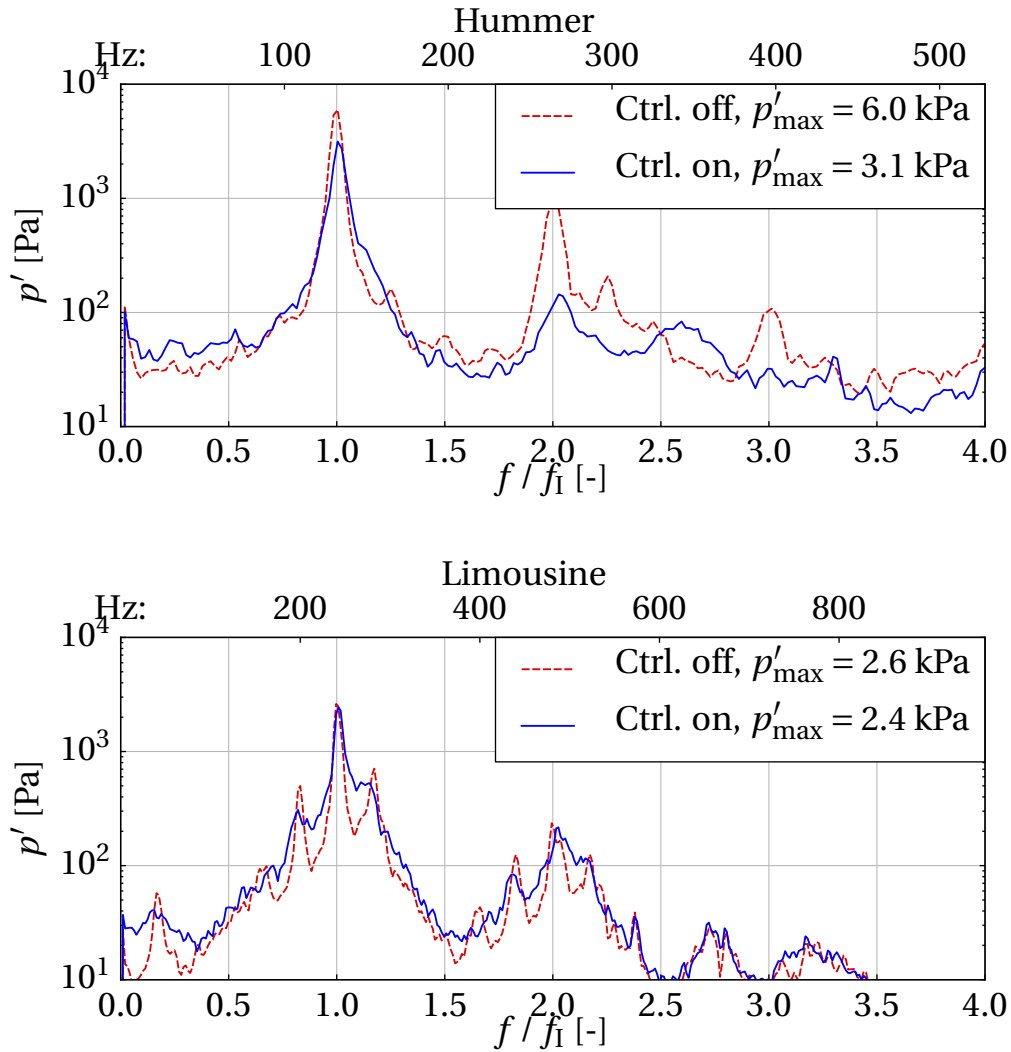
Figure 6.6: Spectra measured at the Hummer (top) and Limousine (bottom) combustors with AIC turned on or off.

At this operating point, AIC reduces the amplitude of the pressure oscillation in the Hummer combustor by about half the magnitude, while the reduction on the Limousine combustor is less than ten percent.

6.2 Analysis in CFD

Until this section, no explanation has been found for the discrepancy in control authority for active control between the Hummer and Limousine combustor. To investigate the influence of the fuel transport and the injection process between actuator and flame, both burners are modelled in ANSYS CFX. Active control is implemented in the model analogous to experiment. Turbulent combustion is modelled by SAS-SST and the *burning velocity model* (BVM). The distribution of the convective time between fuel injector and flame is evaluated and used to estimate the response of the heat release to modulation of the fuel mass flow.

6.2.1 Set-up

6.2.1.1 Combustor geometry and grid

Figure 6.7 gives an overview of the simplified geometries and dimensions for both combustors, as used in CFX. The burner is situated in a duct of rectangular cross-section with closed/open acoustic boundary conditions, approximating a quarter-wave acoustic resonator. The rectangular cross section with relatively large aspect ratio leads to an approximately 2-D flow in the x, y-plane. The computational domain takes advantage of this, representing only a thin slab of the combustor, with symmetry boundary conditions applied on both sides.

For the Hummer, the inner span in z-direction is 180 mm, while the computational domain has a thickness of 2.5 mm. For the Limousine rig, the physical and computational span are 150 mm and 2 mm respectively. The pressure at $x_S = -200$ mm (labelled 'sensor' in fig. 6.7) is sampled and passed to the controller as input. The origin of x is at the top of the flame holder. Note the fuel injector holes of the Limousine are situated further upstream than those of the Hummer, in an effort to improve mixing of fuel and air.

The (choked) air inlet is modelled as a fixed mass flow boundary condition. The open outlet is modelled as an opening (allowing inflow and outflow) at constant pressure. The prismatic flame holder, triangular in cross section, is located at about one quarter of the height (x) of the combustor. Fuel gas (methane) is distributed through the flame holder, and injected into the airflow
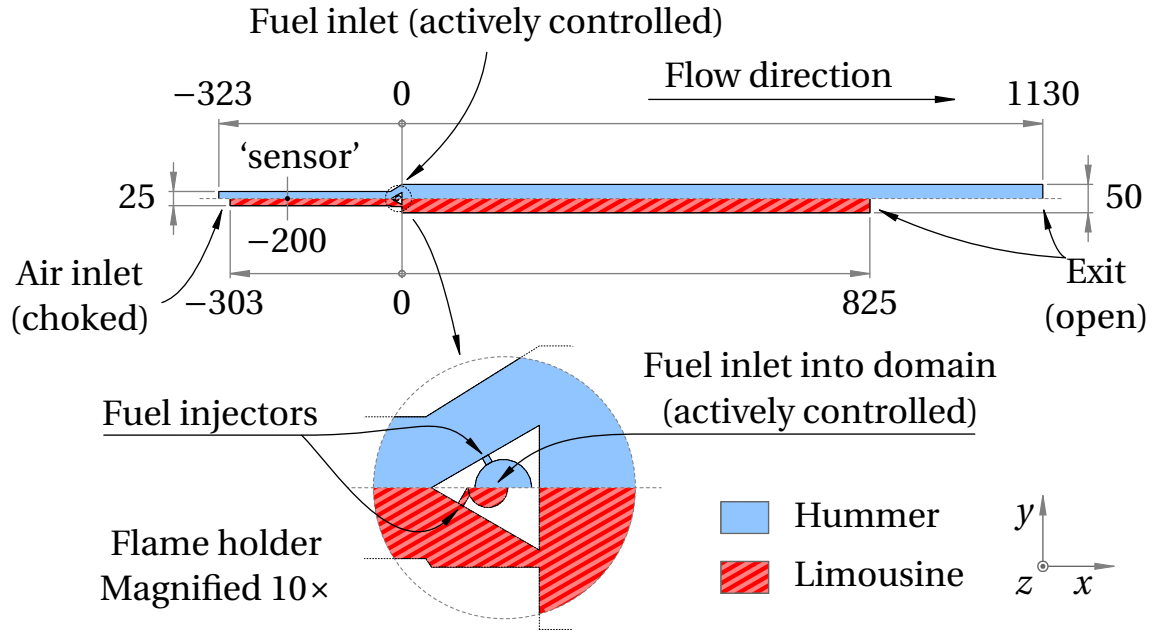
Figure 6.7: Overview of the computational domain for both combustors; Hummer (blue) above and Limousine (hatched in red) below. Dimensions are in mm.

through injector holes along the span (z) of the flame holder. The computational domain includes half an injection hole on either side of the flame holder. The fuel mass flow can be modulated by the controller. A partially premixed flame forms, stabilised downstream of the flame holder. There is a small volume between the fuel inlet and the injector holes (see also fig. 6.7), to represent the compliance of the fuel supply system downstream of the AIC actuator.

Both computational grids are structured meshes of hexahedral elements. The grids are two-dimensional in the plenum and the downstream end of the combustion chamber, where gradients in z-direction are negligible, to save computational cost. The region around the flame holder and extending downstream is three-dimensional, to resolve the intrinsically three-dimensional mixing of the fuel jet into the cross-flow of air. Figure 6.8 shows this 3-D region and the transition to 2-D.

The liner walls are modelled as thermally conductive no-slip walls with a heat transfer coefficient of $50\,\mathrm{W/(m^2\,K)}$, based on an estimate of the heat loss by free convection and radiation towards an environmental temperature of $300\,\mathrm{K}$.

Hummer: 88178 elements

Limousine: 81856 elements
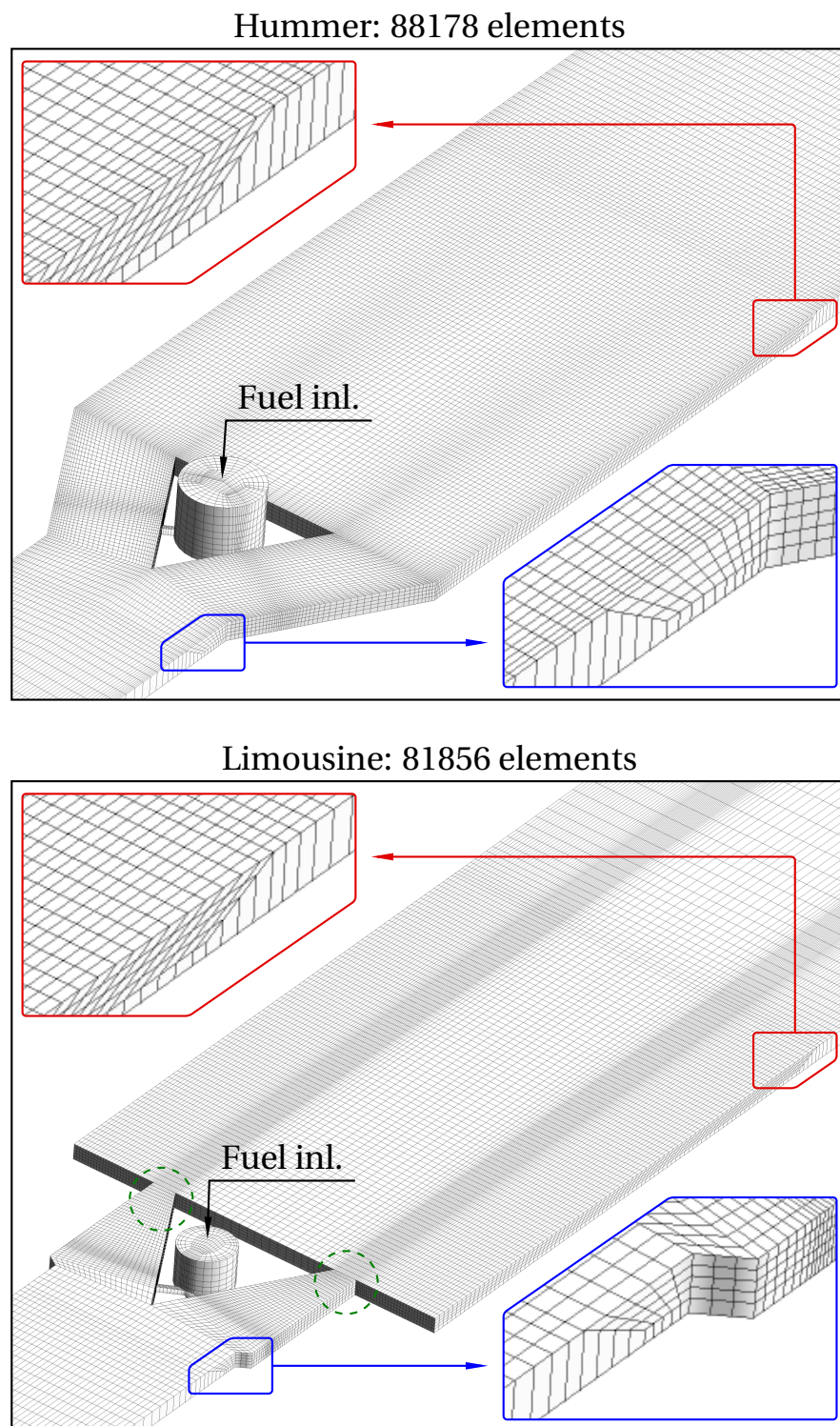
Figure 6.8: Detail of the 3-D grid region with transitions to 2-D, Hummer shown above. For the Limousine below, note the narrow slits (circled) on either side of the flame holder.

6.2.1.2 Computational model

The transient simulation in ANSYS CFX v14.5 used 8 cores, with 10^{-5} s time steps. The thermal power $P_{\text{th}} = 40\,\text{kW}$, and the equivalence ratio $\bar{\Phi} = 0.71$ (air excess ratio $\Lambda = 1.4$). Turbulence is modelled with the scale-adaptive simulation model (SAS-SST) model.[174] Combustion is simulated by the *burning velocity model* (BVM), using a new model option for improving accuracy for non-premixed flames.[80, 185, 214, 295] Other combustion models, such as the eddy dissipation model and the *extended coherent flame model* (ECFM) were used in preliminary simulations, but gave an oscillating behaviour which agreed less with experiment.

A practical advantage of the BVM is that the volumetric heat release rate is readily available for post-processing. In the remainder of this section, this information will be used to estimate optimal controller settings.

Implementation of active control in CFX — The controller is identical to the one used by Hermann and Orthmann.[112] In simple terms, it behaves like an amplification plus phase shift, which can be set according to preferences. The precise workings of the controller are kept confidential, to protect the commercial interests of IfTA. The same controller is used in both cases, so that the controller can be ruled out as the cause of the difference in control authority.

The controller runs as a command line application which reads a log file with under-sampled (in time) pressure data from the sensor position and writes the output value to another file. In CFX, a user function (written in Fortran) updates the pressure log file and reads the output value from the controller. The fuel inlet mass flow is varied according to the controller output.

The goal is to damp the oscillation by reduction of Rayleigh's coefficient.[219, 265] The equivalence ratio is modulated to cause a fluctuating heat release ($\dot{Q}'$) in opposite phase with the pressure fluctuation $p'_{\dot{Q}}$ at the flame. The controller does, however, not know the pressure at the flame directly, since the pressure probe supplying the controller input is situated further upstream, at $x_{\text{S}} = -200\,\text{mm}$; neither can it influence the heat release at the flame instantaneously. In experiment or industrial operation, relatively long time series of input data are available to converge to the optimal control settings. For numerical simulation, another approach is needed. Here, the phase shift

between the pressure at the AIC input sensor and the pressure at the flame can be determined from the mode shape of the oscillating combustor. The time-lag between a fuel mass flow fluctuation caused by the controller and the corresponding heat release fluctuation is mainly caused by the convective time between the fuel injector and the flame. Figure 6.9 gives an overview of the relevant processes.
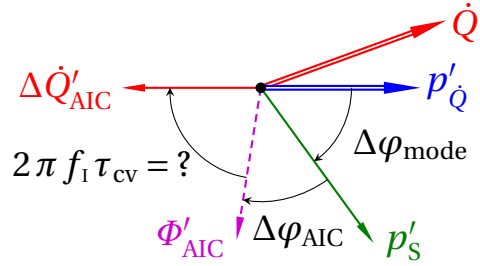
Figure 6.9: Phasor plot giving an overview of the various phase lags relevant for active damping of combustion instability by modulation of the fuel flow. Amplitudes are not to scale. The phase of $p'_{\dot{Q}}$ is defined as zero. A resulting phasor $\dot{Q}$ to the right implies a positive Rayleigh coefficient.

The controller phase shift is defined positive for a phase lag. The value required for a heat release in anti-phase with the pressure fluctuation is found as:

$$\arg \frac{p'_{\dot{Q}}}{p'_{S}} + (\tau_{ac} + \tau_{cv})\, 2\,\pi\, f_{I} + \Delta\varphi_{AIC} = (2\,N+1)\,\pi\,, \qquad (6.1)$$

where f_{I} is the frequency of the dominant oscillation. $\arg(p'_{\dot{Q}}/p'_{S})$ represents the phase difference between the pressure fluctuation p' at the sensor ('S') and at the flame ($\dot{Q}$). Together with the phase shift caused by acoustic ('ac') and convective ('cv') delay, and the phase shift set for the controller, this should add up to N-and-a-half oscillation cycles. Regarding the fuel system as a Helmholtz resonator, its resonance frequency is much higher than that of the oscillation at hand. Therefore the fuel system can be regarded a pure acoustic compliance, and the acoustic time delay between fuel inlet and fuel injector can be neglected ($\tau_{ac} \approx 0$). Since $\tau_{cv} \approx \tau$, the subscript cv will be dropped in the following. The compliance remains significant, so the fuel system should still be included in the computational domain. In reality, τ is not single-valued, but forms a spatial distribution over the flame. Since the flame is unstable, this distribution varies in time as well. This has serious consequences for the control authority, which will be discussed in sec. 6.2.2.2.

Definition of the convective time — Following the procedure proposed by Krebs and Lohrmann,[138] the convective time of fuel 'parcels' from the fuel inlet $\tau(\vec{x}, t)$ towards the flame is computed as an additional field variable. In this approach, two auxiliary field variables, each representing passively convected scalars, are defined: $X_t(\vec{x}, t)$ and $X_1(\vec{x}, t)$. At the air inlet, the boundary conditions are set to $X_1 = X_t = 0$. At the fuel inlet, the boundary conditions are $X_1 = 1$ and $X_t = t$ (the simulation time at which the fuel entered the domain). The expression X_t / X_1 remains constant when the fuel expands, mixes with air, or gets consumed in the flame. Its value represents the time at which the fuel (or corresponding combustion products) entered the domain. The derived variable $\tau(\vec{x}, t) = t - X_t / X_1$ represents thus the convective time from the fuel inlet, viz. the boundary of the domain, to the location $\vec{x}$. This method will be less reliable in situations with recirculation, where τ will be a mixture of the convective time for the direct route, and the route with circulation, but this is thought to be a lesser influence in the current situation.

In the present configuration, there is an additional complication. The quantity of interest is not the time since the fuel entered the computational domain *into* the fuel supply system, but instead the time which has passed since fuel was injected *out of* the fuel supply system into the air flow. Recall the detail of fig. 6.7, where the injectors and inlet into the domain are labelled. To get the desired result, the diffusion coefficient of both X_t and X_1 was set to $10^4 \, \text{m}^2/\text{s}$ inside the fuel supply system, and zero elsewhere. This way, $X_t = t$ and $X_1 = 1$ still hold at the exit of fuel injector tubes, and τ represents the convective time from there on.

As done by Polifke et al.,[215] a distribution of convective time lags τ will be interpreted in the form of a histogram of the heat release rate $\Delta \dot{Q}_i(t)$ plotted against τ_i. While Polifke et al. describe a steady RANS simulation, the simulation discussed in the current paper is unsteady. Therefore, in this paper the effect of temporal variation $\Delta \dot{Q}_i(t)$ can be analysed. The heat release rate $\Delta \dot{Q}_i(t)$ is found by integration of the volumetric density of the local heat release rate $\dot{q}$ over the volume $\Delta V_i(t)$, where $\tau(\vec{x}, t)$ is in the range $\tau_i \pm \frac{1}{2} \Delta \tau$:

$$\Delta \dot{Q}_i(t) \equiv \int_{\Delta V_i(t)} \dot{q}(\vec{x}, t) \, \mathrm{d}V \, . \tag{6.2}$$

Since $\tau(\vec{x}, t)$ is a function of time, so is $\Delta V_i(t)$. The index i correspond to discrete ranges of time delay τ. Figures 6.10 and 6.11 give a visual impression

of the variation of the variables $\dot{q}$ and τ in the flame region. The left-hand side of eq. (6.2) is normalised, and presented as the histogram

$$\mathcal{H}_i(t) \equiv \frac{\Delta \dot{Q}_i(t)}{\Delta \tau \, P_{\text{th}}},$$

with P_{th} the nominal (constant) thermal power. $\mathcal{H}_i(t)$ is now the normalised momentary heat release rate, associated with combustion of fuel that was injected in the interval $\tau_i \pm \frac{1}{2} \Delta \tau$, see fig. 6.12. The total momentary heat release rate is $\dot{Q}(t) = P_{\text{th}} \sum_i \mathcal{H}_i(t) \, \Delta \tau$, i.e. the heat release at time t, associated with fuel injected at any time $t - \tau$ in the past. As fig. 6.12 shows, there is strong temporal variation in overall heat release, mean τ, and shape of the distribution. The time-averaged distribution $\bar{\mathcal{H}}_i$ is much smoother.

Since there the amount of unburned fuel leaving the domain is negligible,

$$\frac{\dot{Q}(t)}{\bar{\dot{Q}}} \approx \frac{\dot{Q}(t)}{P_{\text{th}}} = \sum_i \mathcal{H}_i(t) \, \Delta \tau \, .$$

Consequently, the time-average $\sum_i \bar{\mathcal{H}}_i$ will approach unity for long average time intervals. The momentary heat release of a (lean) flame depends on the local equivalence ratio Φ, the flame surface A_{fl} and the local burning velocity S_{L}, as

$$\dot{Q}(t) \propto \int_{A_{\text{fl}}} \rho(\vec{x}, t) \, \Phi(\vec{x}, t) \, S_{\text{L}}(\vec{x}, t) \, \mathrm{d}A \, .$$

The local equivalence ratio $\Phi(\vec{x}, t)$ along the flame front will first of all change in response to modulation of the fuel mass flow $\dot{m}_{\text{F}}$, resulting in corresponding changes in the overall heat release rate. It is assumed in the following, that this is the dominant mechanism by which the flame responds to controller action, i.e. this is the main mechanism by which control authority is realised. There will be additional contributions to the heat release rate, that result from fluctuations of S_{L} and A_{fl}:

For lean flames, burning velocity is proportional to equivalence ratio, so that S_{L} will fluctuate in phase with Φ. This second contribution to the heat release rate will lead to a slight increase in the effect of active control, independent of controller settings and combustor geometry. This paper is primarily concerned with a comparison between two combustors. Since this second effect influences both combustors similarly, it does not affect the comparison and will be neglected in the following.

Figure 6.10: τ as contour lines and $\dot{q}$ as background colouring for the Hummer: time-average on top gives a quantitatively more readable impression. Qualitatively, the instantaneous fields (for arbitrary time steps) shown below look very different.
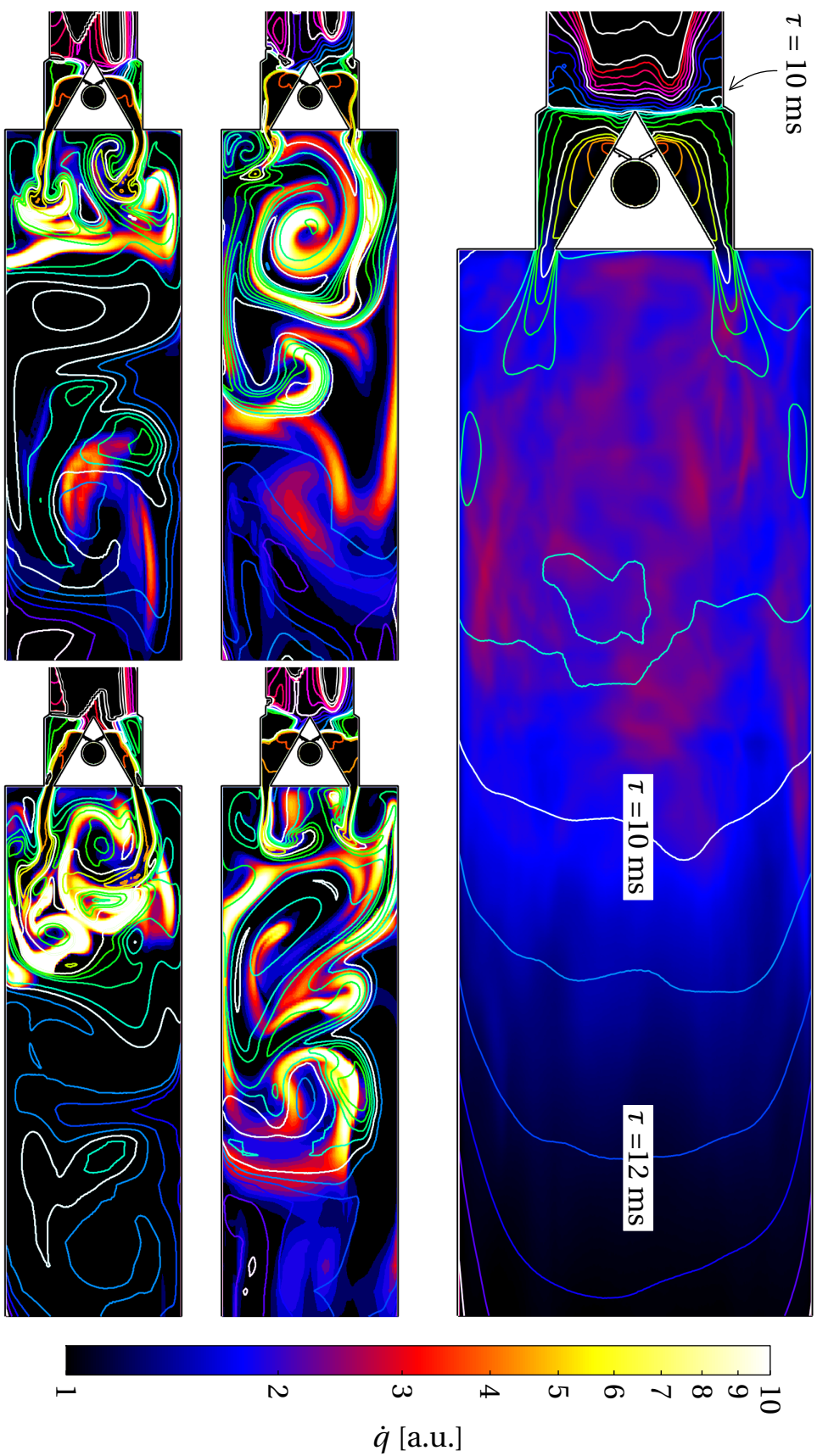
Figure 6.11: τ as contour lines and $\dot{q}$ as background colouring for the Limousine: time-average on top gives a quantitative more readable impression. Qualitatively, the instantaneous fields (for arbitrary time steps) shown below look very different.
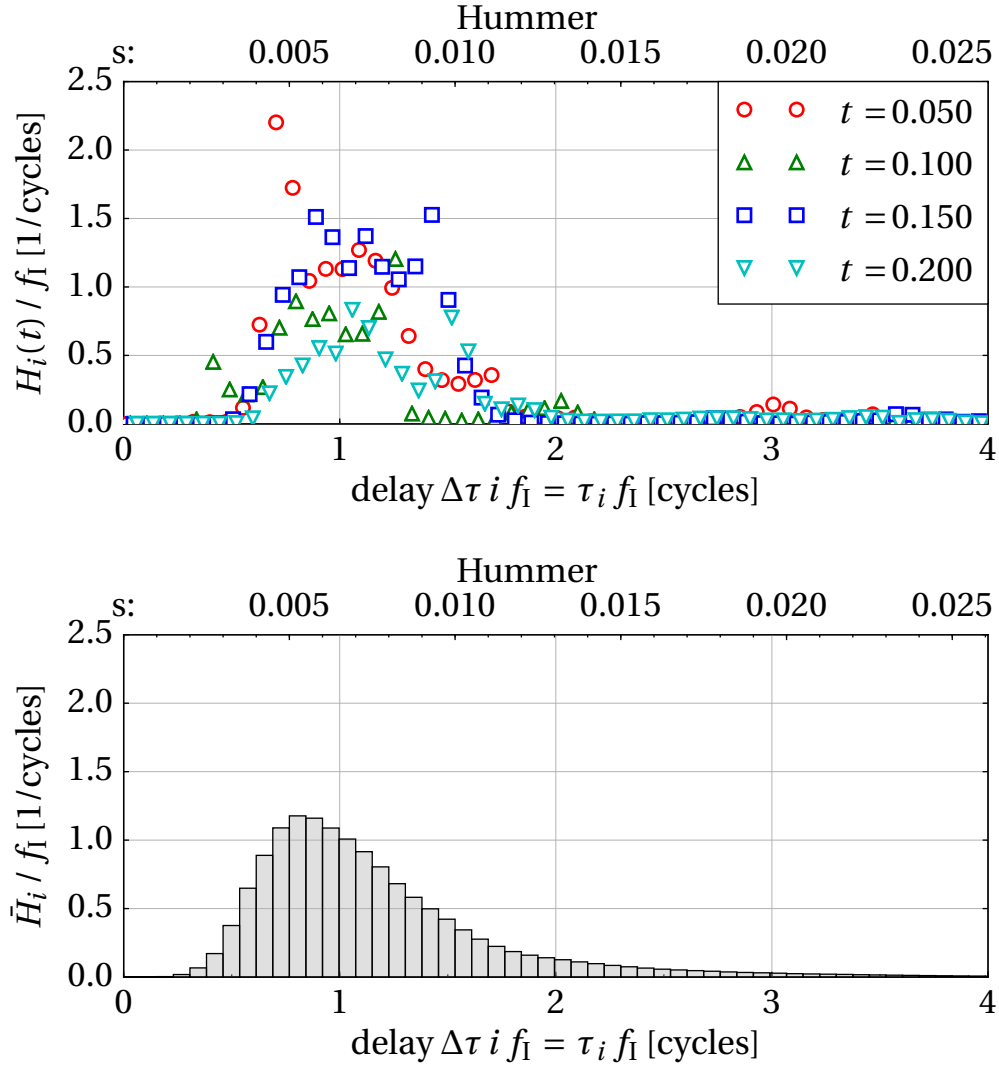
Figure 6.12: Momentary distributions $\mathcal{H}_i(t)$ on top; most fuel is combusted roughly one period of oscillation (7 ms) after it was injected. Averaging over a large number of time steps leads to the much smoother histogram $\bar{\mathcal{H}}(t)$ below.

Finally, there will be a third contribution to the fluctuations in heat release rate due to changes in flame surface area A_{fl}. This is a secondary effect, which results from modulation of the local burning velocity, as shown by Huber and Polifke.[121, 122] Due to the strong fluctuation of the shape of the current flame, influenced by large-scale vortical structures, the coherent response of A_{fl} is expected to be minimal, and will be neglected in the following as well.

Taking the time delay into account, the change in momentary heat release to a modulation of injected fuel mass flow $\dot{m}_F$ is estimated as

$$\frac{\dot{Q}'(t)}{\bar{\dot{Q}}} \approx \sum_i \frac{\dot{m}'_F(t - \tau_i)}{\bar{\dot{m}}_F} \mathcal{H}_i(t) \,. \tag{6.3}$$

Conceptually, $\mathcal{H}_i(t)$ is now similar to, but different from an impulse response, insofar that $\mathcal{H}_i(t)$ relates the heat release rate at the current time t to fuel injection over the past times $t - \tau$. A conventional impulse response would relate heat release at $t + \tau$ in the future to fuel injection at current t. Besides, $\mathcal{H}_i(t)$ is a function of time, strongly influenced by turbulent vortical structures and temporal variation in flame shape, while an impulse response only describes response coherent to the input. These effects will average out over many time steps, so that in the following, the time-averaged distribution $\bar{\mathcal{H}}_i$ will be interpreted as an estimation of the impulse response relating heat release rate to fuel flow modulation. The discrete Fourier transform of $\mathcal{H}_i(t)$ with respect to i is $\mathcal{G}_j(t)$:

$$\frac{\dot{Q}(f_j, t)}{\bar{\dot{Q}}} \approx \frac{\dot{m}_F(f_j, t)}{\bar{\dot{m}}_F} \mathcal{G}_j(t) \,. \tag{6.4}$$

Note that like $\mathcal{H}_i(t)$, $\mathcal{G}_j(t)$ is a function of time. The time-averaged function $\bar{\mathcal{G}}_j$ is taken as an approximation of the transfer function relating heat release rate to fuel flow modulation. Dispersion of the delay τ due to mixing will lead to a reduction of the magnitude of this transfer function as discussed by Mehta et al.[172] The influence of temporal fluctuation of $\mathcal{G}_j(t)$ will be discussed in the following section.

6.2.2 Results

The simulation was run without control for a total time of 0.2 s. The oscillation develops quickly, as shown in fig. 6.13, and mode shapes are evaluated between

0.036 s and 0.2 s. After applying a Blackman window to the time domain data, the frequency of the dominant mode was estimated from the Fourier spectrum. The mode shapes, i.e. amplitude and phase as a function of x, were acquired through evaluation of the Fourier coefficients corresponding to the estimated frequencies.
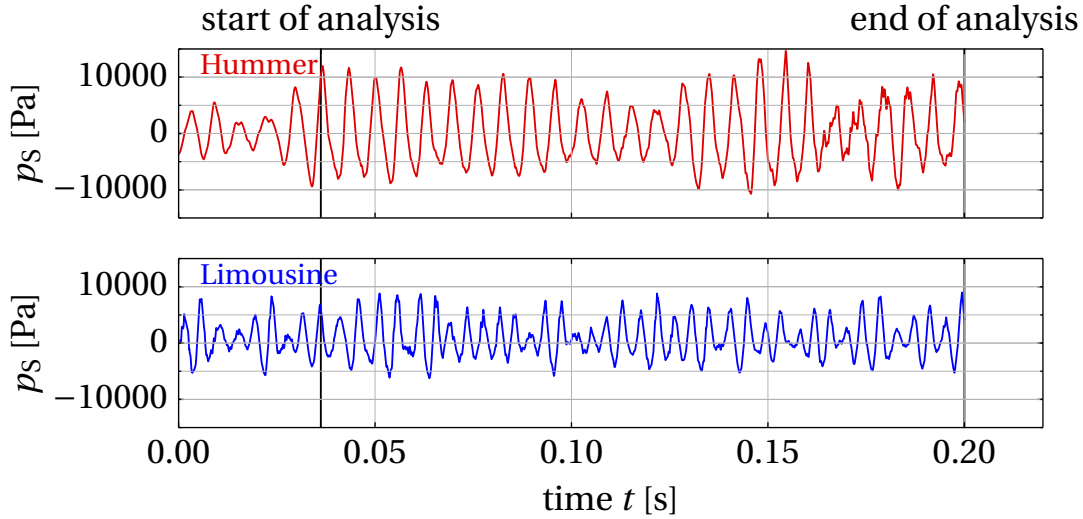
Figure 6.13: Time trace of the pressure at the 'sensor' for both combustors running without active control.

6.2.2.1 Oscillation without control

The mode shapes found this way are presented in fig. 6.14. Phase is defined to be zero for the (spatial mean) pressure at the flame. Besides the difference in amplitude and frequency, Limousine shows a deeper cusp in amplitude at the flame holder, and a significant jump in phase, both caused by the blockage due to the narrow slits around the flame holder.

6.2.2.2 Controller settings and analysis of the convective time delay

The value of the convective time delay at the flame is interpreted in the form of the distribution $\mathcal{H}(\tau_i, t)$ of the heat release. This quantity is plotted for both combustors in the upper half of figs. 6.15 and 6.16. The peak of the heat release lies around $\tau \approx 6$ ms resp. 8 ms, which is similar to the values 10 ± 2 ms found by Krebs and Lohrmann[138] on their swirl burner, so that in perspective
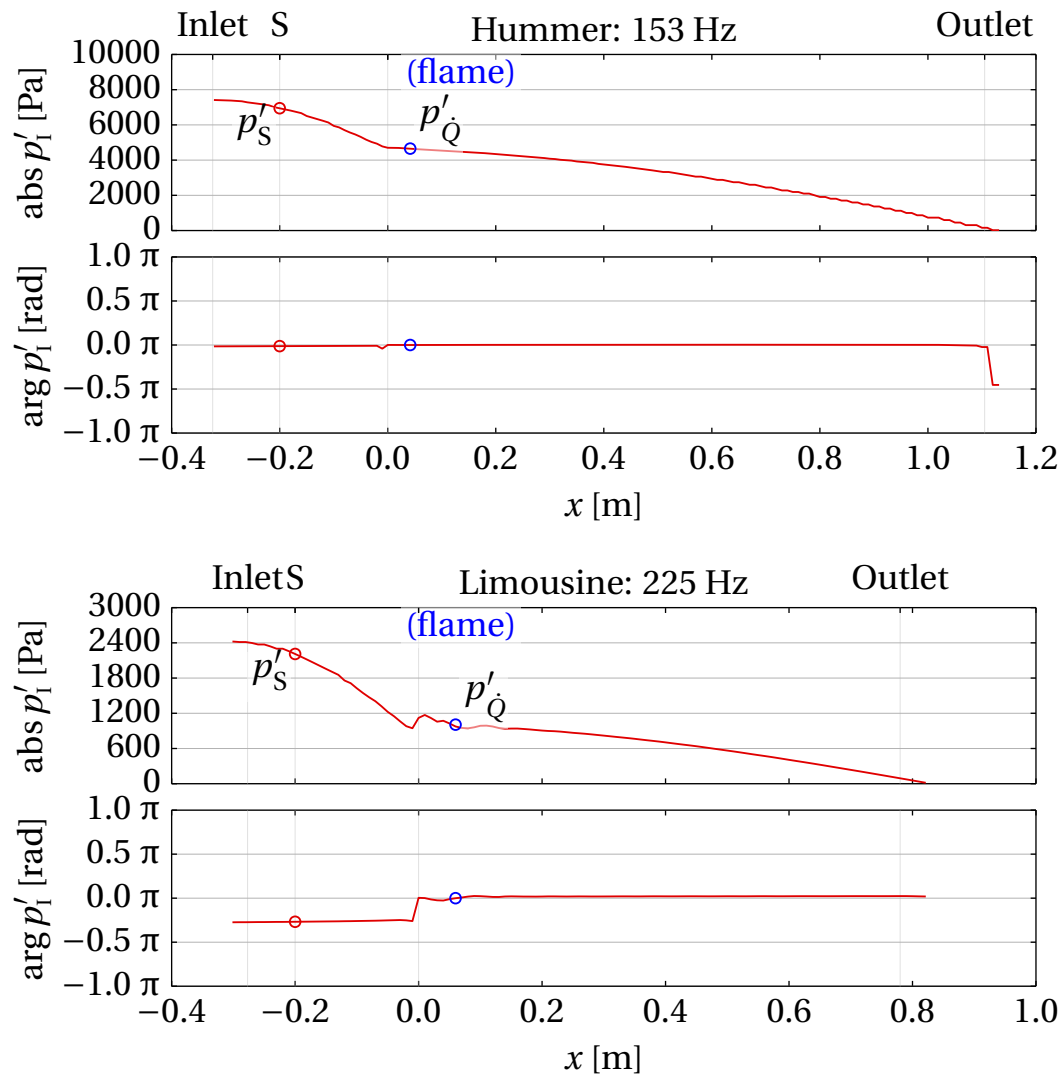
Figure 6.14: Mode shapes without active control; above: Hummer, below: Limousine

of this parameter the laboratory combustors are representative of industrial combustors. $\mathcal{G}(f_i, t)$, the (τ-wise) discrete Fourier transform of $\mathcal{H}$, is shown in the form of a colour wheel graph below. The amplitude abs $\mathcal{G}$ is expressed by the lightness of the colour, while the hue represents the argument arg $\mathcal{G}$. The low-frequency limit of $\mathcal{G}$ approaches unity (bright red). For higher frequencies, the absolute value abs $\mathcal{G}$ decreases to zero, shown as black, while the argument arg $\mathcal{G}$ drops (from red to blue and green etc.) and shows more and more time-wise fluctuation. It can be estimated from the lower plot in fig. 6.15, that the phase shift between fuel injection and heat release is about $0.3\pi = -1.7\pi$ (with quite some variation around this value), i.e. the fuel is consumed almost a full cycle after it is injected into the air flow. This corresponds approximately to the peak in $\mathcal{H}$, while the mean of $\mathcal{H}$ lies at a higher value of τ.

The Limousines rig has a longer delay time in seconds, as shown in fig. 6.16. This difference is even greater when expressed in cycles of the dominant frequency, since this combustor has a higher resonant frequency. Moreover, the flame is less compact in stream-wise direction, so the histogram $\mathcal{H}$ is much wider than for the Hummer. Looking at the colour wheel graph for the Limousine, $\arg(\mathcal{G})$ at the dominant frequency f_I varies so strongly over time that it is not possible to estimate the required controller phase shift from this graph.

To get a more accurate reading, the time-averaged value $\bar{\mathcal{G}}(f)$ is presented in a Bode plot. The controller phase shift $\Delta\varphi_{\mathrm{AIC}}$ was set according to eq. (6.1), using $\arg(\bar{\mathcal{G}})$ instead of the term $(\tau_{\mathrm{ac}} + \tau_{\mathrm{cv}}) \, 2\pi f_I$.

The time-averaged transfer function $\bar{\mathcal{G}}(f) = 1/(t_2 - t_1) \int_{t_1}^{t_2} \mathcal{G} \, \mathrm{d}t$, averaged between $t_1 = 0.036\,\mathrm{s}$ and $t_2 = 0.2\,\mathrm{s}$, is shown in figs. 6.17 and 6.18. The absolute value $\mathrm{abs}\big(\bar{\mathcal{G}}(f)\big)$ decreases with frequency due to two phenomena. Firstly, a flame which is extended in the direction of the flow, will lead to a flatter impulse response $\mathcal{H}(\tau, t)$ and a decrease in $\mathrm{abs}\big(\mathcal{G}(f, t)\big)$ for all t. Secondly, a variation of the time delay τ over time leads to variation in phase $\arg\big(\mathcal{G}(f, t)\big)$ and after averaging to a lower absolute value $\mathrm{abs}\big(\bar{\mathcal{G}}(f)\big)$. To give an impression of the relative importance of both effects, the root-mean-square of the absolute value $\mathcal{G}_{\mathrm{RMS}}(f) = \sqrt{1/(t_2 - t_1) \int_{t_1}^{t_2} \mathcal{G} \mathcal{G}^* \, \mathrm{d}t}$ is plotted as well. $\mathcal{G}_{\mathrm{RMS}}(f)$ decreases due to τ-wise dispersion alone, but is insensitive to variation of arg $\mathcal{G}$ over time. The distance between both lines is the standard deviation of the transfer function over time.
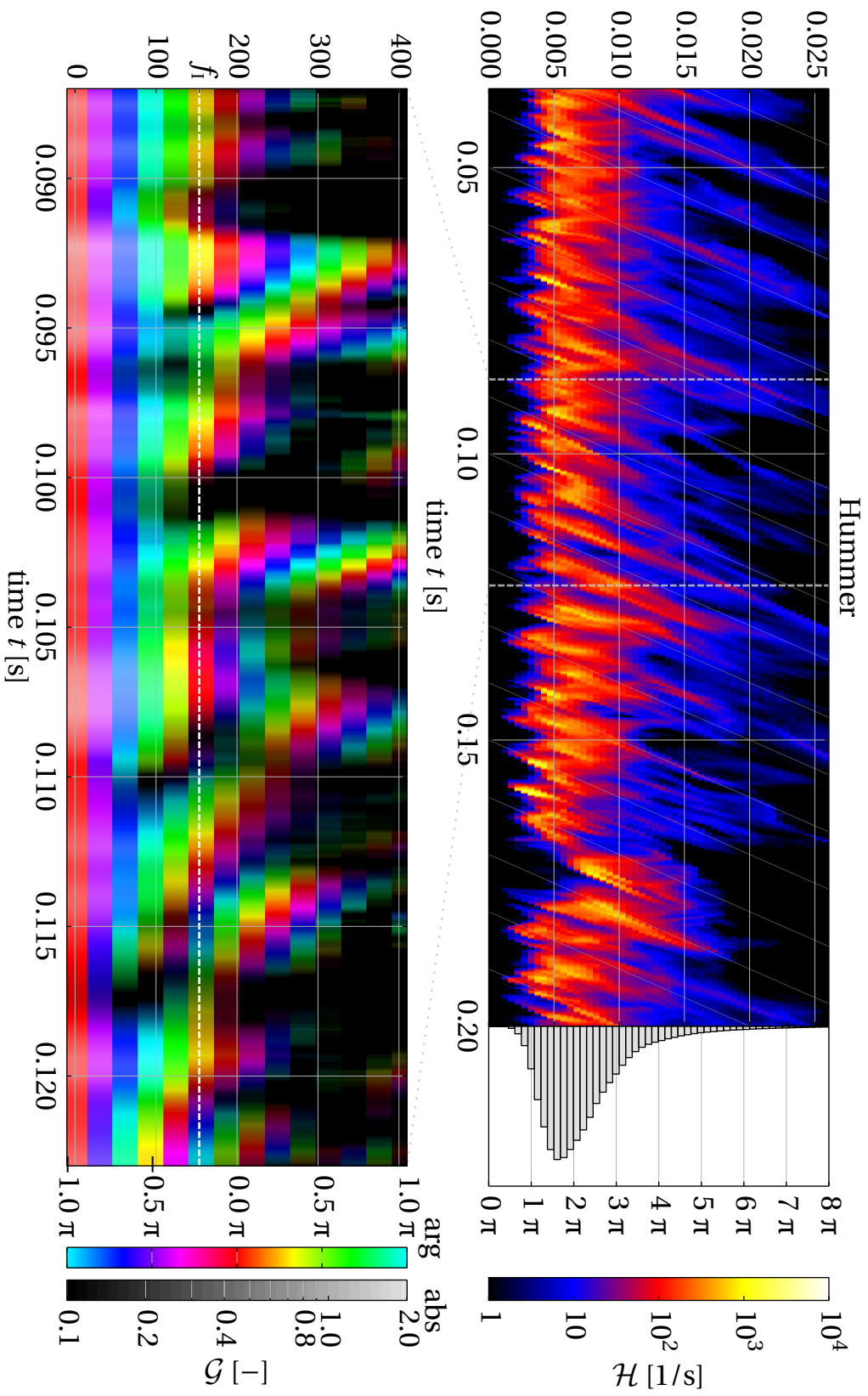
Figure 6.15: Above: Heat release in Hummer as a function of simulation time and time delay. The time-average distribution of the delay is shown as a histogram on the right. Below: Fourier transforming the information above per time step gives an impression of the transfer function $\mathcal{G}$ and its fluctuation over time.
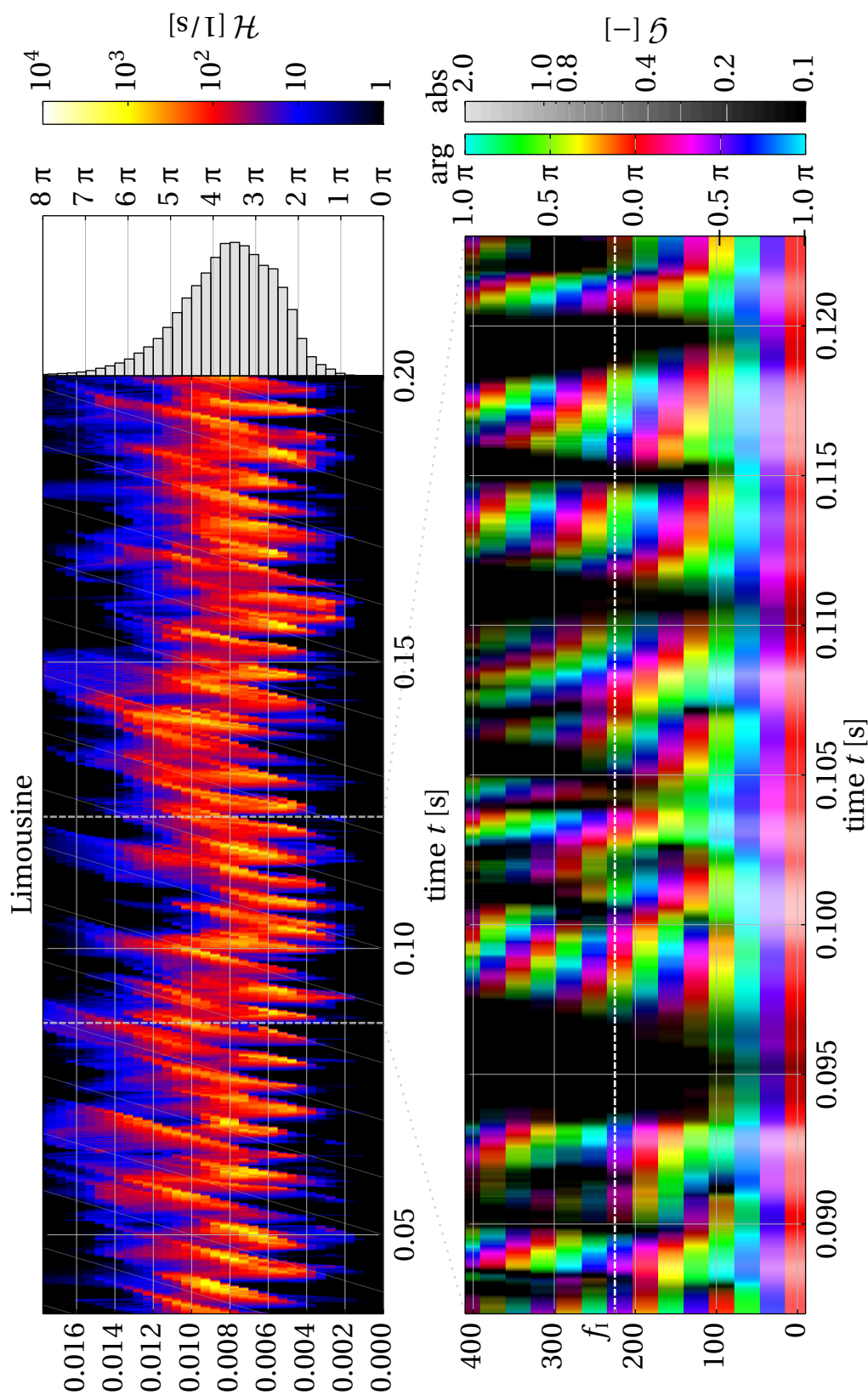
Figure 6.16: Above: Heat release in Limousine as a function of simulation time and time delay. The time-average distribution of the delay time is shown as a histogram on the right. Below: Transfer function $\mathcal{G}$ acquired by Fourier transformation of the upper plot, and its fluctuation over time. The phase of the estimated transfer function at the dominant oscillation frequency shows much more variation than for Hummer.
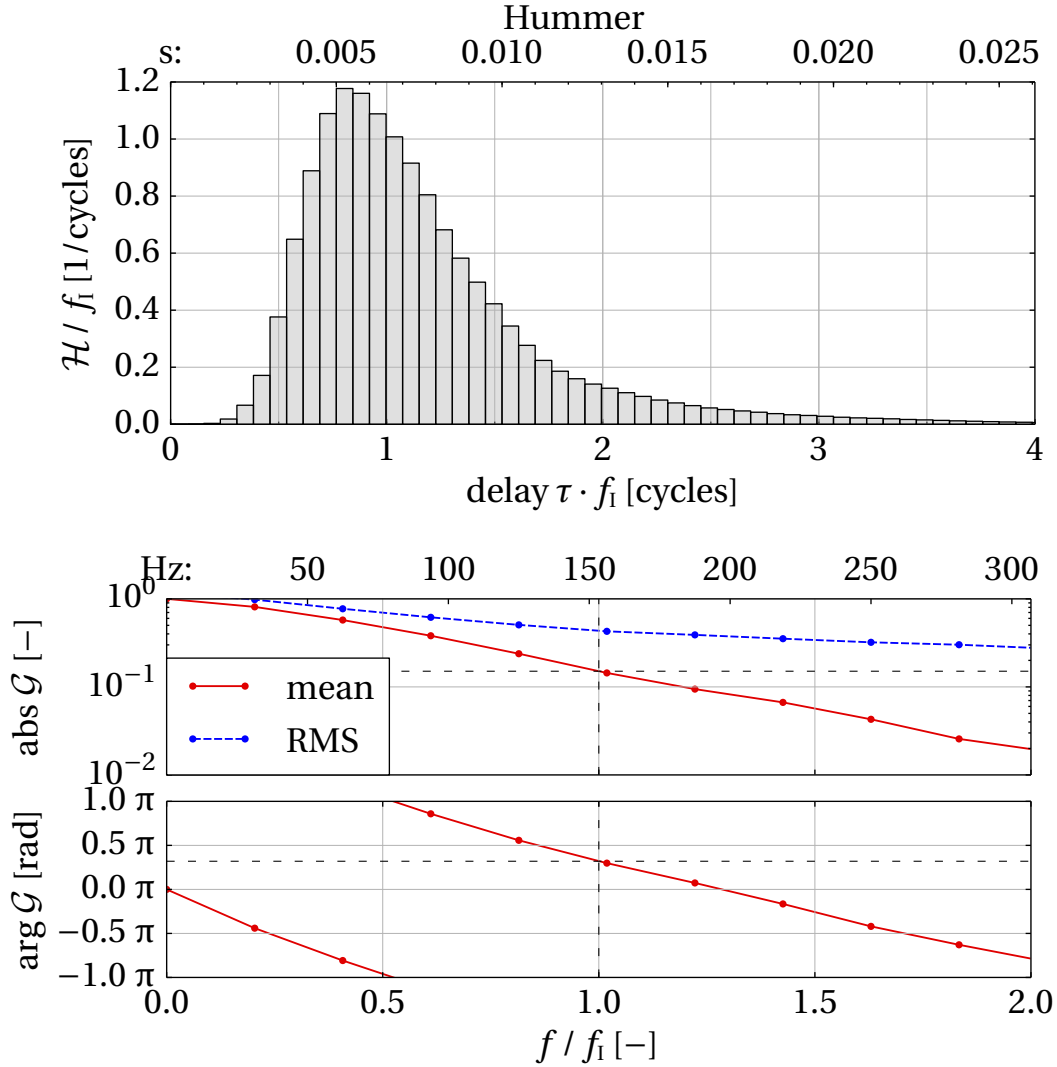
Figure 6.17: Expected impulse response (above) and transfer function (below) relating fuel injection fluctuation to heat release for the Hummer test rig. For the absolute value, both the time-averaged $\mathrm{abs}\big(\bar{\mathcal{G}}(f)\big)$ as well as the time-wise RMS $\mathcal{G}_{\mathrm{RMS}}(f)$ are shown. Frequencies are non-dimensionalised with the respective dominant oscillation frequency.
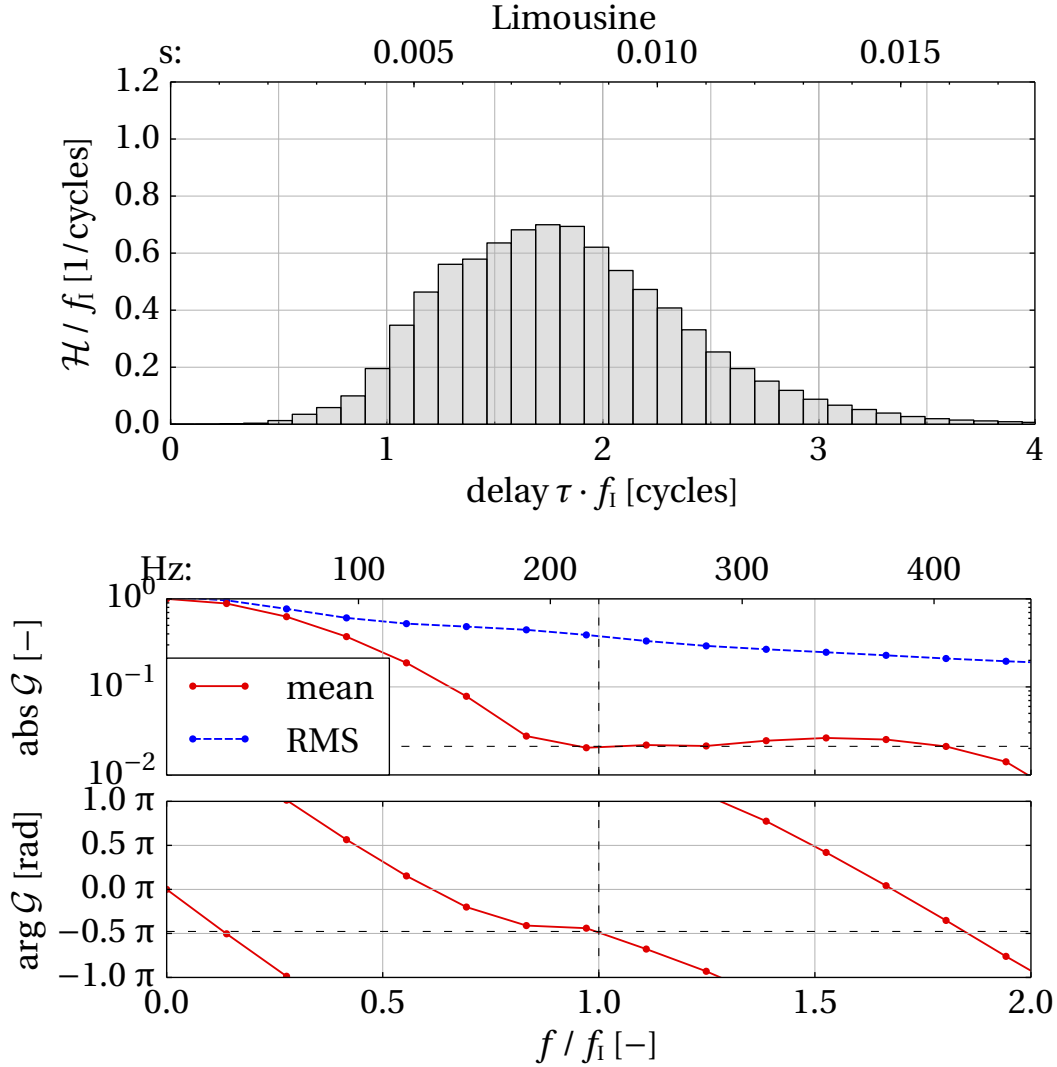
Figure 6.18: Expected impulse response (above) and transfer function (below) relating fuel injection fluctuation to heat release for the Limousine test rig. For the absolute value, both the time-averaged $\mathrm{abs}\big(\bar{\mathcal{G}}(f)\big)$ as well as the time-wise RMS $\mathcal{G}_{\mathrm{RMS}}(f)$ are shown. Frequencies are non-dimensionalised with the respective dominant oscillation frequency.

The absolute value abs $\bar{\mathcal{G}}$ at the dominant frequency is an order of magnitude lower for the Limousine than for the Hummer. The distance between $\mathcal{G}_{\mathrm{RMS}}$ and abs $\bar{\mathcal{G}}$ shows that the mean reason for this difference is the unsteadiness of $\mathcal{H}(\tau, t)$ of the Limousine rig.

Considering the high expected attenuation, the controller gain is set to the value of $0.03\,\%/\mathrm{Pa}$. This leads to a fuel flow modulation of $\pm 100\%$ for an amplitude of $3333\,\mathrm{Pa}$. Not to influence the mean operating conditions, the controller signal is clipped between $\pm 100\%$.

6.2.2.3 Effect of active control

Both simulations were forked at $t = 0.12\,\mathrm{s}$. The controller was activated with settings as described before. Figure 6.19 shows the time traces of pressure at the pressure probe. The pressure oscillation has clearly decreased for Hummer, but not for Limousine.
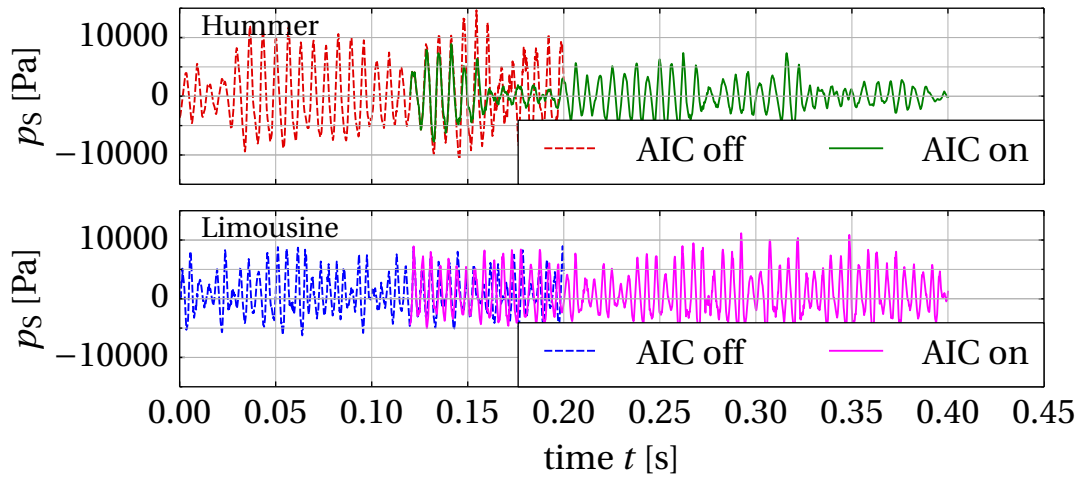
Figure 6.19: Time trace of pressure at the 'sensor' without and with control for both combustors.

The corresponding spectra, plotted in fig. 6.20, can be compared more quantitatively. For Hummer, even the higher modes at 300 and 550 Hz have been reduced significantly in amplitude, even though they lie outside of the frequency range in which the controller is active. The decrease in the peak at 300 Hz is expected, since this peak is a higher harmonic of the dominant oscillation. The peak at 550 Hz is the independent 3/4 wave mode.

Recalling fig. 6.17, no control authority was expected for these higher frequencies either. The results for Limousine on the other hand show no structural in- or decrease of the pressure fluctuations. The results shown in fig. 6.20 compare well to the experimental results given in fig. 6.6, at least in terms of amplitude and frequency of the dominant peaks. Minor peaks and general spectral distribution show some discrepancy. The experimental results show smoother specra, and a lower noise level, since the results could be averaged over a longer time to get statistically more meaningful results.
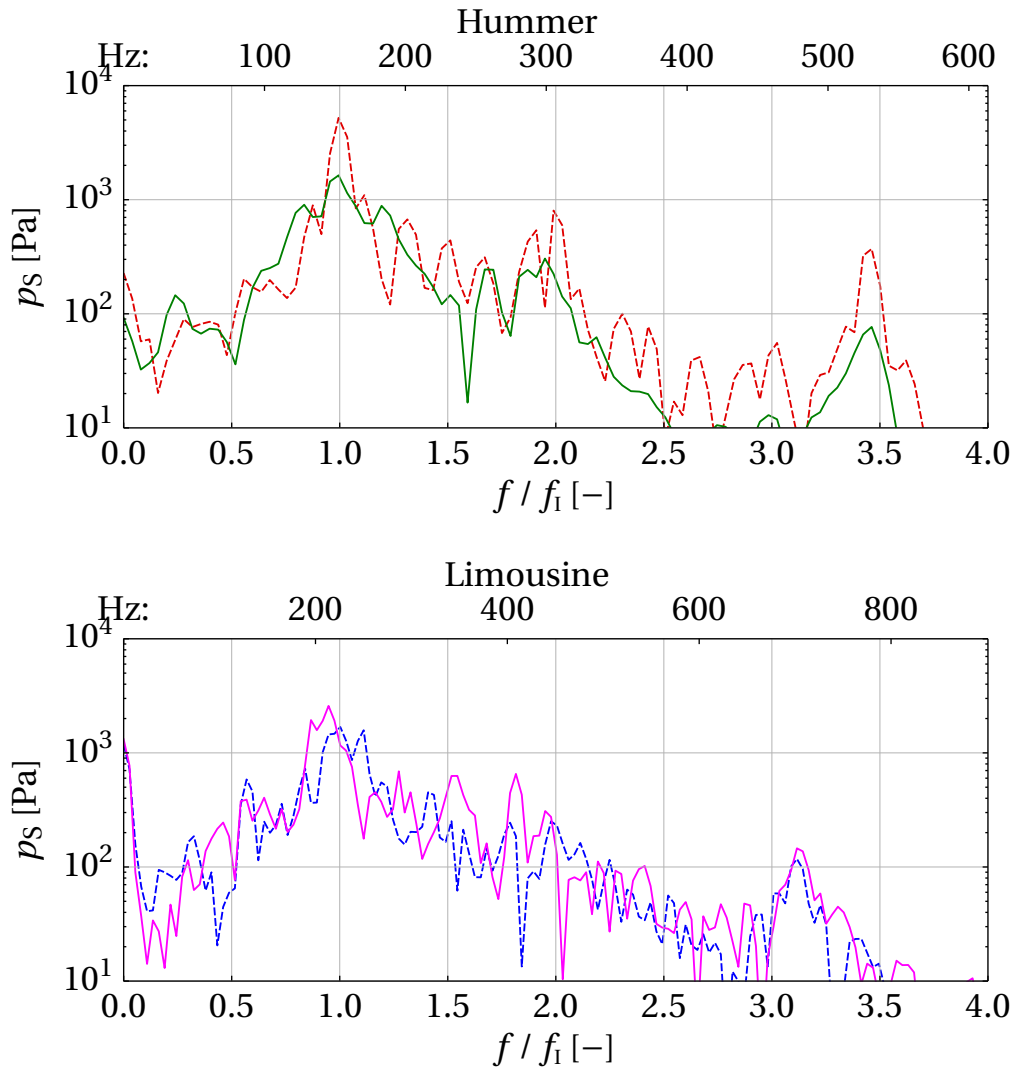
Figure 6.20: Comparison of pressure spectra with and without active control. The frequencies are normalised on the lower axes using the uncontrolled peak frequency.

Now it is interesting to see whether the convective delay has changed due to the operation of active control. To this end, the same analysis as applied to the uncontrolled simulation in sec. 6.2.2.2, was applied to the controlled case, leading to figs. 6.21 and 6.22.
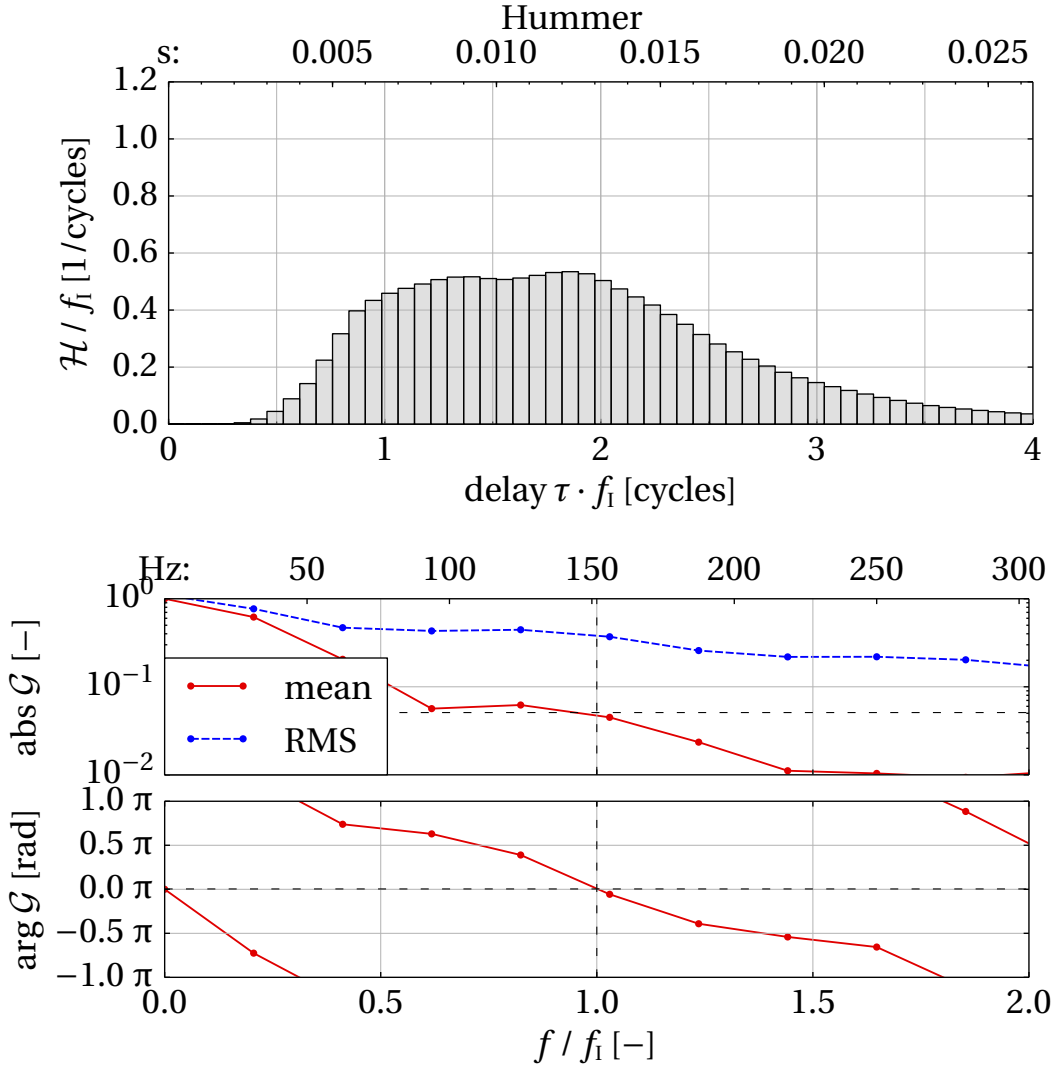
Figure 6.21: Metrics analogous to fig. 6.17 for the Hummer rig with active control applied. Under the influence of active control, the flame has become longer, and moved further downstream.

For Hummer, the controlled flame extended further downstream. Schaffgotsch[241] noted (in 1857) that the *average* flame shape can change under influence an acoustic field, although he reported the unstable flame to be
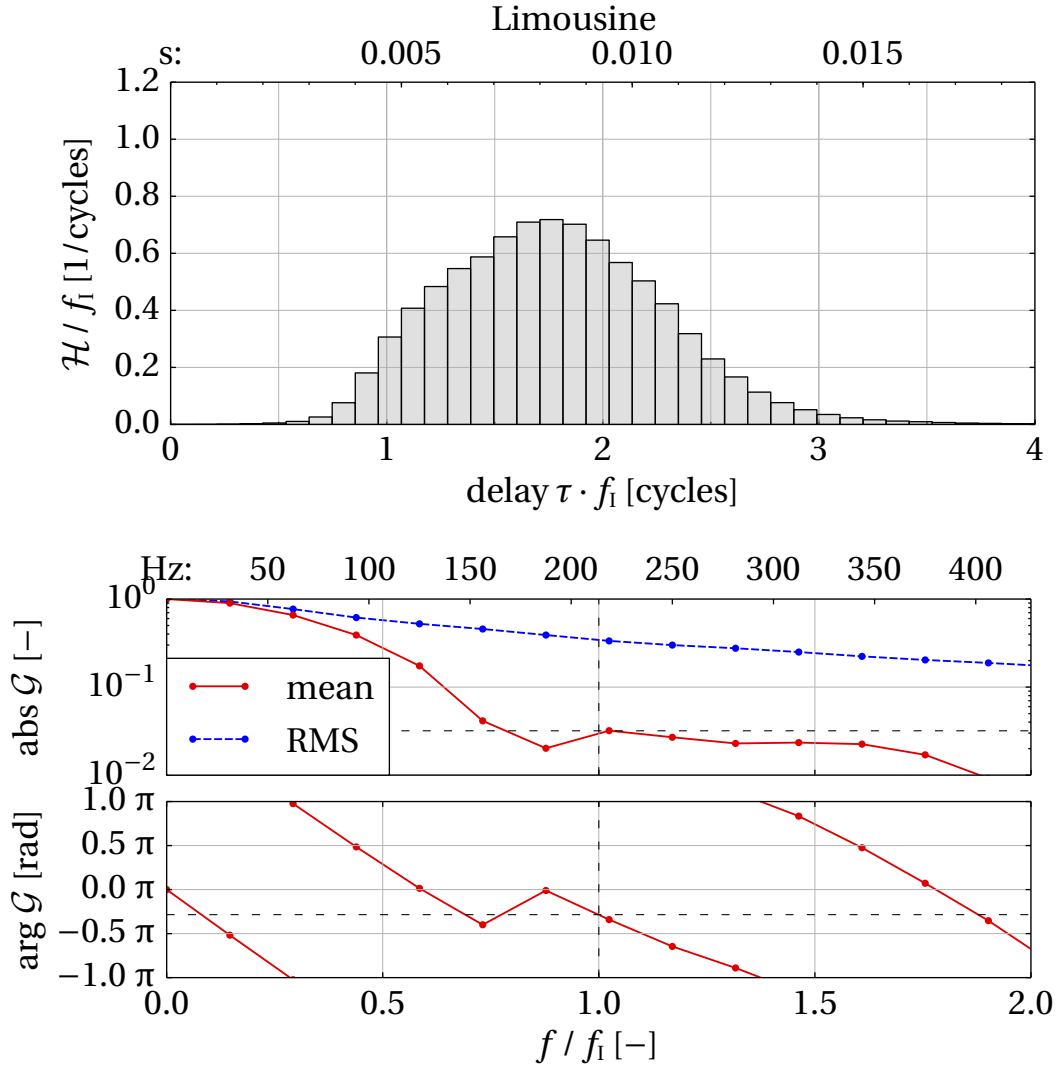
Figure 6.22: Metrics analogous to fig. 6.18 for the Limousine rig with active control applied. Contrary to the situation shown in fig. 6.21, the influence of active control on the flame shape is minimal.

longer. Auer et al.[12: fig.12] describes in greater detail the influence on the flame shape of the phase difference between air and fuel flow fluctuation.

In the current case the change in flame shape and position leads to less control authority (decrease of abs $\bar{\mathcal{G}}$), and more dramatically, a shift in the phase of $\bar{\mathcal{G}}$ (i.e. suboptimal controller settings), which decreases the effect of control with the previously set phase shift. For the Limousine combustor the changes in flame shape are much less. Figure 6.23 shows the evolution of the pressure fluctuation together with movement of the flame in the Hummer rig around $t = 0.16$ s. First the pressure amplitude goes down, then the flame stabilises further down stream (at a larger value of τ). Then the instability recovers with a lower amplitude and the flame returns to an intermediate value of τ.
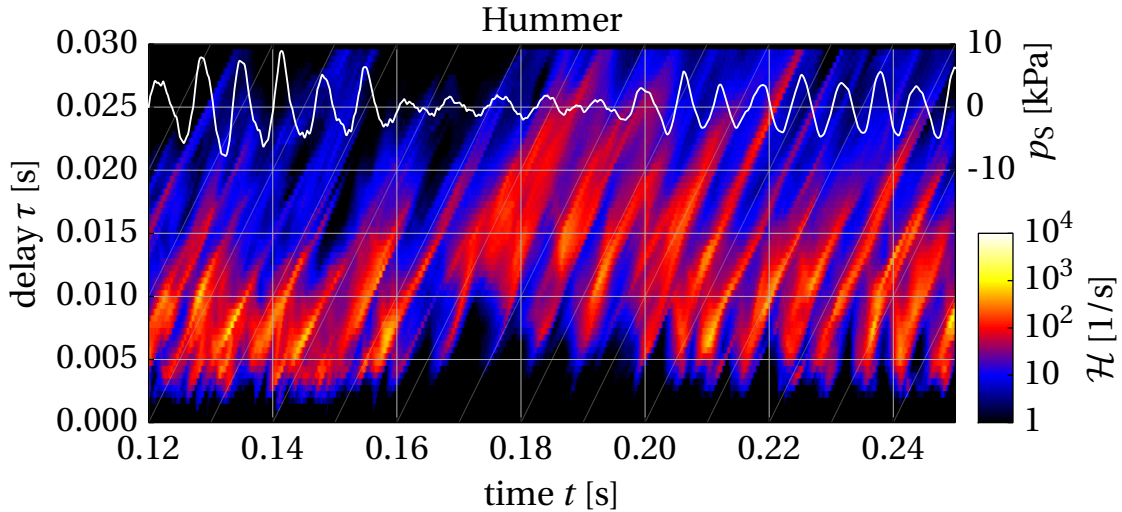
Figure 6.23: The flame of the Hummer combustor moves downstream at $t \approx 0.17$ s, during a period of relatively low pressure fluctuation. Subsequently the pressure fluctuation recovers in amplitude again, but to a lower amplitude than the uncontrolled oscillation.

This process forms feedback loop between the flame position and the amplitude of the instability, at a frequency below that of the instability, which could explain bistable behaviour or intermittent oscillation for instance.

The limitations on active control, posed by time delay, are discussed by Cohen and Banaszuk.[52] The suppression of the oscillation on the Hummer combustor might be improved by adapting the phase shift to the change in flame shape (for instance using the controller discussed by[14]). Experiments on the Hummer combustor showed that the amplitude of the pressure fluctuation was not

always a smooth function of the controller settings, nor was it always single-valued, so that both a stable and unstable state could be found for those conditions. This poses a serious threat to the robustness of adaptive control on this combustor.

6.2.3 Discussion and conclusion

Two combustors were modelled in ANSYS CFX. Active control was implemented analogous to experiment by modulation of the fuel mass flow. The distribution of the convective time between fuel injector and flame is evaluated and used as an estimate for the impulse response relating fuel mass inflow and heat release. Controller settings were based on results from a simulation without active control. The effectiveness of active control was demonstrated on the Hummer rig. Active control was unsuccessful on the Limousine rig in experiment, for reasons then not properly understood. The computational results suggest that the dispersion and temporal variation of the convective time delay are decisive for success or failure of active control by fluctuation of the fuel mass flow.

These criteria can be used for engineering applications. Generally, this form of actuation for active control is considered problematic when either the dispersion or temporal variation of τ is too large, e.g. when the flame is too long, or stabilised too far downstream of the fuel injector, or when mixing causes too much distribution in the convective time between the injector and the flame. When a combustor has only one fuel injector, a conflict of interest can exist. For stable operation a wide dispersion in time delay is preferable,[215] while a narrow dispersion is preferable for active control. In any case, a reliable, constant time delay makes a combustor more reliable in operation. If a combustor has multiple fuel injectors, it is advisable to apply active control on those injectors closest to the flame.

In sec. 6.2.1.2, the response of the heat release to fluctuations of the fuel mass flow was estimated, disregarding the influences of flame surface A_{fl} and the flame speed S_{L}. The impulse response is estimated as the distribution of the heat release over convective time τ.

In the case of the Hummer combustor, the average flame shape changed significantly due to the action of active control. So that ideally the controller settings could be updated. The initial settings for the Hummer combustor

were effective enough to realise a significant reduction in pressure amplitude, legitimating the assumptions made in sec. 6.2.1.2 for this case.

In the case of the Limousine burner, the flame shape varies much more strongly and chaotically over time. It is therefore assumed that the coherent influence of A_{fl} and S_{L} on the impulse response are negligible. Follow-up research might give a more definitive answer. System identification could be performed by analysis of the reaction of the flame to uncorrelated fluctuation of the flame, but this would take a much longer simulated time before the controller could be started.

7 Conclusion and outlook

This research investigated control authority for active damping of combustion instabilities, both experimentally and in CFD (ANSYS CFX). The low-order network modelling package taX was extended to model active instability control (AIC). This chapter will recapture the main findings, and recommend follow-up research.

7.1 Experimental results

Two combustors were constructed, dubbed the Hummer and the Limousine test rig. Both exhibit a clear thermoacoustic instability, corresponding to the axial quarter-lambda mode. AIC was applied to both combustors in experiment. The instability of the Hummer test rig was damped successfully, but that of the Limousine combustor was not. The reason for this discrepancy was investigated in CFX.

A comparison between excitation with direct dive valve (DDV) and loudspeaker showed that the DDV is more effective for greater thermal power P_{th}, while the loudspeaker is more effective for lower thermal power. To generalise these results, and to realise more predictive value, a DDV model was developed for network modelling in taX.

The main challenges that remain from an experimental perspective are the following:

Other actuators — Only two types of actuators (valves and loudspeakers) were investigated. Considering the conclusions drawn from CFD, it would be interesting to see if active control on the Limousine combustor could be realised with other actuators. Actuators which could reduce the delay between controller output and combustion would be specifically interesting, such as spark plugs[296] or air or fuel jets.[280]

Since unstable combustion can be a desirable phenomenon – for instance as marketed by Pulsed Heat[217] – it could be investigated to what extent actively destabilised combustion could improve combustion systems.

Reproducibility — The amplitude of the combustion instability does not always have the same amplitude for the same operating conditions. For this reason, comparative measurements such as in sec. 6.1 were made in prompt succession.

After ignition, the oscillation behaviour changes over minutes due to ambient heating of the liner, but this does not influence the reproducibility for measurements recorded after the heating-up phase. Effects that work over longer time (say, months, many of hours of operation) have not been quantified nor identified thoroughly.

7.2 CFD simulation

AIC was applied to both combustors in CFD, analogous to experiment. In experiment, relatively long series of measurement data are used to converge to optimal controller settings. In CFD on the other hand, the optimal controller settings are estimated by evaluating the distribution of convective time from the fuel injector to the flame. This distribution is taken as an estimate of impulse response relating the heat release of the flame to modulation of the fuel flow, and accordingly its Fourier transform is an estimate of the corresponding transfer function $\bar{\mathcal{G}}(f)$.

The results – i.e. the effectiveness of AIC – compare well to experiment. The absolute value of the estimated transfer function at the dominant frequency $\bar{\mathcal{G}}(f_{I,1})$ is more then ten times higher for the Hummer combustor than for the Limousine. The flame shape is understood to cause the difference in controllability between both combustors. Although this data gives a good impression whether better control authority can be realised on one combustor than on another, it does not tell what would be 'good enough' to realise a certain level of suppression. This question might better be answered by acoustical network modelling.

It was also found that the action of AIC changed the *average* flame shape. This is a factor that should be taken into account by models and controllers for the purpose of thermoacoustics.

The following question remain for follow-up research:

How could the effect of fuel flow fluctuation on the heat release be estimated quicker? — The current simulation took longer to complete than it would normally take to try out AIC in experiment. The results from CFD provided additional insight compared to the experimental results, but the engineering value of the approach followed here would be much higher if $\bar{\mathcal{G}}(f_{I,1})$ could be estimated quicker. The flow downstream from the flame holder is not uniform and not steady, so $\bar{\mathcal{G}}(f)$ cannot be determined straightforwardly from the geometrical position of the flame.

7.3 Network modelling

The low-order thermoacoustic network modelling tool taX was enhanced to model AIC. The Hummer combustor was modelled with and without control. To this end, the loudspeaker element was extended with an option to actuate depending on acoustic fluctuations elsewhere in the system.

Loudspeaker model should predict realisable excitation — In the current formulation, the user has to define the level of loudspeaker excitation in terms of the acoustic particle velocity. This quantity is however not an intrinsic property of the loudspeaker, and as such it cannot be found in a the specification sheet of a loudspeaker. Appendix B presents an outline for a model that would be more practical for engineering applications.

Non-linearities — The amplitude of a limit cycle is an important quantity in gas turbine operation and experiment. The influence of the amplitude of the oscillation on the flame shape for instance, has a great influence on the realisable level of damping.

In a similar vein, it would be useful if random excitation (combustion noise) would be represented by the flame element, so that combustion noise, and the resulting amplitudes of marginally stable modes can be predicted.

7.4 Valve model

Since the loudspeaker was the only available actuator element, an additional element was developed to represent the DDV. Embedded in an acoustic network, it can give a good first prediction of the effectiveness of a certain implementation in an acoustic network.

The accuracy of the valve model could be improved — The model results for the source coefficient shown in sec. 5.4 compare well to experiment. Especially the argument of the reflection coefficient of the modelled valve still shows significant discrepancy with the measurements. More elaborate measurements, where acoustic quantities are determined at the valve inlet as well, might indicate where the cause of this discrepancy is to be found.

There are many area changes and sharp bends in the short ducts inside the bushing of the valve, leading towards and away from the piston. A valve with a 'cleaner' and more accessible geometry might be easier to model.

This data on which the model was based did not differentiate between Mach and Reynolds number effects, since only one fluid (air) was used. For application in fuel systems with other gases, the influence of gas type should be investigated.

The valve element should be make usable for AIC — The valve model described in this thesis does not facilitate feedback yet, as the loudspeaker does. To evaluate AIC by means of valve excitation, this option should be included in the valve element.

Acknowledgements

Bibliography

[1] **M. Åbom and H. Bodén.** Error analysis of two-microphone measurements in ducts with flows. *J. Acoustical Soc. America,* 83(6):2429–2438, 1988. (ref. on p. 99)

[2] **S. A. Abrukov, V. V. Kurzhunov, and V. N. Mezdrikov.** Effect of an electric field on the vibratory combustion of propane. *Combustion, Explosion & Shock Waves,* 2(2):43–44, 1966. ISSN 0010-5082. DOI: `10.1007/BF00749231`. (ref. on p. 52, 58)

[3] **J. Ackeret.** Der Luftwiederstand bei sehr grossen Geschwindigkeiten. *Schweizerische Bauzeitung,* 94:179–183, 1929. DOI: `10.5169/seals-43431`. (ref. on p. 65)

[4] **V. V. Afanas'ev.** Active control of combustion stability by means of an electrical discharge. *Combustion, Explosion & Shock Waves,* 35(3):252–260, 1999. ISSN 0010-5082. DOI: `10.1007/BF02674446`. (ref. on p. 58)

[5] **Air Liquide.** Gas encyclopædia. website, 2009. URL: `encyclopedia.airliquide.com` (ref. on p. xxiii, 127, 227)

[6] **A. C. Altunlu, M. Shahi, A. Pozarlik, P. J. M. N. Hoogt, J. B. W. Kok, and A. N. Boer.** Fluid-structure interaction on the combustion instability. In *19th Int'l Cgr. Sound & Vibration (ICSV19),* Vilnius, LT, 2012. (ref. on p. 109)

[7] **A. Andreini, B. Facchini, I. Vitale, and F. Turrini.** Thermoacoustic analysis of a full annular lean burn aero-engine combustor. In *ASME Turbo Expo,* No. GT2013-94877, San Antoni, US-TX, June 2013. DOI: `10.1115/GT2005-68373`. (ref. on p. 9)

[8] **A. M. Annaswamy, M. Fleifil, J. W. Rumsey, R. Prasanth, J. P. Hathout, and A. F. Ghoniem.** Thermoacoustic instability: Model-based optimal control designs and experimental validation. *IEEE Trans. Control Systems Tech.,* 8(6):905–918, 2000. DOI: `10.1109/87.880593`. (ref. on p. 61)

[9] **A. M. Annaswamy and A. F. Ghoniem.** Active control of combustion instability: Theory and practice. *Control Systems, IEEE,* 22(6):37–54, 2002. (ref. on p. 136, 162)

[10] **P. Argüelles, M. Bischoff, P. Busquin, B. A. C. Droste, R. Evans, W. Kröll, J. L. Lagardère, A. Lina, J. Lumsden, D. Ranque, S. Rasmussen, P. Reutlinger, S. R. Robins, H. Terho, and A. Wittlöv.** European aeronautics: A vision for 2020, Jan. 2001. URL: `www.acare4europe.org/documents/vision-2020` (ref. on p. 9)

[11] **M. P. Auer, C. Hirsch, and T. Sattelmayer.** Influence of the interaction of equivalence ratio and mass flow fluctuations on flame dynamics. In *ASME Turbo Expo,* No. GT2005-68373, 2005. DOI: `10.1115/GT2005-68373`. (ref. on p. 119)

[12] **M. P. Auer, C. Hirsch, and T. Sattelmayer.** Influence of air and fuel mass flow fluctuations in a premix swirl burner on flame dynamics. In *ASME Turbo Expo,* No. GT2006-90127, pages 97–106, 2006. DOI: `10.1115/GT2006-90127`. (ref. on p. 194)

Bibliography

[13] **A. Avogadro.** Essai d'une maniere de determiner les masses relatives des molecules elementaires des corps, et les proportions selon lesquelles elles entrent dans ces combinaisons. *J. Phys., Chimie & Histoire Naturelle*, 73:58–76, 1811. URL: `www.biodiversitylibrary.org/item/29681#page/64/mode/1up` (ref. on p. 21)

[14] **A. Banaszuk, K. B. Ariyur, M. Krstić, and C. A. Jacobson.** An adaptive algorithm for control of combustion instability. *Automatica*, 40(11):1965–1972, 2004. ISSN 0005-1098. DOI: `10.1016/j.automatica.2004.06.008`. (ref. on p. 194)

[15] **M. S. Bartlett.** Periodogram analysis and continuous spectra. *Biometrika*, 37(1-2):1–16, 1950. DOI: `10.1093/biomet/37.1-2.1`. (ref. on p. 30)

[16] **M. S. Bartlett.** Smoothing periodograms from time-series with continuous spectra. *Nature*, 161(4096):686–687, May 1948. DOI: `10.1038/161686a0`. (ref. on p. 33)

[17] **V. G. Bazarov.** Design of injectors for self-sustaining of combustion chambers acoustic stability. In *Int'l Symp. Energy Conversion Fundamentals*, Istanbul, TR, June 2005. URL: `www.dtic.mil/get-tr-doc/pdf?AD=ADA446437` (ref. on p. 53)

[18] **D. Bernoulli.** *Hydrodynamica: sive de viribus et motibus fluidorum commentarii.* Johannis Reinholdi Dulseckeri, 1738. URL: `books.google.com/books?id=7zEVAAAAQAAJ` (ref. on p. 19, 72)

[19] **G. Billoud, M. A. Galland, C. H. Huu, and S. Cancel.** Adaptive active control of combustion instabilities. *Combustion Sci. & Tech.*, 81:257–283, 1992. DOI: `10.1080/00102209208951806`. (ref. on p. 60, 166)

[20] **A. W. Blackman.** Studies of screeching combustion and pressure-wave, flamefront interaction. *Combustion & Flame*, 5(0):175–190, 1961. ISSN 0010-2180. DOI: `10.1016/0010-2180(61)90093-1`. (ref. on p. 52)

[21] **A. W. Blackman.** Effect of nonlinear losses on the design of absorbers for combustion instabilities. *J. American Rocket Soc.*, 30(11):1022–1028, 1960. DOI: `10.2514/8.5307`. (ref. on p. 54)

[22] **R. B. Blackman and J. W. Tukey.** Particular pairs of windows. In *The measurement of power spectra, from the point of view of communications engineering*, pages 95–99. Dover, New York, 1958. URL: `archive.org/details/TheMeasurementOfPowerSpectra` (ref. on p. 30)

[23] **G. J. Bloxsidge, A. P. Dowling, N. Hooper, and P. J. Langhorne.** Active control of reheat buzz. *AIAA J.*, 26(7):783–790, July 1988. DOI: `10.2514/6.1987-433`. presented as AIAA-Paper No. 87-0433 at the 25th AIAA Aerospace Sci. Meeting & Ex. (1987). (ref. on p. 6, 57, 58)

[24] **G. J. Bloxsidge, A. P. Dowling, and P. J. Langhorne.** Reheat buzz: An acoustically coupled combustion instability. Part 2. Theory. *J. Fluid Mech.*, 193:445–473, 1988. DOI: `10.1017/S0022112088002216`. (ref. on p. 62)

[25] **H. W. Bode.** U.S. patent nr. 2,123,178. *Amplifier*, 1938. Filed 1937. (ref. on p. 46)

[26] **H. W. Bode.** Relations between attenuation and phase in feedback amplifer design. *Bell System Tech. J.*, 19(3):421–454, July 1940. (ref. on p. 46)

[27] **H. Bodén and M. Åbom.** Influence of errors on the two-microphone method for measuring acoustic properties of ducts. *J. Acoustical Soc. America*, 79:541–549, 1986. (ref. on p. 99)

[28] **M. S. Bohn.** Response of a subsonic nozzle to acoustic and entropy disturbances. *J. Sound & Vibration*, 52(2):283–297, 1977. ISSN 0022-460X. DOI: `10.1016/0022-460X(77)90647-2`. (ref. on p. 136)

[29] **W. Bollay.** Aerodynamic stability and automatic control: The fourteenth Wright Brothers lecture. *J. Aeronautical Sci.*, 18(9):569–617, 1951. DOI: `10.2514/8.2050`. (ref. on p. 55)

[30] **M. R. Bothien, J. P. Moeck, and C. O. Paschereit.** Impedance tuning of a premixed combustor using active control. In *ASME Turbo Expo*, No. GT2007-27796, pages 607–617, Montreal, CA, May 2007. DOI: `10.1115/GT2007-27796`. (ref. on p. 57)

[31] **M. R. Bothien, J. P. Moeck, and C. O. Paschereit.** Assessment of different actuator concepts for acoustic boundary control of a premixed combustor. *J. Eng. Gas Turbines & Power*, 131(2):021502, Dec. 2009. DOI: `10.1115/1.2969088`. presented as GT2008-50171 at the ASME Turbo Expo 2008. (ref. on p. 57)

[32] **M. R. Bothien, J. P. Moeck, and C. O. Paschereit.** Active control of the acoustic boundary conditions of combustion test rigs. *J. Sound & Vibration*, 318(4–5):678–701, 2008. ISSN 0022-460X. DOI: `10.1016/j.jsv.2008.04.046`. (ref. on p. 99, 148)

[33] **R. Boyle.** *A defence [. . .] against Franciscus Linus.* Richard Davis, 3 edition, 1682. DOI: `10.3931/e-rara-16019`. (ref. on p. 21)

[34] **W. T. Brande.** The Bakerian lecture: On some new electro-chemical phenomena. *Phil. Trans.*, 104:51–61, Jan. 1814. DOI: `10.1098/rstl.1814.0005`. (ref. on p. 52)

[35] **A. Brandt and A. Linderholt.** A periodogram-based method for removing harmonics in operational modal analysis. pages 2625–2633, Leuven, BE, Sept. 2012. KU Leuven. (ref. on p. 33)

[36] **O. Brandt, H. Freund, and E. Hiedemann.** Schwebstoffe im Schallfeld. *Z. Physik*, 104 (7-8):511–533, 1937. DOI: `10.1007/BF01330066`. (ref. on p. 55)

[37] **G. B. Brayton.** U.S. patent nr. 125,166. *Improvements in gas engines*, 1872. (ref. on p. xv, 22)

[38] **S. Candel, S. Ducruix, D. Durox, and D. Veynante.** Combustion dynamics: Analysis and Control-Modeling. In *RTO / AVT Course "Active Control of Engine Dynamics"*, Brussels, BE, May 2001. URL: `ftp.rta.nato.int/public//PubFullText/RTO/EN/RTO-EN-020///EN-020-05.pdf` published in RTO-EN-020. (ref. on p. 63)

[39] **S. M. Candel.** Acoustic conservation principles and application to plane and modal propagation in nozzles and diffusers. *J. Sound & Vibration*, 41(2):207–232, 1975. (ref. on p. 136)

[40] **J. A. Caravalho, Jr. and W. F. N. dos Santos.** Radiation errors in temperature measurements with thermocouples in a cylindrical combustor. *Int'l Comm. Heat Mass Transfer*, 1990. (ref. on p. 122)

Bibliography

[41] **M. W. Chase, Jr.**   NIST-JANAF thermochemical tables. *J. Phys. & Chem. Ref. Data*, Monograph 9:1–1951, 1998.   URL: `webbook.nist.gov/cgi/cbook.cgi?Source=1998CHA1-1951&Units=SI&Mask=1` (ref. on p. xxiii, 228)

[42] **C. C. Cherry and W. G. Haymes.** U.S. patent nr. 3,795,106. *Baffled solid propellant motor*, 1974. Filed 1972. (ref. on p. 54)

[43] **M. Chiollaz and B. Favre.** Engine noise characterisation with Wigner–Ville time–frequency analysis. *Mechanical Systems & Signal Processing*, 7(5):375–400, 1993. DOI: `10.1006/mssp.1993.1022`. (ref. on p. 38)

[44] **E. F. F. Chladni.** Beobachtungen über die durch Brennen der entzündbaren Luft in einer Röhre hervorzubringenden Töne. *Der Gesellschaft naturforschender Freunde zu Berlin, Neue Schriften*, 1:125–130, 1795. URL: `www.ub.uni-bielefeld.de/diglib/aufkl/gesnatfreu/gesnatfreu.htm` (ref. on p. 4)

[45] **J. C. F. Chow.** The attenuation of acoustic waves in a two-phase medium. Technical Report 602622, Brown University, Division of Engineering, Providence, US-RI, May 1963. URL: `www.dtic.mil/dtic/tr/fulltext/u2/602622.pdf` (ref. on p. 55)

[46] **B. T. Chu.** Stability of systems containing a heat source: The Rayleigh criterion. Research Memorandum RN 56D27, NASA, 1956. URL: `ntrs.nasa.gov/archive/nasa/casi.ntrs.nasa.gov/19930089361_1993089361.pdf` (ref. on p. 22)

[47] **B. T. Chu.** On the energy transfer to small disturbances in fluid flow (Part I). *Acta Mechanica*, 1(3):215–234, 1965. ISSN 0001-5970. DOI: `10.1007/BF01387235`. (ref. on p. 22)

[48] **B. T. Chu.** On the generation of pressure waves at a plane flame front. In *4th Symp. (Int'l) Combustion*, pages 603–612, 1953. (ref. on p. 78)

[49] **Y. C. Chu, A. P. Dowling, and K. Glover.** Robust control of combustion oscillations. In *Conf. Control Applications*, Trieste, IT, 1998. DOI: `10.1109/CCA.1998.721642`. (ref. on p. 61)

[50] **B. P. E. Clapeyron.** Sur la puissance motrice de la chaleur. *J. École Polytechnique*, 14: 153–190, 1834. URL: `gallica.bnf.fr/ark:/12148/bpt6k4336791/f157` (ref. on p. 21)

[51] **R. Clausius.** Über die bewegende Kraft der Wärme, Part I. *Ann. Physik*, 155(3):368–397, 1850. URL: `gallica.bnf.fr/ark:/12148/bpt6k15164w/f384` (ref. on p. 19)

[52] **J. M. Cohen and A. Banaszuk.** Factors affecting the control of unstable combustors. *J. Propulsion & Power*, 19(5):811–821, Sept. 2003. DOI: `10.2514/2.6196`. (ref. on p. 194)

[53] **J. W. Cooley and J. W. Tukey.** An algorithm for the machine calculation of complex Fourier series. *Mathematics Computation*, 19:297–301, 1965. (ref. on p. 30)

[54] **Crane Co.** Flow of fluids through valves, pipes, and fittings. Technical Report 410, Crane Co., Chicago, US-IL, 1972. 12th printing. (ref. on p. 141)

[55] **L. Crocco and S. I. Cheng.** *Theory of combustion instability in liquid propellant rocket motors.* Cambridge Univ Press, 1956. URL: `www.dtic.mil/docs/citations/AD0688924` (ref. on p. 78)

[56] **F. E. C. Culick.** Unsteady motions in combustion chambers for propulsion systems. Technical Report RTO-AG-AVT-039, RTO / NATO, 2006. URL: `ftp://ftp.rta.nato.int//PubFullText/RTO/AG/RTO-AG-AVT-039` (ref. on p. 5, 6, 9, 52, 58, 62, 95)

[57] **F. E. C. Culick.** Dynamics of combustion systems: Fundamentals, acoustics and control. In *RTO / AVT Course "Active Control of Engine Dynamics"*, Brussels, BE, May 2001. URL: `ftp.rta.nato.int/public//PubFullText/RTO/EN/RTO-EN-020///EN-020-04.pdf` published in RTO-EN-020. (ref. on p. 63)

[58] **F. E. C. Culick and S. Palm.** Active control of combustors after twenty years' efforts. *Progr. in Propulsion Physics*, 1:441–468, 2009. DOI: `10.1051/eucass/200901441`. (ref. on p. 13, 56, 59, 60, 62, 136)

[59] **d'Alembert.** Recherches sur la courbe que forme une corde tenduë, mise en vibration. *Hist. Ac. Roy. Sci. & Bel.-Let. Berlin*, (1747):214–219, 1749. URL: `bibliothek.bbaw.de/bbaw/bibliothek-digital/digitalequellen/schriften/anzeige/index_html?band=02-hist/1747&seite:int=243` (ref. on p. 65)

[60] **d'Alembert.** Suite des recherches sur la courbe que forme une corde tenduë, mise en vibration. *Hist. Ac. Roy. Sci. & Bel.-Let. Berlin*, (1747):220–249, 1749. URL: `bibliothek.bbaw.de/bbaw/bibliothek-digital/digitalequellen/schriften/anzeige/index_html?band=02-hist/1747&seite:int=249` (ref. on p. 65)

[61] **d'Alembert.** Addition au mémoire sur la courbe que forme une corde tenduë, mise en vibration. *Hist. Ac. Roy. Sci. & Bel.-Let. Berlin*, (1750):355–360, 1752. URL: `bibliothek.bbaw.de/bbaw/bibliothek-digital/digitalequellen/schriften/anzeige/index_html?band=02-hist/1750&seite:int=359` (ref. on p. 65)

[62] **I. Daubechies.** Orthonormal bases of compactly supported wavelets. *Comm. Pure & Appl. Math.*, 41(7):909–996, 1988. (ref. on p. 36)

[63] **J. W. Deardorff.** A numerical study of three-dimensional turbulent channel flow at large Reynolds numbers. *J. Fluid Mech.*, 41:453–480, 1970. DOI: `10.1017/S0022112070000691`. (ref. on p. 25)

[64] **J. C. DeLaat and C. T. Chang.** Active control of high frequency combustion instability in aircraft gas-turbine engines. Technical Report TM-2003-212611, NASA, Cleveland, OH-US, Sept. 2003. ISABE-2003-1054. (ref. on p. 56)

[65] **J. C. DeLaat, G. Kopasakis, J. R. Saus, C. T. Chang, and C. Wey.** Active combustion control for a low-emissions aircraft engine combustor prototype: Experimental results. *J. Propulsion & Power*, 29(4):991–1000, 2013. DOI: `10.2514/1.B34653`. (ref. on p. 9)

[66] **D. W. Derham.** Experiments and observationmotion sounds on the motion of sound &c. *Phil. Trans.*, 5:380–395, 1708. URL: `books.google.com/books?id=Cj7pbpAwBgUC&pg=PA380` Translated from Latin (orig. DOI: `10.1098/rstl.1708.0001`). (ref. on p. 55)

[67] **P. J. Dines.** *Active control of flame noise.* PhD thesis, University of Cambridge, 1983. (ref. on p. 55, 58)

Bibliography

[68] **A. P. Dowling.** Active control of instabilities in gas turbines. In *RTO / AVT Symp. "Active Control Technology…"*, No. RTO MP-051, Braunschweig, DE, May 2000. URL: `ftp.rta.nato.int/public//PubFullText/RTO/MP/RTO-MP-051///MP-051-$K2.pdf` (ref. on p. 9, 58, 59)

[69] **A. P. Dowling.** Modeling and control of combustion oscillations. In *ASME Turbo Expo*, No. GT2005-68452, Reno-Tahoe, US-NV, June 2005. (ref. on p. 22, 25)

[70] **J. D. Eldredge and A. P. Dowling.** The absorption of axial acoustic waves by a perforated liner with bias flow. *J. Fluid Mech.*, 485:307–335, May 2003. DOI: `10.1017/S0022112003004518`. (ref. on p. 54)

[71] **T. Emmert, S. Jaensch, C. Sovardi, and W. Polifke.** taX – a flexible tool for low-order duct acoustic simulation in time and frequency domain. In *Forum Acousticum*, Krakow, PL, Sept. 2014. URL: `www.fa2014.pl` (ref. on p. 63)

[72] **P. S. Epstein and R. R. Carhart.** The absorption of sound in suspensions and emulsions. I. Water fog in air. *J. Acoustical Soc. America*, 25(3):553–565, 1953. DOI: `10.1121/1.1907107`. (ref. on p. 55)

[73] **L. Euler.** Principes généraux du mouvement des fluides. *Mém. Acad. Sci. Berlin*, 11:274–315, 1757. URL: `www.math.dartmouth.edu/~euler/pages/E226.html` (ref. on p. 18)

[74] **European Comission.** Large Combustion Plants (LCP) directive, Nov. 2001. URL: `ec.europa.eu/environment/air/pollutants/stationary/lcp/legislation.htm` (ref. on p. 8)

[75] **M. Faraday.** Experimental researches in electricity. *Phil. Trans. R. Soc. London*, 122:125–162, Jan. 1832. DOI: `10.1098/rstl.1832.0006`. (ref. on p. 230)

[76] **E. C. Fernandes and R. E. Leandro.** Modeling and experimental validation of unsteady impinging flames. *Combustion & Flame*, 146:674–686, 2006. (ref. on p. 107)

[77] **J. E. Ffowcs Williams.** Review lecture: Anti-sound. *Proc. R. Soc. London; Ser. A*, 395 (1808):63–88, Sept. 1984. DOI: `10.1098/rspa.1984.0090`. (ref. on p. 55)

[78] **J. E. Ffowcs Williams, P. J. Dines, and M. A. Heckl.** U.S. patent nr. 4,557,106. *Combustion system for a gas turbine*, 1985. Filed 1984. (ref. on p. 56)

[79] **B. S. Finn.** Laplace and the speed of sound. *ISIS*, 55(179):7, 1964. URL: `www3.nd.edu/~powers/ame.20231/finn1964.pdf` (ref. on p. 21)

[80] **H. Forkel.** Modification to the burning velocity model at ANSYS Germany. Private communication, 2012. (ref. on p. 26, 175)

[81] **J. Fourier.** Mémoire sur la propagation de la chaleur dans les corps solides. *Nouveau Bull. Sci. Soc. Philomatique Paris*, 1(6):112–116, Mar. 1808. URL: `www.biodiversitylibrary.org/item/24789#page/120` (ref. on p. 27)

[82] **J. L. Fox.** Preliminary investigation of Helmholtz resonators for damping pressure fluctuations in 3.6 inch ram jet at Mach number 1.90. Technical Report RM E51CO5, NACA, 1951. URL: `naca.central.cranfield.ac.uk/reports/1951/naca-rm-e51c05.pdf` (ref. on p. 6, 54)

[83] **M. Fukuda.** A study on the exhaust muffler of internal combustion engine. *Bull. JSME*, 6(22):255–269, 1963. DOI: `10.1299/jsme1958.6.255`. (ref. on p. 62, 69)

[84] **Y. T. Fung and V. Yang.** Active control of nonlinear pressure oscillations in combustion chambers. *J. Propulsion & Power*, 8(6):1282–1289., 1992. DOI: `10.2514/3.11474`. (ref. on p. 60)

[85] **Y. T. Fung, V. Yang, and A. Sinha.** Active control of combustion instabilities with distributed actuators. *Combustion Sci. & Tech.*, 78(4-6):217–245, 1991. DOI: `10.1080/00102209108951750`. (ref. on p. 60)

[86] **D. Gabor.** Theory of communication. Part 1: The analysis of information. *J. IEEE; Ser. III: Radio & Communication Eng.*, 93(26):429–441, Nov. 1946. DOI: `10.1049/ji-3-2.1946.0074`. (ref. on p. 29, 36)

[87] **Gay-Lussac.** Mémoire sur la combinaison des substances gazeuses, les unes avec les autres. *Mém. Soc. Arcueil*, 2:207–234, 1809. URL: `books.google.com/books?id=hnJKAAAAYAAJ&pg=PA207` (ref. on p. 21)

[88] **J. L. Gay-Lussac.** Recherches sur la dilatation des gaz et des vapeurs. *Ann. Chimie*, 43:137–175, 1802. URL: `books.google.com/books?id=Z6ctSn3TIeYC&pg=PA137` French Republican date: an X. (ref. on p. 21)

[89] **General Electric Company.** 9HA gas turbine: World's largest, most efficient gas turbine, 2014. URL: `efficiency.gepower.com/pdf/GEA31097%209HA_Gas_Turbine_FINAL.pdf` (ref. on p. 6)

[90] **GHM Messtechnik GmbH.** Handmessgeräte » Druck » Geräte. website. URL: `https://greisinger.de/index.php?task=2&wg=165` (ref. on p. 96)

[91] **J. Goldmeer, S. Sanderson, G. Myers, J. Stewart, and M. D'Ercole.** Passive control of dynamic pressures in a dry, low NO_x combustion system using fuel gas circuit impedance optimization. In *ASME Turbo Expo*, No. GT2005-68605, 2005. (ref. on p. 53)

[92] **E. Gutmark, D. M. Hanson-Parr, T. P. Parr, K. C. Schadow, R. A. Smith, R. A. Stalnaker, and K. J. Wilson.** U.S. patent nr. 5,361,710. *Method and apparatus for the active control of a compact waste incinerator*, 1994. Filed 1993. (ref. on p. 58)

[93] **E. Gutmark, T. P. Parr, D. M. Hanson-Parr, and K. C. Schadow.** Use of chemiluminescence and neural networks inactive combustion control. In *23rd Symp. (Int'l) Combustion*. The Combustion Institute, 1990. DOI: `10.1016/S0082-0784(06)80370-X`. (ref. on p. 58, 60)

[94] **E. Gutmark, K. Schadow, R. Smith, and K. Wilson.** US patent nr. 5,428,951. *Method and apparatus for active control of combustion devices*, 1995. Filed 1993. (ref. on p. 58)

[95] **E. Gutmark, K. Wilson, K. Schadow, B. E. Parker, Jr., R. Barron, and G. C. Smith.** Dump combustor control using Polynomial Neural Network (PNN). In *AIAA 31st Aerospace Sci. Meeting*, No. AIAA-93-0117, Reno, US-NV, Jan. 1993. DOI: `10.2514/6.1993-117`. (ref. on p. 60)

[96] **A. Haar.** Zur Theorie der orthogonalen Funktionensysteme. *Mathematische Ann.*, 69 (3):331–371, 1910. ISSN 0025-5831. DOI: `10.1007/BF01456326`. (ref. on p. 36)

Bibliography

[97]   **T. Hammer, G. Lins, D. Branston, F. Dinkelacker, A. Sakhrieh, and A. Leipertz.** Electro-hydrodynamic control of premixed turbulent methane flames at pressures above 1 atm. In *ASME Turbo Expo*, No. GT2005-69137, Reno-Tahoe, US-NV, June 2005. (ref. on p. 52)

[98]   **G. H. Hardy.** On Hilbert transforms. *Quarterly J. Math.; Ser. os-3*, 1:102–112, 1932. DOI: `10.1093/qmath/os-3.1.102`. (ref. on p. 28, 36)

[99]   **D. T. Harrje and F. H. Reardon, editors**. *Liquid propellant rocket combustion instability*. Scientific and Technical Information Office, National Aeronautics and Space Administration, 1972. URL: `ntrs.nasa.gov/search.jsp?R=19720026079` NASA SP-194. (ref. on p. 5, 54)

[100]   **J. P. Hathout, A. M. Annaswamy, M. Fleifil, and A. F. Ghoniem.** A model-based active control design for thermoacoustic instability. *Combustion Sci. & Tech.*, 132(1-6):99–138, 1998. DOI: `10.1080/00102209808952012`. (ref. on p. 61)

[101]   **J. P. Hathout, A. M. Annaswamy, and A. F. Ghoniem.** Modeling and control of combustion instability using fuel injection. In *RTO / AVT Symp. "Active Control Technology..."*, Braunschweig, DE, May 2000. URL: `ftp.rta.nato.int/public/PubFullText/RTO/MP/RTO-MP-051/MP-051-PSP-23.pdf` published in RTO MP-051. (ref. on p. 61)

[102]   **J. P. Hathout, M. Fleifil, A. M. Annaswamy, and A. F. Ghoniem.** Why do secondary peaks occur in experimental active controllers of thermoacoustic instability? MIT Industrial Liaison Program Report 9-33, MIT, 1997. (ref. on p. 61)

[103]   **M. A. Heckl.** *Heat sources in acoustic resonators.* PhD thesis, University of Cambridge, Apr. 1985. (ref. on p. 55, 59)

[104]   **M. A. Heckl.** Active control of the noise from a Rijke tube. *J. Sound & Vibration*, 124(1): 117–133, 1988. DOI: `10.1016/S0022-460X(88)81408-1`. (ref. on p. 55, 60, 62)

[105]   **M. A. Heckl.** Non-linear acoustic effects in the Rijke tube. *Acustica*, 72:63–71, 1990. (ref. on p. 73, 78)

[106]   **H. Helmholtz.** Theorie der Luftschwingungen in Röhren mit offenen Enden. *J. reine & angew. Math.*, 57:1–131, 1860. URL: `openlibrary.org/books/OL6947572M` (ref. on p. 38)

[107]   **H. Herlufsen.** Dual channel FFT analysis. Technical Report 1, Brüel & Kjær, 1984. (ref. on p. 36)

[108]   **J. Hermann.** Private communication. (ref. on p. 13)

[109]   **J. Hermann.** *Anregungsmechanismen und aktive Dämpfung (AIC) selbsterregter Verbrennungsschwingungen in Flüssigkraftstoffsystemen.* PhD thesis, Technische Universität München, 1996. VDI-Fortschrittsbericht No. 364—Reihe 6. (ref. on p. 59, 95)

[110]   **J. Hermann, S. Gleis, and D. Vortmeyer.** Active instability control (AIC) of spray combustors by modulation of the liquid fuel flow rate. *Combustion Sci. & Tech.*, 118:1–25, 1996. DOI: `10.1080/00102209608951969`. (ref. on p. 58)

[111]   **J. Hermann, C. Hantschk, P. Zangl, S. Gleis, D. Vortmeyer, J. Seume, N. Vortmeyer, W. Krause, and A. Orthmann.** Aktive Instabilitätskontrolle an einer 170 MW Gasturbine. In *VDI-Bericht No. 1313, 18. DE–NL Flammentag*, pages 337–344, Delft, NL, Aug. 1997. (ref. on p. 166)

[112] **J. Hermann and A. Orthmann.** Combustion dynamics: Application of active insta-bility control on heavy duty gas turbines. In *RTO / AVT Course "Active Control of Engine Dynamics"*, 2001. URL: `ftp://ftp.rta.nato.int/PubFullText/RTO/EN/RTO-EN-020/EN-020-06.pdf` published in RTO-EN-020. (ref. on p. 14, 56, 57, 59, 60, 135, 139, 166, 175)

[113] **B. Higgins.** On the sound produced by a current of hidrogen gas passing throug a tube. With a letter from Dr. Higgins respecting the time of its discovery. *J. Natural Phil., Chemistry, & Arts*, 1:129–131, 1802. URL: `books.google.com/books?id=iAgAAAAMAAJ&pg=PA129` (ref. on p. 3, 4)

[114] **D. Hilbert.** *Grundzüge einer allgemeinen Theorie der linearen Integralgleichungen*. B. G. Teubner, Leipzig, 1912. URL: `https://archive.org/stream/grundzugeallg00hilbrich` (ref. on p. 28, 36)

[115] **S. J. Hiller, J. Hermann, and R. Widhopf-Fenk.** High pressure compressor stabilization by controlled pulsed injection. In *ASME Turbo Expo*, No. GT2012-68460, Copenhagen,DK, June 2012. (ref. on p. 14, 135)

[116] **A. Hirschberg.** Introduction to aero-acoustics of internal flows. Revised version of chapter from the course Advances in Aeroacoustics (VKI, 12-16 March 2001), 2009. (ref. on p. 152)

[117] **A. Hirschberg and S. W. Rienstra.** Elements of aeroacoustics. In *Lecture Series 1994-04*. Von Karman Institute for Fluid Dynamics, 1994. (ref. on p. 142)

[118] **H. W. M. Hoeijmakers.** Gasdynamics. Lecture notes, Univerity of Twente, 2009. (ref. on p. 16)

[119] **M. D. Horton and M. R. McGie.** Particulate damping of oscillatory combustion. *AIAA J.*, 1(6):1319–1326, 1963. DOI: `10.2514/3.1787`. (ref. on p. 55)

[120] **A. Huber.** *Impact of fuel supply impedance and fuel staging on gas turbine combustion stability*. PhD thesis, Technische Universität München, 2009. URL: `www.td.mw.tum.de/tum-td/de/forschung/dissertationen/download/N2009/huber09.pdf` (ref. on p. 62)

[121] **A. Huber and W. Polifke.** Dynamics of practical premixed flames, part I: Model structure and identification. *Int'l J. Spray & Combustion Dynamics*, 1(2):199–228, 2009. DOI: `10.1260/175682709788707431`. (ref. on p. 182)

[122] **A. Huber and W. Polifke.** Dynamics of practical premixed flames, part II: Identification and interpretation of CFD data. *Int'l J. Spray & Combustion Dynamics*, 1(2):229–249, 2009. DOI: `10.1260/175682709788707440`. (ref. on p. 182)

[123] **K. Ichikawa.** Frequency-domain pole assignment and exact model-matching for delay systems. *Int'l J. Control*, 41(4):1015–1024, 1985. DOI: `10.1080/00207518508961180`. (ref. on p. 61)

[124] **IfTA Ingenieurbureau für Thermoakustik GmbH.** Argus OMDS 3.0—Advanced Oscillation Monitoring and Diagnostic System. product flyer. (ref. on p. 93)

[125] **Inter Mercador.** IMG Stage Line: PA-Aktiv-Baustein AKB-50. manual, 2007. URL: `www.imgstageline.nu/manualer/AKB50.pdf` (ref. on p. 229)

Bibliography

[126] **S. H. Jang and J. G. Ih.** On the multiple microphone method for measuring in-duct acoustic properties in the presence of mean flow. *J. Acoustical Soc. America*, 103(3): 1520–1526, Mar. 1998. DOI: `10.1121/1.421289`. (ref. on p. 99)

[127] **M. G. Jones and T. L. Parrott.** Evaluation of a multi-point method for determining acoustic impedance. *Mechanical Systems & Signal Processing*, 3(1):15–35, Jan. 1989. DOI: `10.1016/0888-3270(89)90020-4`. (ref. on p. 99)

[128] **F. Joos and D. Vortmeyer.** Self-excited oscillations in combustion chambers with pre-mixed flames and several frequencies. *Combustion & Flame*, 65(3):253–262, 1986. ISSN 0010-2180. DOI: `10.1016/0010-2180(86)90039-8`. (ref. on p. 58)

[129] **J. P. Joule.** On the existence of an equivalent relation between heat and the ordinary forms of mechanical power. *Phil. Magazine; Ser. 3*, 27(179):205–207, 1845. DOI: `10.1080/14786444508645256`. (ref. on p. 19)

[130] **T. Kaiser.** Experimentelle Untersuchung von Servo-Linearmotor-Ventilen der Firma Moog. Technical report, IfTA Ingenieurbüro für Thermoakustik GmbH, 2012. (ref. on p. 141)

[131] **J. J. Keller.** Thermoacoustic oscillations in combustion chambers of gas turbines. *AIAA J.*, 33(12):2280–2287, Dec. 1995. DOI: `10.2514/3.12980`. (ref. on p. 9)

[132] **Kibitsu Jinja.** Narukama Shinji, 2011. URL: `kibitujinja.com/about/narukama.html` (ref. on p. 3)

[133] **Y. Kobayashi.** Experiment No. 24: 'steam pot' sound with empty cans. URL: `members.jcom.home.ne.jp/kobysh/experiment/kama/cankama.html` (ref. on p. 3)

[134] **J. Kok, S. Matarazzo, and A. K. Pożarlik.** The bluff body stabilized premixed flame in an acoustically resonating tube: Combustion CFD and measured pressure field. In *16th Int'l Cgr. Sound & Vibration (ICSV16)*, Kraków, PL, 2009. (ref. on p. 11)

[135] **R. König.** On manometric flames. *Phil. Magazine; Ser. 4*, 45(298):105–114, 1873. DOI: `10.1080/14786447308640822`. (ref. on p. xv, 42)

[136] **B. Kosztin, M. Heckl, R. A. J. Müller, and J. Hermann.** Instabilities in a model gas turbine combustor: Theory and experiment. In *17th Int'l Cgr. Sound & Vibration (ICSV17)*, Cairo, EG, 2010. (ref. on p. 11, 88)

[137] **B. Kosztin, M. Heckl, R. A. J. Müller, and J. Hermann.** Instabilities in a model gas turbine combustor with different mean-temperature profiles. In *18th Int'l Cgr. Sound & Vibration (ICSV18)*, Rio de Janeiro, BR, 2011. (ref. on p. 119)

[138] **W. Krebs and M. Lohrmann.** Thermoacoustic flame response of swirl flames. In *ASME Turbo Expo*, pages 333–344, Amsterdam, NL, June 2002. DOI: `10.1115/GT2002-30065`. GT-2002-30065. (ref. on p. 177, 183)

[139] **Lagrange.** Nouvelles recherches sur la nature et la propagation du son. *Mélanges de Philosophie et de Mathématique de la Société Royale de Turin*, 2:11–172, 1762. URL: `www.biodiversitylibrary.org/item/32644#page/247/mode/1up` (ref. on p. 16)

[140] **W. Lang, T. Poinsot, and S. Candel.** Active control of combustion instability. *Combustion & Flame*, 70(3):281–289, Jan. 1987. DOI: `10.1016/0010-2180(87)90109-X`. (ref.

on p. 56)

[141] **P. J. Langhorne, A. P. Dowling, and N. Hooper.** Practical active control system for combustion oscillations. *J. Propulsion & Power*, 6:324–333, 1990. DOI: `10.2514/3.25437`. (ref. on p. 56, 166)

[142] **P. S. Laplace.** Mémoire sur les approximations des formules qui sont fonctions de très grands nombres. *Mém. Acad. Sci.*, 1782:209–291, 1785. URL: `gallica.bnf.fr/ark:/12148/bpt6k775981/f218` (ref. on p. 27)

[143] **P. S. Laplace.** Mémoire sur les approximations des formules qui sont fonctions de très grands nombres (suite). *Mém. Acad. Sci.*, 1783:295–338, 1786. URL: `gallica.bnf.fr/ark:/12148/bpt6k775981/f304` (ref. on p. 27)

[144] **M. Lauer, M. Zellhuber, C. J. Aul, and T. Sattelmayer.** Determination of the heat release distribution in turbulent flames by a model based correction of OH* chemiluminescence. In *ASME Turbo Expo*, June 2011. DOI: `10.1115/1.4004124`. GT2011-45105. (ref. on p. 95, 105)

[145] **C. J. Lawn and W. Polifke.** A model for the thermo-acoustic response of a premixed swirl burner: Part II: The flame response. *Combustion Sci. Tech.*, 176(8):1359 – 1390, Aug. 2004. (ref. on p. 78)

[146] **D. K. Le, J. C. DeLaat, and C. T. Chang.** Control of thermo-acoustics instabilities: The multi-scale extended Kalman approach. In *39th AIAA/ASME/SAE/ASEE Joint Propulsion Conf. & Ex.*, vol. 4934, Huntsville, US-AL, July 2003. Citeseer. (ref. on p. 61)

[147] **R. Leandro, A. Huber, and W. Polifke.** *taX manual.* Technische Universität München, v0.9 edition, Oct. 2010. URL: `www.td.mw.tum.de/tum-td/en/forschung/infrastruktur/scientific_comp/taX_manual.pdf` (ref. on p. 14, 62, 136, 162)

[148] **J. LeConte.** On the influence of musical sounds on the flame of a jet of coal gas. *American J. Sci. & Arts; Ser. 2*, 25:62–67, 1858. URL: `www.biodiversitylibrary.org/item/88073#page/70` (ref. on p. 4)

[149] **D. C. Leinhos, S. G. Schneider, L. Fottner, F. Grauer, J. Hermann, M. Mettenleiter, and A. Orthmann.** Experiments in active stall control of a twin-spool turbofan engine. In *ASME Turbo Expo*, No. GT-2002-30002, Amsterdam, NL, June 2002. (ref. on p. 14)

[150] **H. Levine and J. Schwinger.** On the radiation of sound from an unflanged circular pipe. *Physical Review*, 73(4):383–406, Feb. 1948. DOI: `10.1103/PhysRev.73.383`. (ref. on p. 71, 73, 114)

[151] **Lewis Laboratory Staff.** A summary of preliminary investigations into the characteristics of combustion screech in ducted burners. Technical Report NACA TR 1384, NACA Lewis Flight Propulsion Laboratory, 1958. URL: `ntrs.nasa.gov/search.jsp?R=19930092364` (ref. on p. 6)

[152] **Lienhard and Lienhard.** *A heat transfer textbook.* Phlogiston Press, 3 edition, 2002. (ref. on p. 124, 125)

[153] **J. H. Lienhard.** Julius Robert Mayer. *The Engines of Our Ingenuity* 722. URL: `www.uh.edu/engines/epi722.htm` (ref. on p. 21)

Bibliography

[154] **T. Lieuwen, V. McDonell, E. Petersen, and D. Santavicca.** Fuel flexibility influences on premixed combustor blowout, flashback, autoignition, and stability. *J. Eng. Gas Turbines & Power*, 130(1):1–10, 2008. DOI: `10.1115/1.2771243`. 011506, Originally published as ASME GT2006-90770 (2006). (ref. on p. 9)

[155] **T. Lieuwen and G. Richards.** Recent progress in predicting, monitoring and controlling combustion driven oscillations in gas turbines. In *Power-Gen 2003*, Dec. 2003. (ref. on p. 7)

[156] **T. Lieuwen and B. T. Zinn.** Theoretical investigation of combustion instability mechanisms in lean premixed gas turbines. In *AIAA 36th Aerospace Sci. Meeting & Ex.*, No. AIAA-98-0641, 1998. DOI: `10.2514/6.1998-641`. (ref. on p. 9)

[157] **M. J. Lighthill.** The response of laminar skin friction and heat transfer to fluctuations in the stream velocity. *Proc. R. Soc. London; Ser. A*, 224(1156):1–23, June 1954. DOI: `10.1098/rspa.1954.0137`. (ref. on p. 5, 63)

[158] **M. J. Lighthill.** On sound generated aerodynamically. I. General theory. *Proc. R. Soc. London; Ser. A*, 211(1107):564–587, Mar. 1952. DOI: `10.1098/rspa.1952.0060`. (ref. on p. 63)

[159] **J. P. Longwell.** Combustion problems in ramjets. In *5th Symp. (Int'l) Combustion*, pages 48–56. The Combustion Institute, 1955. DOI: `10.1016/S0082-0784(55)80012-4`. (ref. on p. 6)

[160] **H. A. Lorentz.** *La théorie électromagnétique de Maxwell et son application aux corps mouvants.* E. J. Brill, 1892. URL: `https://archive.org/details/lathorielectrom00loregoog` (ref. on p. 229)

[161] **E. Lubarsky, D. Shcherbik, O. Bibik, and B. T. Zinn.** Active control of combustion oscillations by non-coherent fuel flow modulation. In *9th AIAA/CEAS Aeronautics Conf. & Ex.*, No. AIAA 2003-3180, Hilton Head, US-SC, May 2003. DOI: `10.2514/6.2003-3180`. (ref. on p. 61)

[162] **P. Lueg.** US patent nr. 2,043,416. *Process of silencing sound oscillations*, June 1936. Filed 1934. (ref. on p. 55)

[163] **D. G. Luenberger.** *Determining the state of a linear system with observers of low dynamic order.* PhD thesis, Stanford University, 1963. (ref. on p. 60)

[164] **E. Mach and P. Salcher.** Photographische Fixirung der durch Projektile in der Luft eingeleiteten Vorgänge. *Sitzungsberichte der Kaiserlichen Akademie der Wissenschaften (Wien); Ser. Math. -Naturw. Classe*, 95(2):764–780, 1887. (ref. on p. 65)

[165] **R. Mani.** Low-frequency sound propagation in a quasi-one-dimensional flow. *J. Fluid Mech.*, 104(1):81–92, 1981. DOI: `10.1017/S0022112081002826`. (ref. on p. 136)

[166] **A. Manitius and A. W. Olbrot.** Finite spectrum assignment problem for systems with delays. *IEEE Trans. Automatic Control*, 24(4):541–552, Aug. 1979. DOI: `10.1109/TAC.1979.1102124`. (ref. on p. 61)

[167] **F. E. Marble and S. M. Candel.** Acoustic disturbance from gas non-uniformities convected through a nozzle. *J. Sound & Vibration*, 55(2):225–243, 1977. (ref. on p. 136)

[168] **D. Marx, X. Mao, and A. J. Jaworski.** Acoustic coupling between the loudspeaker and the resonator in a standing-wave thermoacoustic device. *Applied Acoustics*, 67(5):402 – 419, 2006. ISSN 0003-682X. DOI: `10.1016/j.apacoust.2005.08.001`. (ref. on p. 162)

[169] **J. R. Mayer.** Bemerkungen über die Kräfte der unbelebten Natur. *Ann. Chemie*, 42(2): 233–240, 1842. DOI: `10.1002/jlac.18420420212`. (ref. on p. 19)

[170] **J. R. Mayer.** *Die organische Bewegung in ihrem Zusammenhange mit dem Stoffwechsel ein Beitrag zur Naturkunde.* Drechsler, Heilbronn, 1845. URL: `www.bsb-muenchen-digital.de/~web/web1013/bsb10134292/images/index.html?digID=bsb10134292` (ref. on p. 21)

[171] **D. McFarlane and K. Glover.** A loop-shaping design procedure using H_∞ synthesis. *IEEE Trans. Automatic Control*, 37(6):759–769, June 1992. DOI: `10.1109/9.256330`. (ref. on p. 61)

[172] **P. Mehta, A. Banaszuk, and M. Soteriou.** Impact of convection and diffusion processes in fundamental limitations of combustion control. In *2nd AIAA Flow Control Conf.* American Institute of Aeronautics and Astronautics, June 2004. DOI: `10.2514/6.2004-2410`. (ref. on p. 182)

[173] **F. R. Menter.** Two-equation eddy-viscosity turbulence models for engineering applications. *AIAA J.*, 32(8):1598–1605, 1994. DOI: `10.2514/3.12149`. (ref. on p. 25)

[174] **F. R. Menter and Y. Egorov.** The scale-adaptive simulation method for unsteady turbulent flow predictions. Part 1: Theory and model description. *Flow, Turbulence & Combustion*, 85:113–138, 2010. ISSN 1386-6184. DOI: `10.1007/s10494-010-9264-5`. (ref. on p. 25, 175)

[175] **H. J. Merk.** Analysis of heat-driven oscillations of gas flows. *Applied Sci. Research; Ser. A*, 6(4):317–336, 1957. ISSN 0365-7132. DOI: `10.1007/BF03184653`. (ref. on p. 62)

[176] **Microtech Gefell GmbH.** 1/4″ Kondensator Messmikrofonkapsel MK301. website, 2010. URL: `www.microtechgefell.de/index.php/en/microphones/95-2011-mikrofone-insgesamt` (ref. on p. 95)

[177] **P. J. Mohr, B. N. Taylor, and D. B. Newell.** CODATA recommended values of the fundamental physical constants: 2010. *Reviews of Modern Physics*, 84(4):1527–1605, 2008. DOI: `10.1103/RevModPhys.84.1527`. (ref. on p. xxiii, 228)

[178] **Monacor International.** KU-516 horn driver unit. data sheet, 2011. URL: `www.monacor.com/de/FLE/KU516.pdf` (ref. on p. xxiii, 165, 229, 233)

[179] **MOOG Inc.** Direct-operated servo valves for analog signals D633 and D634 series. Website, retreived April 2013. URL: `www.moog.com/products/servovalves-servo-proportional-valves/industrial/flow-control/analog-with-integrated-electronics/direct-operated-servo-valves-for-analog-signals-d633-d634-series` (ref. on p. 135, 137, 142, 165)

[180] **A. J. Moran, D. Steele, and A. P. Dowling.** Active control of combustion and its application. In *RTO / AVT Symp. "Active Control Technology…"*, Braunschweig, DE, 2000. URL: `www.dtic.mil/cgi-bin/GetTRDoc?Location=U2&doc=GetTRDoc.pdf&AD=ADP011145` (ref. on p. 6, 56, 60)

215

Bibliography

[181] **A. S. Morgans and A. P. Dowling.** Model-based control of combustion instabilities. In *ASME Turbo Expo*, No. GT2005-68897, 2005. (ref. on p. 56)

[182] **J. Morlet, G. Arens, E. Fourgeau, and D. Giard.** Wave propagation and sampling theory – Part I: Complex signal and scattering in multilayered media. *Geophysics*, 47(2):203–221, Feb. 1982. (ref. on p. 36)

[183] **G. Morrell and M. L. Pinns.** Effect of oxidizer particle size on solid-propelland combustion stability. Technical Note D-2736, NASA, Cleveland, US-OH, Apr. 1965. URL: `ntrs.nasa.gov/archive/nasa/casi.ntrs.nasa.gov/19650011392_1965011392.pdf` (ref. on p. 55)

[184] **E. O. Muñiz.** A method for deriving various formulas in electrostatics and electromagnetism using Lagrange's trigonometric identities. *American J. Physics*, 21:140–141, Feb. 1953. DOI: `10.1119/1.1933371`. (ref. on p. 29)

[185] **C. M. Müller, H. Breitbach, and N. Peters.** Partially premixed turbulent flame propagation in jet flames. In *25th Symp. (Int'l) Combustion*, pages 1099–1106. The Combustion Institute, 1994. DOI: `10.1016/S0082-0784(06)80747-2`. (ref. on p. 26, 175)

[186] **R. A. J. Müller, J. Hermann, and W. Polifke.** Stability limits and non-linear characteristics of a self-excited combustion instability. In *19th Int'l Cgr. Sound & Vibration (ICSV19)*, Vilnius, LT, 2012. (ref. on p. 85, 104)

[187] **R. A. J. Müller, J. Hermann, and W. Polifke.** Direct drive valve model for use as an acoustic source in a network model. *Int'l J. Acoustics & Vibration. In review.* (ref. on p. 135)

[188] **R. A. J. Müller, J. Hermann, and W. Polifke.** Direct drive valve model used as an acoustic source in a network model. In *19th Int'l Cgr. Sound & Vibration (ICSV19)*, Vilnius, LT, 2012. (ref. on p. 135)

[189] **R. A. J. Müller, J. Hermann, and W. Polifke.** Control authority over a combustion instability investigated in CFD. *Int'l J. Spray & Combustion Dynamics. Preliminarily accepted for publication.* (ref. on p. 165)

[190] **R. A. J. Müller, C. Temmler, R. Widhopf-Fenk, J. Hermann, W. Polifke, and P. Stopford.** CFD-based feasibility study of active control on a combustion instability. In *20th Int'l Cgr. Sound & Vibration (ICSV20)*, Bangkok, TH, 2013. (ref. on p. 165)

[191] **M. L. Munjal and A. G. Doige.** Theory of a two source-location method for direct experimental evaluation of the four-pole parameters of an acoustic element. *J. Sound & Vibration*, 141:323–333, 1990. (ref. on p. 148)

[192] **M+W Instruments GmbH.** Instruction manual Mass-Stream^TM D-6300. instruction manual, 2103. URL: `www.bronkhorst.com/files/downloads/manuals_english/mw_instruction_manual_d-6300_and_dimensional_drawings.pdf` (ref. on p. 90)

[193] **C. L. M. H. Navier.** Sur les lois du mouvement des fluides. *Mém. Acad. Sci.*, 6:389–440, 1823. URL: `gallica.bnf.fr/ark:/12148/bpt6k3221x/f577` (ref. on p. 16)

[194] **W. Neise and G. H. Koopmann.** Reduction of centrifugal fan noise by use of resonators. *J. Sound & Vibration*, 73(2):297–308, 1980. ISSN 0022-460X. DOI: `10.1016/0022-460X(80)90697-5`. (ref. on p. 54)

[195] **Y. Neumeier, E. Lubarsky, R. Heising, O. Israeli, M. Neumaier, and B. Zinn.** Liquid injector actuator for control of combustion processes. In *34th AIAA/ASME/SAE/ASEE Joint Propulsion Conf. & Ex.*, 1998. DOI: `10.2514/6.1998-3540`. (ref. on p. 58)

[196] **I. Newton.** *Philosophiæ naturalis principia mathematica*. S. Pepys, 1686. URL: `cudl.lib.cam.ac.uk/view/PR-ADV-B-00039-00001` (ref. on p. 18, 25)

[197] **National Institute of Standards and Technology (NIST).** NIST chemistry webbook. website, Feb. 2010. URL: `webbook.nist.gov/chemistry` NIST Standard Reference Database Number 69. (ref. on p. 120, 122)

[198] **N. Noiray, D. Durox, T. Schuller, and S. Candel.** A unified framework for nonlinear combustion instability analysis based on the flame describing function. *J. Fluid Mech.*, 615:139–167, 2008. DOI: `10.1017/S0022112008003613`. (ref. on p. 53)

[199] **A. N. Norris and I. C. Sheng.** Acoustic radiation from a circular pipe with an infinite flange. *J. Sound & Vibration*, 135(1):85–93, 1989. ISSN 0022-460X. DOI: `10.1016/0022-460X(89)90756-6`. (ref. on p. 71, 73)

[200] **H. Nyquist.** Regeneration theory. *Bell System Tech. J.*, 11:126–147, 1932. (ref. on p. 44, 45)

[201] **C. L. Oberg and A. L. Huebner.** Effects of aluminum on solid propellant combustion instability. Technical Report R-6654, Rocketdyne Canoga Park CA, July 1966. URL: `www.dtic.mil/docs/citations/AD0800268` (ref. on p. 55)

[202] **OMEGA Engineering inc.** Digital-Thermometer mit Thermoelement-Eingang und RS232C-Schnittstelle. URL: `www.omega.de/pptst/hh506a_hh506ra.html` (ref. on p. 96)

[203] **K. T. Padmanabhan, C. T. Bowman, and J. D. Powell.** An adaptive optimal combustion control strategy. *Combustion & Flame*, 100(1–2):101–110, 1995. ISSN 0010-2180. DOI: `10.1016/0010-2180(94)00081-3`. (ref. on p. 55, 58)

[204] **J. D. Paduano, A. H. Epstein, L. Valavani, J. P. Longley, E. M. Greitzer, and G. R. Guenette.** Active control of rotating stall in a low-speed axial compressor. *J. Turbomach.*, 115(1):48–56, Jan. 1993. DOI: `10.1115/1.2929217`. (ref. on p. 59)

[205] **S. L. Padula and R. K. Kincaid.** Optimization strategies for sensor and actuator placement. Technical report, NASA, 1999. URL: `ntrs.nasa.gov/archive/nasa/casi.ntrs.nasa.gov/19990036166_1999046403.pdf` TM-1999-209126. (ref. on p. 59)

[206] **R. L. Panton and J. M. Miller.** Resonant frequencies of cylindrical Helmholtz resonators. *J. Acoustical Soc. America*, 57(6):1533–1535, 1975. DOI: `10.1121/1.380596`. (ref. on p. 70)

[207] **J. H. Park and C. H. Sohn.** On optimal design of half-wave resonators for acoustic damping in an enclosure. *J. Sound & Vibration*, 319(3–5):807–821, 2009. ISSN 0022-460X. DOI: `10.1016/j.jsv.2008.06.049`. (ref. on p. 54)

[208] **S. Park, D. Wee, A. M. Annaswamy, and A. F. Ghoniem.** Adaptive low-order posi-cast control of a combustor test-rig model. In *41st IEEE Conf. Decision & Control*, vol. 4, pages 3698–3703. IEEE, 2002. (ref. on p. 61)

Bibliography

[209] **K. C. Patel.** *Production of uniform particles via single stream drying and new applications of the reaction eng. approach.* PhD thesis, Monash University, 2008. URL: `arrow.monash.edu.au/vital/access/services/Download/monash:7774/THESIS01` (ref. on p. 125)

[210] **T. Poinsot, F. Bourienne, S. M. Candel, E. Esposito, and W. Lang.** Suppression of combustion instabilities by active control. *J. Propulsion & Power*, 5(1):14–20, 1989. DOI: `10.2514/3.23108`. (ref. on p. 60, 166)

[211] **T. J. Poinsot, A. C. Trouve, D. P. Veynante, S. M. Candel, and E. J. Esposito.** Vortex-driven acoustically coupled combustion instabilities. *J. Fluid Mech.*, 177:265–292, Apr. 1987. DOI: `10.1017/S0022112087000958`. (ref. on p. 62)

[212] **Poisson.** Mémoire sur la théorie de son. *J. École Polytechnique*, 7(14):1–392, 1808. URL: `gallica.bnf.fr/ark:/12148/bpt6k433670m/f321.image` (ref. on p. 21, 65)

[213] **W. Polifke.** Combustion instabilities. In *Advances in acoustics and applications*, Brussels, BE, 2004. VKI Lecture series. (ref. on p. 46, 62, 128, 140)

[214] **W. Polifke, P. Flohr, and M. Brandt.** Modeling of inhomogeneously premixed combustion with an extended TFC model. *J. Eng. Gas Turbines & Power*, 124(1):58–65, 2002. DOI: `10.1115/1.1394964`. Originally published as ASME 2000-GT-135 (2000). (ref. on p. 26, 175)

[215] **W. Polifke, J. Kopitz, and A. Serbanovic.** Impact of the fuel time lag distribution in elliptical premix nozzles on combustion stability. In *7th AIAA/CEAS Aeroacoustics Conf.*, No. AIAA 2001-2104, Maastricht, NL, 2001. DOI: `10.2514/6.2001-2104`. (ref. on p. 53, 119, 177, 195)

[216] **W. Polifke, C. O. Paschereit, and K. Döbbeling.** Constructive and destructive interference of acoustic and entropy waves in a premixed combustor with a choked exit. *Int'l J. Acoustics & Vibration*, 6(3):135–146, 2001. (ref. on p. 117)

[217] **Pulsed Heat.** website, 2012. URL: `www.pulsedheat.com` (ref. on p. 198)

[218] **A. A. Putnam and W. R. Dennis.** Survey of organ-pipe oscillations in combustion systems. *J. Acoustical Soc. America*, 28(2):246–259, 1956. (ref. on p. 53)

[219] **A. A. Putnam and W. R. Dennis.** Burner oscillations of the gauze-tone type. *J. Acoustical Soc. America*, 26(5):716–725, 1954. DOI: `10.1121/1.1907406`. (ref. on p. 175)

[220] **R. Rajaram.** *Characteristics of sound radiation from turbulent premixed flames.* PhD thesis, Georgia Institute of Technology, 2007. (ref. on p.)

[221] **R. B. Randall.** *Vibration-based condition monitoring: Industrial, aerospace and automotive applications.* John Wiley & Sons, 1 edition, Jan. 2011. ISBN: 978-0-470-74785-8. (ref. on p. 38)

[222] **R. B. Randall.** *Frequency analysis.* K. Larsen & Søn, 1987. (ref. on p. 106)

[223] **R. L. Raun, M. W. Beckstead, J. C. Finlinson, and K. P. Brooks.** A review of Rijke tubes, Rijke burners and related devices. *Progr. in Energy & Combustion Sci.*, 19(4):313–364, 1993. DOI: `10.1016/0360-1285(93)90007-2`. (ref. on p. 4)

[224] **M. J. Reader-Harris, J. A. Sattary, and E. P. Spearman.** The orifice plate discharge coefficient equation—further work. *Flow Measurement & Instrumentation*, 6(2):101–114,

1995. DOI: `10.1016/0955-5986(94)00001-0`. (ref. on p. 92)

[225] **O. Reynolds.** An experimental investigation of the circumstances which determine whether the motion of water shall be direct or sinuous, and of the law of resistance in parallel channels. *Phil. Trans.*, 174:935–982, 1883. DOI: `10.1098/rstl.1883.0029`. (ref. on p. 18)

[226] **O. Reynolds.** On the dynamical theory of incompressible viscous fluids and the determination of the criterion. *Phil. Trans. R. Soc. London; Ser. A*, 186:123–164, Jan. 1895. DOI: `10.1098/rsta.1895.0004`. (ref. on p. 24)

[227] **R. R. Rhinehart, S. Gebreyohannes, U. M. Sridhar, A. Patrachari, and M. S. Rahaman.** A power law approach to orifice flow rate calibration. *ISA Trans.*, 50:329–341, 2011. (ref. on p. 141)

[228] **P. Riess.** Das Anblasen offener Röhren durch eine Flamme. *Ann. Physik*, 184:653–656, 1859. DOI: `10.1002/andp.18591841219`. (ref. on p. 4)

[229] **P. Riess.** Anhaltendes Tönen einer Röhre durch eine Flamme. *Ann. Physik*, 185:145–147, 1860. DOI: `10.1002/andp.18601850113`. (ref. on p. 4)

[230] **P. L. Rijke.** Notiz über eine neue Art, die in einer an beiden Enden offenen Röhre enthaltene Luft in Schwingungen zu versetzen. *Ann. Physik*, 183(6):339 – 343, 1859. DOI: `10.1002/andp.18591830616`. (ref. on p. 4)

[231] **W. Ritz.** Über eine neue Methode zur Lösung gewisser Variationsprobleme der mathematischen Physik. *J. reine & angew. Math.*, 135:1–61, 1909. URL: `www.digizeitschriften.de/dms/img/?PPN=PPN243919689_0135&DMDID=dmdlog4` (ref. on p. 24)

[232] **W. Ritz.** Theorie der Transversalschwingungen einer quadratischen Platte mit freien Rändern. *Ann. Physik*, 333:737–786, 1909. DOI: `10.1002/andp.19093330403`. (ref. on p. 24)

[233] **J. C. Román Casado and J. Kok.** Flame describing function measurements for limit cycle characterization. In *19th Int'l Cgr. Sound & Vibration (ICSV19)*, Vilnius, LT, 2012. (ref. on p. 11)

[234] **A. Saini.** High-temperature materials increase efficiency of gas power plants. *MRS Bull.; Ser. Energy Quarterly*, 37:550–551, June 2012. (ref. on p. 8)

[235] **E. Saint-Edme.** Appareil nouveaux contruits par M. R. Kœnig. *Cosmos; Ser. 2*, 1:457–462, 1865. URL: `babel.hathitrust.org/cgi/pt?id=nyp.33433057764437;view=1up;seq=479` (ref. on p. xv, 42)

[236] **Satelite TODAY.** Ariane 5 failure will cause 2 months delay. *News Feed*, Aug. 2001. URL: `www.satellitetoday.com/publications/st/feature/2001/08/15/ariane-5-failure-will-cause-2-months-delay` (ref. on p. 6)

[237] **K. C. Schadow.** Combustion dynamics: Passive combustion control. In *RTO / AVT Course "Active Control of Engine Dynamics"*, Brussels, BE, May 2001. URL: `ftp.rta.nato.int/public//PubFullText/RTO/EN/RTO-EN-020///EN-020-07.pdf` published in RTO-EN-020. (ref. on p. 53)

Bibliography

[238] **K. C. Schadow and H. Y. Ken.** Active combustion control: Recent R&D and outlook for implementation. In *Int'l Symp. Air Breathing Engines (ISABE)*, No. ISABE-2001-1018, 2001. (ref. on p. 14, 57, 135)

[239] **K. C. Schadow, V. Yang, F. E. C. Culick, T. J. Rosfjord, G. Sturgess, and B. T. Zinn.** AGARD workshops on active combustion control for propulsion systems. Technical Report 820, AGARD, 1997. URL: `ftp.rta.nato.int/Public/PubFullText/RTO/MP/RTO-MP-014/$MP-014-36.pdf` (ref. on p. 8, 9)

[240] **F. G. Schaffgotsch.** Akustische Beobachtungen. *Ann. Physik*, 177:471–487, 1857. DOI: `10.1002/andp.18571770711`. (ref. on p. 4)

[241] **F. G. Schaffgotsch.** Eine akustische Beobachtung. *Ann. Physik*, 176:352, 1857. DOI: `10.1002/andp.18571760220`. (ref. on p. 192)

[242] **B. Schuermans.** *Modeling and control of thermoacoustic instabilities.* PhD thesis, École Polytechnique Fédérale de Lausanne, 2003. URL: `biblion.epfl.ch/EPFL/theses/2003/2800/EPFL_TH2800.pdf` (ref. on p. 57, 59, 61, 166)

[243] **B. Schuermans, F. Bellucci, V. Guethe, F. Meili, P. Flohr, and C. O. Paschereit.** A detailed analysis of thermoacoustic interaction mechanisms in a turbulent premixed flame. In *Int'l Gas Turbine & Aeroengine Cgr. & Ex.*, No. GT2004-53831, Atlanta, US-GA, June 2004. (ref. on p. 78)

[244] **U. Schumann.** *Ein Verfahren zur direkten numerischen Simulation turbulenter Strömungen in Platten- und Ringspaltkanälen und über seine Anwendung zur Untersuchung von Turbulenzmodellen.* PhD thesis, Universität Karlsruhe, 1973. URL: `elib.dlr.de/53697` (ref. on p. 25)

[245] **C. Sensiau, F. Nicoud, and T. Poinsot.** A tool to study azimuthal standing and spinning modes in annular combustors. *Int'l J. Aeroacoustics*, 8(1):57–67, 2009. DOI: `10.1260/147547209786235037`. (ref. on p. 105)

[246] **C. J. T. Sewell.** The extinction of sound in a viscous atmosphere by small obstacles of cylindrical and spherical form. *Phil. Trans. R. Soc. London; Ser. A*, 210:239–270, Jan. 1911. DOI: `10.1098/rsta.1911.0007`. (ref. on p. 55)

[247] **A. F. Seybert and D. F. Ross.** Experimental determination of acoustic properties using a two-microphone random-excitation technique. *J. Acoustical Soc. America*, 61(5): 1362–1977, May 1977. (ref. on p. 98, 148, 149)

[248] **C. E. Shannon.** Communication in the presence of noise. *Proc. IRE*, 37(1):10–21, Jan. 1949. Reprint as classic paper in: Proc. IEEE 86(2), (Feb. 1998). (ref. on p. 33)

[249] **Siemens Saudi Arabia.** Turbine for combined cycle power plant. URL: `www.siemens.com.sa/en/products/energy/fossil_power_generation.htm` (ref. on p. 8)

[250] **M. Sliphorst.** *High frequency combustion instabilities of LOx/CH$_4$ spray flames in rocket engine combustion chambers.* PhD thesis, Technische Universiteit Delft, 2011. URL: `repository.tudelft.nl/assets/uuid:403ca079-82db-4d09-9676-c3b38c007283/Dissertation_Online.pdf` (ref. on p. 6)

[251] **J. Smagorinsky.** General circulation experiments with the primitive equations. *Mon. Wea. Rev.,* 91:99–164, 1963. DOI: `10.1175/ 1520-0493(1963)091<0099:GCEWTP>2.3.CO;2`. (ref. on p. 25)

[252] **R. H. Small.** Direct-radiator loudspeaker system analysis. *J. Audio Eng. Soc.,* 20:383–395, 1972. (ref. on p. 62, 162, 229)

[253] **R. H. Small.** Vented-box loudspeaker systems—Part 1: Small-signal analysis. *J. Audio Eng. Soc.,* 21(5):363–372, 1973. URL: `www.aes.org/e-lib/browse.cfm?elib=1967` (ref. on p. 231)

[254] **O. J. M. Smith.** US patent nr. 3,141,982. *Control system for use in control of loops with dead time,* July 1964. Filed 1960. (ref. on p. 61)

[255] **A. V. Sreenath and M. L. Munjal.** Evaluation of noise attenuation due to exhaust mufflers. *J. Sound & Vibration,* 12(1):1–19, 1970. ISSN 0022-460X. DOI: `10.1016/ 0022-460X(70)90045-3`. (ref. on p. 62)

[256] **K. R. Sreenivasan and S. Raghu.** The control of combustion instability: A perspective. *Computers & Structures,* 79(6):867–883, Sept. 2000. (ref. on p. 13)

[257] **D. St. John and G. S. Samuelsen.** Active, optimal control of a model industrial, natural gas-fired burner. In *25th Symp. (Int'l) Combustion,* pages 307–316, 1994. DOI: `10.1016/ S0082-0784(06)80657-0`. (ref. on p. 55)

[258] **L. Stanković.** An analysis of some time-frequency and time-scale distributions. *Ann. Télécommunication,* 49:505–517, 1994. DOI: `10.1007/BF02999442`. (ref. on p. 38)

[259] **W. H. Sterbentz and J. C. Evvard.** Criterions for prediction and control of ram-jet flow pulsations. Technical Report RM E51C27, NACA, May 1951. (ref. on p. 54)

[260] **G. G. Stokes.** On the steady motion of incompressible fluids. *Trans. Cambridge Phil. Soc.,* 7:439–454, 465, 1842. URL: `archive.org/stream/transactionsofca07camb#page/ n415` (ref. on p. 16, 18, 25)

[261] **G. G. Stokes.** On the friction of fluids in motion. *Trans. Cambridge Phil. Soc.,* 8(3): 287–319, 1849. URL: `www.biodiversitylibrary.org/item/49441#page/309` (ref. on p. 16, 18)

[262] **P. Subramanian, S. Mariappan, R. I. Sujith, and P. Wahi.** Bifurcation analysis of thermoacoustic instability in a horizontal Rijke tube. *Int'l J. Spray & Combustion Dynamics,* 2(4):325–355, Dec. 2010. DOI: `10.1260/1756-8277.2.4.325`. (ref. on p. 107)

[263] **X. Sun.** Vortex sound interaction and its application in aerospace propulsion system. In *19th Int'l Cgr. Sound & Vibration (ICSV19),* Vilnius, LT, 2012. URL: `www.iiav.org/ icsv19/speakers.html` (ref. on p. 54)

[264] **W. Sutherland.** The viscosity of gases and molecular force. *Phil. Magazine; Ser. 5,* 36 (223):507–531, 1893. DOI: `10.1080/14786449308620508`. (ref. on p. 124)

[265] **Rayleigh.** The explanation of certain acoustical phenomena. *Nature,* 18(455):319–321, July 1878. DOI: `10.1038/018319a0`. (ref. on p. 4, 22, 175)

[266] **Rayleigh.** *The theory of sound,* vol. 2. Macmillan, 1878. URL: `gallica.bnf.fr/ark:/ 12148/bpt6k95131k` (ref. on p. 73)

Bibliography

[267] **B. Taylor.** *Methodus incrementorum directa et inversa.* Impensis Gulielmi Innys, 1717. URL: `www.theeuropeanlibrary.org/tel4/record/1000126568674` (see also `www.17centurymaths.com/contents/taylorscontents.html`). (ref. on p. 34)

[268] **C. Temmler.** n, τ, Φ-Model in taX. Technical report, IfTA Ingenieurbüro für Thermo-akustik GmbH, 2013. (ref. on p. 78)

[269] **TEPCO.** Nuclear / TEPCO-power plants, Mar. 2010. URL: `www.tepco.co.jp/en/challenge/energy/nuclear/plants-e.html` (ref. on p. 6)

[270] **A. N. Thiele.** Loudspeakers in vented boxes: Part I. *J. Audio Eng. Soc.*, 19:382–392, 1971. (ref. on p. 62, 162, 229)

[271] **A. N. Thiele.** Loudspeakers in vented boxes: Part II. *J. Audio Eng. Soc.*, 20:471–483, 1971. (ref. on p. 162, 229)

[272] **M. Thiruchengode, S. Nair, S. Prakash, D. Scarborough, Y. Neumeier, J. Jagoda, T. Lieuwen, J. Seitzman, and B. Zinn.** An active control system for LBO margin reduction in turbine engines. In *AIAA 41st Aerospace Sci. Meeting & Ex.*, No. AIAA-2003-1008, Reno, US-NV, 2003. DOI: `10.2514/6.2003-1008`. (ref. on p. 53)

[273] **C. L. Tien and S. C. Lee.** Flame radiation. *Progr. in Energy & Combustion Sci.*, 8(1):41–59, 1982. ISSN 0360-1285. DOI: `10.1016/0360-1285(82)90008-9`. (ref. on p. 125)

[274] **H. S. Tsien.** Servo-stabilization of combustion in rocket motors. *J. American Rocket Soc.*, 22(5):256–262, 1952. DOI: `10.2514/8.4488`. (ref. on p. 55)

[275] **H. S. Tsien.** The transfer function of rocket nozzles. *J. American Rocket Soc.*, 22:139–143, 1952. (ref. on p. 136)

[276] **S. Tufano, P. Stopford, J. C. Román Casado, and J. B. W. Kok.** Modelling flame-generated noise in a partially premixed, bluff body stabilized model combustor. In *ASME Turbo Expo*, 2012. GT2012-69501. (ref. on p. 114)

[277] **J. Tyndall.** On the sounds produced by the combustion of gases in tubes. *J. Franklin Inst.*, 64(6):404–409, 1857. ISSN 0016-0032. DOI: `10.1016/0016-0032(57)90698-1`. (ref. on p. 4)

[278] **J. Tyndall.** The acoustic transparency and opacity of the atmosphere (part 1). *Nature*, 9: 251–253, Jan. 1874. DOI: `10.1038/009251a0`. (ref. on p. 55)

[279] **A. Ueda.** Kibitsu no kama (The cauldron of Kibitsu). In *Ugetsu Monogatari (Tales of Moonlight and Rain)*. 1776. URL: `etext.virginia.edu/japanese/ueda/ugetsu` retreived from Virginia University Library EText Center. (ref. on p. 3)

[280] **J. H. Uhm and S. Acharya.** Open loop control of combustion instability with a high-momentum air-jet. In *ASME Turbo Expo*, No. GT2004-53989, pages 657–664, 2004. DOI: `10.1115/GT2004-53989`. (ref. on p. 62, 197)

[281] **D. H. Utvik, H. J. Ford, and A. W. Blackman.** Evaluation of absorption liners for suppression of combustion instability in rocket engines. *J. Spacecraft & Rockets*, 3(7):1039–1045, 1966. DOI: `10.2514/3.28594`. (ref. on p. 54)

[282] **Verlag Dr. Hut.** Manuskript formatieren, 2013. URL: `www.hut-verlag.de/manuskript_formatieren.html` (ref. on p.)

[283] **H. Vernin and P. Pempie.** LOx/CH$_4$ and LOx/LH$_2$ heavy launch vehicle comparison. In *45th AIAA/ASME/SAE/ASEE Joint Propulsion Conf. & Ex.*, No. AIAA 2009-5133, Denver, US-CO, Aug. 2009. (ref. on p. 6)

[284] **J. Ville.** Théorie et applications de la notion de signal analytique. *Câbles et Transmission; Ser. 2*, June 1948. (ref. on p. 36)

[285] **Y. Wang, T. Megli, M. Haghgooie, K. S. Peterson, and A. G. Stefanopoulou.** Modeling and control of electromechanical valve actuator. In *Soc. Automotive Engineers, Inc.*, No. SAE 2002-01-1106, 2002. (ref. on p. 136, 138)

[286] **P. D. Welch.** The use of fast Fourier transform for the estimation of power spectra: A method based on time averaging over short, modified periodograms. *IEEE Trans. Audio & Electronics*, AU-15:70–73, 1967. (ref. on p. 33)

[287] **C. Wheatstone.** An account of some experiments to measure the velocity of electricity and the duration of electric light. *Phil. Trans. R. Soc. London*, 124:583–591, Jan. 1834. DOI: `10.1098/rstl.1834.0031`. (ref. on p. 4, 42)

[288] **B. Widrow.** *Aspects of network and system theory*, chapter Adaptive Filters, pages 563–586. Holt, Rinehart and Winston, New York, US-NY, 1971. (ref. on p. 60)

[289] **E. Wigner.** On the quantum correction for thermodynamic equilibrium. *Physical Review*, 40:749–759, June 1932. DOI: `10.1103/PhysRev.40.749`. (ref. on p. 36)

[290] **R. N. Wimpress.** *Internal ballistics of solid-fuel rockets; military rockets using dry-processed double-base propellant as fuel.* McGraw-Hill, New York, 1 edition, 1950. (ref. on p. 5, 52)

[291] **K. Yu, K. J. Wilson, T. P. Parr, and K. C. Schadow.** An experimental study on actively controlled dump combustors. In *RTO / AVT Symp. "Active Control Technology…"*, Braunschweig, DE, May 2000. URL: `ftp.rta.nato.int/public//PubFullText/RTO/MP/RTO-MP-051///MP-051-PSP-36.pdf` (ref. on p. 61)

[292] **U. Zechbauer.** Materials for the environment—Ceramic heat shields. *Pictures of the Future*, Fall 2007. URL: `www.siemens.com/innovation/en/publikationen/publications_pof/pof_fall_2007/materials_for_the_environment/ceramic_heat_shields.htm` (ref. on p. 8)

[293] **Y. B. Zel'dovich, G. I. Barenblatt, V. B. Librovich, and G. M. Mikhviladze.** *The mathematical theory of combustion and explosions.* 1985. (ref. on p. 8)

[294] **D. Zhao and A. S. Morgans.** Tuned passive control of combustion instabilities using multiple Helmholtz resonators. *J. Sound & Vibration*, 320(4–5):744–757, 2009. ISSN 0022-460X. DOI: `10.1016/j.jsv.2008.09.006`. (ref. on p. 54)

[295] **V. A. Zimont, W. Polifke, M. Bettelini, and W. Weisenstein.** An efficient computational model for premixed turbulent combustion at high Reynolds numbers based on a turbulent flame speed closure. *J. Eng. Gas Turbines & Power*, 120:526–532, 1998. DOI: `10.1115/1.2818178`. Originally published as ASME 97-GT-395 (1997). (ref. on p. 26, 175)

[296] **B. T. Zinn.** Smart combustors — just around the corner. In *ASME Turbo Expo*, No. GT2005-69138, 2005. (ref. on p. 197)

Bibliography

[297] **B. T. Zinn, E. Lubarsky, and Y. Neumeier.** Overview of different approaches for active control of combustion instabilities. In *14th Int'l Conf. Sound & Vibrations (ICSV14)*, Cairns, AU, July 2007. (ref. on p. 53)

[298] **B. T. Zinn and Y. Neumeier.** An overview of active control of combustion instabilities. In *AIAA Meeting*, 1997. DOI: `10.2514/6.1997-461`. (ref. on p. 55, 166)

[299] **E. Zukoski.** *The aerothermodynamics of aircraft gas turbine engines*, chapter 21: Afterburners. No. ADA059784. University of Washington, 1978. URL: `oai.dtic.mil/oai/oai?verb=getRecord&metadataPrefix=html&identifier=ADA059784` (ref. on p. 9)

Appendices

Appendix A

Gas properties and physical quantities

Property			Dry air	Methane
	Symbol	Units	$(21\,\%\,O_2, 79\,\%\,N_2)$	(CH_4)
Molar mass				
	$\underset{\sim}{m}$	kg/kmol	28.95	16.043
Heat capacity				
	$\underset{\sim}{C}_p$	J/(kmol K)	$29 \cdot 10^3$ [(I)]	$35 \cdot 10^3$ [(II)]
	$\underset{\sim}{C}_V$	J/(kmol K)	$20 \cdot 10^3$ [(I)]	$27 \cdot 10^3$ [(II)]
Heat capacity ratio				
	γ	–	1.4028	1.3055
Dynamic viscosity				
	μ	Pa s	$16.95 \cdot 10^{-6}$ [(III)]	$10.27 \cdot 10^{-6}$ [(III)]

[(I)] Determined at $p = 101.3 \cdot 10^3$ Pa, $T = 21\,°C$
[(II)] Determined at $p = 100 \cdot 10^3$ Pa, $T = 25\,°C$
[(III)] Determined at $p = 101.3 \cdot 10^3$ Pa, $T = 0\,°C$

Table A.1: Properties of dry air and methane according to Air Liquide[5]

Gas	Symbol	Formation enthalpy $\overset{\star}{\underset{\sim}{H}}$ (J/kmol)	Molar mass $\underset{\sim}{m}$ (kg/kmol)
Nitrogen	N_2	0.0 [I]	28.0134
Oxygen	O_2	0.0 [I]	31.9988
Methane	CH_4	$-74.87 \cdot 10^6$	16.0425
Water vapour	H_2O	$-241.83 \cdot 10^6$	18.0153
Carbon dioxide	CO_2	$-393.52 \cdot 10^6$	44.0095

[I] Zero by definition for the most stable form of mono-atomic gases

Table A.2: Properties of pure gases according to Chase[41]

Quantity	Symbol	Units	Value
Absolute gas constant	$\tilde{R}_{abs}$	$J/(kmol\,K)$	$8314.472(15)$
Stefan–Boltzmann constant	σ_{SB}	$W/(m^2\,K^4)$	$56.70400(40) \cdot 10^{-9}$
Avogadro's number	N_A	mol^{-1}	$602.214479(30) \cdot 10^{21}$

Table A.3: Other quantities according to Mohr et al.[177: p.1586]

Appendix B

Physics-based description of a loudspeaker

The current research makes use of the horn driver unit KU-516 by Monacor International,[178] powered by the IMG Stage Line amplifier AKB-50 by Inter Mercador.[125] The horn driver unit modulates the flow by moving its diaphragm or cone over a certain distance. As a result, a small volume V_{ls} is cyclically added to and removed from the flow, which can be used as a velocity boundary condition:

$$\frac{\dot{V}_{\text{ls}}}{A_{\text{ref}}} = u'_{\text{ls}} = f + \mathscr{g} \, .$$

The simple loudspeaker in taX is modelled as a pulsating volume source. This is a valid way to describe a loudspeaker over a certain frequency range. From the perspective of control authority, it would be helpful to know over which frequency range this assumption is valid, what happens outside of this range, and how much volume can be modulated by the loudspeaker.

B.1 The dynamic system

Loudspeakers have been studied intensively for the purpose of audio engineering. Thiele[270, 271] and Small[252] for instance made great progress by analysing electric circuit representations of loudspeaker boxes. The dynamical system is shown in fig. B.1.

The voice coil (indicated as motor 'M' or subscript 'vcl') exerts a force on the loudspeaker cone ('cn'), given by the expression for Lorentz[160] force:

$$\vec{F}_{\text{vcl}} = I_{\text{vcl}} \int_{L_{\text{vcl}}} \left(\mathrm{d}\vec{L}_{\text{vcl}} \times \vec{B}_{\text{vcl}} \right) \, .$$
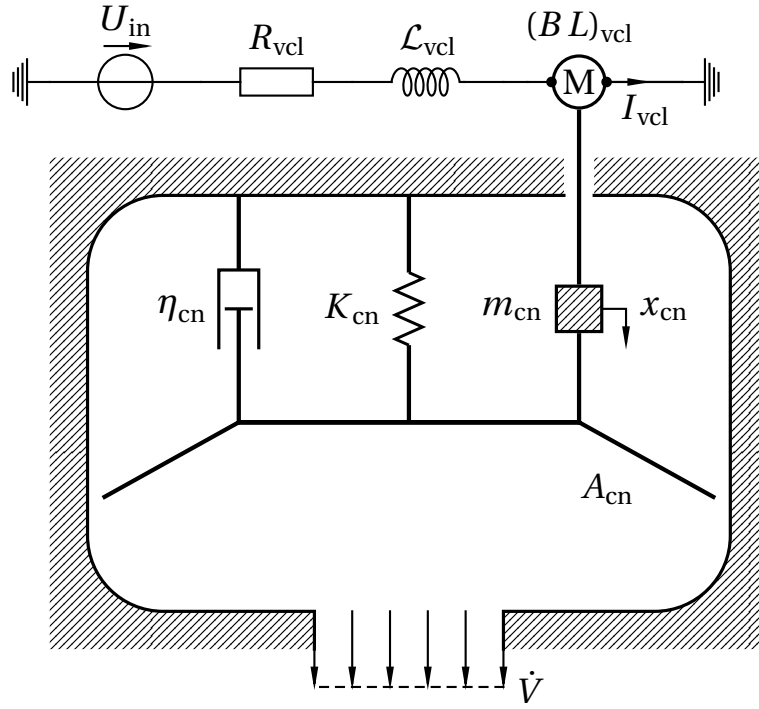
Figure B.1: Main electric and mechanical elements determining the dynamic behaviour of a loudspeaker.

Usually by design $\mathrm{d}\vec{L}_{\mathrm{vcl}} \perp \vec{B}_{\mathrm{vcl}}$ and $\mathrm{sgn}\, F_{\mathrm{vcl}} = \mathrm{sgn}\, I_{\mathrm{vcl}}$, so

$$F_{\mathrm{vcl}} = I_{\mathrm{vcl}}\, L_{\mathrm{vcl}}\, B_{\mathrm{vcl}} \,.$$

Movement of the cone in turn causes a reduction of the voltage over the ends of the voice coil, given by Faraday's[75] law of induction:

$$U_{\mathrm{vcl}} = U_{\mathrm{in}} - \left(\vec{u}_{\mathrm{cn}} \times \vec{B}_{\mathrm{vcl}}\right) \cdot \vec{L}_{\mathrm{vcl}} \,.$$

Again by design

$$U_{\mathrm{vcl}} = U_{\mathrm{in}} - \vec{u}_{\mathrm{cn}}\, \vec{B}_{\mathrm{vcl}}\, \vec{L}_{\mathrm{vcl}} \,.$$

The cone is characterised as a second order spring–mass–damper system:

$$
\begin{aligned}
m_{\mathrm{cn}}\, \partial_t u_{\mathrm{cn}} &= \sum F_{\mathrm{cn}} \\
&= -K_{\mathrm{cn}}\, x_{\mathrm{cn}} - \eta_{\mathrm{cn}}\, u_{\mathrm{cn}} - p'_{\mathrm{ls}}\, A_{\mathrm{cn}} + I_{\mathrm{vcl}}\, L_{\mathrm{vcl}}\, B_{\mathrm{vcl}} \,.
\end{aligned}
$$

The electric current through the voice coil depends on the voltage as

$$I_{\mathrm{vcl}} = \frac{U_{\mathrm{vcl}}}{\mathcal{L}_{\mathrm{vcl}}\, \mathrm{i}\omega + R_{\mathrm{vcl}}} \,.$$

The full system of equations is represented graphically in fig. B.2.

Small[253: p.318] suggests the inductance $\mathcal{L}$ can usually be neglected, as it becomes significant only at much higher frequencies than at which the loudspeaker driver is usually operated. The system can now be described in matrix form as

$$
i\omega \begin{bmatrix} u'_{cn} \\ x'_{cn} \end{bmatrix} = \overbrace{\begin{bmatrix} -\frac{(BL)^2}{Rm} - \frac{\eta}{m} - \frac{A^2_{cn}}{A_{out}}\frac{\bar{\rho}c}{m} & -\frac{K}{m} \\ 1 & 0 \end{bmatrix}}^{A} \begin{bmatrix} u'_{cn} \\ x'_{cn} \end{bmatrix} + \overbrace{\begin{bmatrix} \frac{BL}{Rm} & -A_{cn}\frac{\bar{\rho}c}{m} \\ 0 & 0 \end{bmatrix}}^{B} \begin{bmatrix} U_{in} \\ \mathcal{G} \end{bmatrix}
$$

$$
f = \underbrace{\begin{bmatrix} \frac{A_{cn}}{A_{out}} & 0 \end{bmatrix}}_{C} \begin{bmatrix} u'_{cn} \\ x'_{cn} \end{bmatrix} + \underbrace{\begin{bmatrix} 1 & 0 \end{bmatrix}}_{D} \begin{bmatrix} \mathcal{G} \\ U_{in} \end{bmatrix} ,
$$

or equivalently

$$
f = \frac{A_{cn}}{A_{out}} \frac{\frac{A_{cn}}{m}\bar{\rho}c\,\mathcal{G} - \frac{BL}{Rm}U_{in}}{\left(-\frac{(BL)^2}{Rm} - \frac{\eta}{m} \right) - \frac{K}{m}\frac{1}{i\omega} - i\omega} + \mathcal{G} .
$$

Not all variables need to be determined individually. Instead some meaningful groups can be defined as follows:

- The mechanical resonance frequency of the loudspeaker:

$$
\omega_I^2 = \frac{K}{m} .
$$

- The combined electromechanical quality or Q-factor $\mathcal{Q}_{tot}$ of the loud-speaker is a measure for the sharpness of the resonance peak; half the reciprocal value of the damping ratio:

$$
\mathcal{Q}_{tot}\,\omega_I = \frac{(BL)^2}{Rm} + \frac{\eta}{m} .
$$

- Acoustic absorption or coupling – which is of much smaller importance in audio loudspeaker design,[253] due to the large value of A_{out} – is expressed by the value $\mathcal{A}_0$:

$$
\mathcal{A}_0 = A^2_{cn}\frac{\bar{\rho}c}{m} .
$$
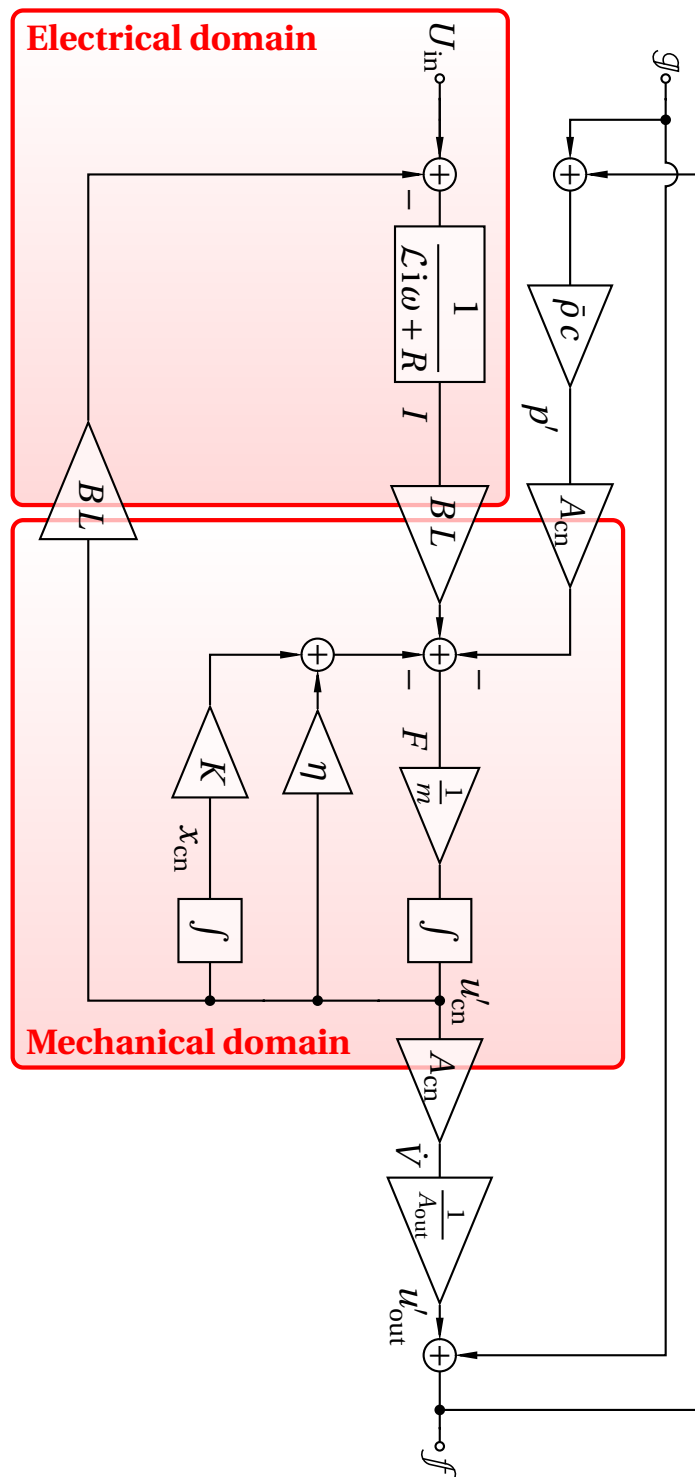
Figure B.2: Overview of the relations governing the dynamic behaviour of the loudspeaker.

- The source term is characterised by the combined value $\mathcal{S}_0$:

$$\mathcal{S}_0 = A_{\text{cn}} \frac{BL}{Rm}\,.$$

Sound emission and reflection are expected to behave globally as

$$A_{\text{out}}\, f = \frac{\mathcal{S}_0\, U_{\text{in}} - \mathcal{A}_0\, \mathcal{G}}{-\mathrm{i}\omega - \mathcal{Q}_{\text{tot}}\,\omega_{\text{I}} - \mathcal{A}_0 \big/ A_{\text{out}} - \omega_{\text{I}}^2 \big/ (\mathrm{i}\omega)} + A_{\text{out}}\, \mathcal{G}\,.$$

B.2 Current hardware

The specifications of the horn driver unit KU-516 according to the manufacturer are listed in tbl. B.1. Unfortunately these quantities correspond not very well to those required in the previous section.

Quantity	Value
Frequency range	$160\,\text{Hz} < f < 6500\,\text{Hz}$
Music power	$75\,\text{W}$
Power rating	$50\,\text{W}$
impedance	$16\,\Omega$
SPL at 1kHz	$113\,\text{dB}\ (1\,\text{W}/1\,\text{m})$
Dimension	$\varnothing 125 \times 100\,\text{mm}$
Weight	$2.1\,\text{kg}$

Table B.1: Specification of the horn driver unit KU-516 according to Monacor International.[178]

Moreover, the quantities from tbl. B.1 are not easily measured directly. Instead, the sound production and reflection could be measured with the two-microphone method as introduced in secs. 4.3 and 5.4.

Appendix C

Reference spectra for the Limousine combustor

C.1 Set-up

The version of the Limousine combustor used at IfTA has 18 holes on the side for sensor access, as shown in figure fig. C.1. These holes are numbered 0 to 20, and are placed at 50 mm intervals. Due to constructional constraints there are no holes at position 5, on the top of the flame holder and at position 8, which is in the top of the window frame. Hole 0 is too close to the air inlet orifice to attach a pressure sensor. To accommodate holes 6 and 7, one quartz window has been replaced by a steel plate.

The frequency spectra are measured for thermal power

$$P_{\text{th}} \in \{20, 30, 40\}\,\text{kW}$$

and equivalence ratio

$$\Phi \in \{0.83, 0.71, 0.63\}\ ,$$

corresponding to air excess ratio

$$\Lambda \in \{1.2, 1.4, 1.6\}\ .$$

C.2 Pressure sensors

Two pressure sensors were used during this measurement. These sensors have a resolution of 0.48 Pa and a resonance frequency > 40 kHz. Before the measurement on the burner, the difference in frequency response between the sensors has been determined in phase and amplitude. The data presented here are compensated for this difference in sensor response.
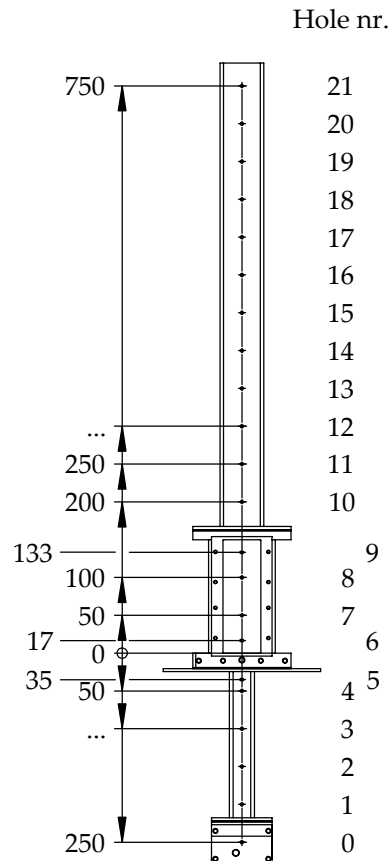
Figure C.1: Position of the sensor-access holes in the Limousine combustor.

C.3 Method

The sensors are located in holes 1 and 6. The data from hole 1 are meant for evaluation of the frequency spectra. The data from hole 6, subject to significant combustion noise, are meant to determine the transfer function of the pressure fluctuations between the two locations. This transfer function can be used by partners who do not have the possibility to measure at the location of the flame.

After the temperature settled to a steady value, measured with a thermocouple above the burner, the signals are recorded and analysed by the Argus system. The signals of the sensors are cut in 0.2 s segments which overlap 50 %. After application of a Blackman window, the signal is transferred to the frequency

domain using a fast Fourier transform. Auto- and cross-spectral-density are computed and averaged over 200 of these cycles. One such measurement takes 20 s, and delivers a spectrum for $f \in [0, 2000]$ Hz.

Before and after the measurement, the sensors were calibrated against each other. Below 1000 Hz, the difference between the phase and magnitude of the sensor signals was less than 0.02 rad and 1 % respectively. The error around the dominant frequency was a fraction thereof. Therefore, no correction was deemed necessary.

The time given for the temperature to settle was different for the transitions between the various operating conditions. To give an idea: the first operating condition, 20 kW and $\Phi = 0.83$ ($\Lambda = 1.2$) was running 9 min before the measurement was started. Subsequent measurements needed less time, since the burner was already warmed up.

C.4 Results

The following tables and graphs give details on the operating conditions and the resulting measured oscillations. The spectra show the square root of the auto correlation function of the sensor at hole 1. This is effectively the L^2 norm (averaged over time) of the absolute value of the Fourier transformed pressure. The rings indicate the frequency and amplitude of the dominant oscillation as identified by the Argus measurement system. In the cases where there is no steady limit cycle, this can be higher than the value shown in the spectrum (in case the frequency is not constant and therefore the frequency is 'smeared out') or lower than the spectrum (in case the amplitude is not constant, and the higher values are more pronounced in the L^2 norm).

O.P.			$\dot{n}_{CH_4}$	$\dot{n}_{air}$	P_{act}	Λ_{act}
P_{nom}	Φ_{nom}	Λ_{nom}	kmol/s	kmol/s	kW	–
20	0.83	1.2	$2.64 \cdot 10^{-5}$	$2.98 \cdot 10^{-4}$	21.2	1.185
20	0.71	1.4	$2.64 \cdot 10^{-5}$	$3.57 \cdot 10^{-4}$	21.2	1.421
20	0.60	1.6	$2.64 \cdot 10^{-5}$	$4.06 \cdot 10^{-4}$	21.2	1.616
30	0.83	1.2	$3.96 \cdot 10^{-5}$	$4.70 \cdot 10^{-4}$	31.8	1.245
30	0.71	1.4	$3.96 \cdot 10^{-5}$	$5.40 \cdot 10^{-4}$	31.8	1.431
30	0.60	1.6	$3.96 \cdot 10^{-5}$	$6.06 \cdot 10^{-4}$	31.8	1.608
40	0.83	1.2	$5.28 \cdot 10^{-5}$	$6.24 \cdot 10^{-4}$	42.3	1.241
40	0.71	1.4	$5.28 \cdot 10^{-5}$	$7.01 \cdot 10^{-4}$	42.3	1.395
40	0.60	1.6	$5.28 \cdot 10^{-5}$	$8.13 \cdot 10^{-4}$	42.3	1.618

Table C.1: Nominal (set) and actual (measured) operating conditions

C.4 Results

| O.P.				f_{dom}	$|p_1|$	$|p_6|$	arg	coh
P_{nom}	Φ_{nom}	Λ_{nom}		Hz	Pa	Pa	rad	–
20	0.83	1.2	LC	192	1050	550	0.35	1.00
20	0.71	1.4	LC	177	900	450	0.28	1.00
20	0.60	1.6	noise	167	25	15	0.31	0.97
30	0.83	1.2	LC	222	1400	580	0.68	1.00
30	0.71	1.4	LC	212	1300	550	0.61	1.00
30	0.60	1.6	noise	185	22	12	0.56	1.00
40	0.83	1.2	LC	253	1800	750	1.19	1.00
40	0.71	1.4	LC	241	1650	720	1.01	1.00
40	0.60	1.6	noise	185	25	15	0.65	0.92

Table C.2: Characterisation of the dominant oscillation for the measured operating conditions. LC stands for limit cycle.
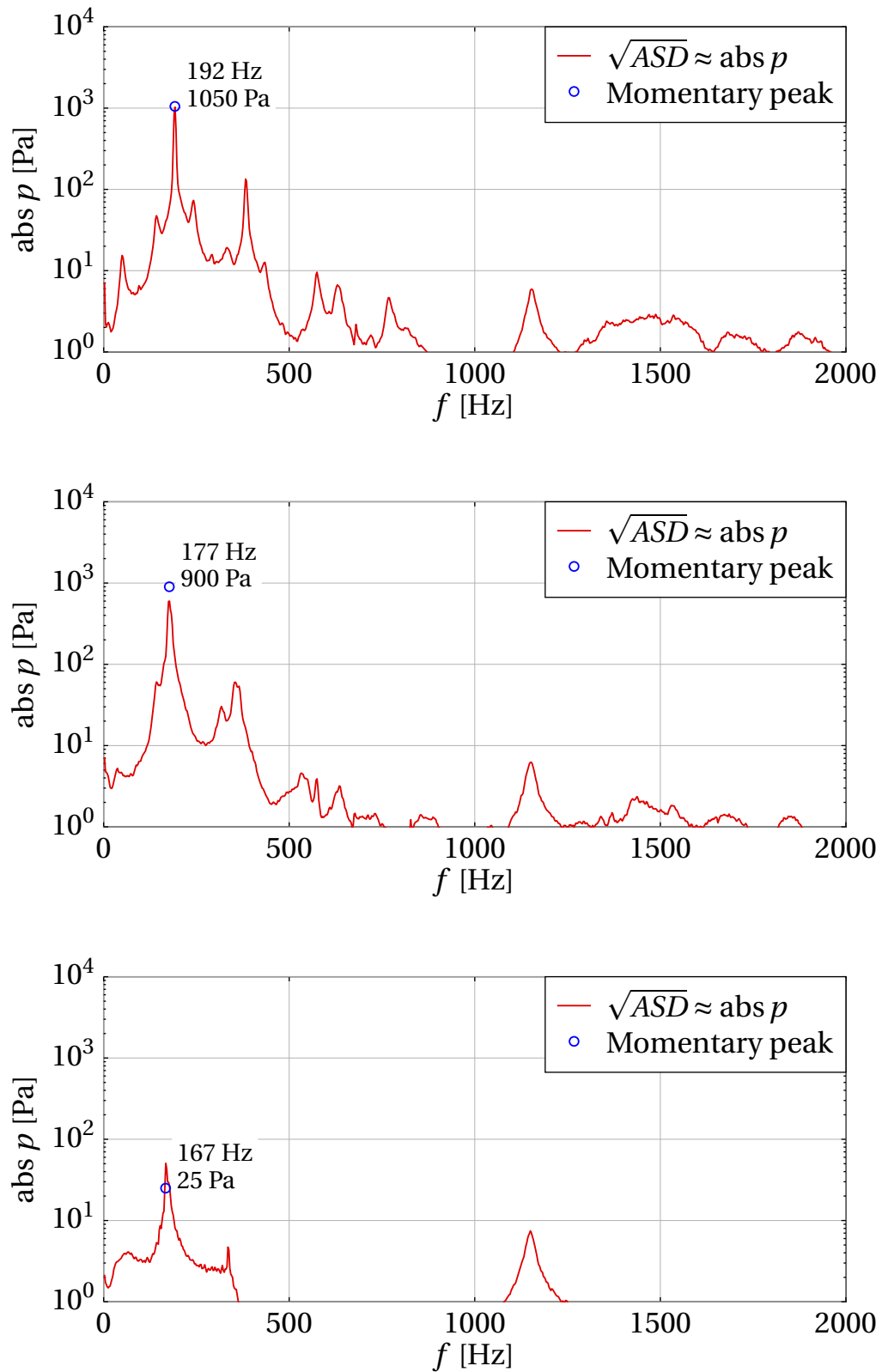
Figure C.2: Measured pressure spectrum for $P_{th} = 20\,\mathrm{kW}$; top: $\Phi = 0.83$ ($\Lambda = 1.2$), middle: $\Phi = 0.71$ ($\Lambda = 1.4$), bottom: ($\Phi = 0.60$) ($\Lambda = 1.6$).
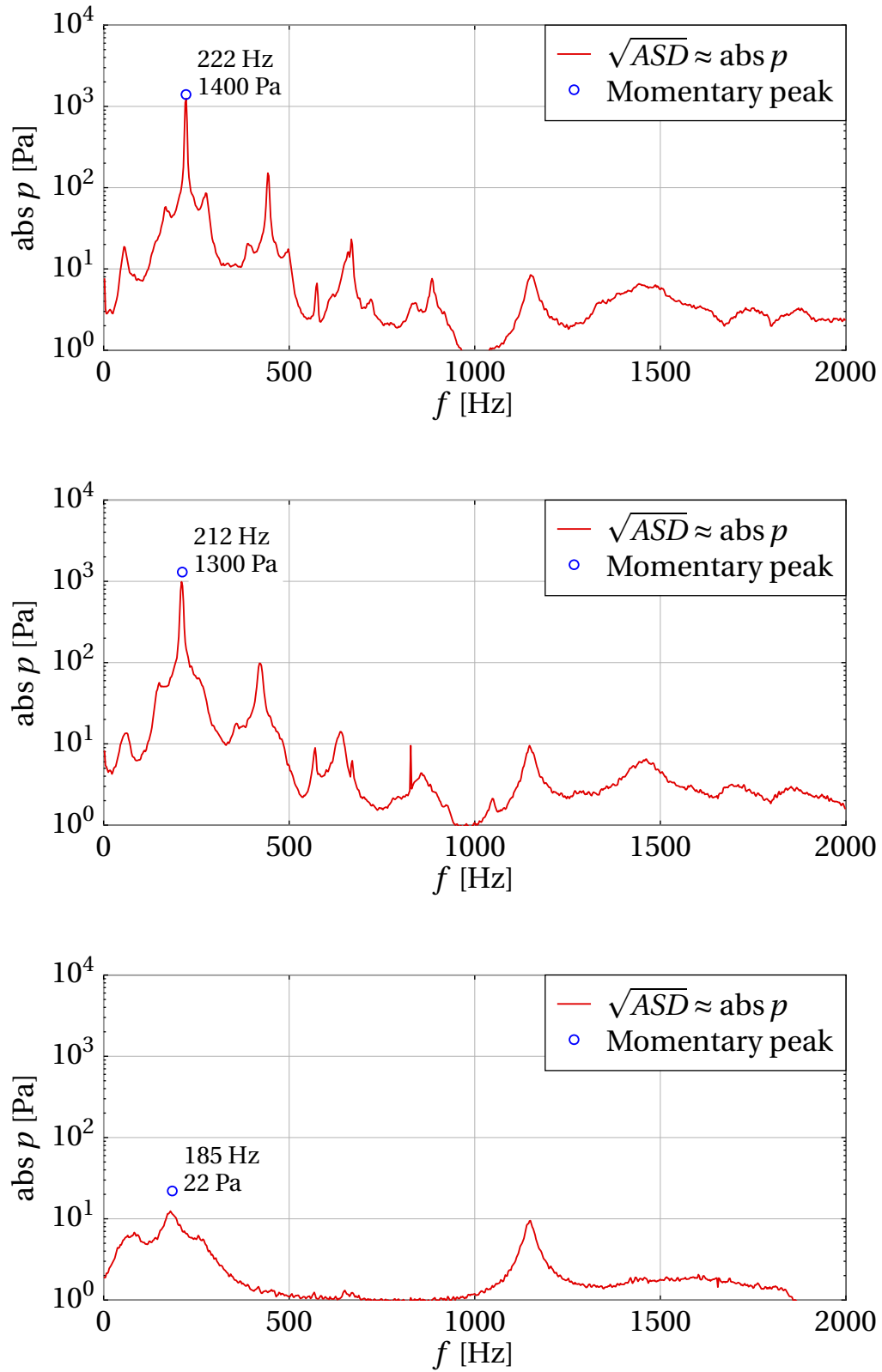
Figure C.3: Measured pressure spectrum for $P_{\mathrm{th}} = 30\,\mathrm{kW}$; top: $\Phi = 0.83$ ($\Lambda = 1.2$), middle: $\Phi = 0.71$ ($\Lambda = 1.4$), bottom: ($\Phi = 0.60$) ($\Lambda = 1.6$).
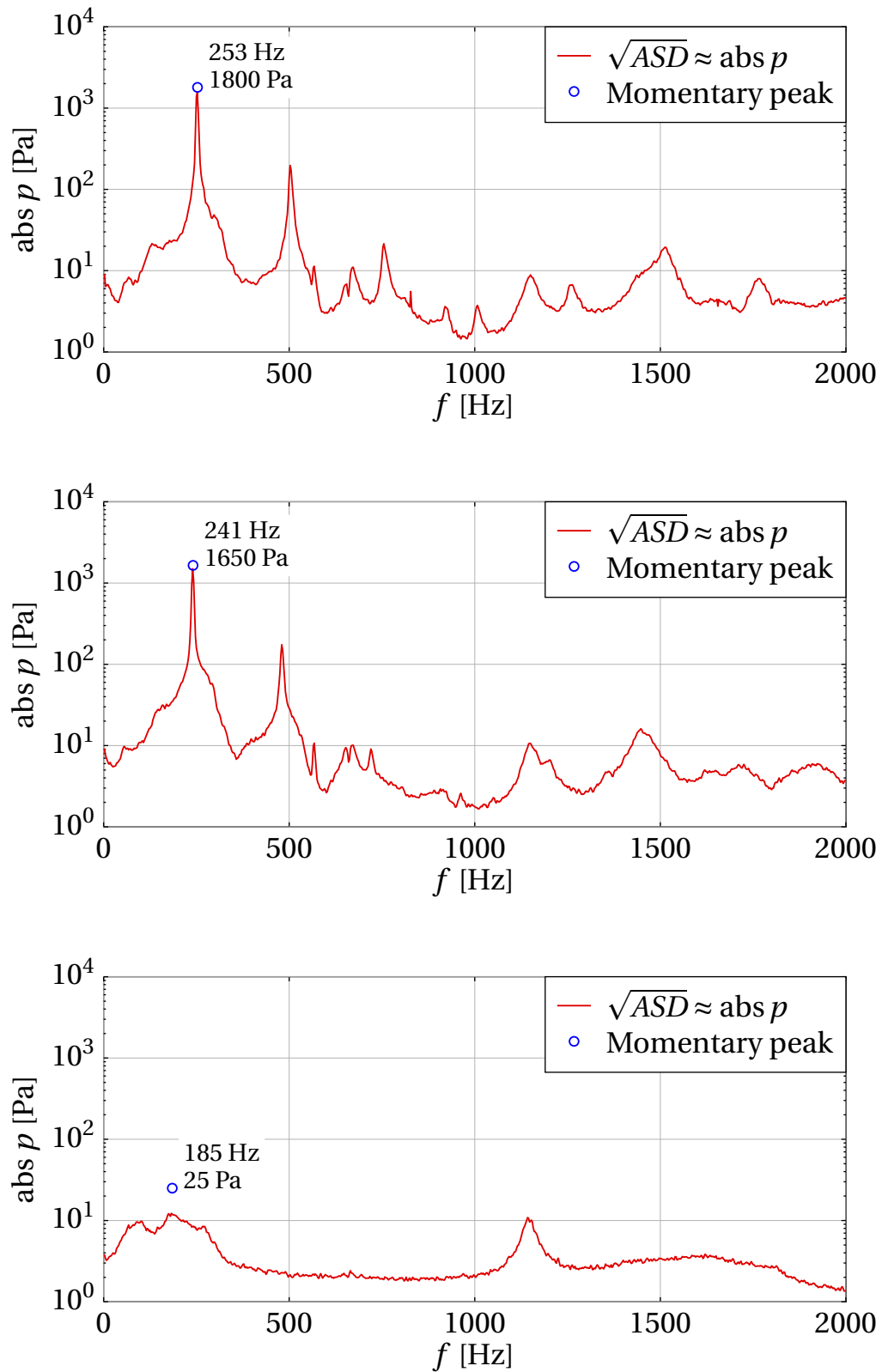
Figure C.4: Measured pressure spectrum for $P_{th} = 40\,\text{kW}$; top: $\Phi = 0.83$ ($\Lambda = 1.2$), middle: $\Phi = 0.71$ ($\Lambda = 1.4$), bottom: ($\Phi = 0.60$) ($\Lambda = 1.6$).